SANDIA REPORT
SAND2019-0290
Printed January 2019

NSRD-16: Computational Capability to Substantiate DOE-HDBK-3010 Data

David L.Y. Louie, John Bignell, San Le, Remi Dingreville, Lindsay N. Gilkey, Natalie Gordon and Dominic G. Fascitelli

Prepared by
Sandia National Laboratories
Albuquerque, New Mexico
87185 and Livermore,
California 94550

Issued by Sandia National Laboratories, operated for the United States Department of Energy by National Technology & Engineering Solutions of Sandia, LLC.

ABSTRACT

Safety basis analysts throughout the U.S. Department of Energy (DOE) complex rely heavily on the information provided in the DOE Handbook, DOE-HDBK-3010, Airborne Release Fractions/Rates and Respirable Fractions for Nonreactor Nuclear Facilities, to determine radionuclide source terms from postulated accident scenarios. In calculating source terms, analysts tend to use the DOE Handbook's bounding values on airborne release fractions (ARFs) and respirable fractions (RFs) for various categories of insults (representing potential accident release categories). This is typically due to both time constraints and the avoidance of regulatory critique. Unfortunately, these bounding ARFs/RFs represent extremely conservative values. Moreover, they were derived from very limited small-scale bench/laboratory experiments and/or from engineered judgment. Thus, the basis for the data may not be representative of the actual unique accident conditions and configurations being evaluated.

The goal of this research is to develop a more accurate and defensible method to determine bounding values for the DOE Handbook using state-of-art multi-physics-based computer codes. This enables us to better understand the fundamental physics and phenomena associated with the types of accidents in the handbook. In this fourth year, we improved existing computational capabilities to better model fragmentation situations to capture small fragments during an impact accident. In addition, we have provided additional new information for various sections of Chapters 4 and 5 of the Handbook on free fall powders and impacts of solids, and have provided the damage ratio simulations for containers (7A drum and standard waste box) for various drops and impact scenarios. Thus, this work provides a low-cost method to establish physics-justified safety bounds by considering specific geometries and conditions that may not have been previously measured and/or are too costly to perform during an experiment.

ACKNOWLEDGEMENTS

The authors express thank to many colleagues at SNL, including Johann D. Snyder for editing and formatting the report, Nicole Lucero and Carol Alvin for their high performance computing support for our SIERRA simulations, and Dr. Michael Tupek for his assistance with the gradient damage explicit model of SIERRA solid mechanics. The authors also express thanks to Gregory Van Soest of LANL for providing the Site TRU waste inventory and Daniel Staber of Nuclear Waste Partnership, LLC for providing the references on waste container test data. Finally, the authors would like to express their appreciation to Dr. Alan Levin and Patrick Frias of DOE Nuclear Safety Research and Development (NSR&D) Program for overseeing this research. The NSR&D Program is managed by the Office of Nuclear Safety, within the Office of Environment, Health, Safety and Security (AU). This work is supported by the DOE NSR&D Program under WAS Project No. 2017-AU33-SNL-NSRD.

CONTENTS

LIST OF FIGURES

LIST OF TABLES

This page left blank

ACRONYMS AND DEFINITIONS

Abbreviation	Definition
1D	One-dimensional
3D	Three-dimensional
AMMD	Aerodynamic equivalent mass median diameter
ASTM	American Society for Testing and Materials
ARF	Airborne release fraction
BC	Bottom center in Table 3-14
CCO	Critically control overpack
CS	contaminated soil
DOE	Department of Energy
DR	Damage ratio
EIE	Evaporation induced entrainment
EOS	Equation of state
FD	Fluid dynamics
Fi	Fixed in Table 3-14
Fr	Free in Table 3-14
FY	Fiscal year
GDE	Gradient damage explicit
HD	heterogenous debris
HEPA	High efficiency particulate air
HGDE	Hierarchical Gradient Damage Explicit
hr	Hour
ID	Identification
ITAR	International Traffic in Arms Regulations
LANL	Los Alamos National Laboratory
LAME	Library for Advanced Materials Engineering (Material models for SIERRA/SM)
LC	Lid-center
Ma	Mach number
mph	Miles per hour
NSRD	Nuclear Safety Research and Development
PARE	Pressurized airborne release tank
POC	pipe overpack container
QoI	quantity of interest
RART	Radioactive airborne release tank
RF	Respirable fraction
SD	Structural dynamics
SI	solidified inorganics
SL	Slide near lid in Table 3-14
SM	Solid mechanics, side middle in Table 3-14
SNL	Sandia National Laboratories
SPH	Smoothed particle hydrodynamics
ST	Source term
SWB	standard waste box
TF	Thermal fluid
TRU	Transuranic
WIPP	Waste Isolation Pilot Plant

Symbols for Chapter 2

Symbol	Definition
A	Correlated coefficient in Equation (2-1), (2-7)
C1, C2	Fitted constants for Equation (2-2)
D	Average diameter in Equation (2-3)
E_{impact}	Impact energy
F	Material flow
Fr	Airborne fraction in Equation (2-5)
Frac	Fraction of particles in Equation (2-3)
H, h	Fall height or distance
G	Fraction of dust particles generated in Equation (2-3)
g	Gravity
M_o	Mass of powder spilled
P	Specimen density
ρ	Density
W	Moisture content in Equation (2-3)
W_m	Kinetic energy or impact energy for Equation (2-2)
m	Mass (kilograms)
N	Dichotmous variable in Equation (2-7)
$\boldsymbol{t}$	Time (seconds)
$\boldsymbol{t_{\frac{1}{2}}}$	Half-Life
U	Wind speed
Superscript	
A, B, C, E	Coefficents for Equation (2-3)
b	Bulk in Equation (2-7)
i	Aerodynamic diameter i in Equation (2-3)
m	Material for Equation (2-2), (2-7) and Table 2-1.
BP	Bulk powder

Symbols for Chapter 4

Symbol	Definition
$A_{0\mu}$	Coupling material constant in Eq. (2-21)
$B_{0\mu}$	Coupling material constant in Eq. (2-21)
Δt	Time-step of microscale model

Symbol	Definition
1D	One-dimensional
A_{GB}	Surface area of a grain boundary
E	Elastic modulus, Energy
ρ	Density
L	Fraction length scale
L_{bar}	Length of 1D bar
p, m	Paramters defined for Equation (4-1)
N_{GB}	Total number of grain boundaries per 1D bar
Ntime	The number o
η	Phase viscosity
σ_0	1D stress
Δx	Length of a single segment
δ	Crack opening distance
D_{GB}	Size of the grain boundary
dt	Macroscale timestep
F_{GB}	Fraction of the element volume composed of grain boundary
G_c	Fracture energy
$g(\phi)$	Stiffness as a function of damage
ψ	Strain energy, Helmholtz free-energy
ψ_e^+	Positive component of strain energy
ψ_e^-	Negative component of strain energy
$\widehat{\psi}_e$	Driving energy in the evolution of damage
ϕ	Phase field damage
θ	Grain boundary orientation angle
ϵ	Strain
v	Velocity
vol	Volume of element
Vol_{GB}	Volume of the grain boundary
w	Grain thickness
σ_c	Critical stress
t	time
Subscript	
old	Old
coh	cohesive

Symbol	Definition
max	maximum
initial	At macroscale time=0
macro	macroscale
dissipated	Associated the dissipated energy
i	Local node
L	Left-hand node
R	Right-hand node
x	x coordinate

1. INTRODUCTION

Safety analysts throughout the U.S. Department of Energy (DOE) complex rely heavily on the data provided in the DOE Handbook (referred to herein as the Handbook), DOE-HDBK-3010 [DOE 1994], to determine radionuclide source terms (STs) in support of safety and risk analyses in documented safety analysis (DSA) or risk analysis documents. In calculating source terms, analysts tend to use the Handbook's bounding values on airborne release fractions (ARF) and respirable fractions (RF) for various categories of insults (representing potential accident release categories). This is typically due to both time constraints and the avoidance of regulatory critique. Unfortunately, these bounding ARF/RFs may represent extremely conservative values. Moreover, they were derived from very limited small-scale and bench/laboratory experiments, as well as from engineering judgment which may not have been substantiated. Furthermore, these previous estimates may not be representative of the actual accident conditions and configurations under consideration. In response, we have proposed including high-fidelity modeling to provide a more accurate and defensible method to identify not only bounding values, but also more representative values that can be used by analysts tasked with risk assessments.

Advances in computing capability at national laboratories have enabled us to use computer simulations to better model hydrodynamic, structural dynamic, and thermal/fluid dynamic phenomena. This provides a better understanding of the insights on the fundamental physics related to potential accident scenarios that could occur or could be postulated. Today, the availability of the high-fidelity computer resources (both hardware and software) that incorporate state-of-the-art models at national laboratories allows safety and risk analysts to utilize these methods for non-weapon-related safety activities. An example of the use of these state-of-the-art models in supporting source term calculations and in particular ARFs for postulated scenarios is the SIERRA high fidelity codes developed at Sandia National Laboratories (SNL). The SIERRA codes are designed to solve multi-physics engineered problems, particularly for weapon applications (see Table 1-1).

Table 1-1. SIERRA Codes at SNL*

Module/Code Name	Description	Potential Application
Solid mechanics (SM) [SIERRA 2017a]	A three-dimensional solid mechanics code with a number of features: versatile element library, nonlinear material models, large deformation capabilities, and contact. • Adagio –The standard SM code that currently provides the full suite of both explicit and implicit capabilities. In the past, the SM code for solving problems in explicit and implicit capabilities was separated into Presto and Adagio, respectively. Thus, Presto executable became obsolete. • Presto_itar – This SM code version provides capabilities to material models with an energy-dependent pressure response, such as for very large deformations and strain rates and for blast modeling [SIERRA 2017b]. The use of this code version falls under the U.S. Department of State's International Traffic in Arms Regulations (ITAR) export-control rules. Many of the material models in this version are similar to those models in CTH code.**** • Peridynamics – an extension of the SM code for modeling classical solid mechanics problems, such as the modeling of bodies in which discontinuities occur spontaneously.	May be used to model impacts, large deformation of solids, powders, and liquid dispersals using a smoothed particle hydrodynamics (SPH) model.
Structural dynamics (SD)	Used to perform most traditional structural dynamics simulations in time and frequency domains, including stress and fatigue calculations. These calculations could include energy dissipation at discrete joints. Since this SD module has a massively parallel capability, it can efficiently perform simulations to millions of degrees of freedom. Its variety of equations solvers enables solving problems with a large number of constraints. This module also includes a structural-acoustics capability for simulating noise-induced structural vibration or response due to a given noise source [SIERRA 2017c].	May be used to determine the failure of the structural-related components in the problem. No apparent applications for this research at this time.
Thermal Analysis**	Aria, Calore, and Chaparral modules comprise the state-of-the-art thermal analysis tools using massive parallel capability: • Aria is a Galerkin finite element-based program for targeting applications that involve incompressible flow and primarily focus on energy transport; species transport with reactions; electrostatics; and the general transport of scalar, vector, and tensor quantities in two and three dimensions for both transient and direct-to-steady state. It is a thermal fluid (TF) code. • Calore approximates linear and nonlinear continuum models of heat transfer. • Chaparral is a library package to address three-dimensional enclosure radiation heat transfer problems.	May be used to determine situations requiring detailed thermal analysis. No apparent applications for this research at this time.

Module/Code Name	Description	Potential Application
Fluid dynamics (FD) with low Mach**	Fuego*** is an FD module for the SIERRA code suite. Fuego is designed to predict low-Mach number (Ma<0.3) reacting flows, and has a capability to model particle and drop transport using a dilute spray approximation Lagrangian/Eulerian coupling. The liquid phase can be modeled as individual Lagrangian drops that interact through momentum source terms with the Eulerian gas phase. It couples with Syrinx, a media radiation heat transfer module, to simulate a more complete heat transfer and FD problems, such as fires. Fuego models particles in terms of user input or code generated as in soot from a fire. With the particle capability, it can model particle dispersal; however, Fuego does not currently model particle interaction, which is important for the particulate release out of a pathway.	Useful to model fire with particulates and droplet/powder release due to an elevated pressure effect.
Fluid dynamics (FD) with high Mach**	Aero module that can model flow problems at Mach numbers in excess of Mach 8. It can model gas flow in two and three-dimensional problems, which can approximate the compressible Navier-Stokes equations on unstructured meshes.	Useful to model deflagration types of accidents, particularly their flow conditions. Aero currently does not have a particle model, and thus has no apparent applications for this research at this time.

This report summarizes our research on the application and use of these types of codes in determining ARFs in the past four years which may be beneficial to the Handbook (see Appendix A for the summary table for the Handbook data, which this research may have focused to).

Starting in FY2015, this research was funded by DOE Nuclear Safety Research and Development (NSRD) Program. Sections 1.1 and 1.2 summarize accomplishments from the first two years of the funded project, which are more extensively documented in SAND reports [Louie 2015] and [Louie 2016]. FY2017 tasks are discussed in Section 1.3. In Section 1.4, the summary of the tasks to be addressed in this report is described.

1.1. FY2015 Accomplishments (Year 1)

Two tasks were assigned in the first year of the project.

- Simulate the liquid fire experiments in the Handbook.
- Conduct exploratory simulations, such as an object hitting a can filled with powders and pressurized release experiments from the Handbook, to identify if SIERRA codes can be used to model solid particle entrainment.

The SAND report "NSRD-6: Computational Capability to Substantiate DOE-HDBK-3010 Data" documents our accomplishments [Louie 2015]. Sections 1.1.1 and 1.1.2 summarize Year 1 accomplishments based on the two tasks assigned.

1.1.1. Simulated Liquid Fire Experiments

For the first task (simulate the liquid fire experiments in the Handbook), we simulated a beaker fire and a gasoline pool fire.

For the beaker fire, there were 25 ml of kerosene with 30% Tributyl phosphine (TBP) and contaminants in a beaker and a chimney apparatus to ensure no cross-flow [Mishima 1973]. A Fuego model was developed for droplet entrainment during the boiling for the release of the contaminants. An initial droplet size distribution was employed to model droplet breakup during rising bubbles. The simulations included a number of parameter variations, such as the initial liquid height and turbulence induced at the boiling surface. The sensitivity to the initial fuel height was significant, since results indicated that this parameter is closely related to the airborne release. The aerosol release for a 20-mm initial liquid height showed reasonable agreement with the data. Beaker wall deposition was also observed in the simulations. Since Fuego does not currently have a liquid level depletion model, no resuspension is used. The beaker simulation study identified these major findings:

- Liquid height might influence the release of contaminant, a parameter not considered in the experiments.
- The effect of flow turbulence was not particularly significant.
- Much of the airborne release was predicted to occur at the beginning of the simulations during the ignition.

In addition to the beaker fire, a gasoline pool fire with ~20 g of UO_2 powder was simulated using Fuego [Mishima 1973a]. For this experiment, a steel pan was located inside a wind tunnel, in which gasoline contaminated with UO_2 was allowed to entrain. In this simulation series, a number of entrainment phenomena were considered in the model such as evaporation induced entrainment (EIE) and agitation by boiling (similar to that in the beaker fire). Although wind can be important for resuspension, this aspect of these tests was not simulated because Fuego currently does not model resuspension. In subsequent work (FY2016), we implemented and tested a resuspension model (see Section 1.2). As demonstrated in the gasoline pool fire simulation, the deposited mass on the walls of the wind tunnel is small compared to the outflow of the airborne materials. The magnitude of the EIE is very small in comparison to the boiling. All cases were found to have higher ARF values than that of the experiments, but this was driven by the assumed boiling time. Better assessments of the boiling time are needed.

The pool fire simulation series concluded that:

- The entrainment mechanism (surface agitation by boiling) significantly dominated the entrainment during flaming.
- Turbulence boundary conditions were not reported, and a practical range of assumptions results in significant uncertainty in the ARF for the above entrainment mechanisms.
- The boiling mechanism was found to be the significant contributor to the amount of entrained mass. Modeling particle entrainment from pool boiling will improve the modeling accuracy.

1.1.2. Exploratory Simulations

In addition to the liquid fire simulations, exploratory simulations were also conducted to identify if SIERRA codes can be used to model solid particle entrainment.

For a projectile impacting a can filled with UO_2 powder, the simulations for the powders included the use of the Mie-Gruneisen Equation of State (EOS) Model and the Soil-Crushable Foam material model using SIERRA/SM.

Two simulation impact speeds of 20 m/s and 175 m/s were conducted. Two mesh models (coarse and fine) were also used for the simulation. A total of five cases were simulated. In general, a 20 m/s impact velocity of the projectile would puncture a hole in the can, which leads to powder escaping. At this velocity, the can remains stationary while the projectile rebounds. On the other hand, when the impact speed increases to 175 m/s, the projectile penetrates the can and becomes lodged inside while the can flies upward. During can lofting, particles escape through the opening. Eventually, the can falls back and hits the floor again. During this time, additional release near the bottom of the can was observed in the simulation. This release may not be realistic. Therefore, additional 20 m/s impact velocity cases were simulated to observe this secondary release. Only cases with the Mie-Gruneisen EOS material model were observed to have this behavior. The use of the Soil-Crushable Foam material model did not exhibit the secondary release. Perhaps the Mie-Gruneisen EOS material model may not appropriate for low impact speed scenarios; it may instead be appropriate for explosion simulations or high-impact velocity simulations where shocks are developed. Further analysis of this behavior for the Mie-Gruneisen EOS model may be needed. On the other hand, the Soil-Crushable Foam material model is useful for modeling the impact from an accident.

From the projectile impact case, we concluded:

- SIERRA/SM code can be used to simulate solid entrainment using an SPH model.
- The use of Mie-Gruneisen EOS material model should be limited for shock related impact type of accidents.
- The use of a Soil-Crushable Foam material model is useful for modeling impact accidents.
- The use of coarse and fine mesh models for the same simulation model suggests that the model may behave well.
- Problems with a longer duration are needed to observe unrealistic model results.

The other exploratory powder simulations involved the pressurized release from a container to a containment type volume [Sutter 1983]. Here, because of known limitations of Fuego's model for particle interactions, the MELCOR code was also used. Although MELCOR is a system-level code, it contains an aerosol physics model [Humphries 2015]. Because the MELCOR aerosol physics model is based on concentrations of the airborne aerosol, multiple volumes were required. A single volume model and a two-volume model have been developed. Two pressure cases were simulated (50 psig and 250 psig). A better modeling method is needed to include the utilization of both Fuego and MELCOR to model this type of simulations.

A preliminary Fuego model was developed to simulate the 50 psig case of the experiment. Although the surfaces for the model are assumed to re-bound rather than stick, a 60-second run showed the impingement of the particles on the ceiling. This result is consistent with the experimental results.

From these exploratory pressurized powder release simulations, we concluded:

- Although MELCOR is a system-level code with a concentration based on an aerosol physics model, it can be used to simulate this type of experiment.
- Fuego, on the other hand, has been used to model fires as described in Section 1.1.1. This FD code can be extended to model pressurized powder release.
- Fuego may not be appropriate for modeling high pressure conditions since it is designed for low-Mach flow.
- Although Fuego currently does not have a particle interaction model, it can be used to identify the particle impingement to walls and ceilings.

Note that these exploratory simulations were intended to demonstrate the code's capability in FY2015. At the year one stage, the simulations were not intended to be compared to experimental results. Further analyses of scenarios using MELCOR and Fuego for pressured powder release were continued in subsequent work (in FY2016).

The following three tables summarize the further work needed from year one (i.e., FY2015). Table 1-2 lists the Fuego improvement proposed for FY2016. Table 1-3 provides the recommendations for modeling mechanical insults using the SM code. Finally, Table 1-4 lists the recommendations for simulating powder release experiments conducted. Many of the code improvements and recommendations were accomplished in FY2016 (see Section 1.2). However, no further study was made for the recommendations described in Table 1-3.

Table 1-2. Fuego Improvement Proposed for FY2016

SIERRA FD code (Fuego) Recommendation	Potential Benefit
Multicomponent particle capability	This capability is particularly useful when fuel and solids (contaminants) are mixed, allowing fuel to evaporate while solids remain during the fire
Resuspension of particle capability	This capability is important for resuspension of deposited materials from the walls or burn residues resuspended under wind conditions

Table 1-3. Recommendation for Modeling Mechanical Insult Accident Using SIERRA SM Code for FY2016

Model and Simulation Improvement	Potential Benefit
Mie-Gruneisen EOS Material Model	This model should be used with caution, particularly with the SPH capability for modeling particle dispersal. It should only be applied to explosion simulations and high-velocity impact cases where shocks can be developed. In addition, this model is only available in Presto (ITAR version) of the SIERRA SM code. Discussions of the model and results are limited.
Soil-Crushable Foam Material Model	This material model should be suitable for modeling low-velocity impact cases as described in Section 1.1.2. It tends to be stable in comparison to the Mie-Gruneisen EOS model above for the same simulation model. Unlike the Mie-Grunesien EOS model, this material model can be obtained from Adagio, which may not be restricted in terms of export controls.

Table 1-4. Recommendations on Modeling Pressurized Powder Release Simulations for FY2016

Model Improvement	Potential Benefit
Multi-volume MELCOR model	This multi-volume MELCOR model may improve results with the experiment since the aerosol physics model depends on concentration.
Flow of Air exchange during experiment needed to be included in MELCOR model	During the aerosol measurement, air inside the containment volume was exchanged 80 times. This exchange may improve MELCOR model results with experimental data.
Refined Fuego model	Proper modeling of the experiments is needed, including those described in the MELCOR model improvement above. This would improve the particle deposition results on the walls and ceiling of containment.
Fuego/MELCOR Coupling	Since Fuego currently does not model particle interactions, the Fuego results, particularly for the wall and ceiling deposition, can be used in conjunction with MELCOR results to compare with the experimental data. This coupling would improve the calculation results to experiments.
Adagio/Fuego/MELCOR Coupling	As described in this research, Fuego can only model pressurized powder release with a 50 psig pressure. To model higher pressure cases, the use of the SPH particle model in Adagio may be required. The results of Adagio are then used by Fuego to predict impingement. Finally, the results are used in MELCOR to determine the final results to compare with the experiments.

1.2. FY2016 Accomplishments (Year 2)

During FY2016, we:

- Improved the Fuego code to add both the multi-component evaporation model and the particle resuspension model.
- Re-analyzed the beaker fire and gasoline pool fire experiment simulations
- Re-analyzed the powder release experiment started in the exploratory simulation of Year 1, and
- Conducted exploratory fragmentation simulations

The recommendations from FY2016 are summarized in Section 1.2.5.

Based on the recommendations from Year 1, we accomplished what was proposed to DOE. A final report documents what was accomplished in FY2016, the second year of the project [Louie 2016]. In this section, we summarize Year 2 accomplishments and the list of recommendations for Year 3.

1.2.1. Fuego Code Improvements

Based on Table 1-2, Fuego was improved in FY2016 to add both the multi-component evaporation model and the particle resuspension model.

Particle Resuspension Model

In the resuspension model effort, we attempted to characterize the model by using a number of parameters that can be input to Fuego, allowing various flow and particle conditions. The basic resuspension model is based on the Wichner resuspension model described in [Young 2015]. This model is a force balance between the lift and adhesive forces. A similar resuspension model has been implemented in MELCOR [Humphries 2015]. To account for a mechanism for the various particle size and surface properties where the particles were originated, this model in Fuego has been extended to be a stochastic resuspension model, accounting for a probability function. In addition, based on the effect of the boundary layer near the surfaces, it is necessary to include a model of calculating the wall shear stress. We have demonstrated development test problems, which illustrates the usefulness of the model. Without additional work, this model may be only suitable for a certain range of particle sizes and flow velocities.

Multi-Component Evaporation Model

In terms of the multi-component evaporation model, we have provided a basic evaporation model, and a simplified approach to model multi-components of an evaporating droplet. We also provided development example inputs for testing this model. The simplified approach describes the beaker fire experiment which was described in detail in Chapter 4 of [Louie 2016]. The resuspension model was used in Chapter 3 for analyzing two experiments from the Handbook.

1.2.2. Re-analyzed Fire Experiment Simulations

Based on the recommendations from Year 1, Fuego improvement, such as resuspension and multi-component evaporation models, has been done. Thus, we re-analyzed the beaker and gasoline pool fire simulations as described in Year 1.

Beaker Fire Experiment:

For this experiment, we concluded the following:

- Our results indicate that contaminant release from a burning fuel with entrained contaminant droplets is not principally due to initial flame dynamics, though that was observed in the original study in Year 1 with non-evaporating inertial particles.
- The variation of the particle insertion data played the largest role with turbulence variation near the pool surface showing less importance. Initial pool height had large impact on the ARF, and, as in the earlier study, it is clear that more experimental results would be helpful in exploring this variation.
- Since the goal of the Handbook is to provide conservative estimates for these scenarios, and greater contaminant release rates were observed both at lower (0mm) and higher (40mm) pool heights than the nominal of 20mm, variation in pool height should be explored further.

Gasoline Pool Fire Experiment:

For this experiment, we concluded the following:

- Multiple entrainment mechanisms were presented as potential methods for hazardous contaminant release from contaminated fuel fires.
- The predicted ARF calculated by a CFD code was compared to the ARF measured in a relevant historical experiment and previous computational work. The addition of multiple species evaporation and deposition for particles provided new insight to the entrainment dynamics. The volatile fuel was seen to evaporate rapidly in the fire above the pool surface, increasing the likelihood that the remaining non-volatile solid contaminant would transport down the wind tunnel and reach the outflow.
- Practical assumptions for the turbulence boundary conditions result in significant uncertainty in the ARF.
- Boiling mechanism duration was again found to be the most significant factor in predicting the ARF. Improved modeling of particle entrainment from pool boiling will help the quantitative accuracy of this type of modeling.
- The particle input temperature did not significantly alter the volatile evaporation, resulting in similar contaminant release.
- Future work would include longer duration simulations of the resuspension of deposits left from a multiple component boiling entrainment scenario in order to detect contaminant release at the collection point, potentially enabling a prediction of the resuspension entrainment ARF.

1.2.3. Re-analyzed Powder Release Experiments

In terms of re-analyzing the powder release experiment started in the exploratory simulations during FY2015, we were able to simulate the pressurized release experiment entirely. In addition, to address the shortcoming of the low Mach limitation of Fuego, we were able to couple SIERRA/SM to Fuego to model high Mach pressurized release experiment. In addition, we included the simulation of the gravitational spill of the powder using Fuego.

In Year 2 (FY2016), three simulations were conducted for the free-fall spills. 50 psig (0.34 MPa) and 250 psig (1.72 MPa) pressurized powder release cases in the experiments were also performed.

Free-Fall Spill

A gravitational (free fall) spill simulation of 100 g of TiO_2 powder in a beaker has been done, 10^8 out of 10^{13} of the particles in 100 g were tracked. We have used a fine mesh for this simulation, which is a significant improvement over that of Year 1. We model the prescribed sample flow and introduce a turbulence model approximation, both improvements over the Year 1 effort. When the beaker is turned, the falling powder will interact the surrounding air, and induce the fluid flow within the radioactive airborne release tank (RART) volume. The induced fluid velocity can be used by MELCOR [Louie 2017]. We were able to run the simulation to the experiment end time of 30 minutes.

However, the aerosol result of the simulation overestimates the ARF in terms of the particles collected in the samples. This difference may be due to the following factors:

- Fuego currently does not model agglomeration, which may cause the settling to be faster.
- The assumption of 10^8 (10^5 with 1000 particles per parcel) particles in the model versus the actual number of particles of 10^{13} may overestimate the number of particles pulled through the samples.
- The turbulence flow model used may influence the mixing that causes the overestimation.
- The percent particle collected is a number percent, which may be different than the experiment data as a mass percent.

Pressurized Release

In the pressurized release experiments, we conducted both 50 psig (0.34 MPa) and 250 psig (1.72 MPa) cases. Because Fuego is a low-Mach number, Ma (< 0.7) fluid code, we can only model the 50 psig (0.34 MPa) case (Ma is about 0.38). For the higher-pressure case, we use SIERRA/SM (Presto) code to perform the initial blast of the powder and pass the particle data to Fuego at a later time for simulating the rest of the experiment condition.

50 psig (0.34 MPa) Case

For the 50 psig (0.34 MPa) pressure case, the simulation of the rupture disk in the experiment for the pressure release from the pressurized airborne release equipment (PARE) to RART was assumed to be done within approximately one millisecond. The fluid velocity of 643 m/s was assumed for this pressure case. The results show that the particle cloud rises up toward the ceiling of RART in a short time, while the sampling (or filters) flow pulls the particles toward the sampling devices. As the simulation continues, particles that impact to the ceiling or hit the PARE walls will stick or deposit. Because of the difficulties to observe any deposition, additional simulation runs with fluid open boundary conditions were used to allow depositions. Despite this issue, the deposition values were reported for both the ceiling and filters.

250 psig (1.72 MPa) Case

For the 250 psig (1.72 MPa) pressure case, the simulation of the powder release of 250 psig (1.72 MPa) was first done using Presto code. Initially, a coarse mesh was used to model the TiO_2 powder by using SPH model in the PARE with the prescribed pressure as the induced pressure (or stress) load. However, the size of this stress is insufficient to induce the release of the powder. Therefore, a multiplication of 1000 is applied to this stress. This increase in value is justified because Presto can model solids. Presto does not model fluid, even though there is an ideal gas model (only in the ITAR version), which is not truly modeling the gas as in a fluid code like Fuego. In reality, when the PARE is pressurized, both powder and air inside the PARE are at pressure. Without modeling the gas portion, the induced stress needed to be larger in order to push the particles out of the PARE volume. When passing the particles to Fuego, the induced fluid flow by the injecting particles may not yield the actual fluid conditions as in the experiment. That is why the use of the multiplier is justified.

At first, the coarse particle sizes in the order of millimeters from the Presto run were input to the Fuego run. The Fuego model was based on the "no flow" case for the 50 psig (0.34 MPa) simulation described. In this case, the Fuego run showed that the particles were stuck to the surfaces early because the particles are too large. In the fine particle size run (using the results of Presto in the second run), the Fuego results showed that the particles were very slow because the micron-sized particles could not influence the fluid in the RART volume. Therefore, the multi-size particle run (using final run of Presto simulation) was conducted. In this simulation, the results are more encouraging. However, the results showed slightly improved deposition onto the middle ring of the RART ceiling in comparison to what was observed in the same case for the 50 psig (0.34 MPa) simulation. This may be because of the selection of the turbulence model chosen or other effect associated with the boundary layer. Thus, iterations may be required to model the condition of the experiment correctly.

In conclusion, the coupled method of using Presto and Fuego has proven to be useful to address high Mach number flow, which Fuego alone cannot be able to handle. However, iterations and the use of a multi-size particle approach are needed in order to produce meaningful results.

1.2.4. Fragmentation Exploratory Simulations

In addition to above, the fragmentation analysis in Year 2 was intended to explore if SIERRA/SM code can be used to simulate the fragmentation experiment data described in Section 4.3.3 of the Handbook.

The two-scale modeling approach uses the finite element method to simulate dynamic fracture under general loading and boundary conditions to determine macro-scale fragmentation. At the lower length scale, a 1-D model is used to determine the micro-scale fragmentation. Boundary conditions for the 1-D model are derived from the macro-scale model. Fragmentation characteristics from both length scale models are combined to determine the resulting fragment size distribution spanning both length scales.

The two-scale modeling approach presented has been shown to be capable of providing reasonably accurate particle size distribution predictions across the entire particle size range of interest for brittle radioactive material forms susceptible to fracture through its application to a laboratory scale UO_2 impact test. The approach is particularly promising because it provides the necessary level of accuracy, fidelity, and versatility for making safety assessments of brittle radioactive materials subjected to wide ranging accident conditions while remaining computationally tractable.

1.2.5. Improvement Identified

In Year 2, we provided several needed code and simulation improvements to assess the Handbook data.

Fuego Code Improvement

In Year 2, we implemented two new particle models into SIERRA/FD (Fuego): resuspension and multi-component evaporation models. Both models have been tested. We offer several Fuego improvements to better model the ARF data in the Handbook (see Table 1-5).

Table 1-5. Fuego Particle Model Improvement Needs

Model	Description
Agglomeration	Although the adhesive model is being implemented in the code, the completion of the agglomeration model will help to better model the powder release simulations as described in Chapter 5.
Deposition	Deposition is an important model for aerosol physics. In this research we have encountered a number of issues relating to the deposition (*sticking* in Fuego's terms) when the particles are deflected from the surfaces. If the deposition allows the particles to agglomerate as in a real situation, then the particle resuspension model can be more realistic, since the current resuspension only models the resuspension according to the same particle deposition size distribution (that ignores agglomeration).
Boundary Layer	The particle impact behavior in the boundary layer needs further validation.

Fuego Resuspension Model Testing

We attempted to test the particle resuspension model by selecting resuspension experiment data from the Handbook and a reactor experiment of STORM SR-11 (see Chapter 3 of [Louie 2017]). However, we decided to stop the simulation of the STORM SR-11 test because the high fluid velocity creates a large computational cost to resolve the flow for the long duration of the experiment. On the other hand, we successfully demonstrated model predictions for the human activity resuspension experiment (see Chapter 3 of [Louie 2017] for the Fish experiment) from the Handbook. Because the experiment was not well described in the test report, (conditions such as the pace of the human walking on a contaminated surface and the collection method) it is difficult to assess model accuracy. Therefore, a number of assumptions were used to model the human walking and duration. The Fuego calculation with the resuspension model did not compare well with the experiment data. Because the calculation was done using an older version of Fuego which did not include turbulent variations in the wall shear stress, it is recommended that the calculation be re-done with the final version of the resuspension model. In addition, a separate calculation without the use of the resuspension model should be conducted to ensure that the assumed human walking motion model in the Fuego simulation induces realistic resuspension.

Fire Experiments

In Year 2, we have demonstrated that the improved Fuego models—such as the multi-component evaporation model—could contribute better predictions of the experimental data in both beaker and gasoline pool fires. We were not able to demonstrate the resuspension model fully for the gasoline pool fire test due to lack of a relevant model parameter set. The deposition model in Fuego may require the addition of particle agglomeration models to capture some of the relevant deposition processes. To better observe the resuspension phenomena, the simulations needed to be run longer to be more consistent with the experiment.

Powder Release Experiments

In Chapter 5 of [Louie 2017], we modeled the gravitational (free-fall) experiment and two pressurized release cases (50 psig and 250 psig) of TiO_2 powders in RART. For both free fall and the 50 psig pressurized release experiments, we were able to demonstrate the simulations out to 30 minutes. For the free-fall case, we estimated the ARF and compared it with the experimental data. If the agglomeration physics were included in the Fuego particle physics model, then the comparison might be better. We recommend repeating the free-fall case simulation once the particle agglomeration model is added to Fuego. In addition, the free-fall experiments as described in [Sutter 1981] contained different fall height and powder material. The additional cases should be run to substantiate the data for these experiments as well. For the pressurized release cases of [Sutter 1983], the inclusion of boundary layer entrainment and other particle forces (e.g. Van der Waal or electrostatic) may change the simulated particle interactions with the RART ceiling. To model the 250 psig pressure case, we used a number of Presto models to obtain energetic particles (kinetic energies) to be passed to Fuego simulations, so that they can be compared to the experimental data. We determined that multi-size particle models were needed in order to produce reasonable agreement with the experiments. Additional simulations are required to fine tune the multi-size particle models from Presto to Fuego in order to produce meaningful results. Therefore, it is recommended that these additional simulations be performed and that the simulations should be conducted out to 30 minutes. If the Fuego improvements, as described in Table 1-5, were added, these additional simulations could be more realistically modeled.

Fragmentation Analysis

As described in Chapter 6 of [Louie 2017], we demonstrated the ability to model the fragmentation experiment data of the Handbook. A two-scaled modeling approach was employed to address the disparate length scales involved (particles ranging in size from millimeters to microns). The two-scale model results match the impact test data reasonably well. The choice of strain rate used to initialize the micro-scale model simulations has a significant effect on the resulting particle size distribution; particularly in the particle size range of interest for safety evaluations. Results from the three rates selected do bound the test data, which is encouraging, and potentially indicates that improved results may be obtained if strain rate time-histories from the macro-scale model are used instead to define the boundary conditions for the micro-scale model simulations. Therefore, it is recommended to further develop this capability in FY2017 (Year 3).

1.3. FY2017 Accomplishment (Year 3)

During FY2017 [Louie 2018], we:

- Developed the capability of the SIERRA/SM code to model the fragmentation experiment of a UO_2 pellet fracture using a two-scale model approach as described in Year 2.
- Updated Chapter 6 of the Handbook.
- Enhanced Chapter 5 of the Handbook by providing a simulation of a 55-gallon (7A) drum nearby a fire to predict any release.

1.3.1. Implementation of a Micromorphic Fragmentation Model

In this capability, a microscopic 1-D model was developed to provide a way to predict finer fragments in the range of 10 microns or less. The results from this approach seem to agree well with the experimental data. To reduce the explicit coupling between the macro-scaled and micro-scaled simulations, we proposed implementing the microscopic scaled model into SIERRA/SM (Presto) as a material model in FY2017.

1.3.2. Revision of Chapter 6 of DOE-HDBK-3010

We proposed revising this chapter to examine more recent data in the open literature and assess the data within the Handbook. Much of the documented source terms for the nuclear criticality were from NRC regulatory guides that have been cancelled and represented the data that is not thoroughly applicable to DOE facilities and fissile material configuration at DOE sites. Task 2 supported a master thesis student from the University of New Mexico [Skinner 2017].

1.3.3. Drum Fire Simulation

To enhance Chapter 5 of the Handbook, we proposed adding a simulation for a breach and combustion scenario involving the contents of a 55-gallon (7A) waste drum. We proposed this addition because no such data existed previously and because a drum accident occurred recently at the Waste Isolation Pilot Plant (WIPP) which prompted the review of any potential breach of waste drums. Using the existing drum model from the WIPP study and recent pipe over pack fire experiments conducted at SNL, a simulation using SIERRA/FM and SM codes (Aria, Fuego and Presto) was completed to predict DR, ARF and RF.

1.4. FY2018 Tasks (Year 4)

In FY2018, as reported here, we proposed to examine free-fall and impact stress of the materials and containers, since these accidents are associated with human errors with an annual frequency of between 10^{-2} to 10^{-1} and may result in a significant dose to workers. Therefore, the tasks associated in this year include the following:

- **Task 1: Revise sections of free-fall Spills and impact stress in Chapters 5 and 6 of the Handbook.** We proposed to review and provide additional new information on the free-fall spill and impact stress sections in Chapters 4 and Chapter 5 to include recent literatures in these areas.
- **Task 2: Develop damage ratio (DR) for the container breach due to free-fall and puncture situations.** We proposed to examine the DR of the scenarios involving the free-fall of the containers and container rupture due to punctures. These studies involve with the use of the SIERRA/SM to conduct wide ranges of accidents associated with these situations. In addition, realistic content data from the DOE waste stream profiles across the complex. In addition to the 7A (55-gallon) drum container, we are also examining another common used container to store waste.
- **Task 3: Revision of Equation 4-1 of Handbook.** Equation 4-1 in the Handbook is commonly used to predict free-fall of the solids (composite), such as PuO_2 pellets for fragmentation that could result into respirable particulates. This examination utilizes the macro- and micro-fragmentation models developed in the past two years. In addition, a recent literature for this topic area would be examined, including any latest experimental data that could be used to validate the model developed in this task.

This report is divided into six chapters. Suggested revisions for sections of the Handbook are documented in Chapter 2. In Chapter 3, the development of DR for container breach due to free-fall and puncture accident scenarios is described. Chapter 4 describes the improvement of the fragmentation model for revising Equation 4-1 of the Handbook. Both Chapter 5 and Chapter 6 provide the summary and conclusions, and the future works, respectively.

This page left blank

2. REVISION OF SECTIONS ON FREE-FALL SPILLS AND IMPACT STRESS FOR CHAPTERS 4 AND 5 OF HANDBOOK

This task involves the review of recent open literatures on the free-fall spills and impact stress of solids and powders, particularly experiments, since the information in the existing Handbook were derived from experiments done in the 1970s and 1980s. In this chapter, the finding of these additional information would be appended at the end of the sections of Chapters 4 and 5 of the Handbook. This way, no old information is deleted since the information may have been used in the field. In addition, because we did not propose to revise any ARF/RF values in the existing sections of the Hanbook, only adding new information on the ARF/RF values from recent literature review. Note that our objectives are not trying to duplicate what is already in the Handbook, rather we try to substantiate or elaborate the information in the Handbook. Thus, we first summarize the sections in these chapters from the Handbook.

In Chapter 4 of the Handbook, the sections would be reviewed are: Section 4.2.3 on metals, Section 4.3.3 on nonmetal or composite solids, Section 4.4.3 on powders. Note that the ARF information provided is for solids that can be fragmented into small pieces or particulates in the range of RF size so that they would remain in air, waiting for release, if no agglomeration or attenuation occurs.

In Chapter 5 of the Handbook, the sections would be reviewed are: Section 5.2.3 on contaminated combustible solids, Section 5.3.3 on solid, noncombustible unyielding surfaces, and Section 5.4.4 on HEPA filters. The contamination ARF and RF values are intended to be used for applications where there is loose surface contamination only.

2.1. Handbook Section 4.2.3 on Metals

Since the properties of metal solids are very different from the composite or ceramic solids, the fragmentation properties of metal solids require the kinetic energies much higher than the free-fall or impact stress that are commonly found at DOE complex. The high kinetic energy situation primarily is involved with the explosion related accidents which the fragmentation of metal can be possible [Grady 1996]. Thus, there is no proposed changes to the current text for the Handbook.

No experimentally measured values for ARF and RF are available. No significant airborne release is postulated from these types of accident conditions. See Section 2.4 of this report for covering potential releases for loose surface contamination on metal, particularly oxidized surfaces.

Sections 4.2.1.1.4 and 4.2.1.2.2 of the Handbook covers the airborne release from free-fall molten metal as a thermal stress condition.

2.2. Handbook Section 4.3.3 on Nonmetal or Composite Solids

Nonmetal or composite solids can be fragmented easily when drops or impact due to a mechanical insult. Brittle materials (e.g., glass-Pyrex, aggregate, concrete, limestone and ceramics such as UO_2 and PuO_2) are some of examples to be fragmented or crushed upon impact. This section describes the free fall and drop of these solids to yield fragmentation which could be airborne if the fragments are small enough in the range of respirable. The current Handbook describes several references, including experiments conducted at Argonne National Laboratory (ANL) in the 1980s. [Jardine 1982] performed impact experiments to measure the fraction. Our recent literature review identified additional experiments can be suitable for this section of the Handbook.

Three experiments are mentioned in the Handbook. The first, performed by Jardine et al. [Jardine 1982] measured the fraction and size distribution generated by the impact of various materials resting on an unyielding surface. Mecham et al. [Mecham 1981] discussed that the degree of fragmentation and the size distribution are a function of the material, strength and age of the material, as well as the energy input per volume. A third experiment, detailed in subsection 5.1.3, Appendix F in Volume 4 of safety analysis report [SAND 1984], discovered that the fraction of particles in the size range of 10 micrometer AED and less is relatively uniform and empirically correlated with the energy input such that (Equation 4-1 in the Handbook):

$$\mathrm{ARF} \times \mathrm{RF} = \mathrm{A\ P\ g\ h} \tag{2-1}$$

where $\mathrm{ARF} \times \mathrm{RF}$ is the empirical correlation, A is a correlated coefficient as 2E-11 $cm^3/g\text{-}cm^2/s^2$, P is the specimen density in g/cm^3, g is the gravitational acceleration, 980 cm/s^2 at sea level, and h is the fall height in cm. See Chapter 4 of this report for more discussions on substantiating this equation. Note that A in Equation (2-1) is based on the data from Pyrex-glass data from [Jardin 1982] and the rest of the right-hand side of this equation representing the potential energy of the drop or simply an impact energy. Recent literature from [Koch 2004] suggested that this coefficient, A should be a function of the material density. The detail of this experiment and the data are given in Appendix B, Section B.1; however, a summary of the result from this experiment is described below.

[Koch 2004] describes a laboratory experiment using an acceleration tube to impact a brittle material into an unyielding iron plate surface, which is intended to be used in transporting spent nuclear fuel. The brittle material includes small specimens of ceramic materials (such as depleted uranium pellets, CeO_2, $WZrO_2$) at a volume size of 2 cm^3 and, glass at a volume between 2 to 20 cm^3 [Koch 2004]. In terms of the results, [Koch 2004] reported the ARF as functions of the 2 coefficients and density of the materials as:

$$\mathrm{ARF} = \mathrm{C1} + \mathrm{C2}\ \mathrm{W_m} \tag{2-2}$$

Note that C1 and C2 are the fitted constants and $\mathrm{W_m}$is the kinetic energy or impact energy by the projectile. Koch 2004 fitted Equation (2-2) and determined the C1 and C2 constants for the materials tested (see Table 2-1).

Table 2-1. Fitted Constants C1 and C2 for Equation (2-1) [Koch 2004]

Impact material	C1 [-]	C2 [kg/J]	ρ_m [g/cm^3]
AlSi	9.27E-04	4.93E-06	1.6
Glass	3.77E-03	5.15E-06	2.2
CeO2	2.77E-03	3.56E-06	6.8
WZrO2	1.92E-03	4.69E-06	10.3
DUO2	2.82E-03	6.08E-06	11.0

2.3. Handbook Section 4.4.3 on Powders

The scope of free-fall spill and impact stress of powders within the Handbook is comprised of powder dispersal due to acceleration by gravity, impact with unyielding surfaces, and impaction by falling objects of powder lying at rest. Two subsections are described: free-fall spill and impact. Note that there are no suggested changes to the existing Handbook section in this topic. Rather, the summary for the section is provided here.

2.3.1. Free-Fall Spill

This section describes the powder free-fall spill with air velocity and enhanced velocity normal to the direction of fall in the following sections.

2.3.1.1. Free – Fall Spill of Powder with Air Velocity Normal to the Direction of Fall

Three experiments are mentioned for this section within the Handbook. The first is work performed by Plinke et al [Plinke 1991], the second was performed by Sutter, Johnston, and Mishima [Sutter 1981], and the third was performed by Ballinger et al [Ballinger 1988].

[Plinke 1991] surveyed literature and performed tests to ascertain the factors that affect dust generation. Dust generation rates are due to some function of the ratio between the separation forces generated by an event and binding forces. Literature identified the following as factors that affect dust generation: bulk density, fall height, sample mass, particle size distribution, moisture content, and particle shape.

The experiment utilized four readily available powders, sand, limestone, cement, and flour. The four powders were free-fall spilled known distances using a known mass of material. The falling powder impacted a neutral pile of the same material powder formed under the same conditions. The airborne material was collected as a function of aerodynamic particle diameter in a cascade impactor. [Plinke 1981] discovered that dust appears to be generated by impact of the falling stream creating separation forces and change in flow direction of entrained air in impaction area due to inability to enter in the solid powder results in radial flow that transports airborne particles. More recent literatures also describe these phenomena and had developed physical models. These literatures are described in Appendix B, Section B-2. Additionally, this experiment demonstrated that dust generation increased as fall distance increased; decreased with increased material flow rate; and total dust generation rate decreased as moisture content increased.

The Plinke et al. experiment generated the following equation [Plinke 1991]:

$$\mathrm{G_i = const(H)^A(F)^B(W)^C(Frac_i)^E[D_i \ln(D_i/25)]} \tag{2-3}$$

where $\mathrm{G_i}$ is the fraction of dust particles generated with an aerodynamic diameter i, H is the fall distance in cm, F is the material flow in kg/s, W is the moisture content in percent, $\mathrm{Frac_i}$ is the fraction of particles in i size range in the source material, $\mathrm{D_i}$ is the average diameter of particles collected on the cascade impactor stages, and $A, B, C, and\ E$ are coefficients calculated by analysis of variants and varied with the material.

[Sutter 1981] performed experiments to measure the frictional airborne releases of powders during free-fall spill. The powders in this experiment were TiO_2 and depleted UO_2. The powder masses, ranging from 25 to 1000 grams, were spilled from a beaker at the ceiling of a 3-m diameter by 3 m tall stainless-steel vessel. Airborne powder was collected by high volume total particulate and cascade impactor samplers. The bounding ARF and RF values for the largest spill height were 2E-3 and 0.3 with median ARF/RF values of 9E-4 and 0.4 respectively. Bounding ARF/RF values for the lesser spill height are 5E-4 and 0.5 with median values of 8E-5 and 0.5, and average values of 1E-4 and 0.6 respectively. Note that NSRD-11 [Louie 2016] discussed the simulations of this free-fall powder experiment and recommended more experiments should be done to qualify the data from [Sutter 1981].

[Ballinger 1988] proposed a model that assumes powder disperses at a constant angle during falling. The diameter and velocity of the powder front can be calculated from the angle of dispersion and properties of the powder. The assumptions of the model include: growth rate of the powder front is constant and characterized by dispersion angle; the amount of airborne powder is proportional to the drag force on the powder; the diameter of the powder front at the start of the spill is equal to the diameter of the container. The model was incorporated into a computer code, PSPILL, that was developed to model powder spills of varying masses. An algorithm was developed based on the statistical analysis of the computer runs and can be used to predict ARF if air density and viscosity are 1.18 kg/m^3 and 1.85E-5 Pa-sec respectively. The algorithm to calculate ARF is:

$$\mathrm{ARF} = 0.1064\left(\mathrm{M_o}^{0.125}\right)\left(\mathrm{H}^{2.37}\right)/\rho_{\mathrm{BP}}^{1.02} \qquad \text{(2-4)}$$

where ARF is the airborne fractional release, $\mathrm{M_o}$ is the mass of powder spilled in kg, H is the spill height in m, and ρ_{BP} is the bulk density of the powder in kg/m^3. Based on the simulations, the best correlation for particle size of the airborne material is:

$$\mathrm{AMMD} = 12.1 - 3.29(\rho_{\mathrm{BP}}) + 7540(\mathrm{Fr}) \qquad \text{(2-5)}$$

where AMMD is the aerodynamic equivalent mass median diameter in μm, ρ_{BP} is the bulk density of the powder in kg/m^3, and Fr is the airborne fraction. For fall distances that were less than 3 m, the bounding ARF and RF values were 2E-3 and 0.3 with median values of 3E-4 and 0.5 respectively. The bounding ARF/RF values for fall distances greater than 3 m can be estimated using the average ARF calculated by the model multiplied by a factor of 2.

2.3.1.2. Free – Fall Spill with Enhanced Velocity Effects Normal to the Direction of Fall

There was only one experiment on free-fall spill with enhanced velocity effects in DOE-Handbook-3010. Sutter (August 1980) measured the entrainment of dispersed soil that was spilled into flowing air. Contaminated soil deagglomerated and pumped into a 0.61 m by 0.61 m wind tunnel at speeds of 1.4, 4.6, 6.8, and 8.9 m/s. The ARF formulation, for soil or similar characteristic powder, based on the experiment is:

$$\mathrm{ARF} = 0.0134\mathrm{U} + 0.00543 \qquad \text{(2-6)}$$

where U is the windspeed in m/s. The RF values range from 0.44 at 1.4 m/s to 0.90 at 8.9 m/s and the ARF value at 8.9 m/s is 0.125. The bounding ARF value is the result of the expression and the bounding RF value is 1.0.

2.3.1.3. Submicron Free-Fall Spill

This section discusses a research on nanoparticle powders during a free-fall condition [O'Shaughnessy 2012]. Section B.2 in Appendix B describes in details of this experiment and the results. This research used a low mass dustiness tester to measure small quantities of free fall nanometer powder resulting from a single drop of 15 mg, using a small vertical pipe which has an inner diameter of 9.5 mm. An aerodynamic particle sizer was used to measure the particle size distribution in the pipe by particle counting in 51 size channels ranging from 0.5 to 20 μm per second with and a total volumetric flow rate of 5 l/minute. Even though the experiments were designed for medical applications, the powders used in the experiments were of interest, which includes, $\mathrm{TiO_2}$, which is often used in aerosol physics experiments for nuclear facility applications.

The results from this research measured mass release fraction and the resulting particle sizes in terms of median diameter the geometric standard deviation (GSD). See Section B.2 in Appendix B for the data information. A correlation has been developed from this research [O'Shaughnessy 2012]:

$$\mathrm{RF} = 18.97 - 17.73 \ln \rho_b - 6.818\ \rho_m + 30.95\ \mathrm{N} \tag{2-7}$$

Where ρ_b and ρ_m are the bulk and mass densities, respectively. N is the dichotomous variable to indicate whether or not the powder had nano-sized particles.

2.3.2. Impact

Impact of powder is separated into two categories in the Handbook: vibrational shock of powders or large falling object impact/induced air turbulence.

2.3.2.1. Vibration Shock

There was no study directly applicable to this phenomena in the Handbook. Based on experience and judgement, [Mishima 1978], selected a bounding ARF and RF of 1E-3 and 1.0 for the suspension of powder-like surface contamination by shock-vibration. No experiments were performed in this work, but an ARF value of 1E-3 and RF value of 0.1 are recommended for this phenomenon.

2.3.2.2. Large Falling Object Impact or Induced Air Turbulence

One experiment was described for large falling object impact. [Langer 1987] suspended powders on plywood into flowing air by impact of large pieces of debris. The scope was to determine the release of plutonium powders impacted by building debris. Three rocks (1.29 kg, 1.17 kg, and 1.82 kg) were dropped 3.7 m onto powder that was on a plywood sheet (impact area) or held in a can in a vented metal box placed on the impact area. Air was drawn into the box via a filter that removed particles greater than 5 µm in diameter. Four powders were tested as surrogates: sand, sand plus Al_2O_3, Al_2O_3, and nickel metal.

The highest measured ARF was 1E-3 due to Al_2O_3 powder uncontained on the pad with an associated RF of 0.3. The median ARF/RF values were 4E-4 and 0.2 while the average ARF/RF values were 6E-4 and 0.2 respectively. Based on the experimental results, the conservative bounding ARF and RF values are 1E-2 and 0.2.

2.4. Handbook Section 5.2.3 on Contaminated, Combustible Solids

This section describes the loss or dislodgement of surface contamination during free-fall spill of contaminated, combustible materials. The release is due to a free-fall spill of mixtures of materials consisting of contaminated materials and other materials, ranging from small size materials, such as soils to a large-sized material, such as wraps. Depending on the contamination level of the materials of interest, it may be difficult to justify the release during free-fall. However, when the materials hit on the surface, the re-bound or re-suspension may be significant. However, the resuspension is not covered in this section. No up-to-date information was identified. No change to the current sections in Section 5.2.3 of the Handbook.

Free-Fall Spill

No applicable data is documented in the Handbook since there is no significant suspension of surface contamination postulated for materials such as paper, cardboard, plastic sheets, and wrapping. The Handbook suggests that an ARF of 1E-3 and RF of 1.0 be used for material with appreciable mass. These values come from a suspension of surface contamination by vibration-shock.

Impact

No experiments were referenced for impact of contaminated, combustible solids. Guidelines for ARF and RF values are specified for unpackaged and packaged material. The ARF and RF values for unpackaged material, with appreciable mass that can generate significant forces upon impact with a surface, are 1E-3 and 1.0 respectively. These values are the same as those for suspension of surface contamination from shock.

The ARF and RF values for packaged material in a reasonably robust container, such as a drum, that fail due to impact are 1E-3 and 0.1 respectively. These are based on the bounding ARF/RF values for suspension of powder in a can due to debris impact.

2.5. Handbook Section 5.3.3 on Solid, Noncombustible Unyielding Surfaces

This section describes the release of free-fall and impact of the solid, noncombustible on unyielding surfaces. Noncombustible materials are generally large pieces associated with the facility structure that may include hard, unyielding surfaces, deformable surfaces, or even brittle surfaces. Examples of such materials are concrete, metal, and glass.

2.5.1. Free-Fall Spill

No data or experiments were mentioned for noncombustible, unyielding surfaces since no significant suspension is anticipated. The ARF and RF values assessed for crush-impact are recommended as bounding for free-fall spills of noncombustible, unyielding surfaces.

2.5.2. Impact

Impact of this material type is separated into two categories: solids that undergo brittle fracture and solids that do not undergo brittle fracture. For solids that can undergo brittle fracture due to crush-impact forces, such as aggregate or glass, the fragments may carry the activity present on the surface. For these materials, ARFxRF is calculated by the same Equation (4-1) in Chapter 4 of the Handbook:

$$\mathrm{ARF\ x\ RF} = \mathrm{A} \cdot \mathrm{E}_{\mathrm{impact}} \qquad (2\text{-}7)$$

where A is the empirical correlation, 2E-11 $\mathrm{cm}^3/\mathrm{g}\text{-}\mathrm{cm}^2/\mathrm{s}^2$, where $\mathrm{E}_{\mathrm{impact}}$ is the impact energy in dyne. For a given drop height of h, $\mathrm{E}_{\mathrm{impact}} = \rho\, \mathrm{g}\, \mathrm{h}$, where ρ is the specimen density in $\mathrm{g/cm}^3$, g is the gravitational acceleration, 980 $\mathrm{cm/s}^2$ at sea level, and h is the fall height in cm. Refer to Chapter 4 of this report for the discussion of this Equation (4-1).

Solids, such as metals and plastics, that predominately undergo plastic deformation respond to vibration and shock of the substrate by flexing instead of fracturing. The only relevant data pertains to aerodynamic entrainment from surfaces, however, the dislodgement mechanisms are different. Since the surface contaminants tend to be embedded in the surface for these types of materials, the

ARF/RF values would be fewer than those for powders on unyielding surfaces, but greater than those for resuspension of materials from nominal airflow in facilities or outdoors. While no experiments were documented in Handbook for this specific phenomenon, the ARF and RF values of 1E-3 and 1.0 respectively were selected by [Mishima 1978] in an analysis of severe natural phenomena effects. These values are considered bounding for suspension of surface contamination from non-brittle solid material due to impact.

2.6. Handbook Section 5.4.4 on HEPA Filters

This section describes the release due to mechanical insults to the HEPA filters. When surface contamination material on filter media is dislodged by jarring from a single severe shock, such as an earthquake or impact with a heavy object, or by mechanical vibration. It is assumed that the housing holding the filter banks would be compromised and material made airborne in the event of a severe shock. The mechanical insults include the free-fall drop of the filters, and impact stress such as forklift puncture to the filter plenum. Since there are no up-to-date information available on filter releases, the experiments done at Rocky Flats [Arnold 1986] represents the only information on this topic. Thus, the information provided in this section would summarize the results from this Rocky Flats experiment. Additional comments would be provided to identify any needs for this topic.

2.6.1. Rocky Flats Experiments

[Arnold 1986] reported on a series of studies performed at the Rocky Flats Plant on particles generated by HEPA filters and filters used to seal the exhaust outlets on gloveboxes subjected to repetitive slamming on a hard, unyielding surface as well as mechanical crushing. The experiment consisted of five parts:

1. mechanically crushing 30 plenum-sized filters,
2. crushing 30 plenum-sized filters with a hydraulic press,
3. taping and crushing 5 plenum-sized filters,
4. a study of 2 different glovebox-sized filters under the same test conditions, and
5. repeatedly projecting a variety of plenum-sized filters 3 ft. onto an unyielding concrete floor.

In the experiments, the following specifications are done:

- HEPA filters (large plenum sized filters, 2-ft (60.96cm) ×2-ft(60.96cm) ×1-ft(30.48cm)
- Filters used to seal the exhaust outlets on gloveboxes, 8-in (20.32cm) × 8-in (20.32cm) × 6-in (15.24cm) and 12-in (30.48cm) × 12-in (30.48cm) × 6-in (15.24cm).
- In one study, number of used plenum-sized filters were wrapped in two layers of plastic, were mechanically crushed and approximately 0.75 lbs. (0.34 kg) in the outer box holding the filter during transport were collected
    - < 5wt% of the collected material was in the range < 200 μm size
    - <0.5wt% of the collected material was in the range < 25 μm size
- The test matrix in Table A.55 of the Handbook is:
    - Filter weight ranges from 13.19 to 24.38 kg with average of 17.61 kg for the 30 plenum-sized filters
    - Media represents from 5.3% to 12.2% of the total filter weight

    - The total mass collected based on the total filter weight of these 30 filters of 528.39 kg is 255 g, which is 0.0483% of the total weight

The first experiment resulted in the collection of 255 g of particles which represents 0.0483% of the total filter weight. In the second experiment, it was discovered that the particles represent 0.13 weight percent of the total media mass. Additionally, the size distribution of particles generated was found to be 8.525% of the less than 200 μm particles with no measurement of the 10 μm fraction. The result of the third experiment was that generated material was found to represent 0.384% of the total filter weight. During the study of two different glovebox-sized filters, the particles collected represent 0.022 wt% of the filter media mass. The result of the final experiment was that for the fraction of particles 10 μm in diameter and less, generated based on the assumed total media mass, the bound on ARF is 5E-3 with an average ARF of 2E-3.

Note that the results of the release from the experiments contained the following specifications and assumptions:

Additional filter tests were also done for the gloveboxes in this effort. The following information is provided in the Handbook:

- A total of 9 g was collected with a total filter weight of 41.4 kg, which equals to 0.022 wt% collected, assuming 0.43 wt% of the filter media mass.
- Generated particle size distribution was not characterized, but in other studies reported << 10%.
- Under the assumption of 10% for the 10 μm fraction, the same particle generation at 0.043wt% of the media mass is assumed.

Without duplicating the tables in the Handbook, the RF values of the release from the free-fall and impact from the filter media from the Rocky Flat tests under shock/vibration stresses from [Arnold 1986] are bounded by 5E-3 with a median of 2E-3 from the test results ranging from 1E-3 to 7E-3. Although Table 5-6 of the Handbook tabulated the ARF values derived from Table A.55 from the Handbook, the actual fractions reported is for particles < 10 μm, which is RF, rather than ARF.

The following subsections describe the expansion of the experimental results from this Rocky Flat study on enclosed filter media and unenclosed filter media.

2.6.1.1. Enclosed Filter Media

The media in HEPA filters is generally contained within multiple enclosures such as filter housings, plenum enclosures, and plastic wrapping inside waste drums. For enclosed HEPA filter media, the guidance is that severe shock-impact is no worse than the mechanical crushing performed on the filters. The first test that [Arnold 1986] performed with 30 filters resulted in an ARF of 5E-5 and the second test with 30 filters resulted in an ARF of 1E-5. The handbook defines the bounding ARF/RF values as 5E-4 and 1.0 respectively due to great uncertainties.

2.6.1.2. Unenclosed Filter Media

Section 5.4.4.2 of the Handbook describes the following:

- Fractions of < 10 μm particles generated by crushing/repetitive jarring of spent, plenum-sized HEPA filter ranged from 1E-5 to 7E-3. The upper bound was based on Table 5-6 of the Handbook, which was extracted from Table A-55 of the Handbook. Note that this upper bound includes an assumption that the particles generated represent the filter media fragmentation and the contamination associated with the media, so it is specified for the test. It may not be applicable to other filter when the loading is different than the experiment described here.
- Glovebox sized filters may have a bound value of 0.01/1.0 for the ARF/RF.

2.6.2. Summary and Conclusion

The first experiment resulted in the collection of 255 g of particles which represents 0.0483% of the total filter weight. In the second experiment, it was discovered that the particles represent 0.13 weight percent of the total media mass. Additionally, the size distribution of particles generated was found to be 8.525% of the less than 200 μm particles with no measurement of the 10 μm fraction. The result of the third experiment was that generated material was found to represent 0.384% of the total filter weight. During the study of two different glovebox-sized filters, the particles collected represent 0.022 weight percent of the filter media mass. The result of the final Arnold experiment was that for the fraction of particles 10 μm in diameter and less, generated based on the assumed total media mass, the bound on ARF is 5E-3 with an average ARF of 2E-3.

No up-to-date information is available related to this topic. Thus, the experimental data from [Arnold 1986] is only data for filters. Thus, it is recommended that future experiment needs to be re-done to the release from filter media, since many assumptions were used in the experimental results.

2.7. Summary and Conclusion

This section summarizes the review of the sections in the Handbook on free-fall and impact spill of the solids and powder. Impact can include both vibration shock and large falling object or air induced turbulence. The sections in Chapter 4 of the Handbook covered include: Sections 4.2.3, 4.3.3 and 4.4.3 for metals, nonmetal or composite solid, and powders, respectively. Using many derivations from Chapter 4 of the Handbook, the data for contaminated materials are provided in Chapter 5 of the Handbook. The sections from this chapter include: Sections 5.2.3, 5.3.3 and 5.4.4 for contaminated and/or combustible solids, Solids and/or noncombustible on unyielding surfaces and HEPA filters, respectively. In this chapter, we included a number of recent literatures that are recommended to be included in the future update of the Handbook.

Since our intent is not deleting any information from the Handbook and we had not proposed any revision of the ARF/RF values, there is no reason to copy the exact information from the current version of Handbook. In fact, we simply summarize various sections and append the additional information for those sections impacted. If recommendations are needed, we would provide them in the sections. These allow the preparers of the Handbook to review the new information to decide if they need to be incorporated into the Handbook revision.

For this chapter, we have provided the following conclusions:

- Equation (4-1) in the Handbook may need to improve, since recent literature from [Koch 2004] has identified from the experiments that the coefficient in Equation (4-1) should be material density dependent. Further discussion is presented in Chapter 4 of this report.
- Free-fall spill data in the Handbook are limited as indicated in Section 2.3.1.1. Additionally, based on the previous SIERRA study on powder spill experiments from [Sutter 1981] in the NSRD-11 report [Louie 2016], more spill experiments should be done to qualify and supplement to this data. Recent experiments and modeling of bulk material spills described in Appendix B.2 may provide additional physics insights on how particle spill affects hydrodynamically which could influence the ARF/RF.
- We had not identified any recent literature on the HEPA filters that can incorporate in the Handbook. However, based on the review of Section 5.4.4 of the Handbook, only a single data source was used to derive the HEPA filter data from [Arnold 1986]. Thus, the future experiments are recommended for HEPA filters since only single data source was used in the Handbook to derive the ARF/RF values with many assumptions were used to derive the experimental results. The additional experiments may provide confidences and/or uncertainty associated the ARF/RF values in the Handbook.

3. DEVELOPMENT OF DAMAGE RATIO FOR CONTAINER BREACH

This task involves the development of the damage ratio for waste container breach simulation. This chapter describes the SIERRA/SM simulations on the free-fall and impact (such as container puncture) of the waste containers. The motivation behind these simulations is to provide estimates of the DR resulting from a breach of the waste containers from free-fall and puncture due to a forklift impact. The determination of the scenario selection and the waste contents were based on the recent waste container inventory information. Once this information is processed, the simulations were then performed. Because of the difficulty creating a generalized and suitable waste configuration for simulations (since no single waste container was generated or packaged in the same identical way and in many cases, polyethylene bags and sealed liner may be used to prevent releases if the bag or liner remains intact), the simulations focused on calculating the breach area rather than the DR. After that, the attempt was made to estimate DR from the calculated breach area. Utilizing the available DOE standard on waste container DR from Appendix C of the DOE-STD-5506 [DOE 2007], the DR for various waste container simulations in various orientations due to mechanical insults of impacts and drops is then estimated. However, the range of the mechanical insults in this DOE standard were limited.

The accident scenarios were chosen based on accidents that could occur at DOE facilities such as the WIPP in Carlsbad, New Mexico. Free-fall height of the waste containers were based on the stacking drum height and bridge crane height in WIPP. The forklift impact is based on the range of speeds of the vehicle.

In Section 3.1, the selection of the waste containers and the contents were identified. Section 3.2 describes the accident scenarios and test matrix parameters to be simulated using SIERRA/SM.

3.1. Waste Stream Data and Container Selections

Transuranic waste stream data was obtained from Los Alamos National Laboratory (LANL) for the purposes of this analysis [Soest 2017]. The container database was sorted by container type to determine the two most common container types. The utilization for each container type in the database is given in terms of number and waste volume in Table 3-1.

Based on the information in Table 3-1, the 7A (55-gal) drum is the most common container, accounting for nearly 87% of the total number of containers, and the standard waste box (SWB) is the second common at 5.6% of all containers in the database. Together, the 7A drum and SWB account for 92.4% of the total number of containers and 85.9% of the total waste volume; thus, analyzing these containers will prove beneficial to most applications.

3.1.1. Content Selection for 7A Drum

The 7A drums in the LANL database consist of direct-loaded drums, with and without a liner, criticality control overpack (CCO), and pipe overpack containers (POC). Direct load comprises 89.1% of 7A drums in the database, while CCO and POC is 10.9%. Container types in terms of number and volume of waste are specified in Table 3-2.

Table 3-1. Container type utilization per LANL TRU waste stream database in terms of number of containers and volume of waste

Container Type	# of Containers	% of Total
55-gal Drum	202658	86.8%
SWB	13058	5.6%
100-gal Drum	8466	3.6%
Other	9254	4.0%
Total	**233436**	**100.0%**

Container Type	Volume of Waste (m^3)	% of Total
55-gal Drum	42152.9	54.2%
SWB	24679.6	31.7%
100-gal Drum	3208.6	4.1%
Other	7736.5	9.9%
Total	**77777.6**	**100.0%**

Table 3-2. Type of 7A drums in the LANL database in terms of number of containers and volume of waste.

Container Type	# of Containers	% of Category Total	% of Total	Volume of Waste (m^3)	% of Category Total	% of Total
55-gal Drum Dir Ld w/ Liner	130314	64.3%	55.8%	27105.3	64.3%	34.8%
55-gal Drum Dir Ld w/o Liner	50285	24.8%	21.5%	10459.3	24.8%	13.4%
55-gal CCO w/ Liner	20000	9.9%	8.6%	4160.0	9.9%	5.3%
55-gal POC - 6" w/ Liner	1339	0.7%	0.6%	278.5	0.7%	0.4%
55-gal POC - 12" w/ Liner	720	0.4%	0.3%	149.8	0.4%	0.2%
Total	**202658**	**100.0%**	**86.8%**	**42152.9**	**100.0%**	**54.2%**

Since the direct load drums are significantly more common than the CCO and POC 7A drums, the analyses will focus exclusively on direct load 7A drums.

The 7A drum inventory can be further divided by content type. There are eight different waste matrix code groups listed in the LANL database for direct load 7A containers. Table 3-3 provides a listing of the various waste matrix code groups contained within direct load 7A drums.

Table 3-3. Waste content found in direct load 7A drums in the LANL database.

Drum Vol.	0.208	m^3

Container Type	Waste Matrix Code Group	# of Containers	% of Category Total	Avg. Density	Max Density	Avg. Mass	Max Mass
				kg/m^3	kg/m^3	kg	kg
55-gal Drum Dir Ld	Inorganic Nonmetal Waste	1	0%	265.9	265.9	55.3	55.3
55-gal Drum Dir Ld	Composite Filter Waste	36	0%	62.3	266.6	13.0	55.4
55-gal Drum Dir Ld	Salt Waste	165	0%	348.4	1992.0	72.5	414.3
55-gal Drum Dir Ld	Combustible Waste	384	0%	95.5	110.8	19.9	23.0
55-gal Drum Dir Ld	Solidified Organics	517	0%	233.5	599.2	48.6	124.6
55-gal Drum Dir Ld	Contaminated Soil/Debris Waste	37667	21%	944.3	1688.1	196.4	351.1
55-gal Drum Dir Ld	Solidified Inorganics	40748	23%	433.6	2235.6	90.2	465.0
55-gal Drum Dir Ld	Heterogeneous Debris Waste	101081	56%	212.5	1066.1	44.2	221.7
	Total	**180599**	**100%**				

The three most common waste types contained within 7A direct load containers are contaminated soil/debris waste (CS), solidified inorganics (SI), and heterogeneous debris waste (HD). The HD waste are modeled as contaminated gloves and trashes as simulated in the materials described in the drum fire simulation in NSRD-15 [Louie 2018]. These three types of waste will be the focus of the 7A drum analyses.

3.1.2. Content Selection for SWB

The SWB configurations listed in the database include direct load, with and without a liner, as well as four 7A drums contained in the SWB. Direct load accounts for 55.5% of all SWB containers in the LANL database, while 7A loaded SWBs account for the other 44.5%. Container types are listed in terms of number of containers and volume of waste in Table 3-4.

The direct loaded SWB was chosen as the focus of the SWB analyses since it has the highest utilization of SWB containers and to not duplicate the 7A drum analyses.

As with the 7A drums, there are multiple content types stored within the SWB inventory. The six waste matrix code groups for SWB direct load are provided in Table 3-5.

The SWB analyses will focus on only one waste type since 94% of the direct load SWB containers are filled with HD.

Table 3-4. Type of SWBs in the LANL database in terms of number of containers and volume of waste.

Container Type	# of Containers	% of Category Total	% of Total	Volume of Waste (m^3)	% of Category Total	% of Total
SWB Dir Ld w/ Liner	6728	51.5%	2.9%	12715.9	51.5%	16.3%
SWB w/ 4 - 55-gal Drums w/ Liners	5814	44.5%	2.5%	10988.5	44.5%	14.1%
SWB Dir Ld w/o Liner	516	4.0%	0.2%	975.2	4.0%	1.3%
Total	**13058**	**100.0%**	**5.6%**	**24679.6**	**100.0%**	**31.7%**

Table 3-5. Waste content found in direct load SWB containers in the LANL database.

SWB Vol.	1.89	m^3

Container Type	Waste Matrix Code Group	# of Containers	% of Category Total	Avg. Density kg/m^3	Max Density kg/m^3	Avg. Mass kg	Max Mass kg
SWB Dir Ld	Uncategorized Metal Waste	26	0%	238.8	238.8	451.4	451.4
SWB Dir Ld	Combustible Waste	32	0%	100.6	110.8	190.1	209.4
SWB Dir Ld	Contaminated Soil/Debris Waste	48	1%	366.0	574.3	691.7	1085.5
SWB Dir Ld	Composite Filter Waste	48	1%	56.2	57.3	106.3	108.2
SWB Dir Ld	Solidified Inorganics	300	4%	1883.8	2235.6	3560.5	4225.3
SWB Dir Ld	Heterogeneous Debris Waste	6790	94%	153.4	1775.8	290.0	3356.3
	Total	7244	100%				

3.2. Model Development and Validation

SIERRA/SM version 4.48.2 was used for all drop and puncture simulation cases as described in Section 3.2. Cubit version 15.3 [Blacker 2017] was used to generate the model and mesh of the 7A drum and SWB. The 7A drum model was based on the model developed in NSRD-15 [Louie 2018]. The SWB model was developed as a part of this project.

3.2.1. Model Development for 7A Drum

The 7A drum model for the simulation was based on the model developed in NSRD-15 [Louie 2018]. Figure 3-1 shows the 7A drum and the computational model/mesh. Figure 3-2 shows the 7A drum assembly of the mesh models.

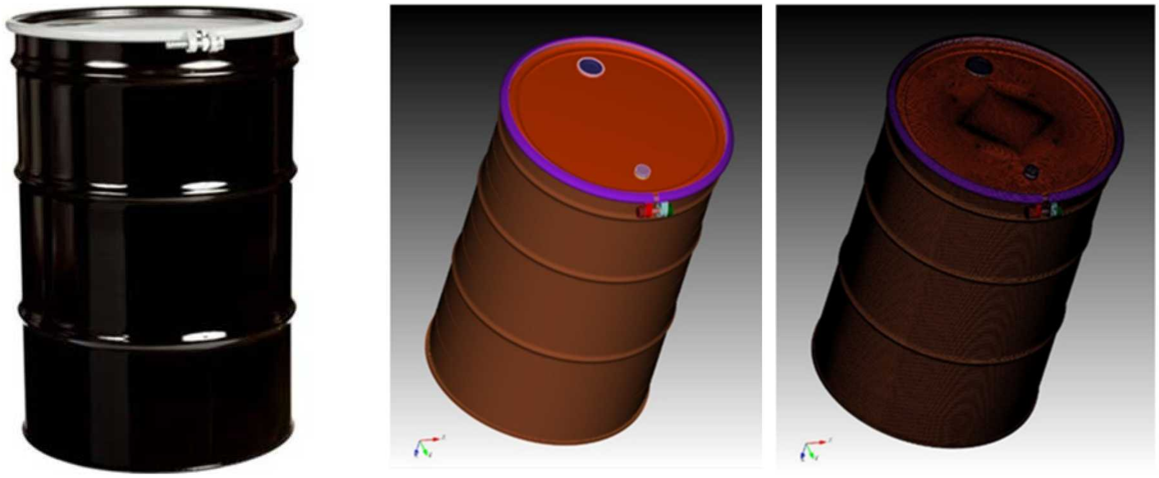

(a) Skolink Drum [Skolnik 2006]

(b) Cubic Model

(c) Mesh

Figure 3-1. 7A (55-gal Drum) Model for Simulations

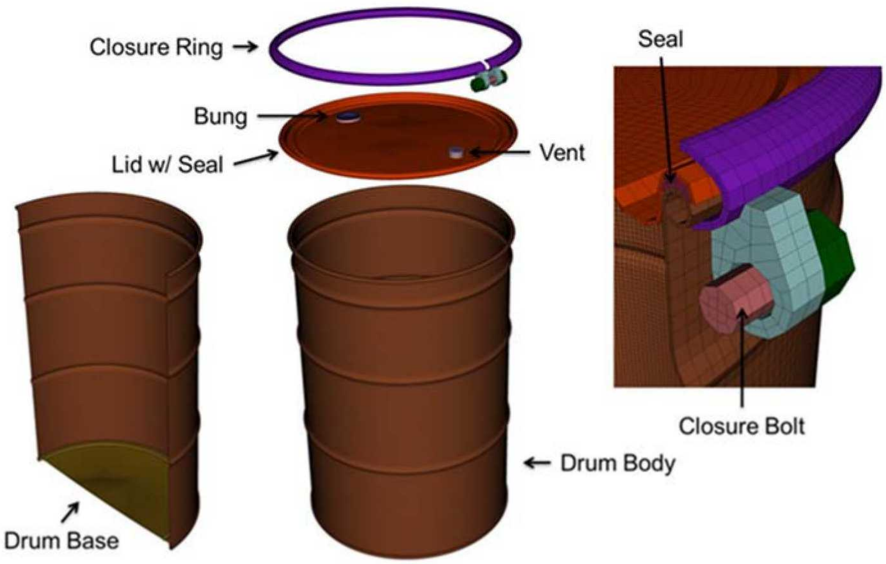

Figure 3-2. Drum Assembly Mechanical Model Mesh

Mesh Model

To reduce the simulation time symmetry about the Y_Z plane was assumed (see Figure 3-3). This reduced the number of elements and nodes to 823829 and 947717 respectively.

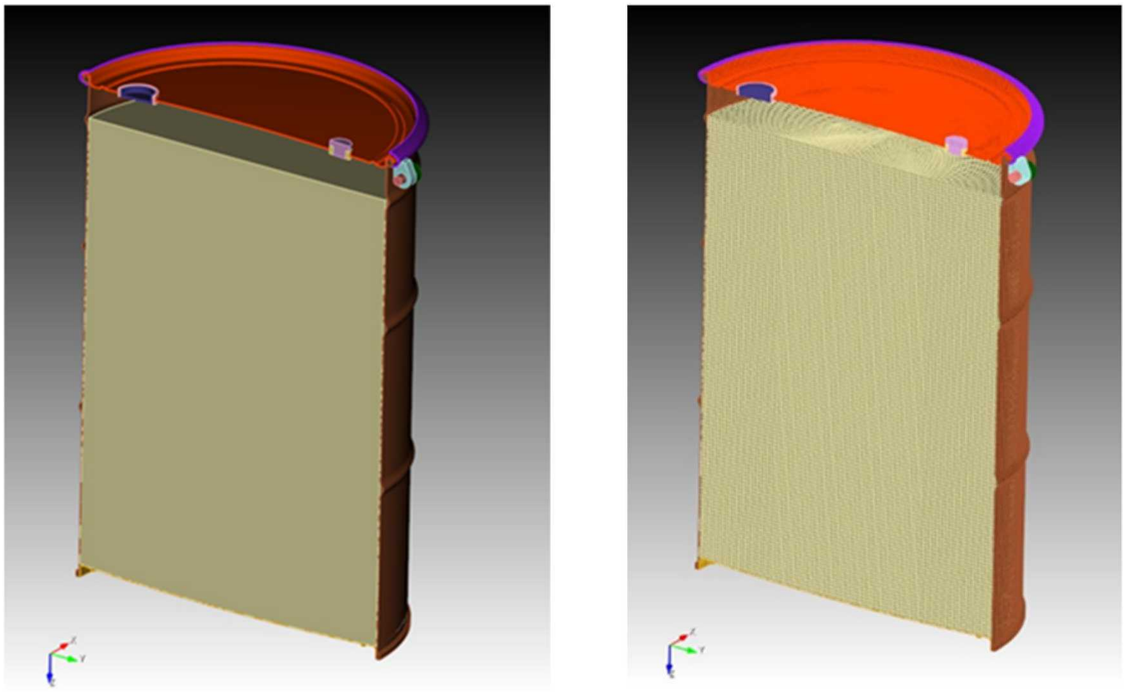

(a) Model (b) Mesh

Figure 3-3. Half-Symmetric Simulation Model showing Contents

The mesh is entirely made of reduced integration hexahedral elements. Figure 3-2 shows the closure ring which holds the lid and the drum body together. The ring itself clamps together the lid and body though the use of a closure bolt which during a pre-load step in the calculation, closes the gap between the two ends of the ring.

The bung hole and vent use the spot weld feature in SIERRA to connect them with their caps. Spot welds allow for the cap to separate from the bung hole or vent if forces pulling them apart exceed a user defined limit.

To make the tine have an impact equivalent to one which is connected to a forklift, the density of the tine mesh was set such that its total mass would be the mass of an average forklift which weighs 4082 kg (9000 lbs.) [Mangan 2006]. The density was set to:

$$4082\ \text{kg}/0.00136\ m^3 = 3001714\ \text{kg}/m^3$$

where the volume of the half tine is 0.00136 m^3.

Material Model

The drum is generally made of different steels which were chosen based on the specifications of the drum [Skolnik 2006]. The cylindrical body, lid, and bung cap are modeled on ASTM A1008 Steel [ASTM 2016]. The closure ring also uses ASTM A1008 steel, but with changes in parameters such as yield stress and parameters which define cracking and other failure modes. The bolt is modeled with ASTM A307 steel [ASTM 2014]. The seal was originally modeled with a foam model, but its low Young's modulus caused issues in the calculation when contacting the much stiffer steel materials, so a n artificially high modulus was used with the Mooney Rivlin rubber material model. To see the materials for every part of the drum, see the Sierra input deck for the simulations. The input decks give details such as Young's Modulus, Poisson Ratio, hardening function, and failure parameters for the materials used. The material model for ASTM A1008 Steel used by the drum body, lid, and bung looks like [ASME, 2015]:

```
  # +-+-+- ASTM A1008 Drum Steel +-+-+- #

  begin material ASTM_A1008_Drum_Steel

    density = 7750.0 # ASME B&PV Code 2015, Section II Part D, Table PRD

    thermal engineering strain function = ASTM_A1008_Drum_Steel_TE_Func

    begin parameters for model thermoelastic_plastic_fail
      youngs modulus = 2.02000e+11 # ASME B&PV Code 2015, Section II Part D, Table TM-1 (Carbon
steels with C <= 0.30%)
      youngs modulus function = ASTM_A1008_Drum_Steel_YM_Temp_Func
      poissons ratio = 0.300 # ASME B&PV Code 2015, Section II Part D, Table PRD
      poissons ratio function = ASTM_A1008_Drum_Steel_PR_Temp_Func
      yield stress = 2.7400e+08 # WIPP Drum Lid Material Test Data
(WIPP_Drum_Material_Test_Data_2017_01_12.xlsx)
      yield stress function = ASTM_A1008_Drum_Steel_YS_Temp_Func
      beta = 1.0
      temperatures = 293 \#
                      423 \#
                      523 \#
                      623 \#
                      723 \#
                      798
      hardening functions = ASTM_A1008_Drum_Steel_Hardening_Func_293 \#
```

```
                            ASTM_A1008_Drum_Steel_Hardening_Func_423 \#
                            ASTM_A1008_Drum_Steel_Hardening_Func_523 \#
                            ASTM_A1008_Drum_Steel_Hardening_Func_623 \#
                            ASTM_A1008_Drum_Steel_Hardening_Func_723 \#
                            ASTM_A1008_Drum_Steel_Hardening_Func_798
      critical tearing parameter = 1.635 # Based on Reduction in Area from WIPP Drum Lid Material
Test Data (WIPP_Drum_Material_Test_Data_2017_01_12.xlsx)
      critical tearing parameter function = ASTM_A1008_Drum_Steel_TP_Temp_Func
      critical crack opening strain = 0.01257 # Based on generic metallic fracture energy of
100.0 MPa x sqrt(m).
      critical crack opening strain function = ASTM_A1008_Drum_Steel_COS_Temp_Func
    end

  end
```

In terms of content models in the drum, three types of contents were used in the simulation, as previously described in Section 3.2. The materials for these content models were from 1) HD, 2) SI waste [Collins, 1991, Brannon, 2009, EPA, 1996], and 3) CS [Holtz, 1981, GEO 2014, GEO 2013, Prokon 2018, Wikipedia, 2016]. Their densities are 1108.5, 2325.0, and 1755.5 kg/m^3 respectively. It is best to look at the Sierra input decks to see the details of each material type. SIERRA/SM has a variety of material models to represent a wide range of material behavior, and the three chosen were Orthotropic Crush, KC Concrete, and Soil Foam models within SIERRA/SM for the HD, SI, and CS materials, respectively. A broad summary of the three material types would be that HD behaves like a single elastic block, SI is a brittle solid block, and CS behaves like particles.

Accident Models

Two types of accidents simulated are 1) drum dropping from various heights and angles and 2) drum punctured by forklift tine running at different speeds. Figure 3-4 shows the models for these two scenarios. As shown in this figure, the drum drop is varied by drop height and angle of impact. For the forklift tine impact, the impact is varied by the orientation of the drum (upright or sideway), impact point at the surface of the drum, and with or without the rigid wall.

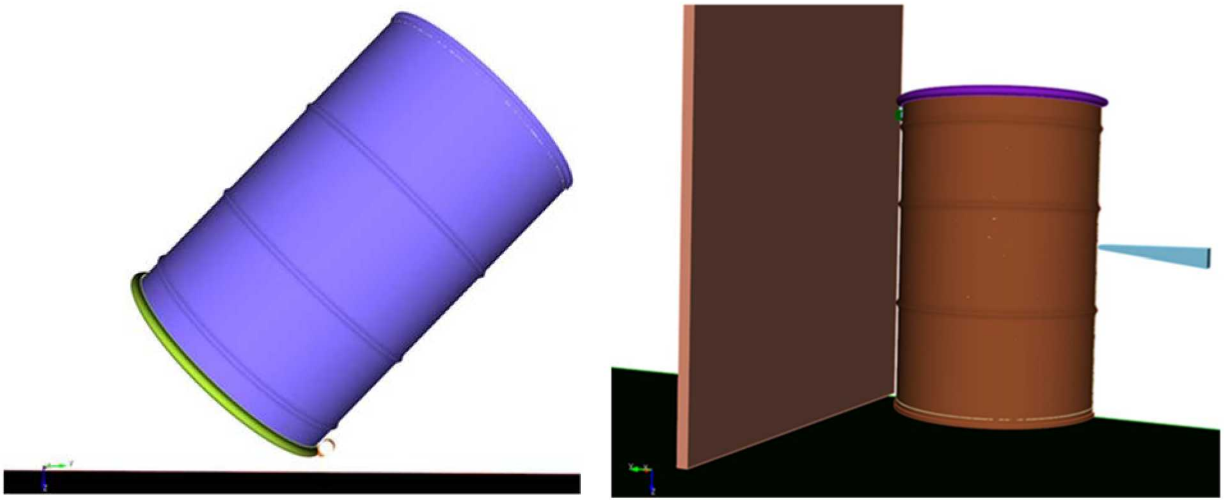

(a) Drum Dropped at 135 °

(b) Forklift Tine Hitting Drum Mid-Level Against Rigid Wall

Figure 3-4. Examples of Drum Simulation Geometries

To do the simulation of drop without compromising computational resource, the initial velocity at impact on the floor was input to simulate the actual drop height. This velocity is computed by determining the velocity of impact of a free-falling body dropped from the specified height as shown for a 20-m drop:

Velocity= 19.806 m/s = $\sqrt{2 \text{ X } 20 \text{ m X } 9.8 \text{ m/s}}$

This velocity is computed based on the assumption of the placement of the drum at a few centimeters above the ground.

Similarly, an initial velocity is prescribed based on the speed of the forklift for the cases involving the impact by its tine.

For example, a drum dropped from 20 m height contains the following input:

```
# Initial Velocity

begin initial velocity
  include all blocks
  remove block = block_1
  component = z
  magnitude = 19.806 # m/s
end


# Gravity

begin gravity
  include all blocks
  component = z
  gravitational constant = 9.80665
end
# Symmetry
```

When the puncture or breach occurs in the simulation as a hole in the drum, the element death capability of Sierra is used remove elements which meet the criteria such as excessive strain or material strength degradation (material criterion = on). The element death block for the drum is shown below:

```
 ### Element Death ###

begin element death death_on_inversion
  include all blocks
  death on inversion = on
  criterion is element value of nodal_jacobian_ratio <= 0.02
  criterion is element value of volume <= 1.0e-20
end

begin element death material_failure
  include all blocks
  material criterion = on
end
```

The material failure is defined in the material definition. For example, in the material block above for ASTM A1008 Steel, material failure is given by:

```
critical tearing parameter function = ASTM_A1008_Drum_Steel_TP_Temp_Func
critical crack opening strain = 0.01257 # Based on generic metallic
                                        # fracture energy of 100. MPax qrt(m).
critical crack opening strain function =
    ASTM_A1008_Drum_Steel_COS_Temp_Func
```

3.2.2. Model Validation Case for 7A Drum

To validate this 7A drum model, an experiment from a 1 m penetration bar dropped onto near the center of a 7A drum lid was used [Skolnik 2009]. This penetration test conformed the guidance described in the Department of Transportation Hazardous materials Regulations contained in Title 49, Code of Federal Regulations parts 171-185. In this experiment, a dent that was measured in 1.263” in diameter and 0.064” deep was obtained from the bar drop test.

A numerical simulation of a rod dropping from 1 m onto the lid of the drum was done. The rod assumed to be 13.2 lbs. (5.99 kgs) with a diameter of 1.25” (3.175 cm). Instead of placing the rod 1 m high from the lid surface of the drum, we started the simulation assuming an initial velocity of the rod at 4.29 m/s which corresponds to a 1 m high drop. The content in the drum was assumed a maximum mass of CS. Figure 3-5 shows the experiment setup and the SIERRA/SM simulation. The simulation result showed no puncture of the lid in this drop height, which is consistent to the finding in the experiment [Skolnik 2009].

(a) Experiment Setup [Skolnik 2009] (b) SIERRA/SM Simulation

Figure 3-5. A Simulation of 1-Meter Rod Drop onto a 7A Drum

3.2.3. Model Development for SWB

The model development for SWB is similar to that for the 7A drum, except that the model was created specifically for this project (see Figure 3-6 for the SWB features). The model development was based on the available SWB detailed drawings [NWP 2014]. Figure 3-7 shows the stimulation model and its mesh.

<u>Mesh Model</u>

Like the 7A drum model in Section 3.3.2, a half-symmetric model was developeds (see Figure 3-7). The total number of nodes and elements in the half-symmetry model are to 854212 and 1072095 respectively.

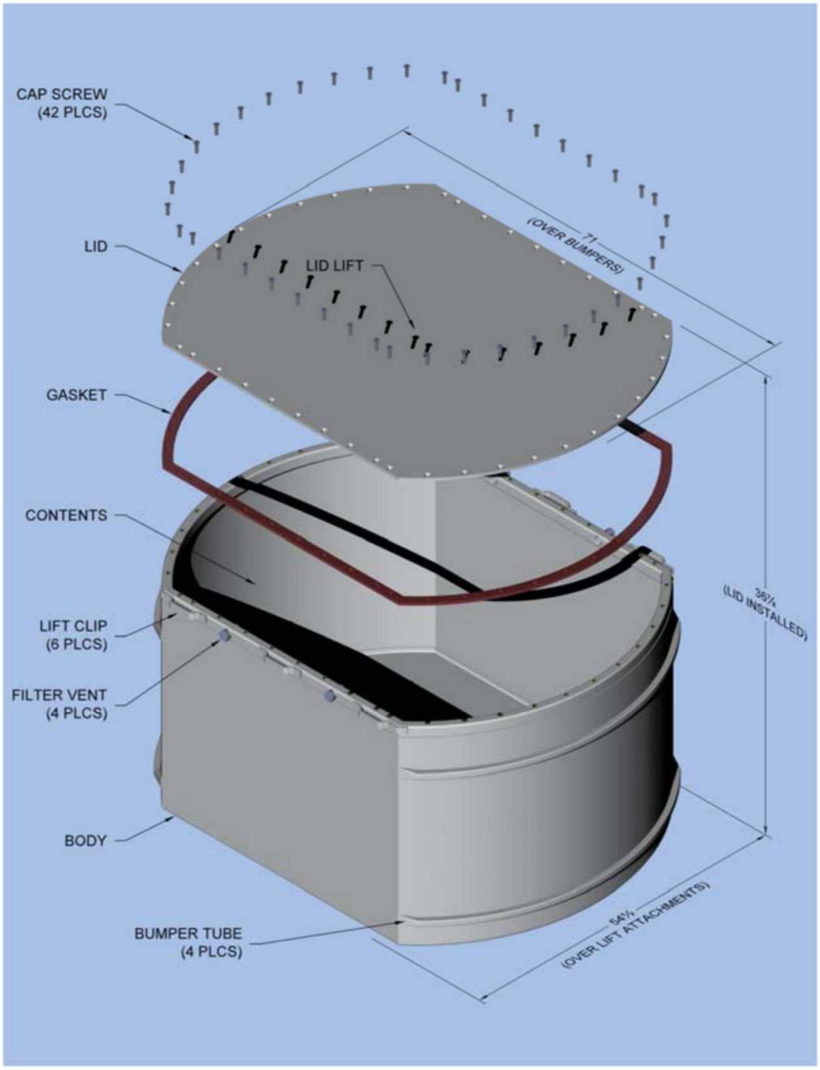

Figure 3-6. Standard Waste Box Feature and Overall Dimensions [NWP 2015]

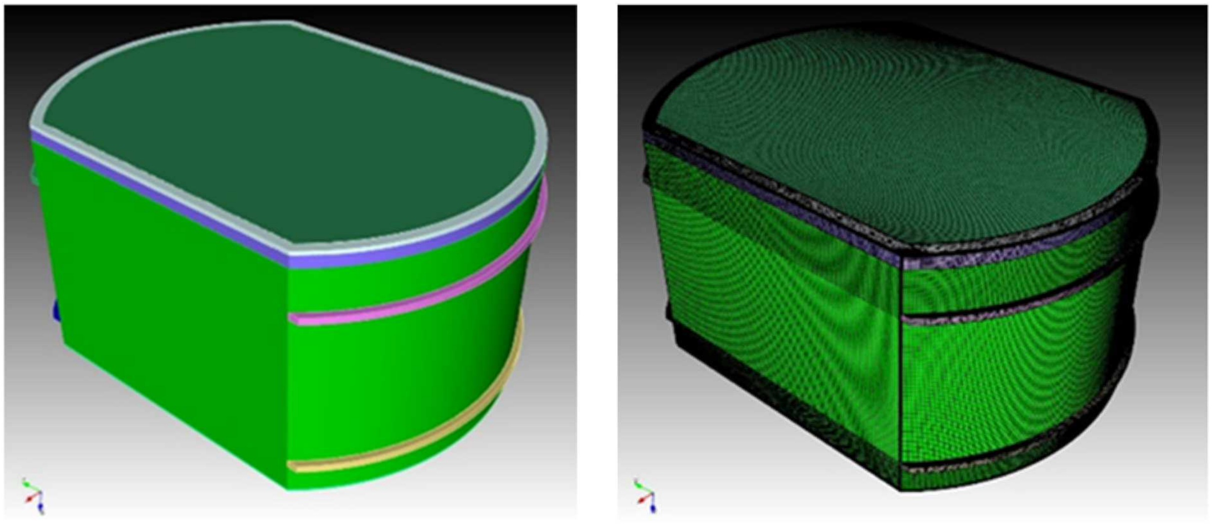

(a) Model Features (b) Mesh Model

Figure 3-7. Standard Waste Box Mesh and Model Features

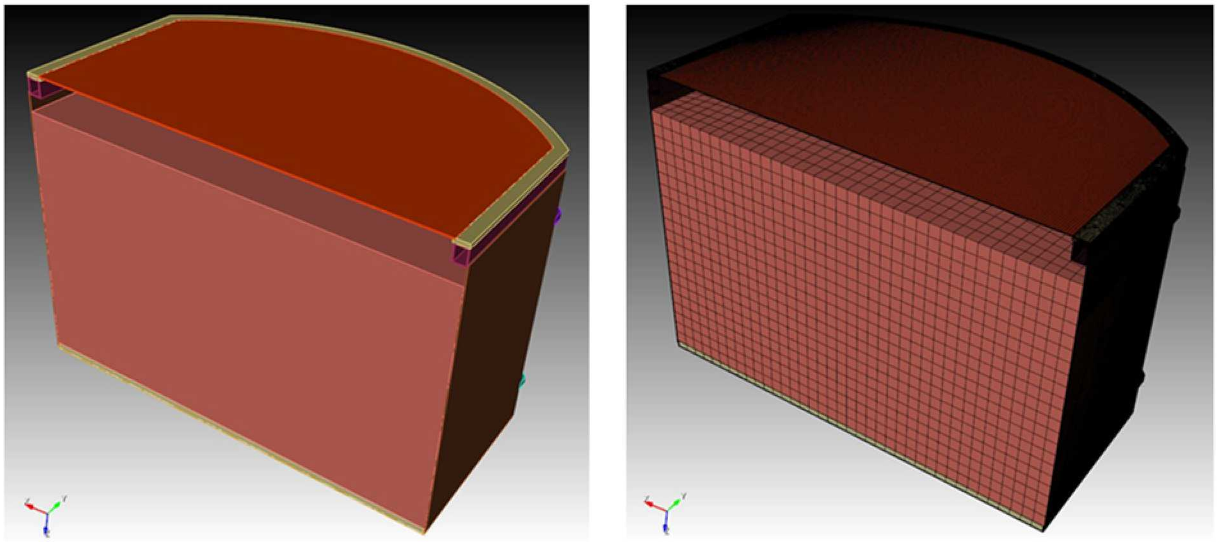

(a) Half Symmetry SWB Model (b) Mesh

Figure 3-8. Half Symmetry SWB Models

As with the drum, the mesh is entirely comprised on reduced integration hexahedral elements. Welds throughout the structure are represented using the spot weld feature in SIERRA. Figure 3-9 shows a detail of the lid and lid frame which has screws which connect the lid to the SWB body. The screws (Flat Head C Sunk CAP screws ½” x 1 ¾”) were also represented by spot weld. The spot weld block for all the screws is shown below:

```
# tube-lid_frame screws
```

```
begin spot weld
  surface = surface_400310
  second surface = surface_310400
  normal displacement function = spot_normal_func
  tangential displacement function = spot_tangential_func
  normal displacement scale factor = 722685350.9
  tangential displacement scale factor = 411930650.0
  failure envelope exponent = 2.0
  search tolerance = 0.0005
  ignore initial offset = yes
end
```

The spot weld model is also used to connect other parts of the SWB such as the main body and bottom plate.

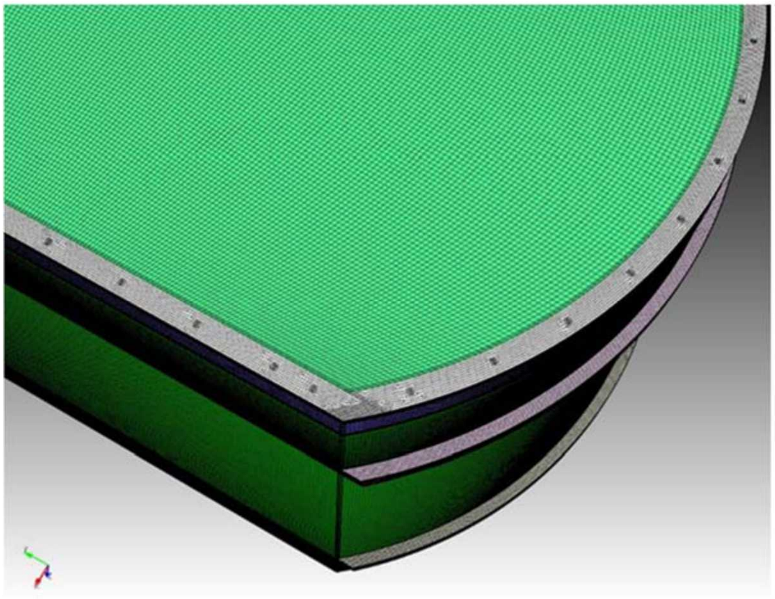

Figure 3-9. Details of Screws Used to Fasten SWB Lid onto SWB Body

Material Model

The SWB uses ASTM A1008 Steel for all components except the bumpers which use ASTM A307 Steel.

For the contents, the only HD waste was simulated according to Section 3.2. Based on the observation from the 7A drum simulations, the CS material model yields a better particle behavior than the actual HD material model, CS material model was used in the SWB simulation model, keeping the HD density instead. (See Section 3.2.1 for the material model input block examples.)

Accident Models

Similar to the discussions for the 7A drum accident models in Section 3.2.1, the SWB accident models are done for both drop with different impact angles and forklift puncture scenarios. Figure 3-10 shows the examples of the SWB drop at 135-degree impact angle, and SWB laying down on its side being hit by a forklift tine at the center surface.

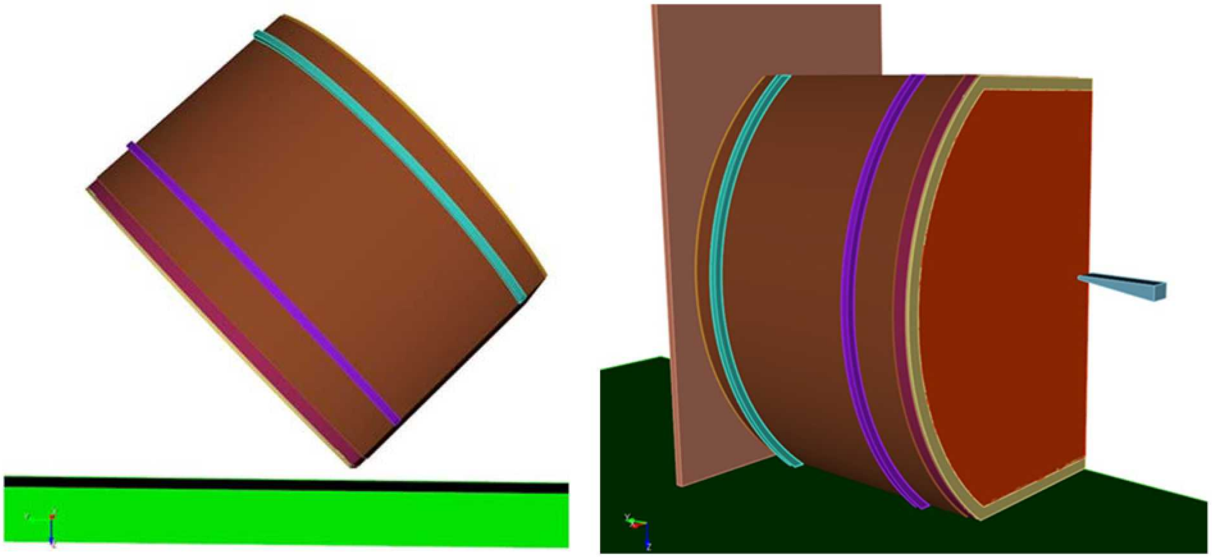

(a) SWB Drop at 135°

(b) SWB Puncture by Forklift Tine at Center Surface

Figure 3-10. SWB Accident Simulation Examples

3.3. Simulation Discussions and Results

This section describes the simulation results of the half-symmetry models for both the 7A drum and SWB based on the simulation test matrix discussed in Section 3.2. Appendix B displays the final or near final timestep of the images of selected simulation cases for both the 7A drum and SWB.

Table 3-6 and Table 3-7 show the number of SIERRA/SM cases to be simulated for the free-fall drop and forklift tine impact scenarios for both types of containers. As shown in Table 3-6, there are 60 and 20 drop case simulations for 7A drum and SWB, respectively. Table 3-7 shows that there are 72 and 24 puncture cases for the 7A drum and SWB, respectively. The completion of the simulations took longer than expected, because a secondary impact due to the container bouncing off the ground was possible. Section 3.4.1 discusses the resultsof the simulations. Section 3.4.2 discusses the method of estimating the breach area for the cases that had container breach. Section 3.4.3 gives a summary discussion of the simulation cases with a breach, and the estimate of the breach area.

Table 3-6. Total SIERRA/SM Simulations on Free-Fall Drop Scenarios

Parameters	7A (55-Gal) Drum	SWB
Content type: HD, SI, Cs	3	1 (HD only)
Drop height (m): 2.5, 5, 10, 20	4	4
Orientation (°): 0, 45, 90, 135, 180	5	5
Weight (kg): 453.6	1	1
Total	**60**	**20**

Table 3-7. Total SIERRA/SM Simulations for Forklift Tine Impact Scenarios

Parameters	7A (55-Gal) Drum	SWB
Content type: HD, SI, Cs	3	1 (HD only)
Constraint: Free or Fixed	2	2
Impact Location: Lid-Center, Side-Lid, Side-Middle, Bottom-Center	4	4
Impact Speed (m/s): 0.5, 2.5, 5	3	3
Total	**72**	**24**

Figure 3-11 shows the definition for the reference points for the 7A drum and the drop orientation. As shown in Figure 3-11(a), the reference point of the drum component and surfaces are identified. In this figure, zero-degree orientation refers to as the drum is in its upright position where its lid is on the top. As shown in Figure 3-11(e), the 180-degree orientation refers to as the bottom of the drum on the top whereas the lid is facing downward.

3.3.1. Discussion of the Results

As indicated before, SIERRA version 4.48.2 was used for all simulations. To simulate these many cases, a python script was created to generate all the different scenarios and submit them to Sandia's high-performance computer clusters. The run time for the drop cases are sometimes longer because the rebound of a drum off the ground required simulations to continue to see if the rebound resulted in further damage. In general, when the lid came off from the container, it is assumed that the container is fully breached. To do post-processing, we created another python script to automatically generate video/image clips from all the runs. Determination of breach is based on visual inspection of the images or movies created for the simulation runs. If a breach is seen and it is not a full breach, the breach area is calculated based on the void which remains after "dead elements" (defined to be elements which undergo excessive strain) are removed.

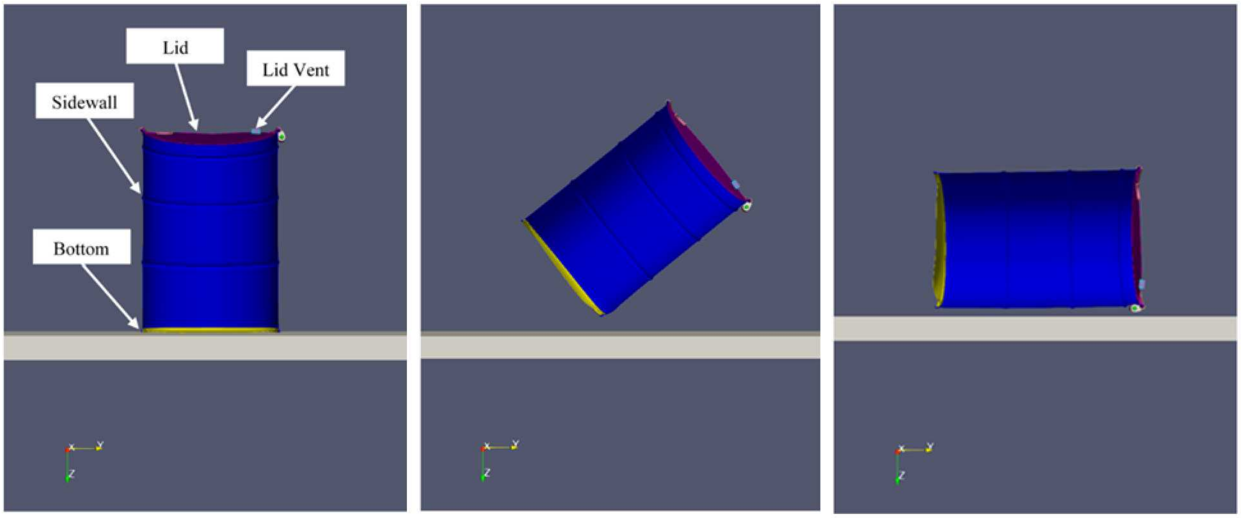

(a) 0-degree (b) 45-degree (c) 90-degree

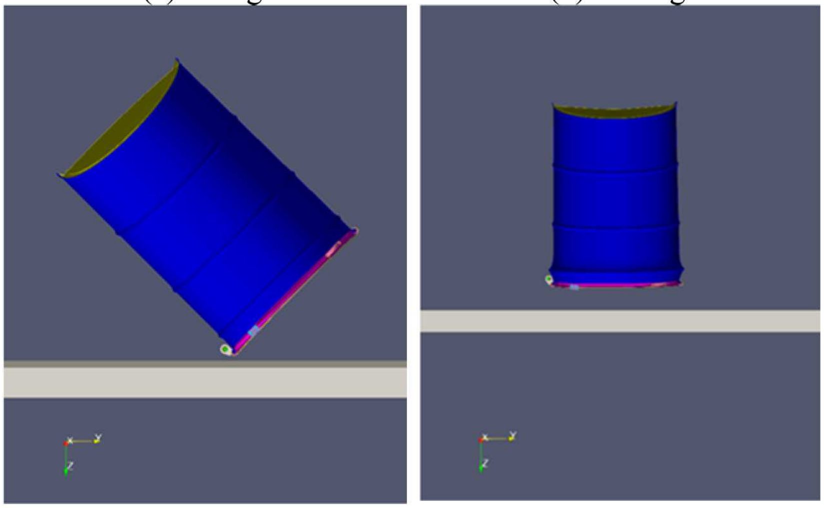

(d) 135-degree (e) 180-degree

Figure 3-11. Orientation of the Drop Respected the Drum Angle

3.3.1.1. Drop and Puncture Results for Drums

Figure 3-12 shows percentage of drum breach cases resulting from the 7A drum drop simulations for HD, SI and CS content types. Among the three content types, the smallest breach cases were from HD, which consists primarily of trash. On the other hand, SI contains the most breach cases among the three types. For the parameters of drop height and drum orientation, Figure 3-13 and Figure 3-14, respectively. As shown in these two figures, the number of the failures is affected by the drop height. For all three contents, 10 m and 20 m drop heights always resulted in failure. Only a SI content case with a 5-m drop yielded a failure.

The drums were seen to fail in one of four ways in the drop tests. When the drum was oriented at either 0- or 90- degree, however, no failure was seen in the system at any of the drop heights. These cases of 0- and 90-degree are the safest of the orientations in the drop tests, unlike the cases of 135 and 180 degrees that were most prone to failure. At 45-degrees the drum contacted the surface along the edge where the bottom and sides connect. The failure in these cases occurred directly at this junction, but rarely led to significant breach area. In contrast, the 135-degree orientation was the most damaging scenario of the drop tests, having the most number of and worst failures. The mechanism in which the system failed when dropped at the 135-degree orientation was along the seal where the lid and sides meet. If the system had any lid separation, it was likely that all the contents would spill out. For the 180-degree orientation, the drum typically ruptured from failure of the lid vent. The lid vent was either pushed into the container or completely released from the lid. If this happened, the contents would escape from the hole that the vent occupied. Taking a conservative approach, any test in which movement was seen in the lid vent was seen as a failure in the system. Although the likelihood of failure for the 180-degree orientation case was on par with the 135-degree orientation, the magnitudes of breach areas measured from the lid vent opening were a mere fraction of the breach areas from complete lid failure.

The failure modes of the drop for the drum are shown in Figure 3-15. As shown in this figure, the failure mode can be described in general to be the separation of the drum wall with either the drum bottom or lid.

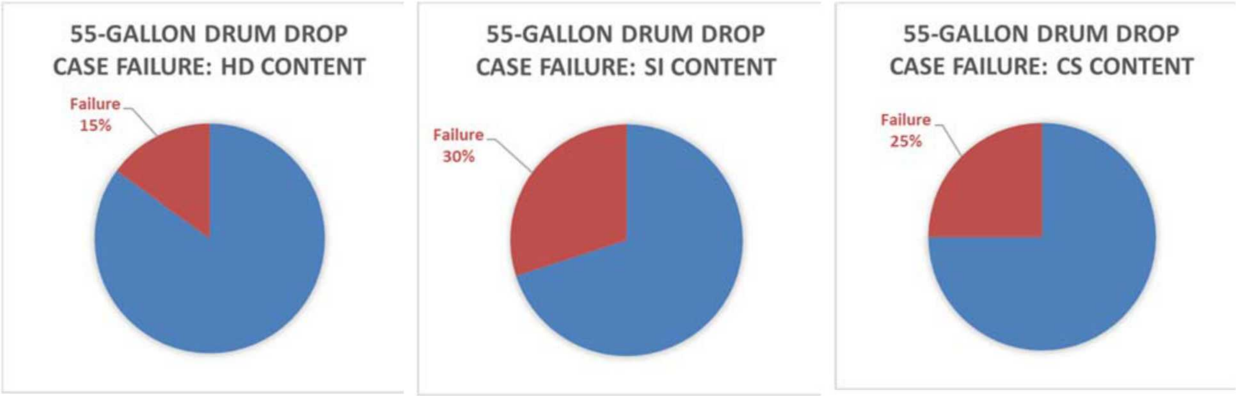

(a) (b) (c)

Figure 3-12. Percentage of Failure Cases Resulted from 7A Drum Drop Simulations for Each of the Content Type.

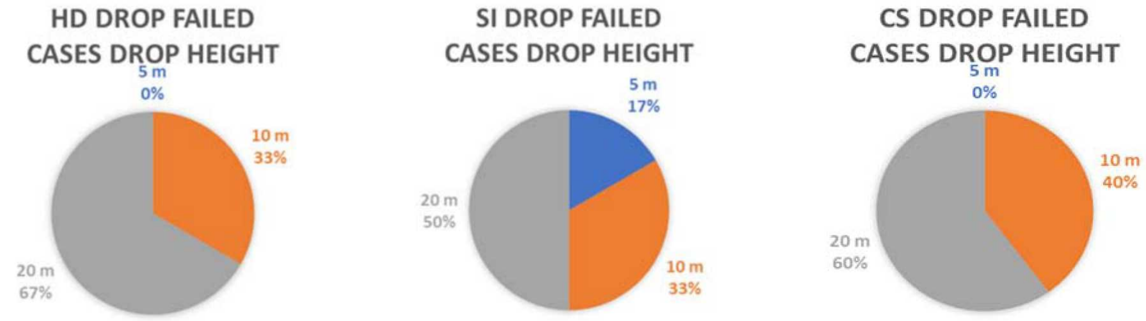

(a) (b) (c)

Figure 3-13. Percentage of Failure Resulted from Drop Height for 7A Drum Drop Simulations

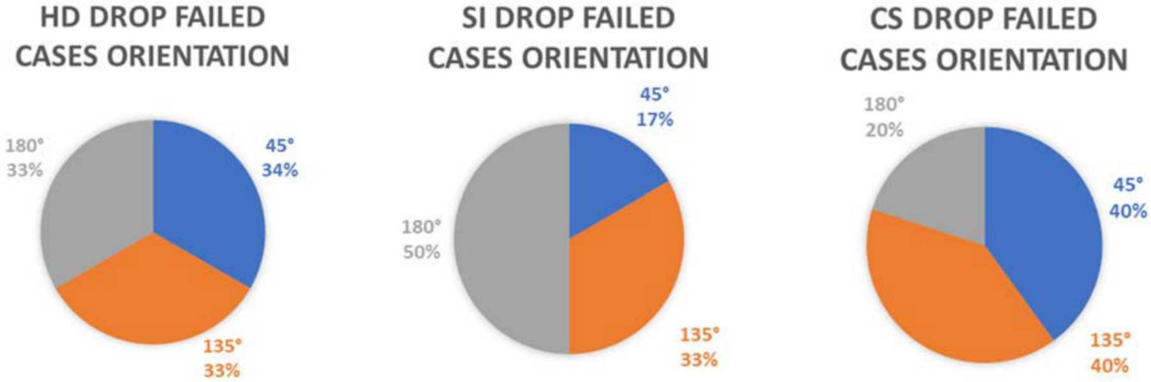

(a) (b) (c)

Figure 3-14. Percentage of Failure Resulted from Drop Orientation for 7A Drum Drop Simulations

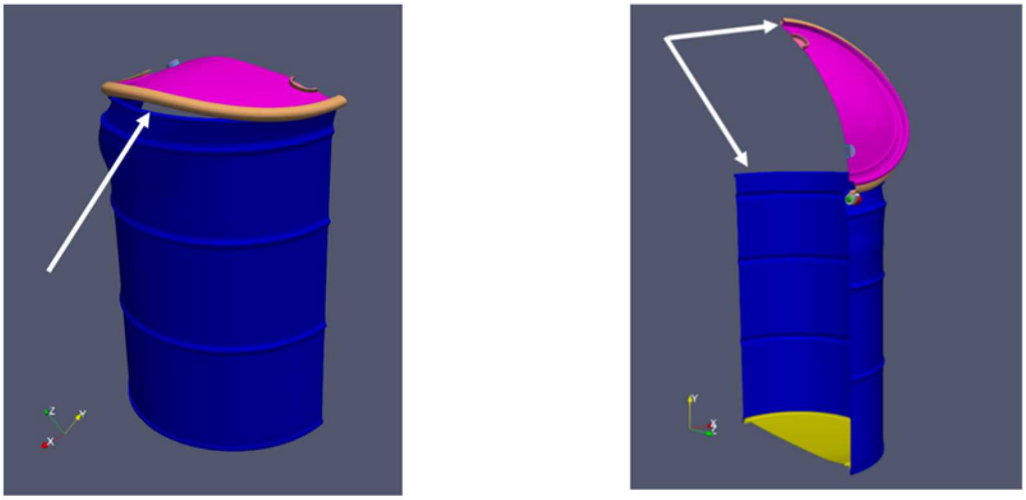

(a) Failure due to Lid and Sidewall Separation (b) Complete lid failure

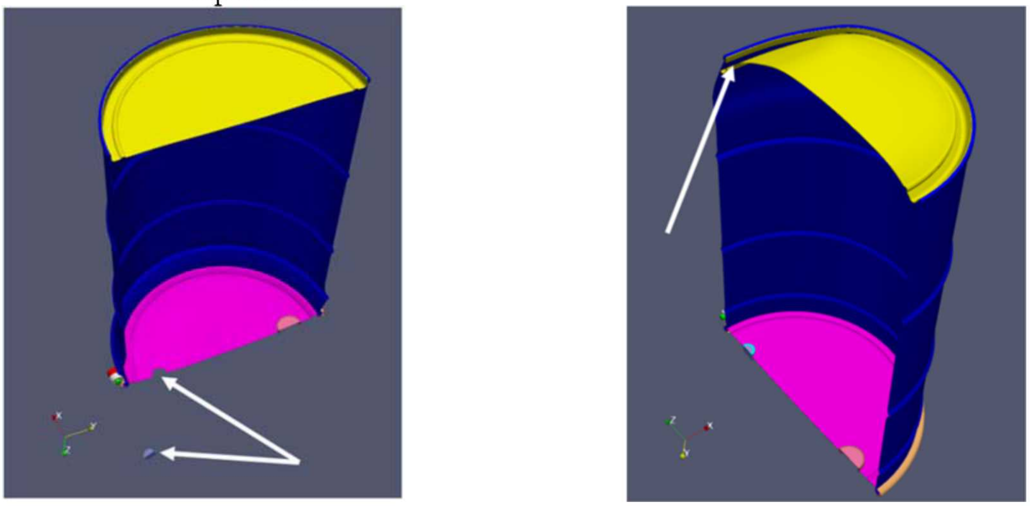

(c) Lid Vent Failure (d) Bottom Failure

Figure 3-15. Typical Drum Drop Failure Modes

For the puncture cases due to the forklift tine impact, a total of 24 simulation cases were run for each of the three content types, varying the impact location, constraint, and tine initial velocity. For illustrations, Figure 3-16 shows the selected drum puncture cases as functions of the impact locations for constrained versus unconstrained.

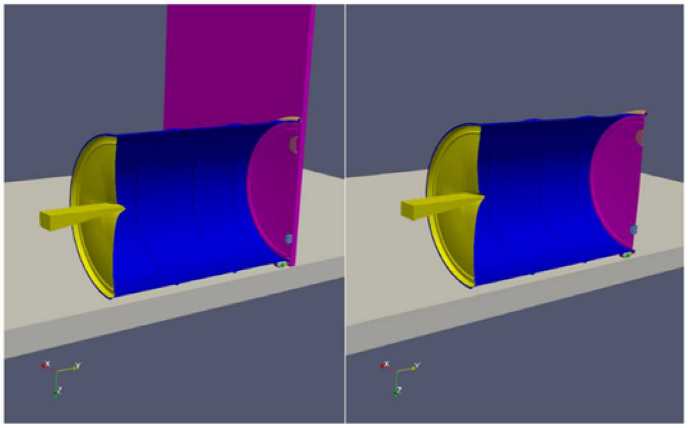

(a) Comparison of Restraint (Fixed) versus No Restraint (Free) for Bottom-center Impact Cases

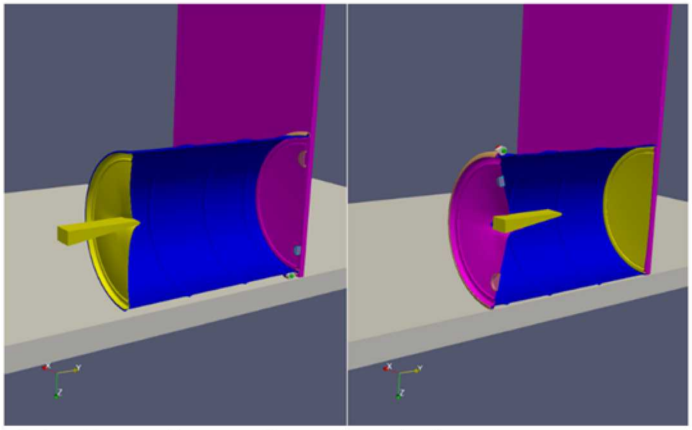

(b) Comparison of the Center Impact Locations (at bottom-center versus lid-center) of Drum Puncture Cases

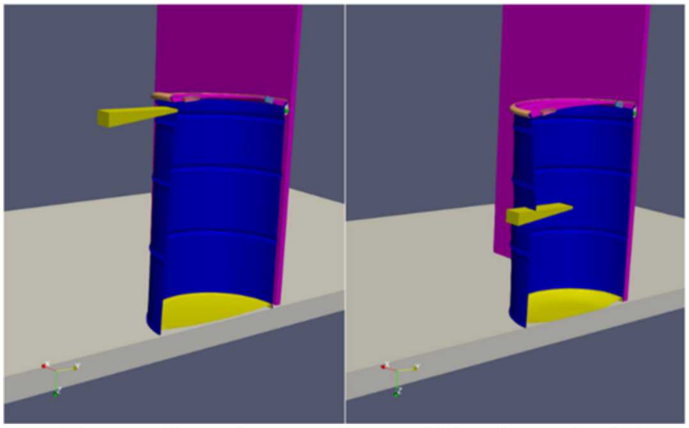

(c) Comparison of Impact Locations on Drum Sides (near the lid and drum center) for Restrained Drum Puncture Cases

Figure 3-16. Selected Comparison of the Drum Puncture Cases

Drum failurec was affected by every variable such as content type, tine speed, and location of impact. The HD and CS contents yielded similar results whereas failure was more likely to occur with the SI content type. The drum never resulted in failure when being impacted by the tine traveling at 0.5 meters per second.

Figure 3-17 shows the percentage of 7A drum failure due to this impact for various content types. As shown in this figure, SI content tends to yield a higher percentage of failures compared to the other material content types. It is consistent to the finding for the drop scenarios as reported in Figure 3-12. In terms of the effect of the parameters, the impactor speed, the constraint type, and puncture locations on the drum, Figure 3-18, Figure 3-19 and Figure 3-20 show the corresponding failure results, respectively. In the simulations, the tine impacted the drum in one of four locations (see Figure 3-20). The locations at which failure occurred are shown in Figure 3-20. Striking the middle of the outside wall of the drum resulted in the fewest cases of failure.

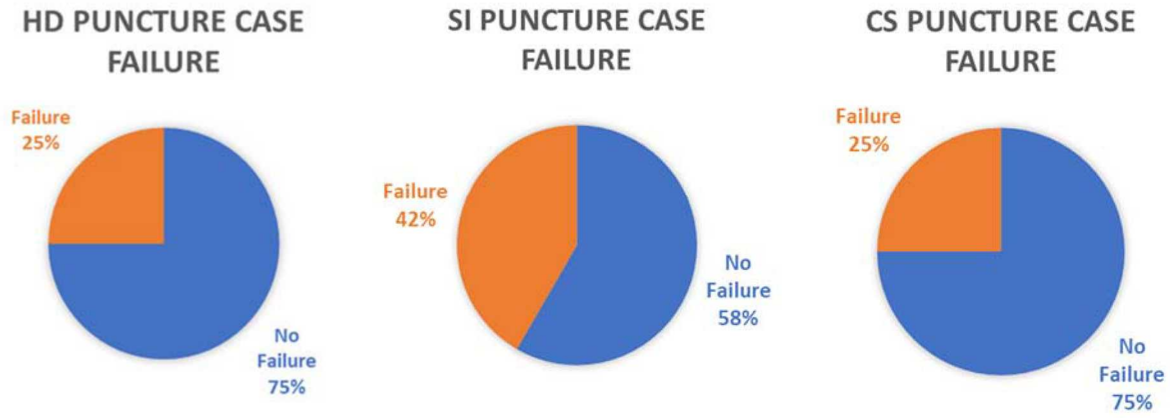

(a) (b) (c)

Figure 3-17. Percentage of Failure Resulted from Forklift Impact for 7A Drum Drop Simulations

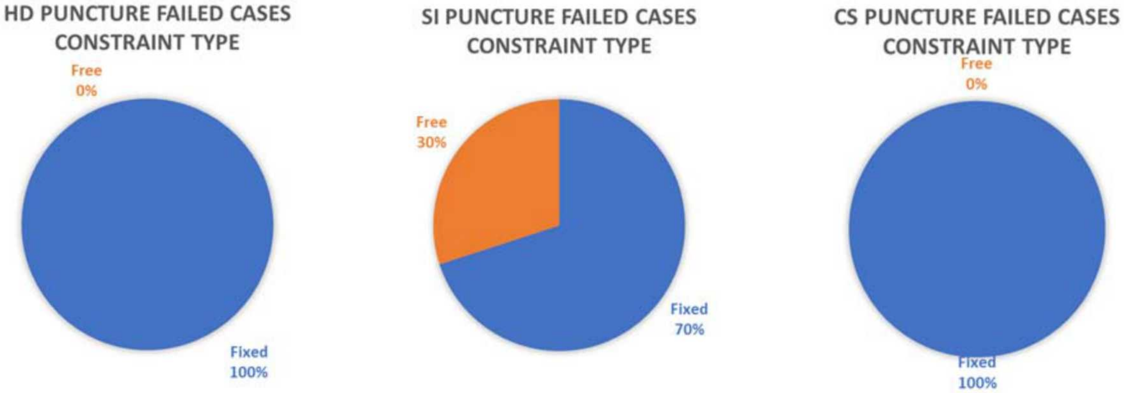

(a) (b) (c)

Figure 3-18. Percentage of Failure Resulted from Constraint Type for 7A Forklift Impact Simulations

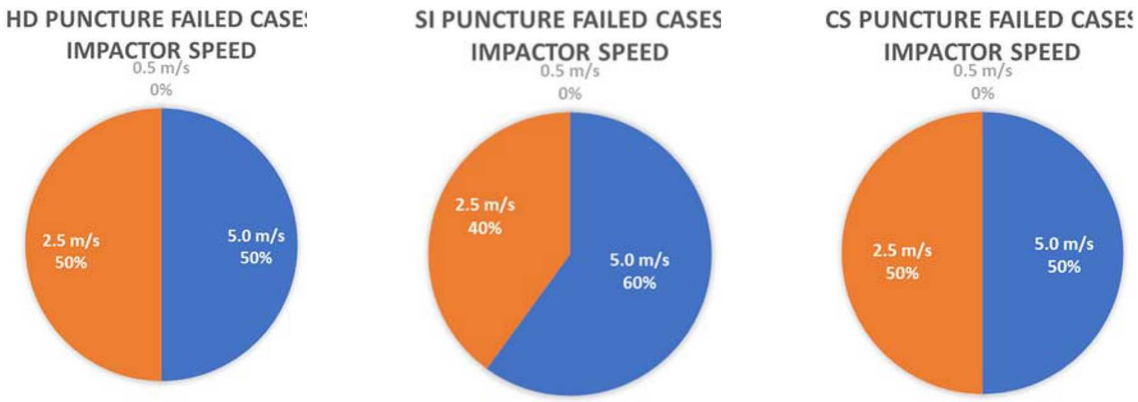

(a) (b) (c)

Figure 3-19. Percentage of Failure Resulted from Impactor Speed for 7A Forklift Impact Simulations

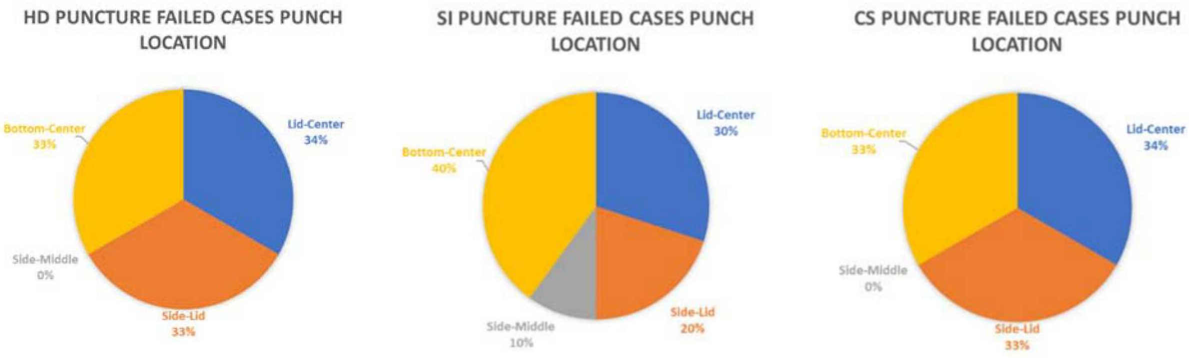

(a) (b) (c)

Figure 3-20. Percentage of Failure Resulted from Puncture Location for 7A Forklift Impact Simulations

3.3.1.2. Drop and Puncture Results for SWB

Similar to the 7A drum, puncture and drop tests were run on the SWB assembly. The puncture tests were run at the same three tine impact speeds of 0.5, 2.5, and 5.0 meters per second. The tine impacted the SWBs at four separate locations with the SWB being either fixed or free of constraints. Drop tests were run in the same exact manner as the drums. SWBs were dropped from heights of 2.5, 5, 10, and 20 meters at orientations ranging from 0 to 180 degrees. The SWB tests were run with the HD as the only content type, significantly decreasing the number of test trials to analyze.

Figure 3-21shows the percentage of failure for the SWB puncture simulations. As shown in this figure (a), only a quarter of the cases has resulted in failure. In terms of the puncture locations, the puncture near the side of the drum at the location near the lid will result a higher percentage of the failure under the restraint scenario. Figure 3-22 shows the percentage of failure due to SWB drop simulations. As shown in this figure only 29% cases result in failure.

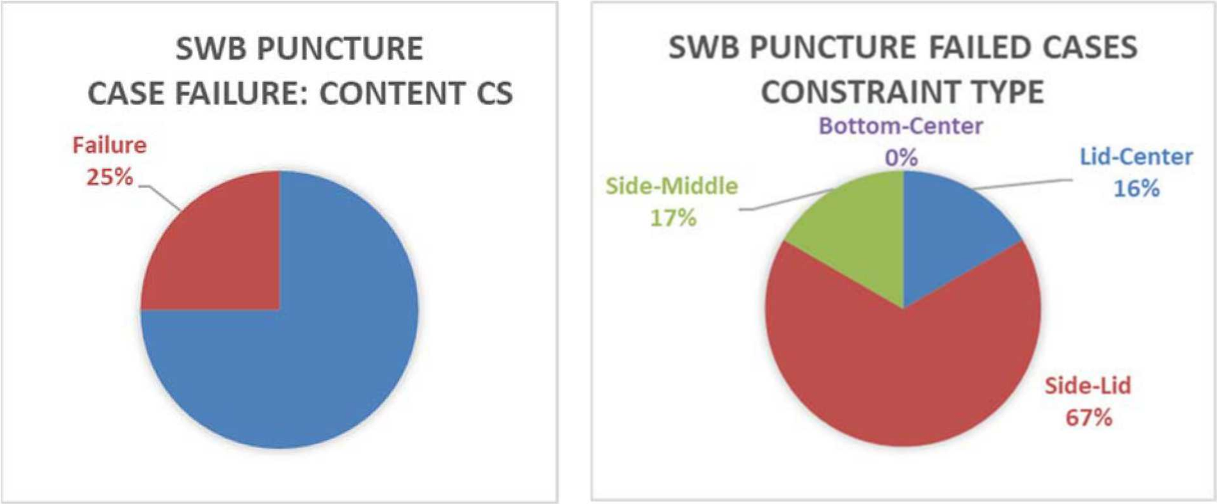

(a) Total Failure (b) Location Failure

Figure 3-21. Percent of Failure for SWB Puncture Simulations

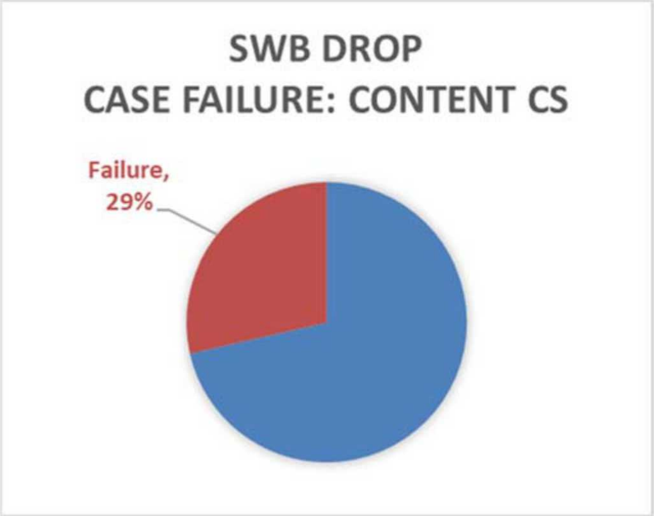

Figure 3-22. Percent of Failure for SWB Drop Simulations

3.3.2. Determination of the Breach Area

This section briefly discusses the analysis procedure required to calculate breach area from drop-test or puncture simulations. The tests have been executed in SIERRA/SM. To visualize the output, applications such as ParaView [Ayachit 2018] or EnSight [Ensight 2018] are used. Figure 3-23 (a) shows the initial problem set up for one of the puncture tests for a 7A drum. Displacements are applied to the system and the results from the final time step of the simulation is exported. Figure 3-23 (b) shows the frame that will be exported and used for further analysis.

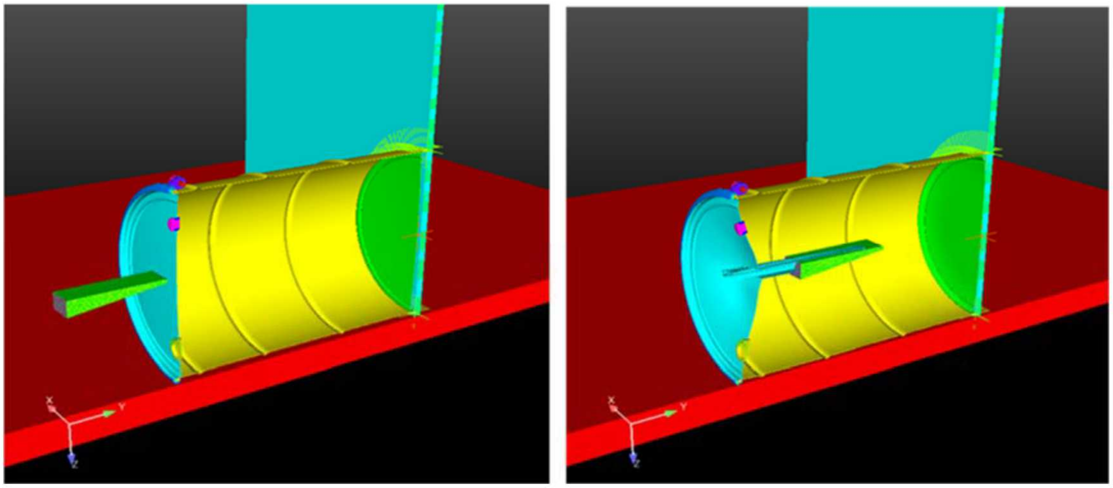

(a) Initial Time (b) Final Time (Penetration)

Figure 3-23. Example of 55-gal Drum Impact Simulations for Measuring the Breach Area

Using ParaView, the user can filter out dead elements (elements that have been severely distorted) to help identify the boundaries of the breach locations. Death status for elements is a binary variable of either 0 or 1. A threshold that filters elements out based on their respective element death status is applied by setting the minimum scalar value between 0 and 1, and the maximum to a value greater than one. Setting this filter then removes all the dead elements leaving the remaining mesh with the hole caused by the breach. This feature is particularly helpful for the puncture simulations, as can be seen from Figure 3-24. The data with the threshold applied can then be saved as an exodus file and imported into another program for further analysis.

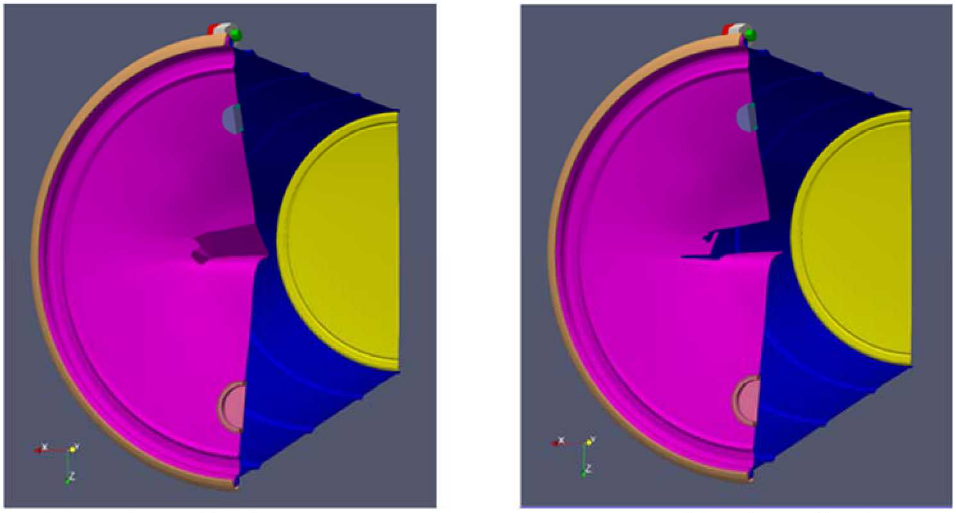

(a) Before Filtering (b) After Filtering

Figure 3-24. Example of Filtering of the Dead Elements for a Puncture Scenarios

Upon exporting the desired time step from the visualization application, the file is then loaded into Cubit, a meshing tool for SIERRA [Blacker 2017]. Cubit allows the user to mesh and isolate surfaces and bodies in the problem output (see Figure 3-25). The geometric entities where the breach occurs must be isolated to calculate the total breach area in the system. Breaching can be in the form of puncturing the container directly, or by causing separation between the components of the system. In the case of the tine-puncture tests, puncture and separation of components can be identified easily. For drop tests, deformation of the container will result in the separation of parts in the system. After the breach location has been identified and the surfaces involved have been isolated, breach area can then be calculated.

As shown in Figure 3-25, surfaces are created to cover and calculate the extent of the breach area. These artificial surfaces are created using the surface creation tool in Cubit which allows the user to select nodes in the mesh and form a surface. The breach area is estimated by numerous finite surfaces to accurately represent the area. Relatively flat, simple breach areas can be represented with a limited number of surfaces. However, curved or more complex regions will need a larger number of surfaces to obtain accuracy. Figure 3-26 shows the individual patches which represent the beach. After creating the surfaces that accurately represent the breach area, Cubit allows the user to easily determine geometric properties and values of components in the system. The surface area can be determined by using the Cubit "list <entity names and IDs> geometry" command. The total breach area would then be the sum of the areas of all of the surfaces created.

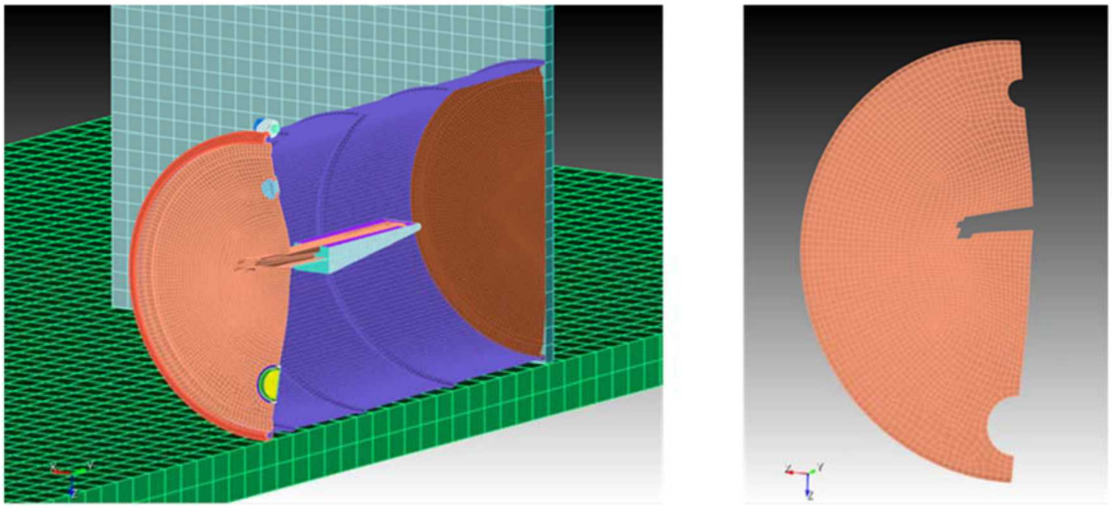

(a) Meshing (b) Isolation

Figure 3-25. Example of Using Cubit to Process Images for Calculating Breach Area

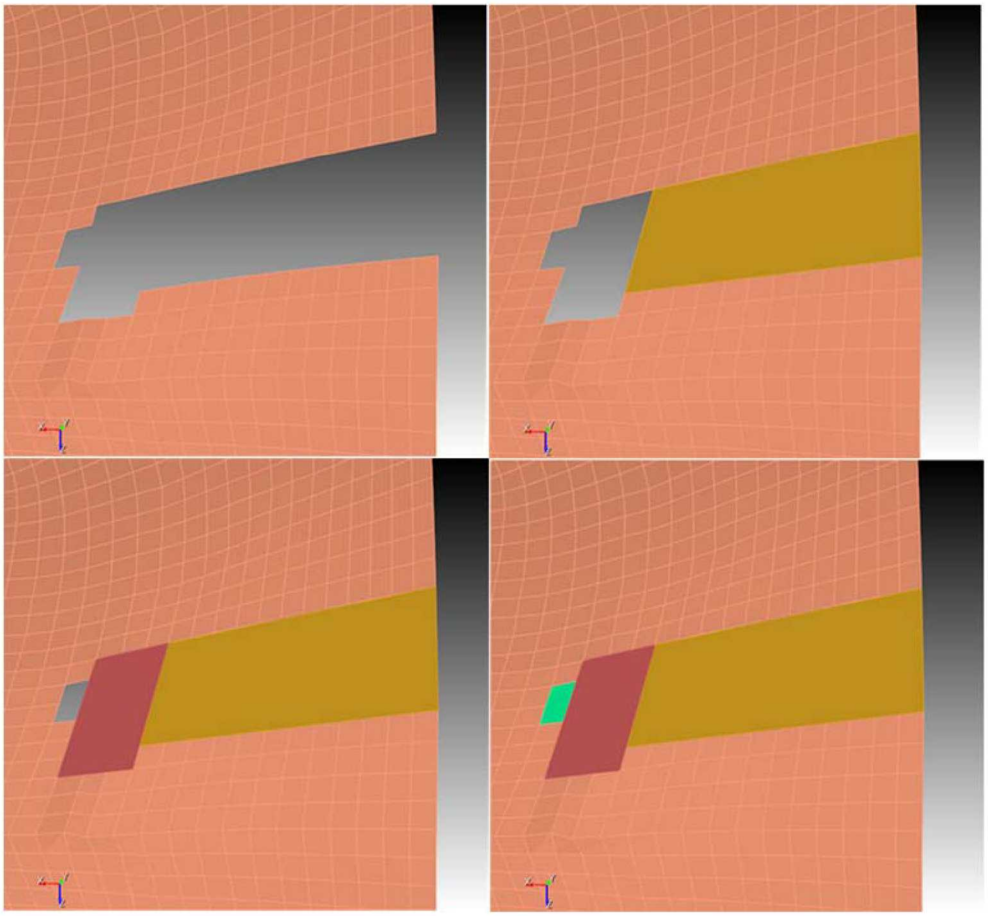

Figure 3-26. Manually Selected Mesh Regions for Calculating Breach Area

Calculating breach area using finite surfaces allow for the user to obtain quick and accurate approximations of the breach area in a situation where breach occurs. The same process for visualizing and calculating the breach area was similar for both the puncture and drop simulations of container type such as 55-gallon (7A) drum or SWB, or content type such as HD, SI, CS.

3.3.3. Breach Area Estimates

This section describes the estimate of the breach area for simulation cases that had resulted in a breach. The estimate is based on the previous section to determine the breach area. This method can be extended for analyzing SWB results as well.

3.3.3.1. 7A (55-gal) Drum

This section provides the breach area calculated for the 7A(55-gal) drum simulations for both puncture and drop simulations. As shown in Table 3-8, the largest breach areas calculated are those cases with the container being restrained at the wall. Because the impact is due to a single forklift tine, the breach area resulting from a tine puncture may not be much larger than the largest tine cross sectional area unless the impact is near the edge of the drum lid or bottom of the drum. For those cases, any impact that results in the component separation may cause the container to lose its integrity. Note that the breach area shown in this table is based on the half-symmetry configuration model. The actual total breach area should be twice of this value. Similarly, the drop scenario simulations show number of cases that had yielded breach (see Table 3-9). More detailed discussions on these breach areas are shown in Section 3.4.2.

Table 3-8. Calculated Drum Puncture Breach Area

Content Type	**Constraint**	**Impact Location**	**Impactor Speed (m/sec)**	**Breach Area (10^{-3} m^2)**	**Mode of Failure**	
					Puncture	Lid, Sidewall Separation
HD	Fixed	Lid-Center	2.5	2.639870	✓	
HD	Fixed	Lid-Center	5.0	5.771339	✓	
HD	Fixed	Side-Near Lid	2.5	1.855003		✓
HD	Fixed	Side-Near Lid	5.0	14.271866	✓	✓
HD	Fixed	Bottom-Center	2.5	1.685229	✓	
HD	Fixed	Bottom-Center	5.0	4.069057	✓	
SI	Fixed	Lid-Center	2.5	8.127033	✓	
SI	Fixed	Lid-Center	5.0	6.869964	✓	
SI	Fixed	Side-Near Lid	2.5	2.259687		✓
SI	Fixed	Side-Near Lid	5.0	49.154048		✓
SI	Fixed	Side-Middle	5.0	4.318277	✓	
SI	Fixed	Bottom-Center	2.5	2.790919	✓	
SI	Fixed	Bottom-Center	5.0	3.224823	✓	
SI	Free	Lid-Center	5.0	4.564275	✓	
SI	Free	Bottom-Center	2.5	0.267000	✓	
SI	Free	Bottom-Center	5.0	2.485696	✓	
CS	Fixed	Lid-Center	2.5	2.717847	✓	
CS	Fixed	Lid-Center	5.0	4.463526	✓	
CS	Fixed	Side-Near Lid	2.5	47.24652		✓
CS	Fixed	Side-Near Lid	5.0	82.940775		✓
CS	Fixed	Bottom-Center	2.5	1.956335	✓	
CS	Fixed	Bottom-Center	5.0	4.005066	✓	

Table 3-9. Calculated Drum Drop Breach Area

Content Type	Drop Height (m)	Orientation (deg)	Breach Area (10^{-3} m^2)	Mode of Failure			
				Lid, Sidewall Separation	Complete Lid Failure	Lid Vent Failure	Bottom Failure
HD	20	135	4.605148	✓			
HD	20	180	0.743268			✓	
SI	5	180	0.808858			✓	
SI	10	135	127.13272		✓		
SI	10	180	0.788763			✓	
SI	20	45	4.387404				✓
SI	20	135	124.95101		✓		
SI	20	180	0.815839			✓	
CS	10	45	5.464377				✓
CS	10	135	125.68497		✓		
CS	20	45	86.786316				✓
CS	20	135	124.45447		✓		
CS	20	180	0.795928			✓	

3.3.3.2. SWB

This section provides the breach area calculated for the SWB simulations for both puncture and drop simulations. Table 3-10 shows the breach area estimates for SWB puncture simulations. Note that the breach area shown in this table is based on the half-symmetry configuration model. The actual total breach area should be twice of this value. Table 3-11 shows the breach area estimates for SWB drop simulations. In this drop simulation, when there is a failure, it is always a full breach due to the separation of the lid/bottom cover from the container body. No area calculation was necessary for the drop simulations. More discussions are presented in Section 3.4.2.

Table 3-10. Calculated Puncture SWB Breach Area

Content Type	Constraint	Impact Location	Impactor Speed (m/sec)	Breach Area (10^{-3} m^2)	Mode of Failure	
					Puncture	Lid, Sidewall Separation
CS	Fixed	Side-Near Lid	2.5	65.599728		✓
CS	Fixed	Side-Near Lid	5.0	106.448776		✓
CS	Free	Side-Near Lid	2.5	10.625484		✓
CS	Free	Side-Near Lid	5.0	135.583108		✓
CS	Fixed	Side-Middle	5.0	5.945719	✓	
CS	Fixed	Lid-Center	5.0	6.581837	✓	

Table 3-11. Calculated Drop SWB Breach Area

Content Type	Drop Height (m)	Orientation (deg)	Breach Area (10^{-3} m^2)	Mode of Failure
				Complete Lid Failure
CS	2.5	135	Full Breach	✓
CS	5	45	Full Breach	✓
CS	5	135	Full Breach	✓
CS	10	45	Full Breach	✓
CS	10	135	Full Breach	✓
CS	20	45	Full Breach	✓
CS	20	90	Full Breach	✓
CS	20	135	Full Breach	✓

3.4. Development of Correlations and DR×ARF×RF Examples

This section describes the method to estimate the DR based on the previously calculated the breach areas for simulations that resulted in container beach. Because our focus was on breach area, the correlation between the breach area and DR is being investigated. Since Appendix C in DOE-STD-5506 [DOE 2007] discusses the derived DR from breached containers, we apply the similar methodology to derive the DR for our study. DOE-SRTD-5506 will be described first.

3.4.1. DOE-STD-5506 DR Results

Two types of mechanical insults from experiments are described in this standard [DOE 2007]. Two experimental test series were reported for single drum drop tests. No SWB drop/impact tests was done.

<u>Drum Drop</u>

The first series was from SNL and the other series was from Hanford.

The SNL tests composed of 12 static crush tests with eight drums in the lateral configuration (or sideways) and four in the longitudinal direction (or upright) and 17 drop tests in the lateral impact configuration. The main purpose of these SNL tests was to observe the drum deformation and lid behavior. All 17C drums contained contents in polyethylene liner and bag, which provided layers of confinement. Note that four of the crush tests and six of the drop tests were empty drums. The results of the single drum drop tests for the DOT-17C drums are:

1. No lid failure or material release was observed for drop height < 13 m (44 ft) or impact velocity of < 35 mph (15.6 m/s).
2. Four lid failures have been found in the 17 drop tests but only one test with the heaviest content of 748 lbs resulting the loss of the contents. It amounted to about 5%.
3. The conclusion of these tests indicated that drum deformation cannot be predicted by considering only the kinetic energy of the system. Drum contents are important factors because different materials absorb energy differently.

The Hanford tests consisted of six drum drops: 3 Type 17C and 3 Type 17H. The contents were primarily sands and lead bricks without any liner or bag. Maximum weight was used in all cases (~1000 lbs.). The drop height was from ~3.3 m (11 ft). The findings of these tests are:

1. The impact angles of 45 to horizontal to the locking ring with 1000 lbs of content are likely to result in the release of the contents
2. For the Type 17C drums, the release amounted to about 27% of the contents with 250 lbs. The average weight of the three drums is about 103 lbs. with a release of 11% of their contents
3. For the Type 17H drums, the maximum release is about 53% (about 500 lbs.). The average release is about 170 lbs. (18% of the drum contents).
4. All tests had initial void volumes of 10%. All lids stayed attached to the drum for the tests
5. The drum failure occurred at the drum/lid seal area in all tests. A small damage to the drum/lid interface may cause lid separation and result container integrity loss.
6. One observation was that highly visible damage to the drum may not be an indicator of drum integrity as the damage may only be superficial On the other hand, extensive damage to the drum walls may not be indicator for a container breach.

Summarizing the single drop container tests and the extrapolation of the results, the following conclusions were made [DOE 2007]:

- A fall from 3.3 ft (~1m) or equivalent to 2nd tier in the stacked array would not result any release. Thus, DR of 0 is assumed. This corresponds to the qualification for Type A containers.
- For a fall from 6.7 ft (~2m) or equivalent to 3rd tier in the stacked array may not result in release. However, no test was done at this height. Because the kinetic energy is larger than the height for the qualification, it is assumed a DR of 0.01 as a conservative value
- For a fall from 4th and 5th tier in the stacked array at about 44 ft (~13 m), the experiments described in this section above concluded the following:
    - SNL tests above concluded that no lid failures (and no material release) occurred for the drop from 44 ft (~13 m) height.
    - The worst damage occurred with the drum of 748 lbs. and the inner bag was broken, resulting in minor amount of release at about 11 ft (~3.3 m). Because the release amount did not measure, it is assumed a DR of 0.1 for the contaminated solids
    - The Hanford tests contained contents at the maximum quality, the 3.3 m drop would yield a DR of 0.5 for sand-like contents.

SWB Drop

Although no SWB test was done for this standard, the standard provided criteria for the SWB drop DR [DOE 2007]:

- 1 m (~4-ft) drop of the SWB should also be qualified as for the case of the Type A for the drums. Thus, DR of 0 is assumed.
- Based on the Rocky Flat DOT 7A welded metal box drop tests, there was no apparent failure of seams or closure welds and no contents were lost from the box for the 15-ft (4.6 m) drop. For a 25-ft drop, a pin hole leak was detected in test container. The leak was located at a corner of the waste box, adjacent to a lifting loop. No apparent content release was observed. However, because this box was different from the actual SWB, it is recommended that a DR of 0.1 for 4th tier high is used. For sand-like content materials, it recommended a DR of 0.25 is used instead of 0.5 for the drum with the same content material because of its larger volume and self-shielding effect. For 3rd tier high drop, it recommended a value of 0.01 be used for DR similar to that of the drum.

Forklift Tine Puncture

There was no experimental data for this type of puncture accident for both the drum and SWB. The standard only provides the reasoning to derive the value of DR for both drum and SWB. Note that no speed associated with the forklift tine puncture was provided or if the impact is located such that the container is fixed at the wall. It might assume that the forklift tine had sufficient kinetic energy to cause the breach.

For a breached drum, it considers a value of 0.1 for DR. This judgment is based on the following considerations:

A forklift tine puncture only creates a small breach area of the container;

- Non-liquid wastes would flow out of the container through the breach area;
- Any packaging (such as a plastic bag) will tend to inhibit the waste flow due to recovery from the breach rather than having permanent deformation as might be the case with the metal container wall.
- Sand-like waste material that is capable of flowing could clog at the exit before much material has passed through the container. A conservative value of 1 for DR is assumed for this waste material.

For a breached SWB, the tines would create two holes as opposed to one for a drum. In addition, because the content mass for SWB can be four times higher than that of the drum, and the breach area from a tine provided only a small fraction of the entire surface area available compared to that of the drum, a factor of 2 reduction is conservative considering that the contamination may not be uniformly distributed.

In summary, the standard provides a range of DR values as described in this section (see Table 3-12).

Table 3-12. Container Drop and Impact Damage Ratio DOE Standard [DOE 2007]

Accident Stress	Damage Ratio (DR)	
	Drum	SWB
1. Stress within container qualification (2nd tier, ~1 m high, in stacked array drop)	0	0
2. Minor stress causes breach: • Single container dropped from 3rd tier (or ~2 m high) in stacked array	0.01	0.01
3. Single container dropped from 4th or 5th (or ~13 m high) tier in stacked array: • Contaminated solids • Sand-like materials	 0.1 0.5	 0.1 0.25
4. Container(s) punctured by forklift tines: • Contaminated solids • Sand-like materials	 0.1 1.0	 0.05 0.5

3.4.2. *Estimate of DR from Simulations*

In summary, the SIERRA/SM simulation results described in Section 3.3 provide data to estimate DR for both drums (7A or 55-gal) and SWB for a free-fall height of 2.5, 5, 10 and 20 m, and the forklift tine velocity of 0.5, 2.5 and 5 m/s. In the puncture case, both free (unconstraint) and fixed (constraint) container configurations are modeled. In both mechanical insults, the maximum content mass was used. Only drum simulations contained three types of contents, whereas the SWB only utilized a single content.

In contrast, the DOE-STD-5506 [DOE 2007] only examined the drop height from 1 m to 13 m. In terms of impact cases, no actual experiments of the drum and SWBs were performed. Despite this limited experimental set and the conservative estimations used in the standard for estimating DR values, we extrapolated their conclusions to our results, and the following assumptions are made: assumptions are made:

Material Behavior Assumptions:

- Contaminated soils/debris waste (CS) in our simulations is similar to the sand-like materials in DOE-STD-5506
- Solidified inorganics (SI) in our simulations is similar to the contaminated solids in DOE-STD-5506
- Only CS may experience releases through the opening of the breach because the material is assumed to be sand-like.

Free-Fall Assumptions:

- If the impact causes the lid or the bottom surface to separate from the container wall, then a DR of 1 is assumed for CS type content. (See Figure 3-15 for the definition of the drop failure modes.) Note because of the sand like material, it can easily flow out with the available kinetic energy.
- However, for both SI and HD, it is assumed that only 50% of the materials can get out because most of the kinetic energy is used to breach the container leaving a smaller amount to eject the

contents. The rationale is that the large solids/pieces are not easily to eject out when the lid or bottom cover separates from the container body.

Forklift Puncture Assumptions:

- Both SI and HD in our simulations may consist of solids that can be greater than the breach area caused by a forklift tine. Because of the kinetic energy of impact, the contaminant may loft up and release through the breach area. DR is assumed to be 0.1, which is consistent with Table 3-12. If the speed is double, the release is assumed to be twice of this value. Unless the opening is sufficiently large to allow a large solid to eject out (DR is four times larger than 0.1), this value is assumed to be the same.
- Depending on the breach location for the CS, it can influence the potential release. If the breach area is located mid-height (literally or vertically), it is assumed that half of the sand-like material is released out. If rolling occurs after the impact, particularly when the opening is not on the lid nor the bottom cover of the container, the release may be higher than the half. If the impact is located near the lid from the side of the container, then the release is small because the content may not be fully filled up to the lid inside the container. In addition, the amount that can lead through this path is insignificant. If the impact is located near the bottom cover of the container and caused a breach, the amount would be significant. However, the force required to cause a breach at this location is higher compared to the location near the lid because of the material at the bottom is compressed and resists puncture.
- If the impact location is at the lide from the side of the container, then the release should be small. It is assumed a DR of 0.01, which is equivalent to ~2m drum drop as shown in Table 3-12. For SWB, use the puncture value as shown in Table 3-12.

Based on the above assumptions, Table 3-13 and Table 3-14 show the estimate for the DR from the drum simulations for the drop and puncture scenarios, respectively. As shown in Table 3-13, the HD content tends to absorb the kinetic energy resulting in smaller breach areas for the drum. On the other hand, the SI content (large pieces) that do not damp or absorb the impact kinetic energy leads to larger breaches, even at a lower drop height. Note that in comparison to the single drum drop test at 4th or 5th tier high (see Table 3-12), the DR estimate shown in Table 3-13 is about the same in terms of the CS, sand-like material content, the high DR value was assumed because the combination of the complete lid separation, maximum content and high kinetic energy. This value is twice the values assumed in Table 3-12. In terms of puncture scenarios, Table 3-14 shows that the assumed DR values for both HD and SI contents should be consistent with that were listed in Table 3-12. However, since impact location of our puncture simulations is located at the mid-point of the container, any breach resulting from the insult would only result in 50% release.

Based on the above assumptions, the following tables show the estimate for the DR from the SWB simulations. Unlike the drum cases where there were three types of contents for SWB, CS is only content used. CS behaves like sand, so when the lid or bottom cover separated from sidewall, the content is completely released. For the puncture cases, DOE-STD-5506 discussed that both tines from the forklift could impact to the SWB. Thus, two breach areas may result. In our simulations, we assumed only a single tine impacting the center of the SWB. However, the kinetic energy associated with the tine was equivalent to the entire mass of the forklift. Table 3-15 and Table 3-16 give DR for the drop and puncture scenarios, respectively. As shown Table 3-15, all drop SWB simulations resulted in complete lid and wall separation are assumed to have a high DR value, which is consistent with the same assumptions used in the drum drop simulations above. For the puncture cases, it is consistent for our drum puncture simulation results, and consistent with the values in Table 3-12.

Table 3-13. Estimate of Damage Ratio from Drum Drop Simulations

Content Type	**Drop Height (m), Orientation (°)**	**Breach Area (10^{-3} m^{2})**	**Damage Ratio**	**Mode of Failure**			
				Lid, Sidewall Separation	Complete Lid Failure	Lid Vent Failure	Bottom Failure
HD	20, 135	9.21	0.04[A]	✓			
HD	20, 180	1.49	0.01[C]			✓	
SI	5, 180	1.62	0.01 [C]			✓	
SI	10, 135	254.30	0.5[B]		✓		
SI	10, 180	1.58	0.02 [C]			✓	
SI	20, 45	8.78	0.04 [C]				✓
SI	20, 135	250.00	0.5[B]		✓		
SI	20, 180	1.63	0.04 [C]			✓	
CS	10, 45	10.93	0.01 [C]				✓
CS	10, 135	251.40	1.0[B]		✓		
CS	20, 45	173.60	1.0[B]				✓
CS	20, 135	248.90	1.0[B]		✓		
CS	20, 180	1.59	0.02 [C]			✓	

[A] Even though there is clear separation, but because the opening is small, it is assumed only very small release

[B] Complete lid failure or bottom failure with a very large breach area calculated. Assumed that sufficient kinetic energy remains to push majority of the materials out for CS type content (see Figure 3-27). For both HD and SI, it is assumed only 50% material release, due to solids and large debris, which unlike sands/soils can easily flows out.

[C] Small breach area, such as lid vent failure and minor bottom separation from sidewall of the container. It is assumed at DR of 0.01, then progress doubling if the kinetic energy is also doubled.

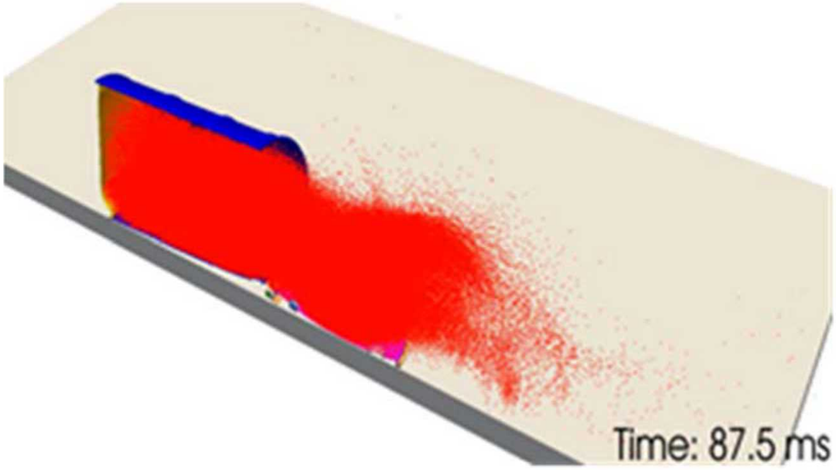

Figure 3-27. Example of Complete Lid Failure for a Case (CS type, 20 m drop and 135°Orientation).

Table 3-14. Estimate of Damage Ratio from Drum Puncture Simulations

Content Type	Constraint, Impact Location, Impactor Speed*	Total Breach Area (10^{-3} m^2)	Damage Ratio	Mode of Failure	
				Puncture	Lid, Sidewall Separation
HD	C(Fi), IL(LC), IS (2.5)	5.28	0.1	✓	
HD	C(Fi), IL(LC), IS (5)	11.54	0.2	✓	
HD	C(Fi), IL(SL), IS (2.5)	3.71	0.01[+]		✓
HD	C(Fi), IL(SL), IS (5)	28.54	0.02[+]	✓	✓
HD	C(Fi), IL(BC), IS (2.5)	3.37	0.1	✓	
HD	C(Fi), IL(BC), IS (5)	8.14	0.2	✓	
SI	C(Fi), IL(LC), IS (2.5)	16.25	0.1	✓	
SI	C(Fi), IL(LC), IS (5)	13.74	0.2	✓	
SI	C(Fi), IL(SL), IS (2.5)	4.52	0.01[+]		✓
SI	C(Fi), IL(SL), IS (5)	98.31	0.02[+]		✓
SI	C(Fi), IL(SM), IS (5)	8.63	0.2	✓	
SI	C(Fi), IL(BC), IS (2.5)	5.58	0.1	✓	
SI	C(Fi), IL(BC), IS (5)	6.45	0.2	✓	
SI	C(Fr), IL(LC), IS (5)	9.13	0.2	✓	
SI	C(Fr), IL(BC), IS (2.5)	0.53	0.1	✓	
SI	C(Fr), IL(BC), IS (5)	4.97	0.2	✓	
CS	C(Fi), IL(LC), IS (2.5)	5.44	0.5**	✓	
CS	C(Fi), IL(LC), IS (5)	8.92	0.5**	✓	
CS	C(Fi), IL(SL), IS (2.5)	94.49	0.01[+]		✓
CS	C(Fi), IL(SL), IS (5)	165.90	0.02[+]		✓
CS	C(Fi), IL(BC), IS (2.5)	3.91	0.5**	✓	
CS	C(Fi), IL(BC), IS (5)	8.01	0.5**	✓	

* For constraint type: Fi=fixed, Fr=free; impact location type: LC=Lid-center, SL=Side near lid, BC=Bottom center, SM=Side middle; impact speed type in meter/second: 2.5 or 5.

[+] For the impact location at SL, it is assumed a small release.

**It is assumed to be 50%, because the impact location is mid-point, regardless the extent of the opening.

Table 3-15. Estimate of Damage Ratio from SWB Drop Simulations

Content Type	Drop Height (m)	Orientation (°)	Damage Ratio	Mode of Failure
				Complete Lid Failure
CS	2.5	135	1.0	✓
CS	5	45	1.0	✓
CS	5	135	1.0	✓
CS	10	45	1.0	✓
CS	10	135	1.0	✓
CS	20	45	1.0	✓
CS	20	90	1.0	✓
CS	20	135	1.0	✓

Table 3-16. Estimate of Damage Ratio from SWB Puncture Simulations

Content Type	Constraint, Impact Location, Impactor Speed (m/s)	Total Breach Area (10^{-3} m^2)	Damage Ratio	Mode of Failure	
				Puncture	Lid, Sidewall Separation
CS	Fixed, Side-Near Lid, 2.5	65.599728	0.05		✓
CS	Fixed, Side-Near Lid, 5.0	106.448776	0.1		✓
CS	Free, Side-Near Lid, 2.5	10.625484	0.05		✓
CS	Free, Side-Near Lid, 5.0	135.583108	0.1		✓
CS	Fixed, Side-Middle, 5.0	5.945719	0.5	✓	
CS	Fixed, Lid-Center, 5.0	6.581837	0.5	✓	

3.4.3. ARF and RF Examples

This section describes the examples of ARF and RF values for the free-fall and puncture scenarios for those drums and SWBs that have failed and resulted in a breach area. The previous section also derives the DR for those failed containers. Because the of difficulties generalized about the release from a failed container, we did not simulate any small particulates for airborne release.

In this section, the discussions utilize the DR values assumed from Section 3.4.2, and formulate the ARF/RF values based on the scenarios where a breach has occurred for a container. When a container (such as a drum or a SWB) has a breach, the content spills out through the breach area. If the kinetic energy is sufficiently high, then the spill can be airbone. Once airborne, any small turbulence will allow the micron sized particles to remain in the air until agglomeration takes place with subsequent settling or depositing. Here, we are not interested in discussing the aerosol physics, rather how the particulates can be lifted from the solids' surfaces (such as large trash item or large metal piece) or within other particulates (such as sands).

For the drop cases, the kinetic energy is based on the potential energy calculated from the drop height and the mass of the container, including the content. A portion of this energy is used to deform and breach the container. The remainder of the energy should be used to loft any particulates in the content, and if the content contains solids, a portion of this energy would be used to deform or break it apart. If the content is HD, containing trash that absorbs a portion of the energy, this permits the rest of the energy to loft any contaminant on the surface. In this case, the ARF/RF should be low. If the content is sand, then all particulates would be lofted and released through the breach . In this case, when the particulates contain kinetic energies, they will release withsome initial velocities. Thus, the ARF/RF should be larger. Consult Sections 2.4, 2.5, 2.6 for cases that the impact energy is sufficient to loft contaminansts inside the container. If fragmentation inside the container is expected, then data from Section 2.2 may be used.

For the puncture cases, the kinetic energy is generated by the moving forklift in which its tine could punch a hole in the container's surface. This impact may not generate enough energy to dislodge any contaminant on a solid or imbedded in the sand like material. However, if the breach occurs at a height off the ground, allowing the sand-like material to flow out, then the release (ARF/RF) is equivalent to that of the free-fall spill at a specific height. (See Section 2.3 for details on the treatment of free-fall spill of powders.)

In general, the ARF/RF values discussed in Chapter 2 of this report can be used for the container breach simulations. If no specific case can be fitted or identified from Chapter 2, then the bounding ARF/RF values should be used.

3.5. Summary and Conclusion

This chapter summarized the SIERRA/SM simulations on container breach resulting from a free-fall drop and impact from a forklift tine puncture. The container selection and container content were based on the recent waste stream data from LANL. The scenarios simulated were chosen based upon the WIPP facility data for drop accidents and commercial forklift data for the impact accidents. Hundreds of simulations of runs were conducted for the 7A drum and SWB. The contents chosen for the drum include: HD, SI and CS. For the SWB, only CS is used because of the waste stream data. In terms of the drop scenarios, 2.5, 5, 10 and 20 m were chosen were chosen representing the range from 2-tier stacking to the height of a bridge crane in the WIPP facility. The drop angles chosen were based on what would be most severe while also representing a full spectrum of possible ground impacts. The content weight used was the maximum allowable in the WIPP-WAC. In terms of the forklift tine puncture scenarios, 2.5 and 5 m/s were chosen as the impact velocities, with 5 m/s being the maximum allowable forklift speed. The impact locations for the containers were the centers of the lid, bottom, and lateral side as well as the top of the container near the lid which is where an impact would most likely lead to a breach. The puncture simulations also demonstrate that a container held in place yields a higher probability of breach compared to one that is free to move after forklift tine impact.

The results show that the content type played more of a role in the drop tests than in the puncture tests with significant variability in terms of likelihood of failure. Drums filled with the SI content type most often led to failure whereas the HD-filled drums were much less prone to failure. For drops from 20 meters at 135 and 180-degree orientations, there was always failure for every material type.

Once the breach area was determined, an estimate of the DR was done using the DOE-STD-5506 as a guide. The results in this report are considered to be conservative estimates of DR since they are larger than those reported in the standard (see Sections 3.4.1 and 3.4.2) . We also attempted to quantify the magnitude of the ARF/RF by referencing the data in Chapter 2 of this report, and providing the arguments to determine these magnitudes.

This information in this chapter demonstrates that simulations can be used to model a broad range of accident scenarios and content types to predict container breach. The parameters tested go beyond those cases described in DOE-STD-5506. Thus, the information provided in this chapter should bound those described in the standard (see the DR values provided in Table 3-13 to Table 3-16 for our study and those values in Table 3-12 for the standard).

This page left blank

4. EXPANSION OF EQUATION 4-1 OF HANDBOOK

The work completed for this task was to implement a hierarchical multi-scale fragmentation model in the Library of Advanced Materials for Engineering (LAME) [Scherzinger 2016] that is part of the finite element solid mechanics code SIERRA/SM [SIERRA 2017a]. The model includes continuously updating boundary conditions and two-way transfer of information between a macro and microscale model to capture the complex coupling between the fragmentation behavior at the two different length scales.

In the following section, the coupled model is described and the results of predictions of impact loading scenarios using the model are presented and discussed. The section concludes by discussing the behavior of the presented model compared to Equation 4-1 in the DOE Handbook [DOE 1994] and has recommendations for future work that could be performed to verify and validate the fragmentation model. Understanding the fragmentation behaviors of brittle materials such as UO_2 is important to evaluate the risk of impact loading scenarios and the release of airborne particles. The presented model is very complicated due to the coupled nature of the physics at different length scales, which makes verification and validation an important and recommended step for improving the model confidence.

4.1. Concurrent-Coupled Fragmentation Model

The concurrently-coupled fragmentation model consists of two models (macro and micro) applied in SIERRA/SM, with a two-way transfer of information between models. The concurrently-coupled fragmentation model is implemented as a LAME material model in SIERRA/SM and is called the Hierarchical Gradient Damage Explicit (HGDE) model. The models employed at each length scale, and the transfer of information between them, is described in the following sections.

4.1.1. Macroscale Model

At the macroscale, the brittle material is represented using the Gradient Damage Explicit (GDE) model, which is an implementation of the model described by Lorentz et al [Lorentz 2011]. The GDE model calculates the macroscale fragmentation behavior of the material and removes elements from the model when they are damaged past a specified threshold.

Starting from an energetic point of view, the Helmholtz Free-Energy (ψ) depends on strain (ϵ) and phase field damage (ϕ). If ϕ=0, the material is undamaged, whereas ϕ=1 indicates the material is fully damaged. The Helmholtz Free-Energy is defined as

$$\psi(\epsilon,\phi) = g(\phi)\psi_e^+ + \psi_e^- + \frac{3}{4}\frac{G_c}{L}\phi + \frac{3}{16}LG_c\nabla\phi\cdot\nabla\phi \tag{4-1}$$

where $g(\phi) = \frac{(1-\phi)^2}{1+(m-2)\phi+(1+pm)\phi^2}$ defines stiffness as a function of damage and $m = \frac{3}{2}\frac{EG_c}{\sigma_c^2 L}$. The parameters in these equations are the positive and negative components of the strain energy ($\psi_e^+$and ψ_e^-), the fracture length scale (L), the fracture energy (G_c), elastic modulus (E), and critical stress value (σ_c). The parameter p is subject to the limitations $p \geq 1$ and $p \leq m-2$. It influences the shape of the stress decay following the initiation of damage accumulation.

The evolution of damage in the material is governed by the following equation

$$\eta\dot{\phi} = -g'(\phi)\widehat{\psi}_e^+ - \frac{3}{4}\frac{G_c}{L}\phi + \frac{3}{16}LG_c\nabla^2\phi \tag{4-2}$$

where $\eta \geq 0$ is the phase viscosity and $\widehat{\psi}_e$ is the driving energy.

Damage in the material can only accumulate once a critical threshold is exceeded. The gradient damage explicit model can be implemented with a stress-based or strain-energy based approach. If a stress-based approach is implemented, damage can only accumulate if the maximum element principle stress is greater than the element critical stress. In the stain-energy based approach, damage evolution can only occur when strain energy exceeds a critical strain energy,

$$\widehat{\psi}_c = \frac{1}{2}\frac{\sigma_c^2}{E} \tag{4-3}$$

The strain-energy approach is energy consistent with the phase field approach in SIERRA/SM. For this reason, all results that are described in the following sections implemented the strain-energy based approach.

Elements were removed from the analysis when their damage values exceeded a user specified threshold. The microscale model was initiated when the critical threshold (either stress or strain-energy based) was exceeded and the element began to accumulate damage. The following variables are passed from the macroscale model to the microscale model: initial one-dimensional stress (σ_0), one-dimensional strain rate ($\dot{\epsilon}_{1D}$), and macroscale timestep (dt). The initial one-dimensional stress value is only used to initialize the 1D bar in the microscale during its first evaluation. The one-dimensional strain rate and macroscale timestep are supplied at each macroscale timestep to the microscale model.

After the completion of the microscale model, the element fracture energy at the macroscale is updated to reflect the energy that has been dissipated at the microscale. This results in the macroscale model dissipating the same amount of energy as the microscale model, which results in an energy consistent implementation of the coupling between the two length scales. This is described in Section 4.1.2.

Additional information about the gradient damage explicit implementation can be found in the final report for NSRD11 [Louie 2016].

4.1.2. Microscale Model

The microscale model is similar to the prior implementations documented in the NSRD-11 [Louie 2016] and NSRD-15 [Louie 2017] final reports. A high-level summary is provided below, which includes descriptions of changes in the implementation from previous years.

The microscale model takes a one-dimensional approach to describing fragmentation as a result of elastic wave propagation coupled with a cohesive failure process. This approach was developed by Zhou et al [Zhou 2005] and was used for the previously implemented sequential model. The microscale model is initiated when a critical threshold value is exceeded at the macroscale, as described in 4.1.1. The microscale model represents each element in the analysis as a 1D bar of length $L_{bar} = \sqrt[3]{vol}$, where vol is the volume of the element. Each element contains a total of $N_{seg} = L_{bar}/\Delta x$ segments that are each joined by a cohesive zone, where Δx is the length of a single segment.

The length Δx is determined by a user specified grain thickness (w) and size (D_{GB}). The fraction of the element volume composed of grain boundaries is a modified version of an equation found in Capolungo et al [Capolungo 2007], which assumed the grain boundaries can be represented as spheres and the fraction of the material volume that is composed of grain boundaries is calculated as

$$F_{GB} = 1 - \frac{(D_{GB}-w)^3}{D_{GB}^3} \tag{4-4}$$

The volume of the grain boundaries is therefore $Vol_{GB} = F_{GB} \times vol$ and the total surface area of the grain boundaries is equal to $A_{GB} = Vol_{GB}/w$. The total number of grain boundaries per 1D bar of length L is estimated to be equal to $N_{GB} \sim \left(\frac{A_{GB}}{Vol_{GB}}\right)^{2/3} + 1$. This value is rounded down to the nearest integer and the length of the 1D bar segments is equal to $\Delta x = L_{bar}/(N_{GB} - 1)$. In the implementation of the microscale model, it is possible to specify a 1D bar length different than $L_{bar} = \sqrt[3]{vol}$. More information on this implementation is given later in this section.

The number of timesteps in the microscale model ($Ntime$) per macroscale scale timestep (dt), is determined by the following equation:

$$Ntime = floor\left(\frac{dt+t_{OLD}}{\Delta x/\sqrt{E/\rho}}\right) \tag{4-5}$$

where dt is the current macroscale timestep, and t_{OLD} is the balance of the previous macroscale timestep, defined as

$$t = dt + t_{OLD} - Ntime\ \Delta x/\sqrt{E/\rho} \tag{4-6}$$

In this way, the microscale model has the same approximate elapsed time as the macroscale model. The macroscale model timestep is controlled by the size of the smallest element in the simulation. Cases can occur with the coupled model where the smallest element deforms such that the $Ntime$ calculated for the microscale model is equal to zero. If this occurs, the macroscale timestep is added to the remainder time (t_{OLD}) and the microscale model is skipped for that macroscale timestep. The microscale model resumes during the next macroscale evaluation. During the resumed evaluation, $Ntime$ accounts for the time elapsed during the previous and current macroscale timesteps.

The one-dimensional strain rate ($\dot{\epsilon_{1D}}$) is supplied from the macroscale model and is used to determine the velocities of the end nodes of the 1D bar. To prevent large gradients in the velocities from occurring, resulting from a sudden change from the one-dimensional strain rate value, a linear change in end node velocity is applied from the previous macroscale timestep and the current macroscale timestep over $Ntime$ timesteps.

The end node velocity at the right and left-hand nodes is

$$v_R = -v_L = \dot{\epsilon_{1D}}\ (L_{bar}/2) \tag{4-7}$$

The value of the strain rate is updated at each macroscale step, which results in the end node velocities being updated.

In the microscale model, damage can only initiate when the local node stress exceeds the local critical stress, $\sigma_i \geq \sigma_{c,i}$. When this threshold is exceeded, crack opening distance and the local node stress is determined by the cohesive law such that

$$\frac{\sigma_{coh}}{\sigma_c} = 1 - \frac{\delta_{coh}}{\delta_c} \text{ for } \dot{\delta}_{coh} > 0, \delta_{coh} = \delta_{max}, D < 1 \tag{4-9}$$

$$\frac{\sigma_{coh}}{\sigma_c} = 1 - \frac{\delta_{max}}{\delta_c} \text{ for } \delta_{coh} < \delta_{max}, D < 1, \tag{4-10}$$

with δ_{coh}, δ_c, and δ_{max} as the current crack opening distance, the critical crack opening distance and the maximum crack opening distance. D is the damage number associated with the node, which is defined as $D = \min\left(\frac{\delta_{max}}{\delta_c}, 1\right)$. When a node is damaged, ($D > 0$), the energy that has been dissipated at the node is equal to $D_i^2 G_{c,i}$ where $G_{c,i}$ is the nodal fracture energy. This is illustrated in Figure 4-1. The total energy dissipated due to fracture at the microscale is equal to

$$E_{dissipated} = \sum_{i=1}^{N_{gb}} G_{c,i} D_i^2 - \max(G_{c,i} D_i^2) \tag{4-11}$$

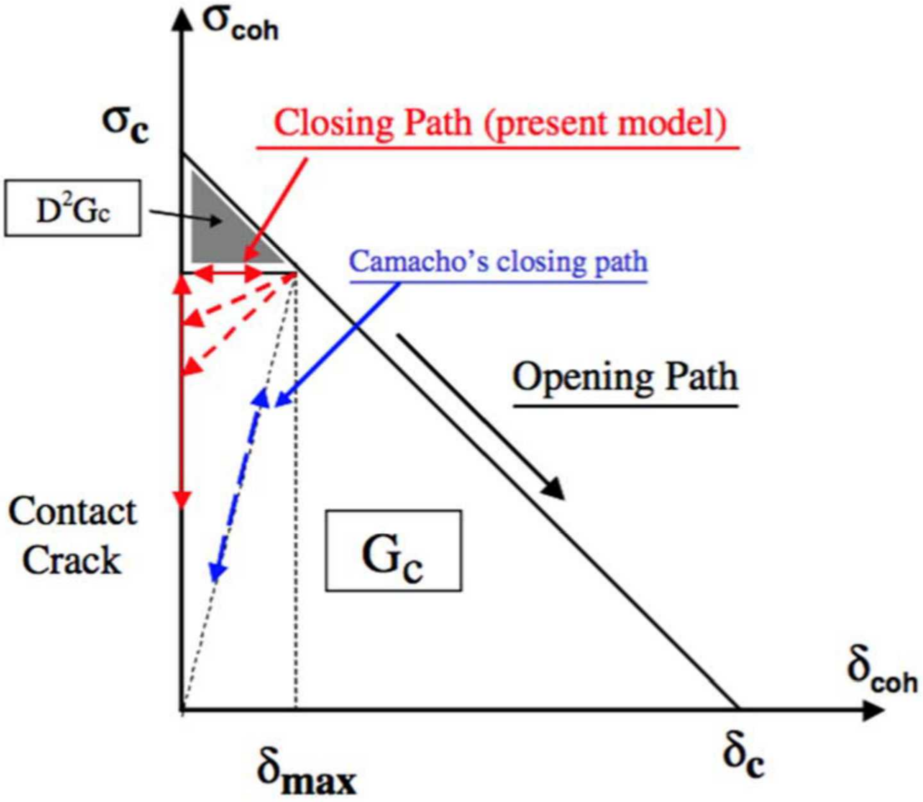

Figure 4-1. Representation of the cohesive law developed by Zhou and Molinari and Camacho and Ortiz [Zhou 2005].

The implementation allows for the user to specify directly the length of the 1D bar, instead of being based on the element size. This was implemented to allow the 1D bar to be the length of the phase field width. For the gradient damage explicit model, this is twice the fracture length scale. If a 1D bar length is specified, the damage accumulated on the 1D bar must be scaled such that the microscale model dissipates an amount of energy that is consistent with the energy dissipated for a 1D bar with $L_{bar} = \sqrt[3]{vol}$. This behavior was enforced by scaling the amount of dissipated energy by the ratio of the characteristic length of the element to the length of the user specified 1D bar.

$$E_{\text{dissipated,scaled}} = E_{\text{dissipated}} \times \sqrt[3]{\text{vol}}/L_{\text{bar}} \tag{4-12}$$

The total energy dissipated due to fracture at the microscale is used to update the macroscale fracture energy. This ensures that the energy dissipated at both length scales is consistent. This is implemented as

$$G_{\text{c,macro}} = G_{\text{c,initial}} + E_{\text{dissipated}} \tag{4-13}$$

where $G_{\text{c,initial}}$ is the element fracture energy at macroscale time = 0.

Distributions were implemented at the microscale on the parameters for the nodal critical stress, fracture energy, and grain boundary orientation values. In the current implementation of the 1D model, calculations of the stress in the 1D bar occur in the direction of the bar (with no stress projection required), however the calculation of the crack opening displacement and resulting damage per node require a projection to the grain boundary surface, which is orientated at an angle θ. Detail is given in Section 4.1.3 about the 1D model parameter distributions and their implementation.

4.1.3. Parameter Distributions

One of the major changes from previously performed work is the inclusion of the ability to vary model parameters based on a given distribution, both at the macro and microscale scales. Previously, macroscale parameters were varied. The current implementation applies a distribution to the microscale model parameters as well as the macroscale parameters. The macroscale model has distributions on the values of critical stress and fracture energy, whereas the microscale model has distributions on the values of the critical stress, fracture energy, and the grain boundary orientation. The values at both lengths scales are not independently determined, they are coupled.

The values of critical stress and fracture energy at the macroscale are determined by the microscale model parameter distributions. At the microscale model, each node has a critical stress, fracture energy, and grain boundary orientation parameter. Since a grain boundary orientation is assumed, the effective critical stress value that is used to determine the crack opening displacement is a projection of the node critical stress value onto the grain boundary surface, at a grain boundary orientation angle, θ. This projected critical stress value is equal to

$$\sigma' = \sigma_c \cos^2 \theta \tag{4-14}$$

The projection of the stress on the grain boundary surface is illustrated in Figure 4-2. In the case where the grain boundary orientation angle is zero, this means that the grain boundary is orientated in such a way that all applied force acts on the grain boundary surface. In the case where the grain boundary orientation is $\pi/2$ radians, the grain boundary surface is not aligned with the applied force direction, so no force acts on the grain boundary surface. A uniform distribution was assumed for the grain orientation angles.

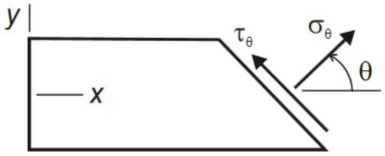

$$\sigma_\theta = \frac{Force}{Area} = \frac{N}{Area} = \frac{P\cos\theta}{A/\cos\theta} = \frac{P}{A}\cos^2\theta$$

$$\sigma_\theta = \sigma_x \cos^2\theta = \frac{\sigma_x}{2}(1+\cos 2\theta)$$

Figure 4-2. Projection of the stress onto grain boundary surface at angle θ.

A Weibull distribution was applied at the microscale model for the critical stress values. This and the grain boundary orientation parameter yields a projected critical stress value for each nodal location at the microscale model. To find the macroscale value for the critical stress, the smallest value of projected critical stress per macroscale element was set as the macroscale critical stress value. The reasoning behind this is that the node associated with the smallest projected critical stress value is the location that should break first in the microscale model. The mean value of the macroscale critical stresses should be equal to the user inputted critical stress value. To ensure this, the microscale model values of the nominal critical stress were scaled such that the mean macroscale critical stress yielded the corrected value.

The fracture energy at the microscale model used a Weibull distribution to populate the nodal values. The macroscale fracture energy is assigned the value of the fracture energy at the node that has the smallest projected critical stress, which is the node that will break first in the microscale model. The microscale model values for fracture energy are scaled such that the mean value of the fracture energy at the macroscale is equal to the user specified value for the fracture energy.

4.1.4. Differences from the Sequentially-Coupled Fragmentation Model

The sequentially-coupled fragmentation model was a prior implementation of the fragmentation model [Louie 2017]. The sequentially-coupled fragmentation model also uses a gradient damage explicit approach to model the macroscale fragmentation behavior. The microscale behavior is modeled using an implementation of the 1-D cohesive-zone model; the same approach was used for the concurrently-coupled model.

The primary difference between the sequentially-coupled and concurrently-coupled fragmentation models is the concurrently-coupled model uses continuously updating boundary conditions and two-way transfer of data between the macro and microscale models. The sequentially-coupled model in comparison used an initial strain rate from the macroscale model and applied it over a user specified number of microscale timesteps to obtain microscale fragmentation data. Output from the microscale model was not used to update the macroscale model during the sequential approach.

4.2. Validations

Three different validation cases are included in this report. The first two compare the results of the unirradiated UO_2 and Pyrex from [Jardine 1982] and in the Handbook. The final case is a comparison to the crushing of a brittle sphere during an impact test.

4.2.1. Validation with Handbook Data

The Handbook provides two tests for validation involving the impact of unirradiated UO_2 and Pyrex glass. The information for the Pyrex glass was used to establish the Handbook equation 4-1 for calculating the fraction of particles that are below 10 microns. However, for a better comparison to experimental data, the UO_2 and Pyrex impact tests conducted by Jardin, et al. [Jardine 1982], are used for comparison and to perform validation of the HGDE model. These model validations are described in this section.

4.2.1.1. Model Description

A plane-strain representation of the impact test conducted by Jardin was created to reduce the model size and computational time. This simplification was deemed to be acceptable for the current validation. More information can be found in the NSRD-15 Report [Louie 2017]. In Figure 4-3 , the upper and lower plates, the drop weight, and the location of the pellet are shown. This figure shows the UO_2 pellet case; the setup for the Pyrex case is similar. The components were represented using reduced order hexahedral elements with a single integration point.

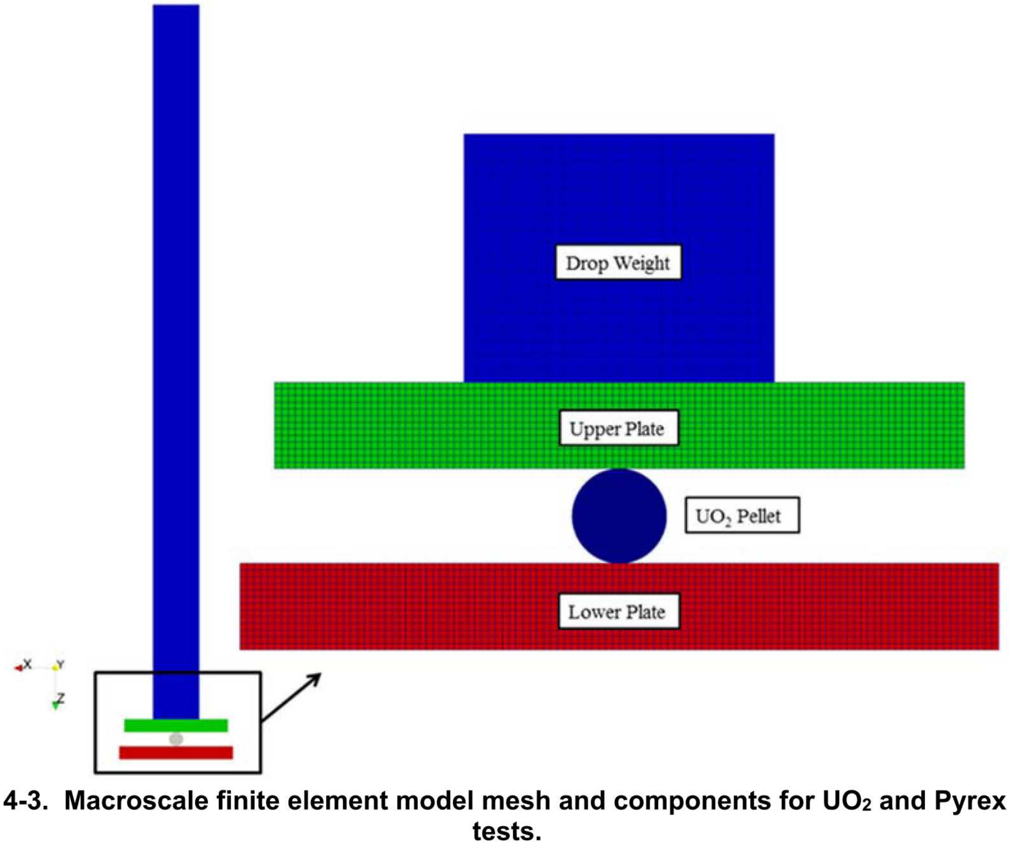

Figure 4-3. Macroscale finite element model mesh and components for UO_2 and Pyrex impact tests.

For the UO_2 validation case, the pellet had a diameter 13.7 mm and a thickness of 0.03 mm and was composed of 198,720 elements. For the Pyrex validation case, the pellet had a diameter 12.7 mm and a thickness of 0.03 mm and was composed of 171,312 elements. The characteristic element size for both validation cases was 0.03 mm.

The plates and the drop weight were specified as steel. The drop weight was given an initial velocity such that it would impart an impact energy of 1.2 J per cubic centimeter to the pellet. These components were meshed more coarsely than the pellet, using approximate element sizes of 1.0, 1.0, and 2.0 mm for the upper plate, lower plate, and drop weight, respectively. In order to impart the correct amount of energy to the Pyrex and the UO_2 cases, the length and initial velocity of the drop weight was adjusted such that 1.2 J per cubic centimeter of the pellet was the impact energy in each case. As the pellets have different diameters, this resulted in the UO_2 case having an initial drop weigh velocity of 1.20 m/s and the Pyrex case having an initial drop weight velocity of 1.11 m/s, resulting in 5.29e-03 J and 4.56e-3 J, respectively, of impact energy.

The material parameters of the UO_2 (density $\rho = 10500$ kg/m^3, elastic modulus $E = 137.9$ GPa, Poisson's ratio $\upsilon = 0.3$, critical fracture stress $\sigma_c = 82.7$ MPa, and fracture energy $G_c = 75.0\ \mathrm{J}/$m^2) were estimated from material test data for an related UO_2 ceramic material. The gradient damage explicit model fracture length parameter should be at least three times the width of the smallest characteristic element size, which resulted in using a fracture length of 0.1 mm. The cohesive shape factor was specified as 2.0 and the strain-energy based approach was used. For the validation case, the length of the 1D bar was specified to be 0.2 mm, which is the width of the phase field. Additionally, the grain size and thickness of the 1D bar were 5e-6 m and 1e-8 m, respectively, which resulted in 120 segments per 1D bar, with each segment being 1.67 microns in length. Elements were removed from the model when their strength degraded below 1e-3 of the strength of the undamaged element.

The material parameters of the Pyrex (density $\rho = 2230$ kg/m^3, elastic modulus $E = 62.75$ GPa, Poisson's ratio $\upsilon = 0.2$, critical fracture stress $\sigma_c = 20.3$ MPa, and fracture energy $G_c = 4.7\ \mathrm{J}/$m^2) were drawn from a variety of literature sources since these were not explicitly reported in the Handbook or the referenced reports. The same values were used as the UO_2 ceramic material for the cohesive shape factor, length of the 1D bar, and grain size and thickness. Elements were removed from the model when their strength degraded below 1e-4 of the strength of the undamaged element.

4.2.1.2. UO_2 Pellet Results

Figure 4-4 shows the macroscale stress degradation that was predicted by the finite-element model for the UO_2 pellet case for the deformed and nondeformed mesh after 500 μs. The stress degradation output from SIERRA/SM is equivalent to the stiffness function ($g(\phi)$) as described in Section 4.1.2. Figure 4-5 shows the macroscale damage for the deformed and nondeformed mesh after 500 μs. Fully damaged elements were removed from the simulation, which represented approximately 4.6% of the total pellet mass.

The results of the HGDE model plotted in Figure 4-6 reasonably match the macroscale behavior (above 1000 microns) of the experimental data. However, they do not match the experimental data below 1000 microns. The model shows a larger cumulative percentage of mass at the microscale scale than was seen for the experimental results. Due to limitations of the SIERRA/SM output, it was only possible to output a histogram for each element, which was used to determine the cumulative histogram at the microscale. The largest percentage of microscale fragments are approximately 1.67 microns in length, meaning they are composed of a single 1D bar segment. The number of fragments that are composed of a single 1D bar segment make up a significant percentage of the microscale mass, which accounts for the large relative percentage of the mass consisting of fragments that are less than 2 microns seen in the mass histogram.

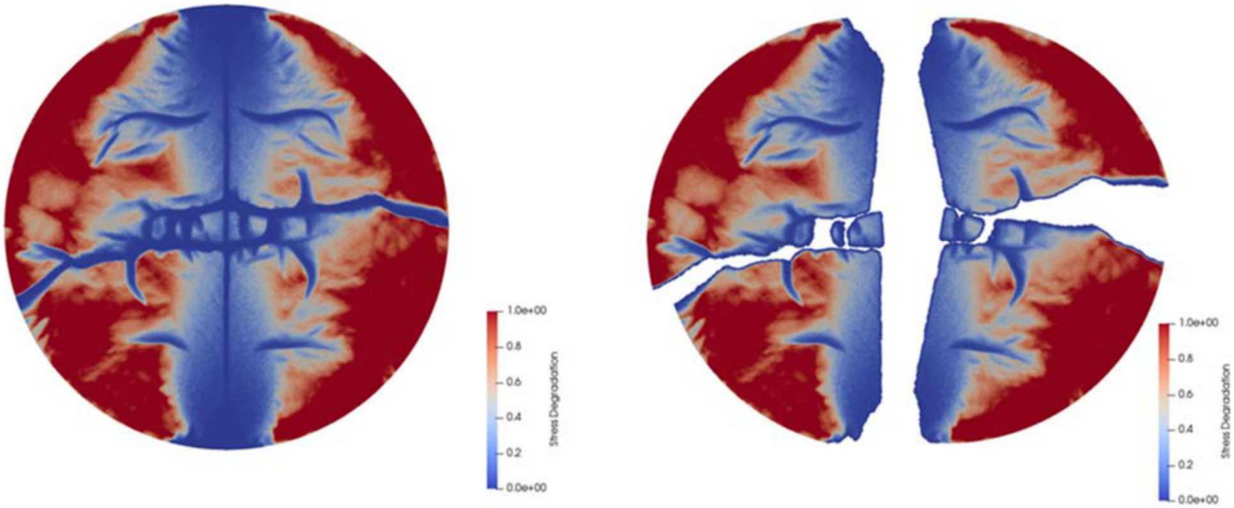

Figure 4-4. Macroscale stress degradation predicted by the finite-element model for UO_2, 500 μs after impact for the undeformed (left) and deformed (right) mesh.

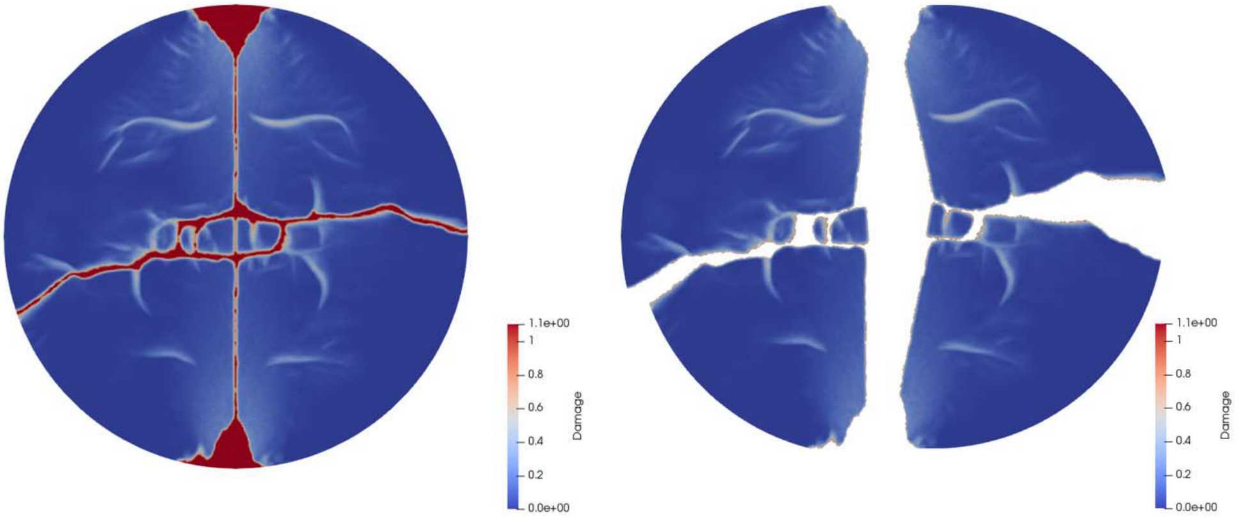

Figure 4-5. Macroscale damage predicted by the finite-element model for UO_2, 500 μs after impact for the undeformed (left) and deformed (right) mesh.

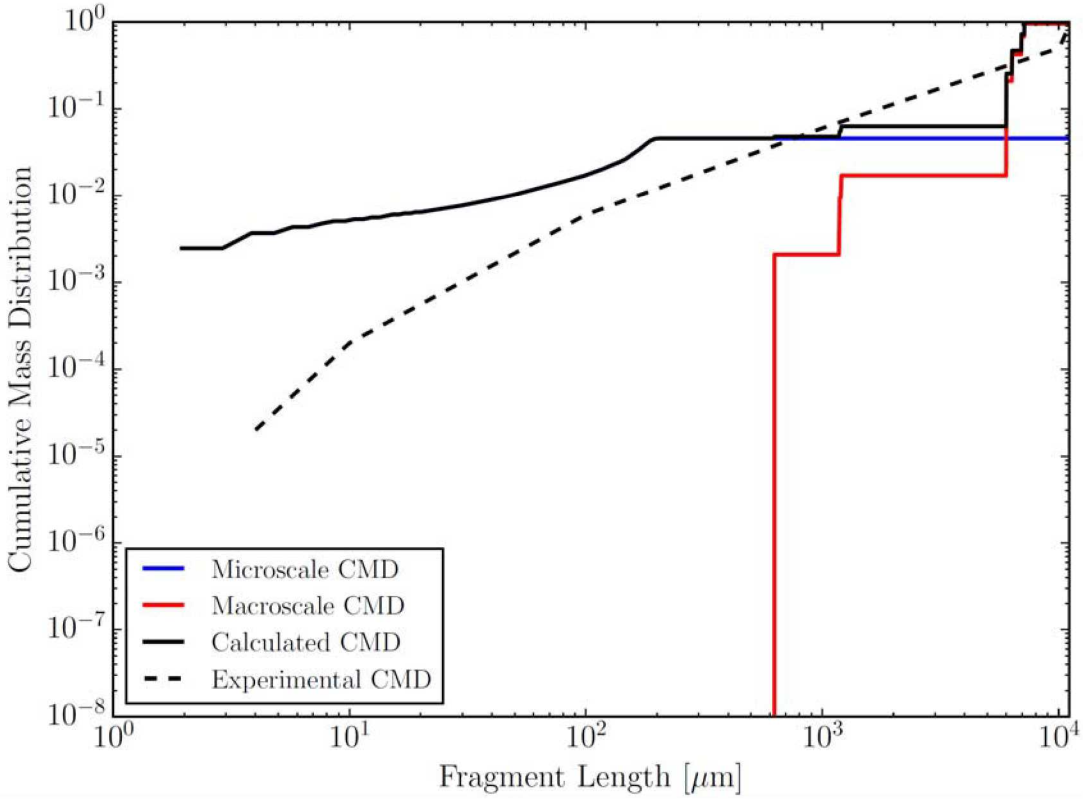

Figure 4-6. UO_2 impact test cumulative mass distribution (microscale in blue, macroscale in red) compared to test data (dotted) [Jardine 1982].

4.2.1.3. Pyrex Pellet Results

Figure 4-7 shows the macroscale stress degradation that was predicted by the finite-element model for the Pyrex pellet case for the deformed and nondeformed mesh. Figure 4-8 shows the macroscale damage that was predicted by the finite-element model for the Pyrex pellet case for the deformed and nondeformed mesh. Fully damaged elements were removed from the simulation, which represented approximately 5.4% of the total pellet mass.

The result of the HGDE model plotted in Figure 4-9 under-predict the macroscale cumulative mass curve. However, the mass of the microscale fragments reasonably matches the experimental data. As for the UO_2 model, due to limitations of the SIERRA/SM output, it was only possible to output a histogram for each element, which was used to determine the cumulative histogram at the microscale. The largest percentage of microscale fragments are approximately 1.67 microns in length, meaning they are composed of a single 1D bar segment, which was the same as seen in the UO_2 pellet.

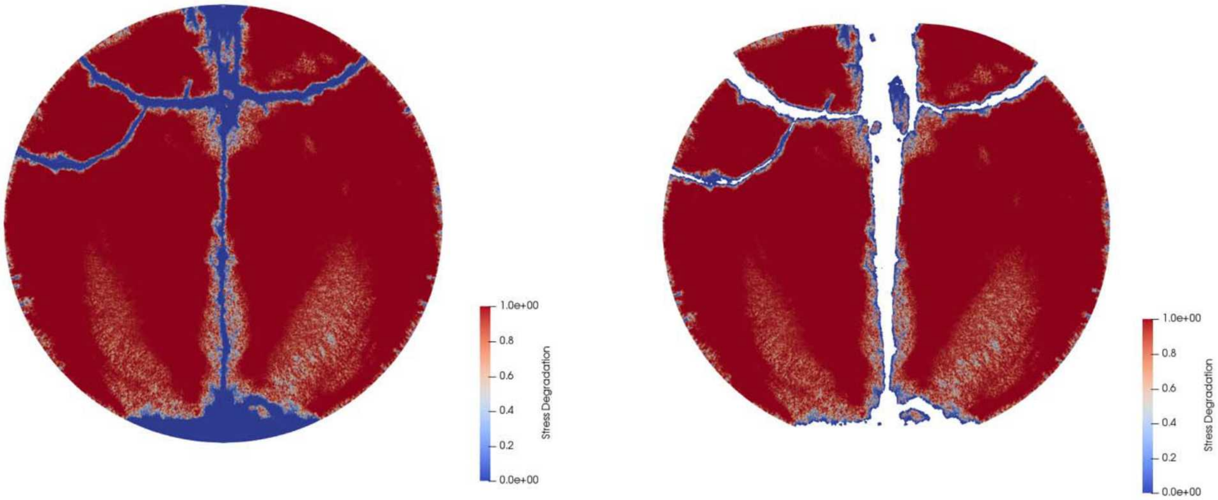

Figure 4-7. Macroscale stress degradation predicted by the finite-element model for Pyrex, 500 µs after impact for the undeformed (left) and deformed (right) mesh.

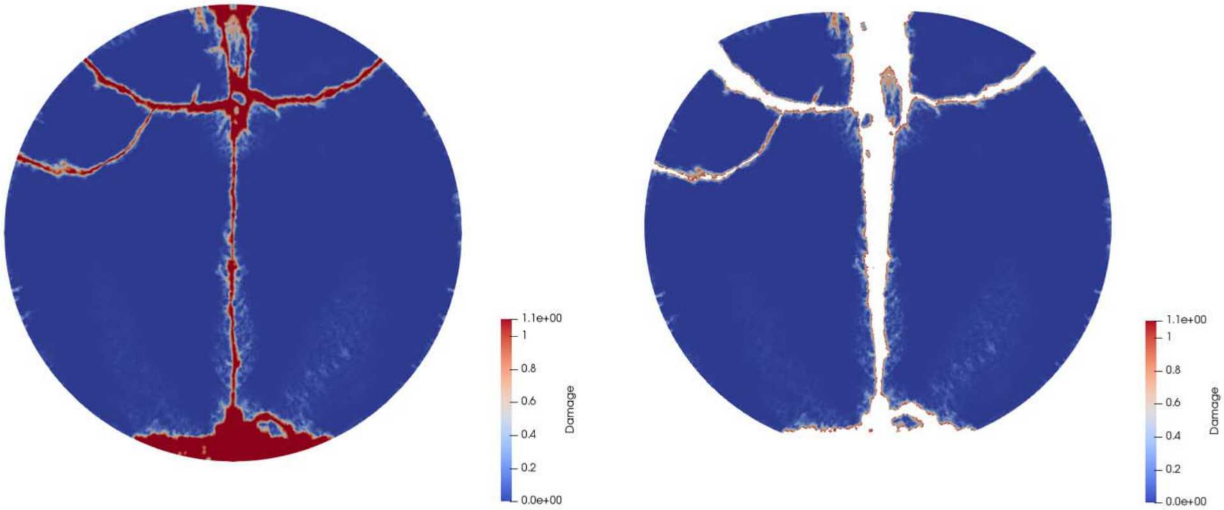

Figure 4-8. Macroscale damage predicted by the finite-element model for Pyrex, 500 µs after impact for the undeformed (left) and deformed (right) mesh.

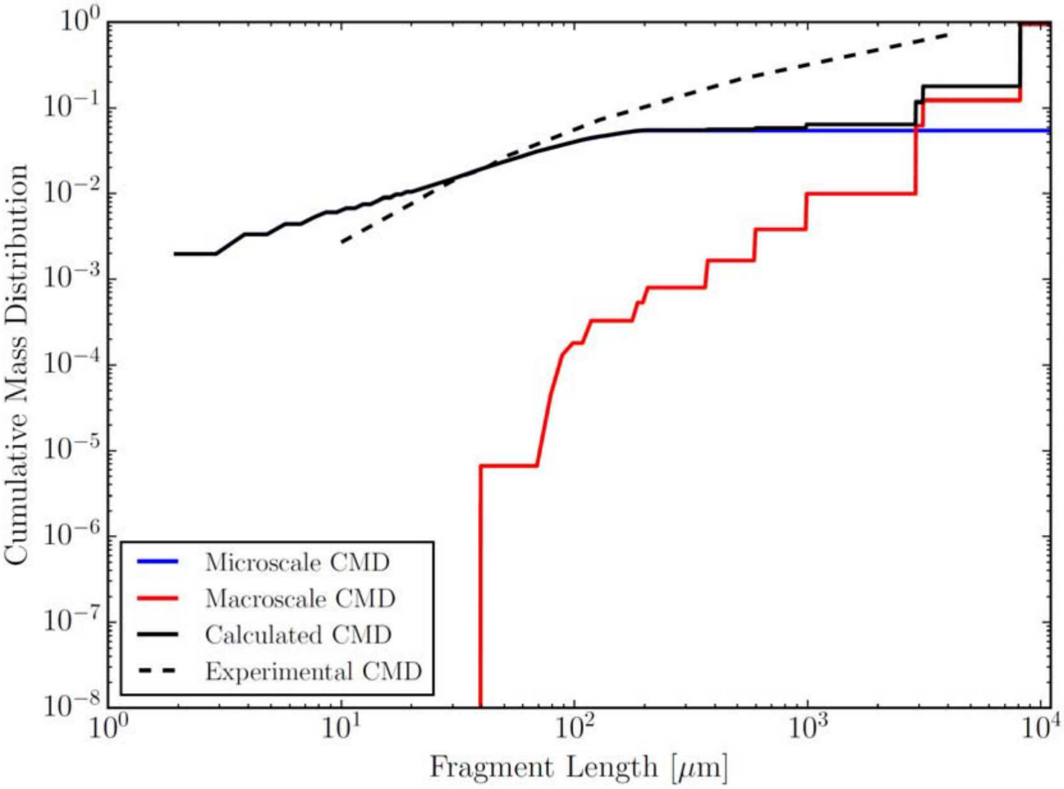

Figure 4-9. Pyrex impact test cumulative mass distribution (microscale in blue, macroscale in red) compared to test data (dotted) [Jardine 1982].

4.2.1.4. Analysis

Both the UO_2 and Pyrex models were able to capture fragmentation behavior at the macro and microscales, but the cumulative mass distribution observed was different than observed for the experimental data. However, the data used for validation may not be the most appropriate to use as the data is sparse. An additional metric for comparison and validation would be ideal. In addition, the source of discrepancies between the model and the experimental data are difficult to determine due to the coupling and two-way feedback between the macro and microscale models. A proper validation of the microscale model is needed before the coupled model can be properly validated. A complete validation of the microscale model was not completed due to time constraints. If this model is to be further developed, additional validation should be performed.

The coupling between the two length scales makes it difficult to determine the cause of discrepancies between the validation data and the model output. Higher strain rates given by the macroscale to the microscale model will result in more energy imparted to the 1D bar and result in smaller fragments. The damage accumulated at the microscale is in turn used to update the macroscale model's fracture energy by increasing its value. A higher fracture energy for a given element results in greater amount of energy required to further damage the element. The microscale model is very sensitive to the strain rates imparted from the macroscale model. Large strain rates will result in a large velocity being imparted to the end nodes of the 1D bar at the microscale. This will result in increased damage accumulation on the 1D bar and ultimately more fragments. The coupled nature of the model makes the behavior at the microscale difficult to understand. Further discussion of the microscale model as well as recommendations going forward are presented in Section 4.4.

4.2.2. *Validation with Sphere Experiment*

The second validation source is from impact tests conducted on brittle spheres performed by Wu et al [Wu 2004]. See Appendix C, Section C.1 for the details of this experiment. These impact tests examined two varied materials with three different sizes that were impacted against rigid steel plates at velocities ranging from 1 to 9 m/s. The macroscopic failure modes of the plaster spheres were studied and recorded, however no ARFs/RFs were reported as part of this work. A single case was chosen from the impact tests and was simulated in SIERRA/SM using the HGDE model. The case that was chosen corresponding to material A, with a spherical diameter 50 mm and an impact energy of 13.8 J. This impact test was used to evaluate if the model can predict the macroscale fracture behavior. Information from the microscale fragments was not collected for this validation case.

4.2.2.1. Model Description

The upper and lower plates, the drop weight, and the location of the plaster sphere are shown in Figure 4-10. The setup of this model was similar to the previously described Pyrex and UO_2 model, however the plaster sphere model did not use a plain-strain simplification and the model components were represented in 3D. The plates and drop weight components were represented using reduced order hexahedral elements with a single integration point. The sphere was represented using tetrahedral elements.

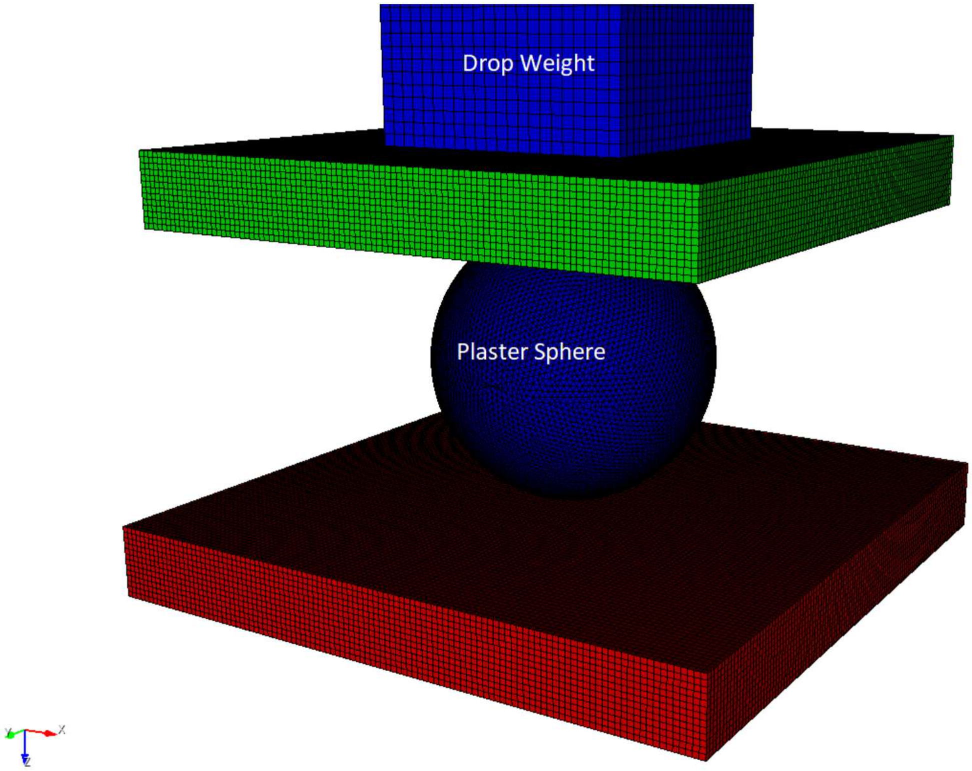

Figure 4-10. Macroscale finite element model mesh and components for the brittle sphere impact test.

The sphere had a diameter of 50 mm and was composed of 652,672 elements. The characteristic element size for the sphere was approximately 0.5 mm. The plates and the drop weight were specified as steel. The drop weight was given an initial velocity of 5.64 m/s, which resulted in the sphere being impacted with an impact energy of 35.7 J. These components were meshed using approximate element sizes of 1.0, 1.0, and 2.0 mm for the upper plate, lower plate, and drop weight, respectively.

The material parameters of the sphere (density $\rho = 1529\ \mathrm{kg/m^3}$, elastic modulus $\mathrm{E} = 13$ GPa, Poisson's ratio $\upsilon = 0.22$, critical fracture stress $\sigma_c = 37.6$ MPa) were taken from the reported test data [Wu 2004]. The fracture length used for the model was 1.5 mm, which is three times the characteristic length of the elements composing the sphere. The cohesive shape factor was specified as 2.0 and the strain-energy based approach was used. The length of the 1D bar was specified to be 3 mm, the width of the phase field. The grain size was chosen to be 20e-6 m and the grain thickness was 1e-8 m, resulting in 450 segments per 1D bar. The value of the grain size was chosen to limit the model size by decreasing the number of nodes at the microscale. While detailed micro-fragmentation information was not extracted from the model, the coupling between the two length scales was still active. Elements were removed from the model when their strength degraded below 1e-4 of the strength of the undamaged element.

4.2.2.2. Results and Discussion

The brittle sphere finite element simulation was run for 1 ms. Figure 4-11 shows the fracture behavior on the nondeformed mesh. At the end of this time, the sphere had fragmented into four slices of approximately equal in size and two additional smaller fragments. Fully damaged elements were removed from the simulation, which represented approximately 23% of the total sphere mass.

The failure mode predicted by the finite element model is similar to failure modes reported by Wu et al. Table 4-1 lists some of the observed failure modes seen by Wu et al. The first column corresponds to the failure mode (and number of slices observed), and the second columns lists the impact energy and the number of times this failure mode was observed. The impact energy used for the finite element model corresponds to failure model IIIb, which as Figure 4-12 shows, was observed to split into three equal sized slices; however, the failure mode predicted by the model corresponds to test IVa, which split into four equal slices. The difference in the impact energy between these two cases is 4.2 J and the failure mode associated with test IVa is close to the failure mode for case IIIb. Table 4-1 is a summary of the results and does not list every failure mode seen for every sphere. Failure mode IIIb was observed for a total of four instances. More impact energy should yield more fragments, however, Table 4-1 shows that failure mode Va (five slices) was observed for an impact energy of 35.4 J, which is less than the impact energy of failure modes IIIb or IVa. Therefore, the model prediction of failure mode Va for the given impact energy is possible in the bounds of the observed failure modes and the model was able to capture the macroscale failure behavior of the brittle sphere.

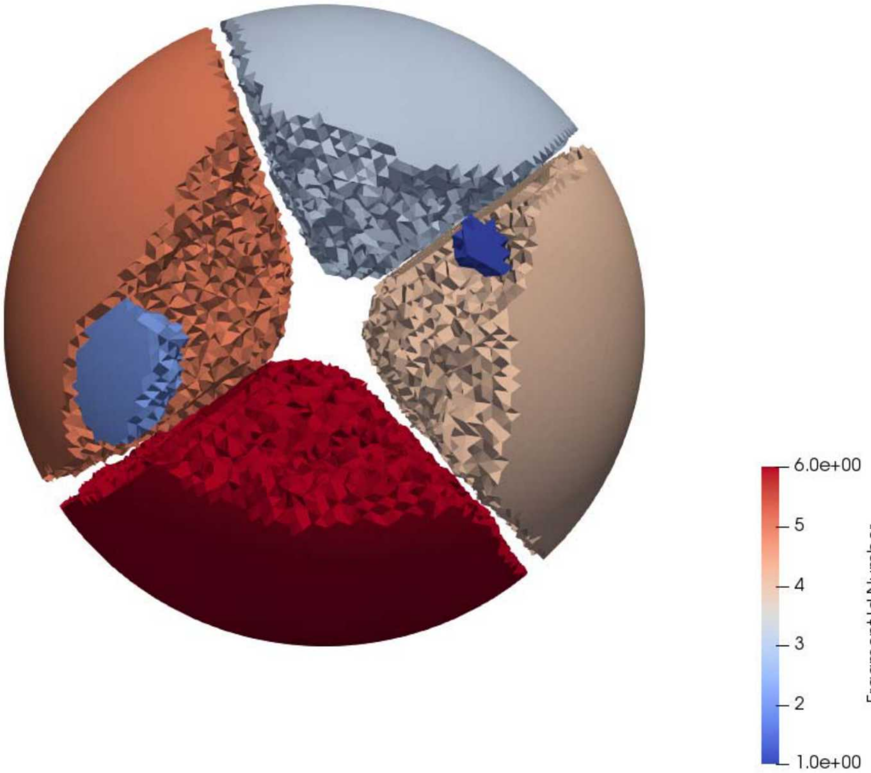

Figure 4-11. Macroscale fracture behavior of the brittle sphere on an undeformed mesh, 1 ms after impact.

Table 4-1. Material A, 50 mm diameter sphere failure modes and impact energy [Wu 2004].

Failure Mode	Ein (J) / Number of Times Observed
II	16.0 / 2
IIIa	17.9 / 4
IIIb	35.7 / 4
IVa	39.9 / 5
Va	35.4 / 1
Vb	154.0 / 1

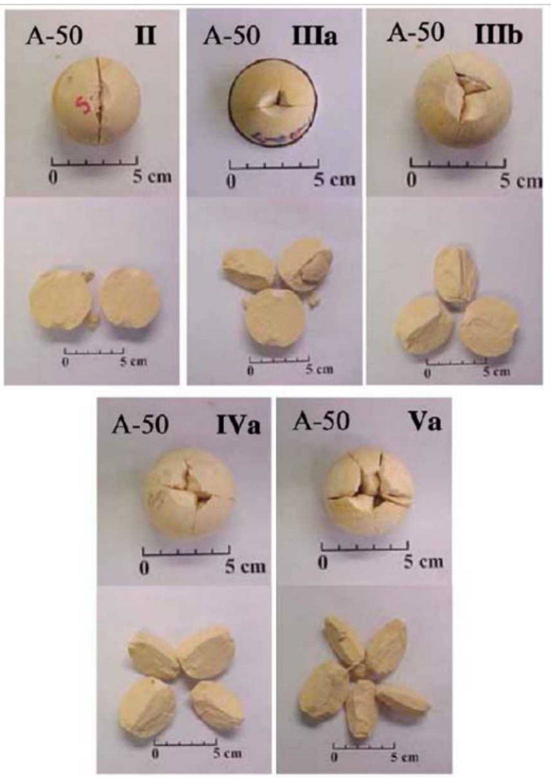

Figure 4-12. Material A, 50 mm diameter sphere failure modes II, IIIa, IIIb, IVa, and Va [Wu 2004].

4.3. Microscale Model Sensitivity Analysis with DAKOTA

A sensitivity analysis was performed of the microscale model to determine if there is sensitivity to input parameters to the microscale model. A description of the procedure for this analysis, as well as the results, are in the following section. DAKOTA was used to drive the sensitivity analysis. DAKOTA is a Sandia developed computational toolkit for iterative studies such as sensitivity analysis, calibration, and uncertainty quantification.

4.3.1. Stand-Alone Microscale Model Description

A stand alone verison of the microscale model was created to perform the sensitivity analysis. This step was required as sensitivity analysis for the microscale model parameters would require hundreds to thousands of evaluations, which would not be possible to implement with a coupled macro and microscale case due to time and resource constraints. However, the microscale model requires updated boundary conditions from the macroscale model. These values were obtained by extracting values from the SIERRA/SM macroscale model when the microscale model first initiated for a single-element test problem. These values were used to set the microscale model parameters for the macroscale timestep and the initial one-dimensional strain rate.

The stand-alone microscale model implementation consists of the following steps:

A specified number of elements are simulated at the macroscale. Their macro and microscale parameters are generated to be consistent with the parameter distributions laid out in Section 4.1.3.

For each element, a simulation of the microscale model is performed by using the previously obtained macroscale timestep dt and the initial strain rate to calculate microscale $Ntime$ and the boundary node velocities. At the first iteration of the microscale model, the stress per node is initialized to be 99% of the element critical stress value. Each microscale model iteration is equivalent to a single macroscale model timestep. After the first iteration, the strain rate is increased by 5% each iteration. This increase in strain rate will slowly change the boundary velocity nodes. Since this is a stand-alone model with no feedback from SIERRA/SM, this value is estimated.

After the microscale model calculates fragmentation for a user specified number of macroscale timesteps, a cumulative mass histogram is calculated for each element. Once the stand-alone model progresses through all elements, their histograms are summed and normalized to give a cumulative mass histogram that simulates the microscale portion (1D bar) of the SIERRA/SM generated cumulative mass histograms seen previously for UO_2 and Pyrex.

For each evaluation of the stand-alone model, a set of elements were generated that had distributions at both a simulated macroscale and a microscale level that were the same as those specified in Section 4.1.3. As the macroscale and microscale parameters were generated using a different seed for each stand-alone model evaluation, there is inherently some variability to the final output from the stand-alone model. A convergence study was performed to determine how many elements of number of simulations were needed to capture converged microscale fragmentation behavior. The standard deviation of the quantity of interest (QoI), percentage of the 1D bar mass below 10 microns, was determined to scale according to $1/N^2$ where N is the number of elements. A separate convergence study was performed to determine the number of microscale iterations needed to sufficiently converge the quantity of interest. A single microscale iteration is equivalent to a single macroscale timestep dt. In order to keep the model time low, the number of simulation elements used for the following results was 320 elements and the total microscale iterations used was 1000 iterations. With 320 elements, 1000 iterations of the macroscale model, and 50 samples with different seeds for the UO_2 properties, the mean, median, and standard deviation of the QoI was 0.0800, 0.0799, and 0.002, respectively. For the following results, if the QoI is equal to 1.0, this corresponds to a case where all of the 1D bar mass is contained in fragments smaller than 10 microns.

As this sensitivity analysis was performed separately from SIERRA/SM, there is no coupling between the macro and microscale fragmentation behavior. If this study were to be carried out in SIERRA/SM, it would likely show different fragmentation behavior at the microscale. However, when the stand-alone model was used to simulate the UO_2 material parameters for 320 elements, it resulted in a cumulative mass histogram that is sufficiently close to the SIERRA/SM UO_2 cumulative mass histogram for the microscale fragments, as illustrated in Figure 4-13. The stand-alone model cannot capture the coupled macro and microscale behavior; however, it is able to accurately (in comparison to the SIERRA/SM model) capture the microscale behavior and sensitivity to the input parameters.

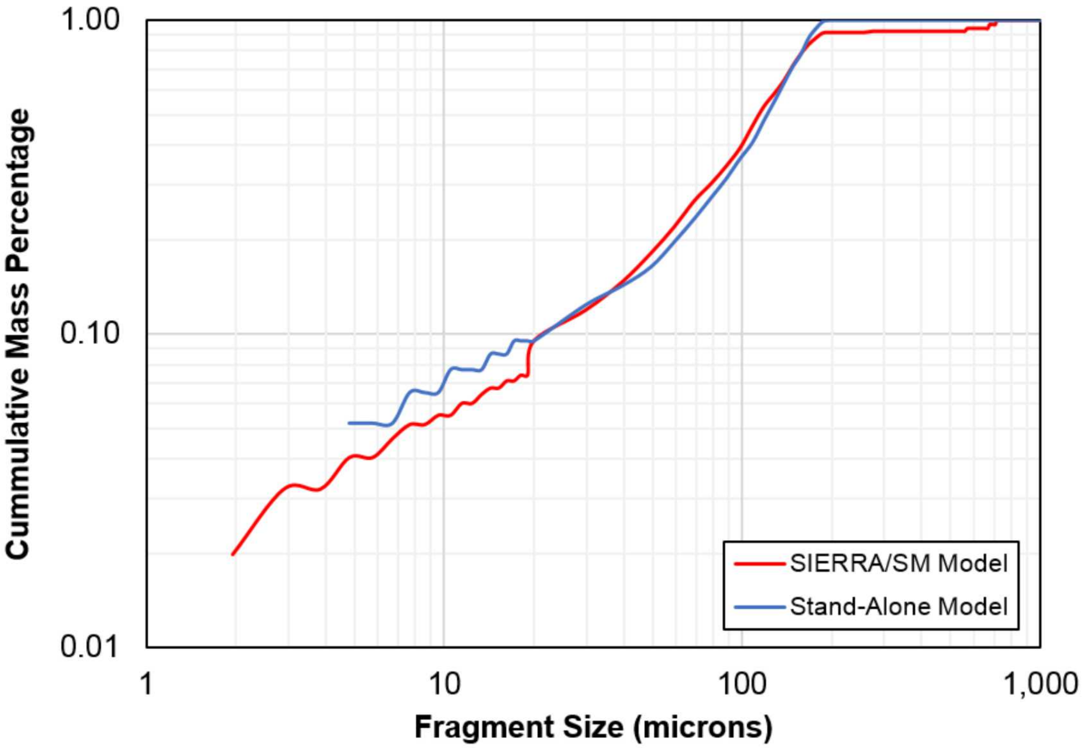

Figure 4-13. Comparison of the coupled UO_2 SIERRA/SM cumulative microscale histogram compared to the histogram generated by the stand-alone model.

Model parameters and inputs for the sensitivity analysis, as well as their base values, are listed in Table 4-2. These values are based on UO_2 and were extracted from a model of a single element.

Table 4-2. Baseline Input Parameters for the 1D model

Parameter	Base Value
Grain Boundary Thickness	1e-8 m
Grain Boundary Size	5e-6 m
1D Bar Length	2e-4 m
Number of Elements	320
Number of Iterations of 1D model	1000
Macroscale Timestep dt	1.229e-8 s
Initial Strain Rate	10.0 1/s
Elastic Modulus	137.9 GPa
Density	10500 kg/m3
Critical Stress	82.7 MPa
Fracture Energy	75.0 J/m2

4.3.2. Results of Sensitivity Analysis

The sensitivity analysis examined the response of the quantity of interest (percentage of mass under 10 microns for the 1D bar) and the microscale model parameters. The model parameters that were examined are the following, defined at the macroscale (and used to determine the microscale parameters):

- Elastic Modulus
- Density
- Critical Stress
- Fracture Energy
- Grain Size
- Initial Strain Rate

The elastic modulus was determined to have no effect on the quantity of interest (QoI) or the shape of the cumulative mass histogram. Figure 4-14 and Figure 4-15 show some variation in the QoI and the mass histogram, however the variations are on the same order of magnitude of the variations that are expected when varying the evaluation seed. Ultimately, no relationship is seen with the response of the QoI or histogram shape and the value of the elastic modulus. This same conclusion can be drawn for density, as seen in Figure 4-16 and Figure 4-17. There appears to be no relationship between density and the histogram shape or the percentage of the 1D bar mass that is below 10 microns. For these two parameters, this result was anticipated as the parameters are only used in the microscale model to determine the value of $Ntime$. There may be sensitivity to elastic modulus and density with the coupled macro and microscale model that is not seen when only modeling the microscale behavior.

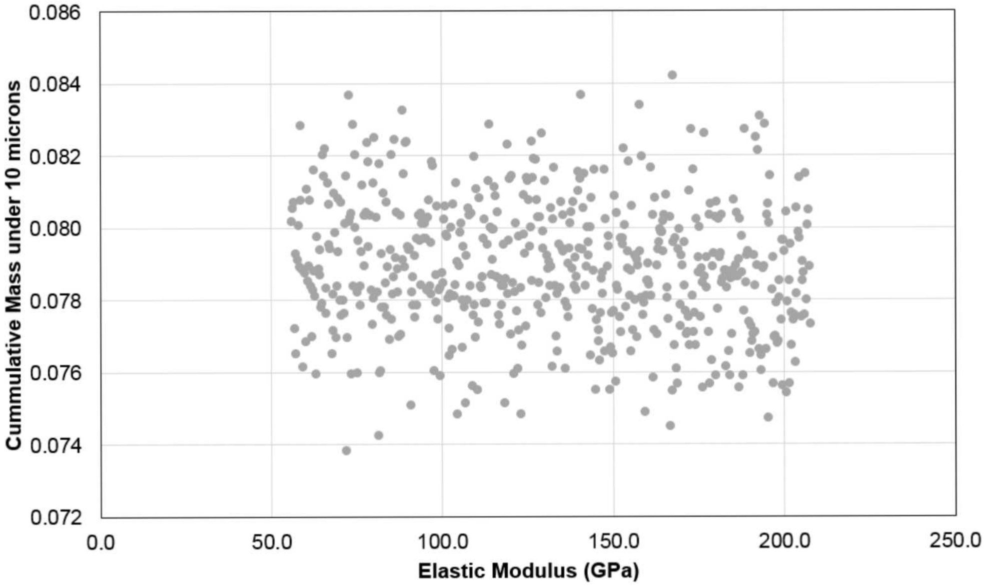

Figure 4-14. Cumulative mass of the 1D bar under 10 microns, varying modulus from 55 to 210 GPa, using UO_2 properties.

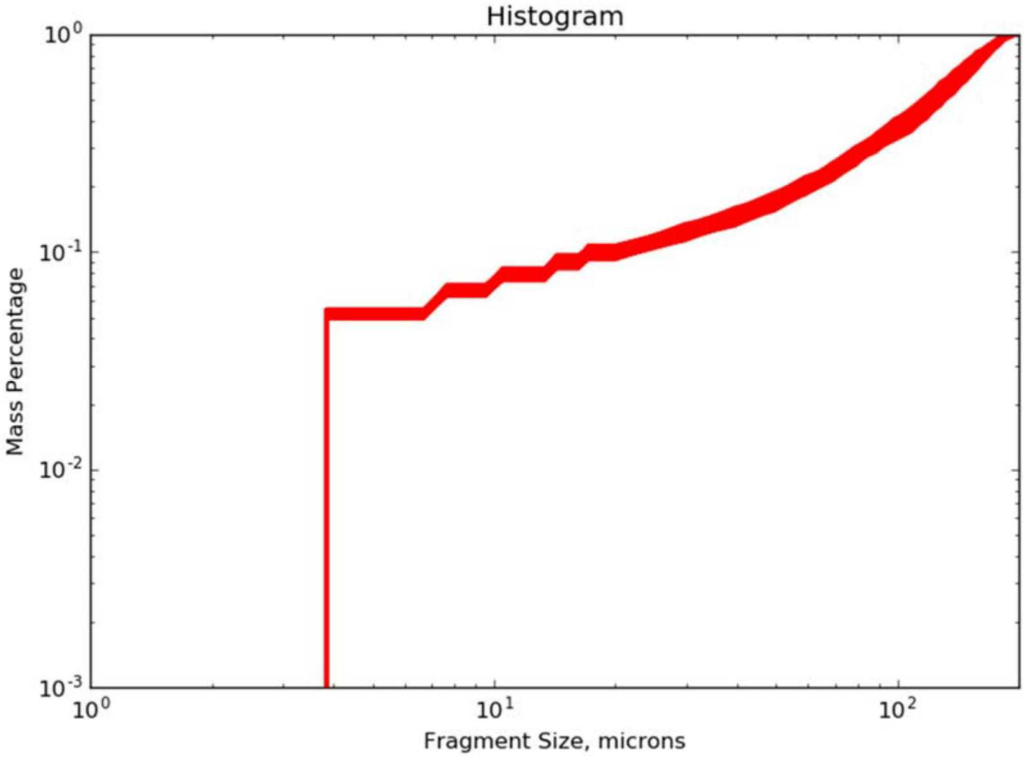

Figure 4-15. Cumulative mass histogram of the 1D bar, varying modulus from 55 to 210 GPa, using UO_2 properties. All histograms are overlaid on the plot.

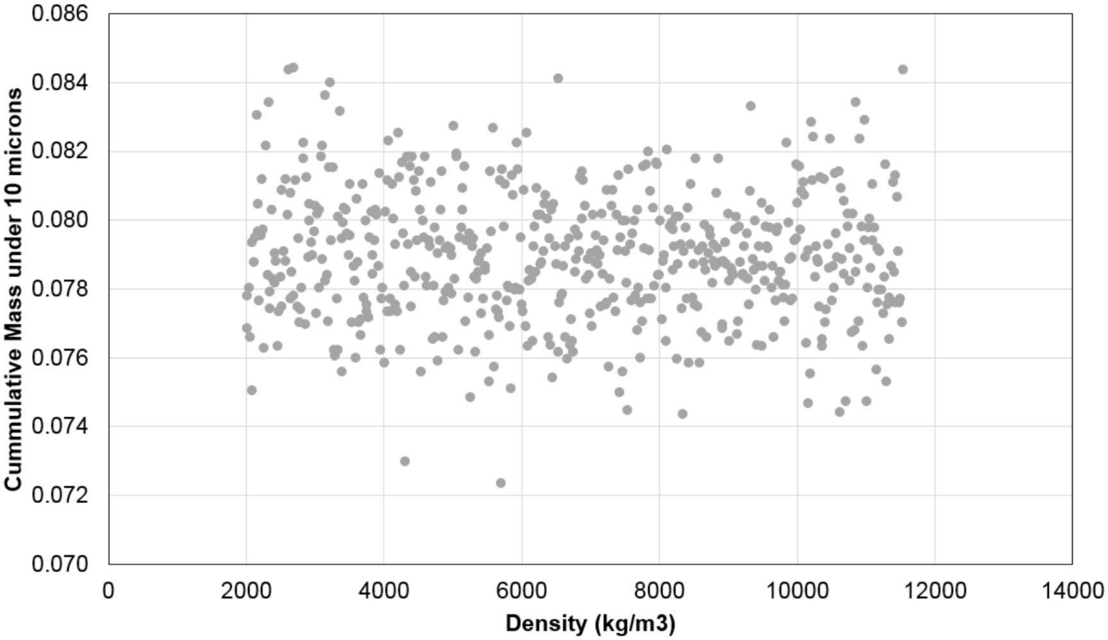

Figure 4-16. Cumulative mass of the 1D bar under 10 microns, varying density from 2000 to 11500 kg/m^3, using UO_2 properties.

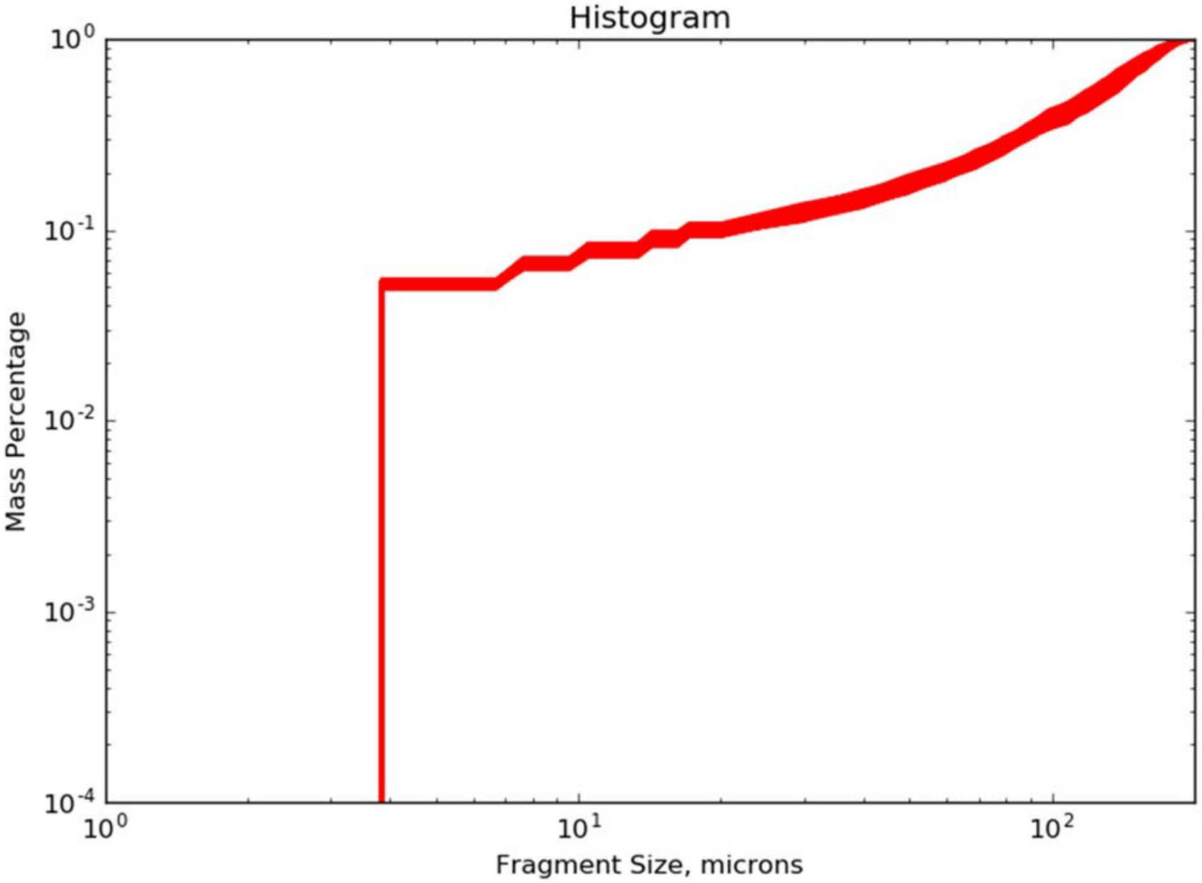

Figure 4-17. Cumulative mass histograms of the 1D bar, varying density from 2000 to 11500 kg/m3, using UO_2 properties. All histograms are overlaid on the plot.

The grain size has a direct relationship with the QoI, as seen by Figure 4-18. The reason for this relationship is uncertain and should be studied. As the grain size increases, the mass of the smallest fragment also increases, which may result in the behavior seen. Figure 4-19 shows the cumulative mass histogram while varying grain size. It can be seen from the figure that while the smallest fragment size changes, the relative shape of the histogram is unchanged as the grain size increases.

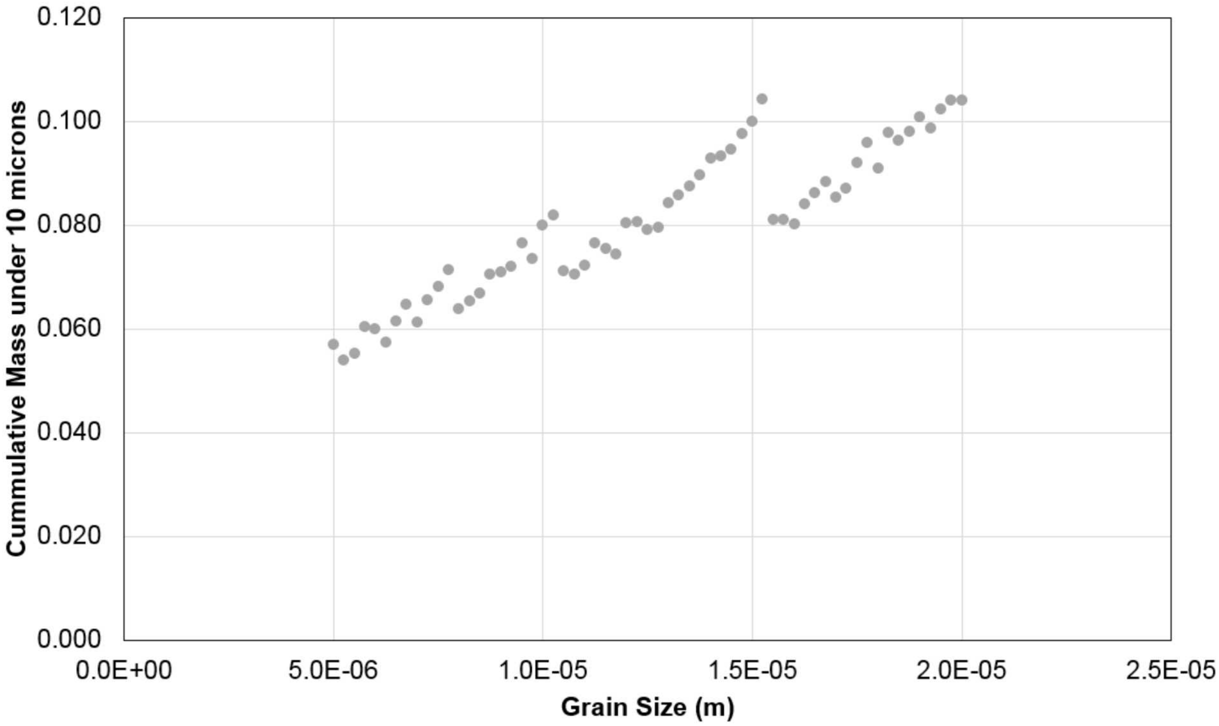

Figure 4-18. Cumulative mass of the 1D bar under 10 microns, varying grain size from 5 to 20 microns, using UO_2 properties.

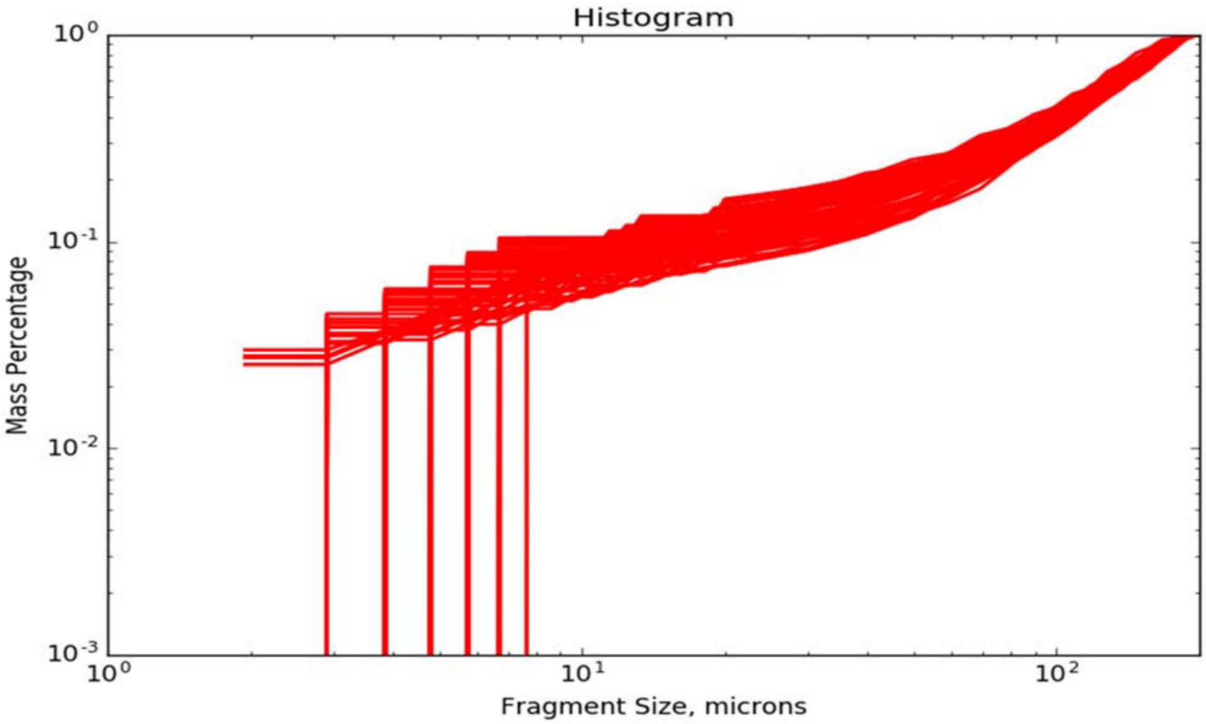

Figure 4-19. Cumulative mass histograms of the 1D bar, varying grain size from 5 to 20 microns, using UO_2 properties. All histograms are overlaid on the plot.

In the case of critical stress and fracture energy, there does appear to be a relationship between the critical stress, fracture energy, and model output as seen in Figure 4-20 and Figure 4-21. However, the relationship is difficult to determine as the values of critical stress and fracture energy are likely not independent for real materials. It is generally assumed that a higher critical stress will correlate with a higher fracture energy. This relationship makes it difficult to perform a sensitivity analysis of the model output in response to the values of the critical stress and fracture energy, since the input parameters are not independent of each other. Independently varying the critical stress and fracture energy can result in the model input being pushed towards unphysical values. The two histograms shown allowed the critical crack opening distance to vary as the values for critical stress or fracture energy were changed. The relationship between critical stress, fracture energy, and crack opening distance is $G_c = \frac{1}{2}\sigma_c\delta_c$ (Figure 4-1).

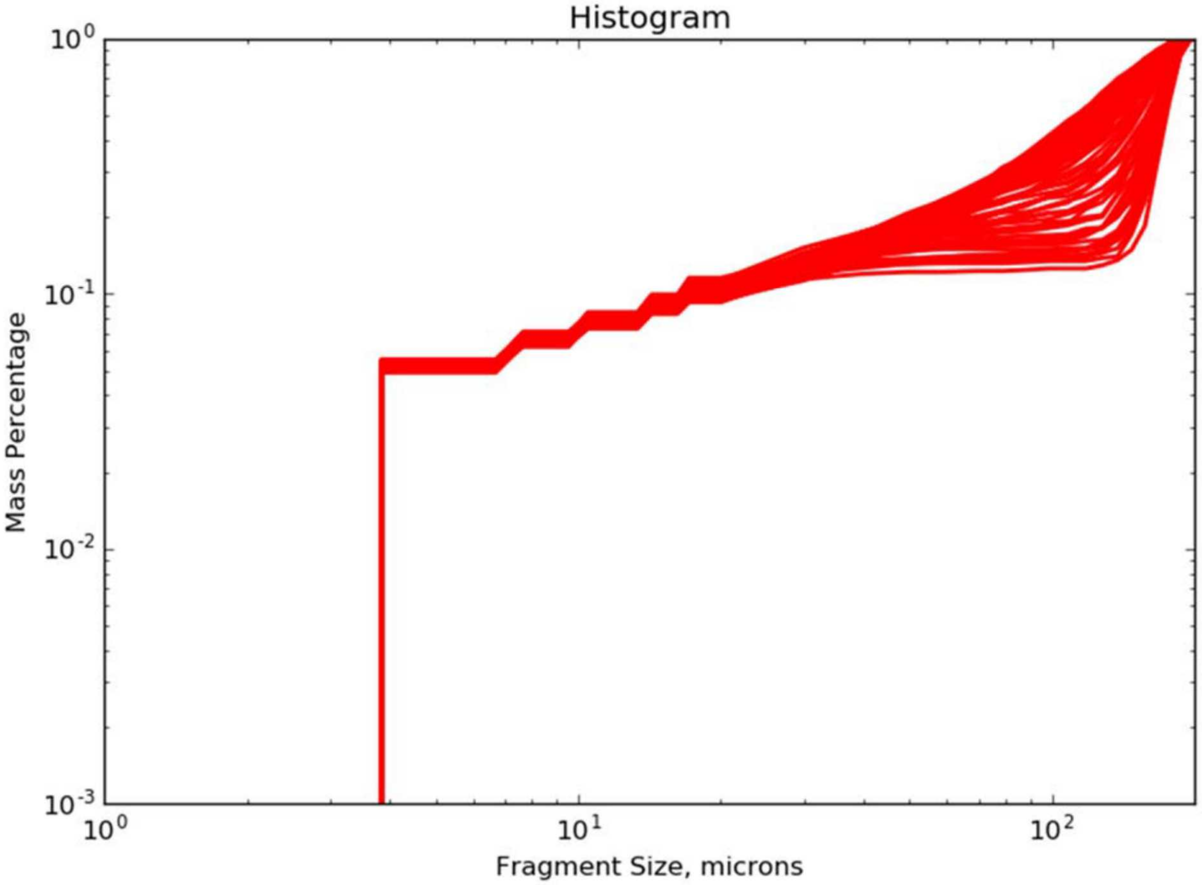

Figure 4-20. Cumulative mass histograms of the 1D bar, varying critical stress from 10 to 167 MPa, using UO_2 properties. All histograms are overlaid on the plot.

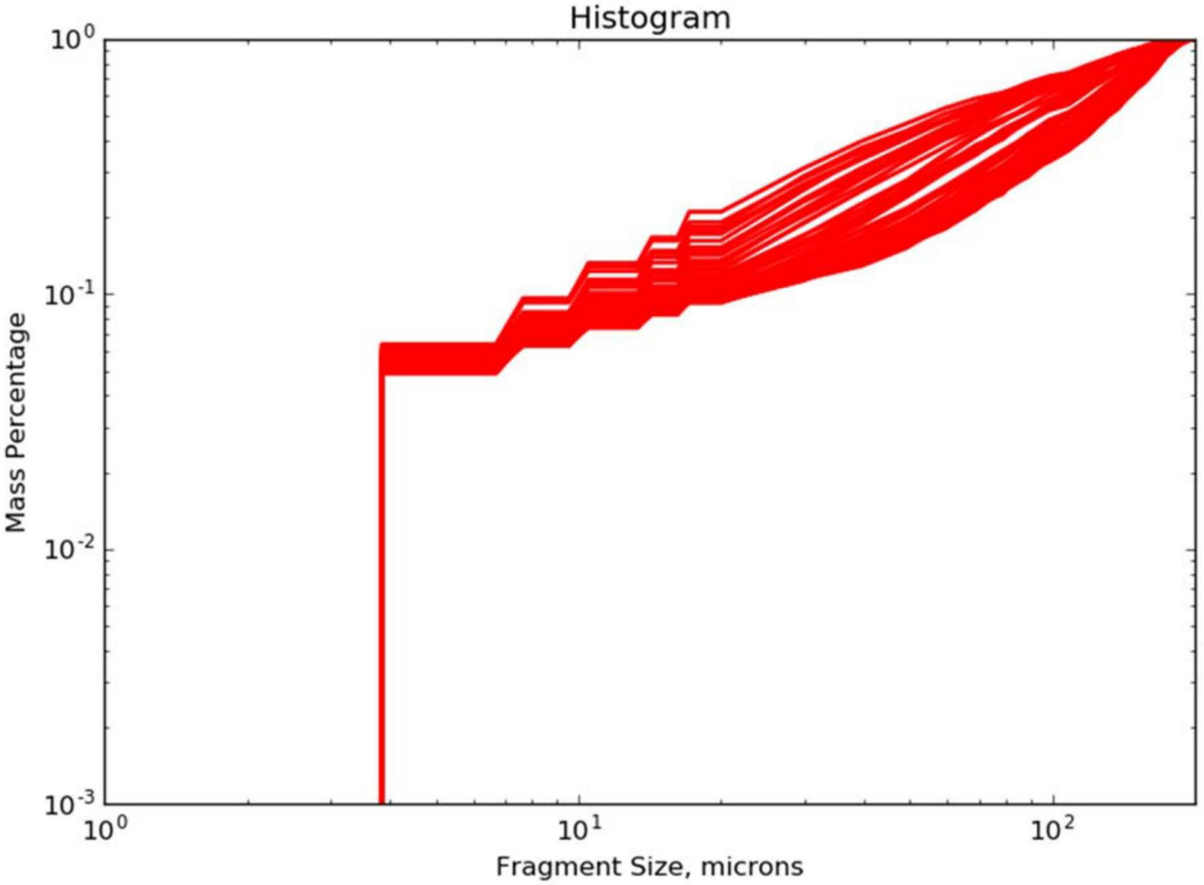

Figure 4-21. Cumulative mass histograms of the 1D bar, varying fracture energy from 1.0 to 150 J/m2, using UO_2 properties. All histograms are overlaid on the plot.

For the UO_2 properties, the crack opening distance is approximately 2e-6 m. Figure 4-22 shows the cumulative mass histograms that are generated by the microscale model while holding the crack opening distance constant and allowing fracture energy to vary such that the relationship between critical stress, crack opening distance and fracture energy holds true. If the crack opening distance is held constant and the fracture energy is directly related to critical stress, the percentage of the particles that are under 10 microns stays relatively constant as critical stress values vary, however the shape of the cumulative mass histograms changes depending on the crack opening distance.

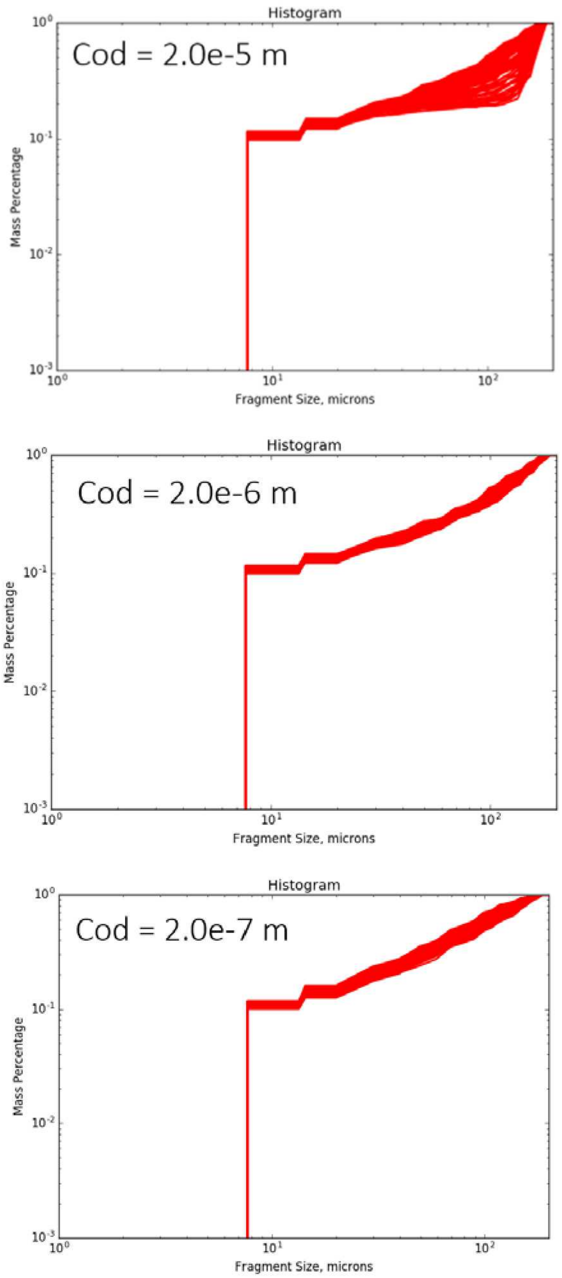

Figure 4-22. Cumulative mass histograms of the 1D bar, varying critical stress from 10 to 167 MPa, using UO_2 properties. Crack opening distance (Cod) is held constant and the value of value of the fracture energy is directly related to the critical stress value. All histograms are overlaid on the plot.

This highlights a difficulty of performing sensitivity analysis of the microscale model as a whole. Parameters such as critical stress and fracture energy are correlated. In addition, changing the elastic modulus, density, and the grain size will affect the $Ntime$ parameter (Section 4.1.2), which is the number of timesteps taken per microscale iteration. In the case of the current implementation of the sensitivity analysis, while the same amount of macroscale time elapses per evaluation of the stand-alone model, a different number of timesteps (and total model evaluations) will occur at the microscale, which will have an effect on the results. There are likely other correlations and relationships between input parameters that will affect the model output. In order to better understand the relationship between the parameters and the microscale model output, these correlations and relationships should be identified and the sensitivity analysis should be repeated. In addition, this sensitivity model only examines the microscale model and the behavior of the coupled model may be different than what was observed for the stand-alone microscale model.

The strain rate was also observed to have an impact on the percentage of the fragments that are under 10 microns. Figure 4-23 shows the relationship between the QoI and the strain rate. For this study, a constant strain rate was used. As the constant strain rate increases, the behavior of the QoI is initially constant and then it begins to increase linearly as the strain rate increases above 100,000 1/s. A direct relationship between the number of small fragments and the energy was observed by Zhou [Zhou 2004] et al and is consistent with Equation 4-1 in the Handbook; however, Equation 4-1 observes a linear relationship. Interestingly, the percentage of the mass under 10 microns appears to dip at a strain rate of approximately 10,000 1/s before increasing. It is unclear if the behavior seen in Figure 4-23 is statistically significant. At strain rates less than 100 1/s (not shown in the figure), the 1D bar has no fragments, which is consistent with what was observed by Zhou, where very small strain rates result in an intact 1D bar. At very high strain rates, the percentage of the bar mass below 10 microns is approximately 1.0, indicating that the energy input into the system was such that nearly all nodes had broken. This behavior may or may not be seen with the coupled macro and microscale models.

A follow-up study was performed with the coupled macro and microscale models in SIERRA/SM for a Pyrex pellet with a diameter of 25.0 mm and varying energy inputs into the model equal to 1.2, 2.5, 5.0, and 10.0 J/cm^3. The study used the same material and fragmentation properties as described in Section 4.2.1 for Pyrex. The mass percentage of the particles smaller than 10 microns increases linearly with impact energy for this study, as seen in Figure 4-24. This linear relationship is consistent with the correlation used in Equation 4-1 in the Handbook, however the slope of the curve does not match the data used to formulate the correlation used in Equation 4-1, which was collected by Jardin [Jardin 1982]. This indicates that the coupled model needs additional verification and validation in order to have confidence in the results.

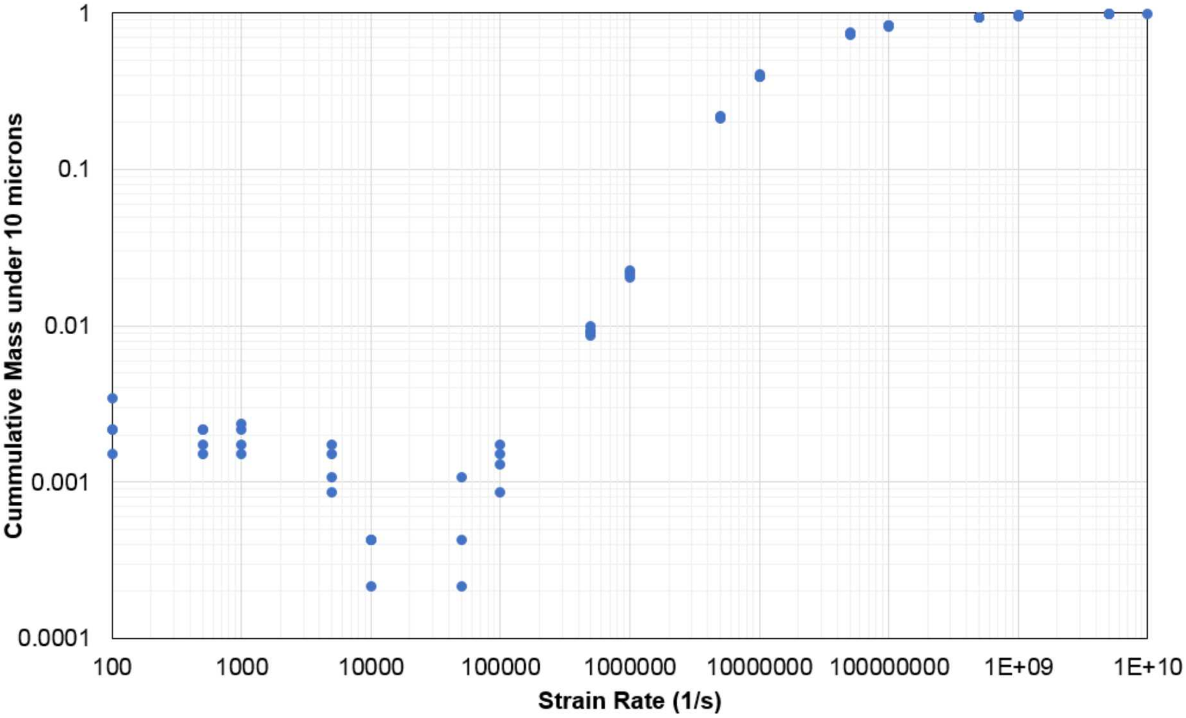

Figure 4-23. Cumulative mass of the 1D bar under 10 microns, varying a constant strain rate value from 100 to 1e10 1/s, using UO_2 properties.

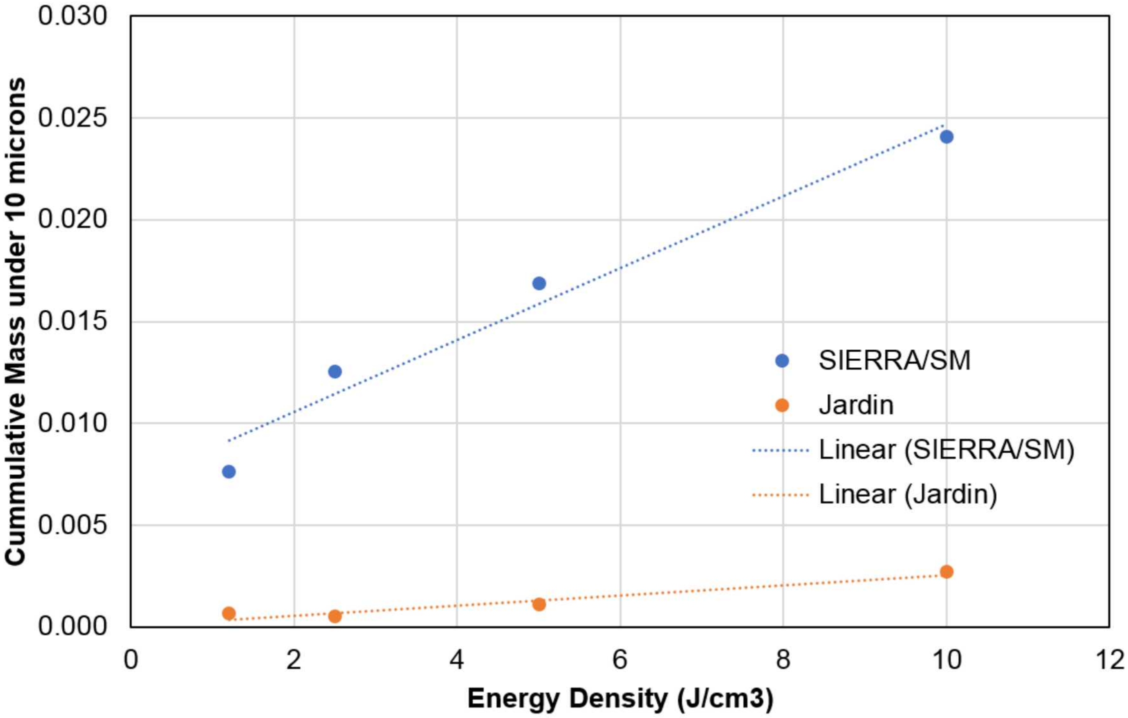

Figure 4-24. Cumulative mass of the 1D bar under 10 microns for Pyrex, using the coupled SIERRA/SM model, compared to the Jardin [Jardin 1982].

4.4. Revision to Equation 4-1 and Recommendations for Future Study

Equation 4-1 in the Handbook is

$$ARFxRF = APgh$$

where A is an empirical correlation, P is the specimen density, g is acceleration due to gravity, and h is the fall height.

Equation 4-1 shows a direct relationship between the input energy and the ARFxRF. This is consistent with what was seen during the sensitivity analysis of the stand-alone 1D model when varying the initial strain-rate and with the study performed with the coupled models in SIERRA/SM with Pyrex while increasing energy density. The relationship between the energy density and the percentage of the mass under 10 microns was linear for the coupled model, which is consistent with the form of Equation 4-1. However, the relationship between the percentage of the mass under 10 microns and the energy (in the form of increasing initial strain-rate) in the stand-alone model was not linear.

The sensitivity analysis performed on the stand-alone microscale model did not show any dependence of density on the percentage of the mass of the 1D bar under 10 microns. This is consistent with the implementation of Equation 4-1 seen in the Handbook; however, density dependence was observed by Koch [Koch 2004]. As was noted previously, the stand-alone microscale sensitivity model was performed without coupled feedback from the macroscale model. The coupled model may show sensitivity to density and different behavior when compared to the stand-alone model. Follow-up work should be performed to determine if the microscale model shows sensitivity to density.

4.4.1. Recommendations for Future Study

For future study, the microscale model should be validated separately from the coupled model. While the model approach for the microscale is consistent with the model implemented by Zhou et al [Zhou 2005], several improvements have been made, such as the distribution of parameters at the microscale. The microscale model should undergo code and solution verification to identify if any code or numerical problems exist. It should then be validated against the data reported by Zhou. As part of this process, parameter correlations and relationships should be identified, either through empirical reasoning or sensitivity analysis. Model inputs may need to be changed to reflect relationships between parameters. Once the microscale model is properly verified and validated, the coupled model can be validated against data. Validation data for the coupled model can include the UO_2 and Pyrex impact tests as performed by [Jardin 1982] and the pellet impact test performed by [Koch 2004].

Once the coupled model is validated against experimental data, a sensitivity analysis can be performed for the coupled SIERRA/SM model. This should give enough information to assess if the validated results are consistent with the form of Equation 4-1 and to make a recommendation for Equation 4-1.

In summary, the recommendations for future study and improvement of the coupled model are to perform the following steps:

1. Verify algorithm that appears in the 1D model.
2. Perform code verification to ensure that the algorithm is implemented correctly in the model.
3. Perform solution verification to identify numerical errors.
4. Validation of 1D model against data presented by [Zhou 2005].
5. Validation of coupled model. Validation data for the coupled model can include the UO_2 and Pyrex impact tests as performed by Jardin and the pellet impact test performed by [Koch 2004].
6. Perform sensitivity analysis for the coupled SIERRA/SM model and use the results to make recommendations for the form of Equation 4-1.

With these steps being completed, the coupled model will have a better pedigree and we will have more confidence in the results, which will allow us to make recommendations for the form of Equation 4-1. Note that we would not modify Equation (4-1) in the Handbook, since this equation may have been used in the field. Rather, the supplemental equation may be provided to include the density dependence as suggested by [Koch 2004] (see Section 2.2).

This page left blank

5. SUMMARY, CONCLUSION AND RECOMMENDATION

This report summarizes the accomplishments made in the first three years of the project as well efforts, and results from those efforts, made during this fourth year. In this year, we proposed changes to various sections in Chapters 4 and 5 of the Handbook for the free-fall and impact of solids and powders, by identifying recent scientific literature for considered for inclusion in in sections of the Handbook. We performed simulations of free-fall impact and puncture scenarios for two waste container types, by first identify the most commonly used containers and their contents based on the transuranic waste stream data from WIPP, and then formulating and performing a set of simulations in which parameters such as drop height, content type, angle of impact, forklift speed, and impact location on the container's surface were varied. We have also revisited the fragmentation model work from FY17 and implemented various improvements, with the intent of utilizing the model to assesses Equation (4-1) of the Handbook. The summary and conclusion of each of the three tasks are described below.

Literature review and Revision of Chapters 4 & 5 in Free-Fall Spills and Impact Stress (Task 1)

A literature review was conducted to identify additional recent experiments that are related to free-fall spills of particulates to supplement the experiments already described in the existing Handbook. In addition, a literature review was performed to identifying recent experiments related to the impact events on containers, solids and powders.

Since our intent is not deleting any information from the Handbook and we had not proposed any revision of the ARF/RF values that can be justified, there is no reason to copy the exact information from the current version of Handbook. In fact, we simply summarize various sections and append the additional information for those sections impacted. The new information is provided for the preparer(s) of the future revision of the Handbook to decide if these information should be included. We also have provided recommendations for these sections as noted in the conclusions below.

For this task, we completed the following:

1. Provided a review of the recent literature on this topic.
2. Summarized or reviewed the current sections of the Handbook on this topic.
3. Appended the up-to-date information to the sections.

The following conclusions are identified for this task:

1. Equation (4-1) in the Handbook may need to be supplemented with additional equation, since recent literature from [Koch 2004] has identified from the experiments that the coefficient in Equation (4-1) should be material density dependent. Further discussion is presented in Chapter 4 of this report.
2. Free-fall spill data in the Handbook are limited as indicated in Section 2.3.1.1. Additionally, based on the previous SIERRA study on powder spill experiments from [Sutter 1981] in the NSRD-11 report [Louie 2016], more spill experiments should be done to quantify and supplement to this data. Recent experiments and modeling of bulk material spills described in Appendix B.2 may provide additional physics insights on how particle spill affects hydrodynamically which could influence the ARF/RF.
3. We had not identified any recent literature on the HEPA filters that can incorporate in the Handbook. However, based on the review of Section 5.4.4 of the Handbook, only a single

data source was used to derive the HEPA filter data from [Arnold 1986]. Thus, additional experiments may be needed to substantiate this single source data which relies on many assumptions to derive the ARF/RF values. The additional experiments would provide conferences and uncertainty of the data in the Handbook.

Development of DR for Container Beach (Task 2)

A series of SIERRA/SM free-fall impact and puncture simulations were performed to determine the resulting performance of two common waste containers, 7A drums and SWB containers. Container selection and container content were based on the recent waste stream data from LANL. Drop and puncture scenario parameters were based on WIPP facility data for drop scenarios and commercial forklift data for puncture scenarios. Content weight was based on the maximum allowable in the WIPP-WAC.

Results from the simulations show that the content type plays more of a role in the behavior of the containers in the free fall impact scenarios than in the puncture scenarios. More variability in container behavior was observed between scenario type than across content type. Drums filled with the SI content type experienced failures more often than the HD-filled drums. Regardless of content type, all drums failed when dropped from a height of 20 meters at 135 and 180-degree orientations.

Once the breach area was determined, an estimate of the DR was done using the DOE-STD-5506 as a guide. The results in this report are considered to be conservative estimates of DR since they are larger than those reported in the standard (see Sections 3.4.1 and 3.4.2) . We also attempted to quantify the magnitude of the ARF/RF by referencing the data in Chapter 2 of this report, and providing the arguments to determine these magnitudes.

This information in this chapter demonstrates that simulations can be used to model a broad range of accident scenarios and content types to predict container breach. The parameters tested go beyond those cases described in DOE-STD-5506. Thus, the information provided in this chapter should bound those described in the standard (see the DR values provided in Table 3-13 to Table 3-16 for our study and those values in Table 3-12 for the standard).

Expansion of Equation 4-1 (Task 3)

This task is intended to expand Equation (4-1) in the Handbook. However, because the issues encountered during the performing the fragmentation model testing and validation, the task was not able to be completed to expand this equation. Rather, much of the time was devoted to debug and improve the micro-fragmentation model and creating the test parameters for the modeling using DAKOTA. However, we have validated parts of the fragmentation models using recent literature data, such as the brittle sphere experiment data [Wu 2004] for validating the macro-scale fragmentation model. We have also attempted to couple the both micro- and macro-fragmentation models for validating brittle material pellet experiments [Jardin 1982], but the validation was not encouraging. Instead, the attempt was to validate the micro-scale model first, and used the parameter distributions of the parameters that we think to be important for the analyses. After this study, we found that the micro-scale fragmentation model may need further improvement.

For future study, the microscale model should be validated separately from the coupled model. While the model approach for the microscale is consistent with the model implemented by [Zhou

2005], several improvements have been made, such as the distribution of parameters at the microscale. The microscale model should undergo code and solution verification to identify if any code or numerical problems exist. It should then be validated against the data reported by Zhou. As part of this process, parameter correlations and relationships should be identified, either through empirical reasoning or sensitivity analysis. Model inputs may need to be changed to reflect relationships between parameters. Once the microscale model is properly verified and validated, the coupled model can be validated against data. Validation data for the coupled model can include the UO_2 and Pyrex impact tests as performed by [Jardin 1982] and the pellet impact test performed by [Koch 2004].

Once the coupled model is validated against experimental data, a sensitivity analysis can be performed for the coupled SIERRA/SM model. This should give enough information to assess if the validated results are consistent with the form of Equation 4-1 and to make a recommendation for Equation 4-1. Note that we would not modify Equation (4-1) in the Handbook, since this equation may have been used in the field. Rather, the supplemental equation is provided to include the density dependence as suggested by [Koch 2004] (see Section 2.2) and other dependence such as temperature, grain size, porosity and impact angle.

This page left blank

REFERENCES

[1] [Ansart 2009] Ansart, R., et al., "Dust Emission in Powder Handling: Free Falling Particle Plume Characterization," Chemical Engineering Journal, Vol. 152 (n2-3), pp.415-420, 2009.

[2] [Ansart 2011] Ansart, R., et al., "Dust Emission by Powder Handing: Influence of the Hopper Outlet on the Dust Plume," Powder Technology, Vol. 212, pp. 418-424, 2011.

[3] [Arnold 1986] Arnold, P.M., Characterization of Spent HEPA Filters from Rocky Flats Plant, AO 6629 UNIF, Rockwell International – Rocky Flat Plant, Golden CO., September 1996.

[4] [ASME 2015] ASME BPVC, "ASME Boiler and Pressure Vessel Code," American Society of Mechanical Engineers, New York, NY, 2015.

[5] [ASTM 2016] ASTM A1008/A1008M – 16, "Standard Specification for Steel, Sheet, Coled-Rolled, Carbon, Structural, High-Strength Low-Alloy, High-Strength Low-Alloy with Improved Formability, Solution Hardened, and Bake Hardenable," American Society of Testing and Materials, ASTM International, West Conshohocken, PA, 2016.

[6] [ASTM 2014] ASTM A307 – 14, "Standard Specification for Carbon Steel Bolts, Studs, and Threaded Rod 60000 psi Tensile Strength," American Society of Testing and Materials, ASTM International, West Conshohocken, PA, 2014.

[7] [Ayachit 2018] Agyachit, U., et al., The ParaView Guide, paraview.org, June 14, 2018.

[8] [Blacker 2017] Blacker, T., et al., CUBIT Geometry and Mesh Generation Toolkit 15.3 User Documentation, SAND2017-6895W, Sandia National Laboratories, Albuquerque, NM July 2017.

[9] [Brannon 2009] Brannon, R.M., Survey for Four Damage Models for Concrete, SAND2009-5544, Sandia National Laboratories, Albuquerque, NM August 2009.

[10] [Capolungo 2007] Capolungo, L., et al., "The Elastic–Viscoplastic Behavior of Nanocrystalline Materials," International Journal of Plasticity, 23(4), page 561-591, 2007

[11] [Collins 1991] Collins, M.P., Prestressed Concrete Structures, Englewood Cliffs: Prentice Hall, 1991.

[12] [DOE 2003] DOE Handbook Nuclear Air Cleaning Handbook, DOE-HDBK-1169-2003, U.S. Department of Energy, Washington DC, 20585, November 2003.

[13] [DOE 2007] DOE Standard Preparation of Safety Basis Documents for Transuranic (TRU) Waste Facilities, DOE-STD-5506-2207, Appendix C, U.S. Department of Energy, Washington DC, 20585, April 2007.

[14] [DOE 2016] Department of Energy, Transuranic Waste Acceptance Criteria for the Waste Isolation Pilot Plant, Revision 8.0, DOE/WIPP-02-3122, July 5, 2016.

[15] [Ensight 2018] https://computing.sandia.gov/ensight/

[16] [EPA 1996] Environmental Protection Agency, Stabilization/Solidification Process for Mixed Waste, EPA 402-R-96-014, Washington D.C., 1996.

[17] [Fastenal 2016] Fastenal.com, Mechanical Properties of Externally Threaded Fasteners January 2016.

https://www.fastenal.com/content/feds/pdf/2016/01/Mechanical%20Properties%20Inch%20Fasteners%20Jan%202016.pdf

[18][Grady 1996] Grady, D.E., and Kipp, M.E., “Fragmentation Properties of Metals,” 1996 Hypervelocity Impact Symposium, October 7-10, Freibug I. Br., Germany, 1996.

[19][GEO 2013] Geotechdata, Soil elastic Young's modulus. September 9, 2013. Retrieved from geotechdata.info: http://www.geotechdata.info/parameter/soil-young%27s-modulus.html

[20][GEO 2014] Geotechdata, Soil Cohesion. October 31, 2014. Retrieved from geotechdata.info: http://www.geotechdata.info/parameter/cohesion.html

[21][Holtz 1981] Holtz, R.D., An Introduction to Geotechnical Engineering. Englewood Cliffs: Prentice Hall, 1981.

[22][Jardine 1982] Jardine, L. J., W. J. Mecham, G. T. Reedy and M. J. Steindler, Final Report of Experimental Laboratory-Scale Brittle Fracture Studies of Glasses and Ceramics, Argonne National Laboratory, 1982.

[23][Langer 1987] Langer, G., Simulated Seismic Event Release Fraction Data, Progress Report April 1986-April 1987, RFP-4161, Rockwell International – Rocky Flats Plant, Golden, CO, Novermber 1987.

[24][Lorentz 2011] Lorentz, E., S. Cuvilliez and K. Kazymyrenko, "Convergence of a gradient damage model toward a cohesive zone model." Comptes Rendus Mecanique 339(1): 20-26, 2011.

[25][Louie 2015] Louie, D.L.Y. and Brown, A. NSRD-6: Computational Capability to Substantiate DOE-HDBK-3010 Data, SAND2015-10496, Sandia National Laboratories, Albuquerque, NM, November 2015.

[26][Louie 2016] Louie, D.L.Y., et.al, NSRD-11: Computational Capability to Substantiate DOE-HDBK-3010 Data, SAND2016-12167, Sandia National Laboratories, Albuquerque, NM, November 2016.

[27][Louie 2018] Louie, D.L.Y., et al., NSRD-15: Computational Capability to Substantiate DOE-HDBK-3010 Data, SAND2018-0436, Sandia National Laboratories, Albuquerque, NM, January 2018.

[28][Mecham 1981] Mecham, W. J., L. J. Jardine, R. H. Pelto, G. T. Reedy and M. J. Steindler, Interim Report of Brittle-Fracture Impact Studies: Development of Methodology, Argonne National Laboratory, 1981.

[29][Madler 1999] Madler, L. et al., “In Situ Aerodynamic Size Classification of Aerosols in the size range between 0.1 and 100 μm for Dustiness Tests and Powder Characterization,” Jounral Aerosol Science, Vol. 30 No.4, pp451-465, 1999.

[30][Minana 2012] Minana, M., Turgeon, J., Lujan, C., Pilch, M., and Hackney, P., Sandia National Laboratories Advanced Simulation and Computing (ASC) Software Quality Plan – ASC Software Quality Engineering Practices, Version 3.1, SAND2008-5517, Sandia National Laboratories, Albuquerque, NM, March 2012.

[31][Mishima 1973] Mishima, J., and Schwendiman, L. C., “Fractional Airborne Release of Uranium (Representing Plutonium) During the Burning of Contaminated

Wastes," BNWL-1730, Pacific Northwest Laboratory, Richland, WA, April 1973.

[32] [Mishima 1973a] Mishima, J., et al., "Some Experimental Measurements of Airborne Uranium (Reprocessing Plutonium) in Transportation Accidents," BNWL-1732, Pacific Northwest Laboratory, Richland, WA, August 1973.

[33] [Mishima 1978] Mishima, J., et al, Increment of Analysis – An Estimate of Airborne Release of Plutonium from Babcock and Wilcox Plant as a Result of Severe Wind Hazard and Earthquake, PNL-2812, Pacific Northwest Laboratory, Richland, WA, October 1978.

[34] [NWP 2014] Nuclear Waste Partnership, LLC, Standard Waste Box Assembly Drawings, 165-F-001-W1 to W4, July 30, 2014.

[35] [NWP 2015] Nuclear Waste Partnership, LLC, Standard Waste Box Type A Evaluation Report, SWB-REP-0001, Rev.1, January 2015.

[36] [NWP 2016] Nuclear Waste Partnership LLC., Waste Isolation Pilot Plant Documented Safety Analysis, DOE/WIPP 07-3372, Rev 5b, April 2016. (http://www.wipp.energy.gov/Special/DSA_Rev_5_Chapters_0-18.pdf)

[37] [O'Shanughnessy 2012] O'Shanughnessy, R.T., et al., "A Novel Device for Measuring Respirable Dustiness Using Low Mass Powder Samples," Journal of Occupation and Environmental Hygiene 9(3) 129-139, 2012.

[38] [Prokon 2018] Prokon.com, Elastic Properties of Soils. Retrieved from prokon.com: https://support.prokon.com/portal/kb/articles/elastic-properties-of-soils

[39] [SAND 1984] MacDougall, H.R., et al., edited, "Appendix F - Preliminary Preclosure Safety Analysis", Site Characterization Plan Conceptual Design Report, SAND84-2641 Vol 4, Sandia National Laboratories, Albuquerque, NM, September 1984.

[40] [Scherzinger 2016] Scherzinger, W. M., B. T. Lester and P. Newell, Library of Advanced Materials for Engineering (LAME) 4.42, Sandia National Laboratories, 2016.

[41] [SIERRA 2016] Sierra Thermal Fluids Development Team, "Sierra Fuego User Manual – Version 4.40," Sandia National Laboratories, SAND 2016-4157, (2016).

[42] [SIERRA 2017] http://compsim.sandia.gov/compsim/Docs/Sierra/4.44/GeneralRelease

[43] [SIERRA 2017b] SIERRA Solid Mechanics Team, Sierra/Solid Mechanics 4.44, User's Guide: Addendum for Shock Capabilities, SAND2017-4014, Sandia National Laboratories, Albuquerque, NM, April 18, 2017.

[44] [SIERRA 2017c] Sierra Structural Dynamics Development Team, Sierra/SD – Theory Manual, SAND2017-3554, Sandia National Laboratories, Albuquerque, NM, April 6, 2017.

[45] [SIERRA 2017d] Sierra Thermal/Fluid Development Team, SIERRA Low Mach Module: Fuego User Manual – Version 4.44, SAND2017-3792, Sandia National Laboratories, Albuquerque, NM, April 13, 2017.

[46] [SIERRA 2018] SNL, SIERRA/Solid Mechanics 4.48 User's Guide, SAND2018-2961, Sandia National Laboratories, Albuquerque, NM, April 2, 2018.

[47] [Skinner 2017] Skinner, C.M., Evaluation of Energy Released from Nuclear Criticality Excursions in Process Solutions, M.S. Thesis, University of New Mexico, December 2017.

[48][Skolnik 2006] Skolnik Industries, Drawing CQ5508, Rev A5, “55 Gallon Open Head Drum, 1.5 – 1.5 – 1.5 CRCQ, 1A2/X430/S & 1A2/Y1.5/175,” Skolnik Industries, Inc., Chicago, IL, November 7, 2006.

[49][Skolnik 2009] Skolnik Industries, Inc., Exhibit 11.2A – Type A Test Report, Rev 03, ID 14-089, Part No. CQ5508, Chicago, IL, July 17, 2009.

[50][Soest 2017] Soest, G.V., Email to David Louie “Re: Digital Data of Site TRU Waste Inventory,” 3:43 pm, November 16, 2017.

[51][Wikipedia 2016] Wikipedia.org, Drucker–Prager yield criterion, August 10, 2016. Retrieved from wikipedia.org: https://en.wikipedia.org/wiki/Drucker%E2%80%93Prager_yield_criterion

[52][Wittel 2008] Wittel, F.K., et al., “Mechanisms in Impact Fragmentation,” International Journal of Fracture, 154:105-117, 2008.

[53][Wu 2004] Wu, S.Z., et al., “Crushing and Fragmentation of Brittle Spheres under Double Impact Test,” Powder Technology 143-144, page. 41-55, 2004.

[54][Zhou 2005] Zhou, F., J. F. Molinari and K. T. Ramesh, "A cohesive model based fragmentation analysis: Effects of strain rate and initial defects distribution." International Journal of Solids and Structures 42(18): 5181-5207, 2005.

APPENDIX A. SUMMARY TABLE FOR HANDBOOK DATA

This appendix provides a summary table for the Handbook, including six columns: Column 1 identifies the chapter or section number; Column 2 identifies the category, such as liquid, solid, etc.; Columns 3 and 4 tabulate the bounding values; Column 5 describes any initial size distribution provided; and Column 6 provides comments. Note that Column 1 intends to provide the information of interests from those chapters/sections from the Handbook. It is not necessarily a complete list, since Chapter 2 of the Handbook deals with gaseous forms, which are often assumed to be released during an accident. Thus, it may not have an interest in this current research in terms of ARF and RF. Note: this summary table is an "in-progress" table, which means that it would be updated as more substantiating studies are done to the data in the Handbook.

Chapter /section	Category	ARF	RF	Initial Size Distribution	Comments*
3.0	***LIQUID***				This chapter divides into types of liquids, which includes aqueous solutions, organic, and combustible solvents.
3.2	*Aqueous solution*			Droplet distribution during bubbling is provided	This section describes models related to evaporation and boiling. Formulations on entrainment of liquid droplets from the surface of a bubbling or boiling pool are provided. Phenomena associated with these entrainments are described. (see Chapter 5 of NSRD-11 for more details about describing the use of these models in the simulations.)
3.2.1	Thermal Stress				
	(a) Heating of aqueous solution in flowing air without surface rupture bubbles	3.00E-05	1		
	(b) Boiling (bubbles continuously breaking the surface of the bulk liquid with < 30% of volume of the liquid as bubbles)	2.00E-03	1		
3.2.2	Explosion Stress				
	Venting of pressurized liquids				
	(a) Venting below liquid level	1.00E-04	1	< 10 µm	
	(b) Venting above liquid level				
	[1] low pressure (< 0.35 MPa)	5.00E-05	0.8		
	[2] high pressure (>0.35 MPa)				
	(aqueous solution)	2.00E-03	1		~1 g/cc solution density
	(conc. Heavy metal solution)	1.00E-03	0.4		≥1.2 g/cc solution density
	[3] superheated liquid				
	(≤ 50°C superheat)	1.00E-02	0.6		
	(50 to 100°C superheat)	1.00E-01	0.7		
	(> 100°C superheat)	$0.33*(MF)^{0.91}$	0.3		MF = mole fraction of pressurized gas/water vapor flashed
3.2.3	Free-Fall Spill				
	3-m distance				
	(a) aqueous solution				
	[1] aqueous solution	2.00E-04	0.5		~ 1g/cc solution density

Chapter /section	Category	ARF	RF	Initial Size Distribution	Comments*
	[2] conc. Heavy metal solution	2.00E-05	1		≥ 1.2 g/cc solution density
	(b)slurries < 40% solids	5.00E-05	0.8		
	(c) viscous solution, viscosity > 8 centipoise	7.00E-06	0.8		
	> 3-m				Both ARF and RF should be larger than the 3-m fall, and the empirical correlations for ARF and drop size presented in Ballinger et.al (Jan 1988)
3.2.4	Aerodynamic Entrainment and Resuspension				Use of these values for < 100 hours would not introduce serious error due to the severe depletion of the source.
	(a) indoor surfaces (SS, concrete) up to normal facility ventilation flow; outdoors, pool for low wind speeds	4.00E-07	1		
	(b)indoor, covered with debris or under static condition	4.00E-08	1		
	(c) outdoors, large pools wind speed ≤ 30 mph	4.00E-06	1		
	(d) outdoors, absorbed on soil, no lengthy pooling wind speed ≤ 50 mph	9.00E-05	1		
3.3	*Organic Combustible Liquids*				No experimental data on the behavior of organic, combustible liquids in response to explosive release, venting of pressurized liquid, free-fall spills or aerodynamic entrainment were found. We are examining some of the experiments referenced in this section for this year in the area of fire in Section 3.3.1 and Section 3.3.6 of the Handbook (see Chapter 4 of NSRD-6, Chapter 4 of NSRD-11)
	Thermal Stress				
	(a) volatiles (i.e., I2)	1	1		
	(b) Quiescent burning, small surface pool, or on larger pool	1.00E-02	1		
	(c) vigorous burning large pools	3.00E-02	1		This includes solvent layer burning over limited aqueous layer with sufficient turbulence to disrupt bulk of aqueous layer
	(d) Same as (C) to complete dryness	1.00E-01	1		
	(e) air-dried salts under gasoline fire	5.00E-03	1		Includes aqueous solution, on a porous or cracks, depression
	(f) same as (e) above, except on metal surface	2.00E-01	1		May not include porous, cracks or depression
4.0	***SOLIDS***				This chapter of the Handbook describes the data related to metals (primarily the release from energetic hydride reactions, nonmetallic (such as ceramics) or composite solids, and powders.

Chapter /section	Category	ARF	RF	Initial Size Distribution	Comments*
	Metal				
4.2.1	Thermal Stress				
	(a) Plutonium				
	[1] oxidation (corrosion) at room temperatures				These values intended for < 100 hours
	(unalloyed Pu)	$2x10^{-6}$ µg Pu/cm^2-hr (dry air)	0.7		
		$7x10^{-3}$ µg Pu/cm^2-hr (100% RH)	0.7		
	(delta-phase metal)	$7x10^{-8}$ µg Pu/cm^2-hr (dry air)	0.7		
		$6x10^{-4}$ µg Pu/cm2-hr (100% RH)	0.7		
	[2] oxidation at elevated temperatures	3.00E-05	0.04		
	[3] self-sustained oxidation	5.00E-04	0.5		Includes molten metal with oxide coat, self-induced convection
	[4] disturbed molten metal surfaces	1.00E-02	1		Such as flowing metal, actions resulting in continual surface renewal, high turbulence at surface. Impacted by high air velocity or free-fall, 95% confidence on these values. It is not applicable to oxidation of trace hydride, metal, powder contamination.
	[5] oxidation of small metal drops	1	0.5		hundreds of µm size, passing through air or explosive reaction of entire metal mass
	(b) Uranium				
	[1] complete oxidation of metal mass	1.00E-03	1		For thermal condition > 500 °C and for upward flow velocity of 0- 2 m/s. It is for airborne particles < 10 µm. A 95% confidence level is for flow velocities < 100 cm/s.
	[2] free-fall of molten metal drops	1.00E-02	1		This is based on an arbitrary increase of 95% confidence to the experiment data.
	[3] explosive dispersal of molten uranium	1	1		If the uranium is molten and subdivided in very small drops and ejected at sonic velocities (very fine particles and aggregates ≤10 µm)
4.2.2	Explosive Stress				No recommended value is given. It refers to the surface contamination section of the handbook. For shock effects, it refers to the size of the TNT equivalent for respirable release. 20% of the metal should be used as respirable fraction. Consult national laboratories for analyses.
4.2.3	Free-Fall and Impaction Stress				No significant release as indicated. Refer to the surface contamination section of the handbook. See Section 2.1 for the update.
4.2.4	Aerodynamic Entrainment and Resuspension				Identical correlations as described in the Thermal Stress type (a)[1] above.
4.3	*NONMETALLIC OR COMPOSITE SOLIDS*				
4.3.1	Thermal Stress				

Chapter /section	Category	ARF	RF	Initial Size Distribution	Comments*
	(a) vitrified waste				No significant release by industrial-type fire.
	(b) aggregate (e.g., concrete and cement)				
	[1] tritium release from concrete				
	(if present and 200 ^{o}C)	5.00E-01	1		
	(if present and 600 ^{o} C)	1	1		
	[2] suspendible powder	6.00E-03	0.01		
	[3] spent commercial nuclear fuel				These materials were discussed in general for accident conditions related to severe accidents in commercial reactors. Thus, release related to thermal stress is related to the release described in Section 4.4.1 of the Handbook.
4.3.2	Explosive Stress				No recommended value is given. It refers to the surface contamination section of the handbook. For shock effects, it refers to the size of the TNT equivalent for respirable release. 20% of the metal should be used as respirable fraction. Consult national laboratories for analyses.
4.3.3	Free-Fall and Impaction Stress	see comment	see comment	A distribution related to the UO_2 pellet impacts is provided	A correlation for a combined value of ARF*RF is given as A*P*g*h, where A is an empirical correlation of 2E-11 cm^3 per g-cm^2/s^2, P specimen density, g/cm^3, g is gravity at sea level, and h is fall height in cm. (See Chapter 4 of this report for discussions of the development and see Chapter 2 for the detailed discussions.)
4.3.4	Aerodynamic Entrainment and Resuspension				No significant release. See contamination section of this handbook.
4.4	*Powders*				For high energy stresses, the bounding values of 10 µm AED and RF =0.1 should be assumed. Note that no powder release due to impact of projectile was given. Exploratory simulation was done to an impact of can containing powder from a projectile (see Chapter 5 of NSRD-6).
4.4.1	Thermal Stress				Based on the thermal condition of < 1000 ^{o}C
	(a) non-reactive compounds	6.00E-03	1.00E-02		Entrainment of pre-formed particles by the flow upwards of heated surface.
	(b) reactive compounds except PuF_4	1.00E-02	1.00E-03		Particles formed by reaction given by the experiments
	(c) PuF_4	1.00E-03	1.00E-03		Particles formed by reaction given by the experiments
4.4.2	Explosive Stress				
	(a) shock effect				No data
	(b) blast effect				Detonations and deflagrations
	[1] above the surfaces	see comment	see comment		No detailed information is provided for detonation. For large deflagration, use ARF of 1 and RF for the original powder size that is < 10 µm. It is for a container failure pressure of ~ < 0.17 MPa.

Chapter /section	Category	ARF	RF	Initial Size Distribution	Comments*
	[2] accelerated airflow parallel to surface	5.00E-03	0.3		This represents a condition of the powders shield from the effects of a detonation or strong deflagration by standard containers.
	(c) venting of pressurized powders for deflagration > 25% confined volume				This also includes the condition of a deflagration and pressurized release. We are examining the pressurized release of powder experiment in this research (see Section 5.2 of [Louie 2015] and Section 5.2 of NSRD-11).
	[1] ≤ 0.17 MPa	5.00E-03	0.4		
	[2] 0.18 to 3.5 MPa	1.00E-01	0.7		
4.4.3	<u>Free-Fall/Impaction Stress</u>				We are examining a projectile hitting a can filled with powder (see Section 5.1 of NSRD-6 [Louie 2015]). No applicable experiments are done or described. The simulations of the free-fall and impact stress simulations of the 7A drum and another container are provided in Chapter 3 of this report. See Chapter 2 for the discussions.
	(a) fall height < 3 m	2.00E-03	0.3		
	(b) fall height > 3 m	See comment. The calculated value must exceed those in (a)	See comment. The calculated value must exceed those in (a). The RF is limited in the total RF in the original powder.	see comment	Using PSPILL code to model powder spills - varying Mo (mass of powder spilled, kg). Air density and viscosity assumes to be 1.18 kg/m3 and 1.85e-5 Pa-sec, respectively. The correlation is given as: $ARF=2*0.1064*(M_o^{0.125})(H^{2.37})/\rho^{1.02}$, where H = spill height, and ρ = bulk density of powder. AMMD = 12.1-329*ρ+7530*F, where F is the airborne fraction (ARF). Note this equation only has a 46% correlation coefficient due to the variability in the data (see Section 5.1 of NSRD-15).
	(c) suspended solid dispersed into flowing air	ARF = 0.0134 v_{wind}+0.00543, where v_{wind} is the wind speed (m/s)	The RF is limited in the total RF in the original powder.		For enhanced air velocities normal to direction of powder flow.
	(d) suspension of bulk powder in confinement	1.00E-03	0.1		Due to vibration of substrate from shock-impact to powder confinement (e.g., glovebox or can) due falling debris or external energy (i.e., seismic vibration)
	(e) suspension of bulk powder in debris impact and air turbulence from falling object	1.00E-02	0.2		No confinement is involved.
4.4.4	<u>Aerodynamic entrainment and resuspension</u>				Use of values given for short time frame (< 100 hours) (See NSRD-11's Chapter 2 for modeling resuspension due to human activity described in [Fish 1967].)
	(a) homogeneous bed of powder exposed to ambient condition	ARR = 4E-5/hr	1		Normal process facility ventilation flow, nominal atmospheric wind speed < 2 m/s, gusts up to 20 m/s, following the event.
	(b) homogenous bed of powder buried under structural debris exposed to ambient condition	ARR = 4E-6/hr	1		Including static conditions within structure following the event.

Chapter /section	Category	ARF	RF	Initial Size Distribution	Comments*
	(c) entrainment of powders from road surface by passage of vehicular traffic	1.00E-02	1		ARF is per passage
5.0	***SURFACE CONTAMINATION***				
5.2	*Contaminated, combustible solids*				
5.2.1	Thermal Stress				No applicable container release experiments due to thermal stress are documented. Mostly the burning of uncontained waste experiments is documented. Chapter 3 of this paper shows the simulation of the DR, ARF and RF of a ruptured drum due to thermal stress of a fire. This simulation is extrapolated from an existing drum fire experiment.
	(a) packaged mixed waste	8.00E-05	1		For contaminated combustible materials heated/burned in packages with largely non-contaminated surfaces
	(b) uncontained cellulosic or largely cellulosic mixed waste	1.00E-02	1		For burning of unpackaged, loosely strewn cellulosic materials
	(c) uncontained plastics				
	[1] except polystyrene	5.00E-02	1		
	[2] polystyrene	1.00E-02	1		
	(d) dispersed ash dropped into air stream or forced draft air				These values are not typically applied to burning mases of combustible material in large fires. These apply to extremely severe conditions where loosely contaminated combustible material is driven airborne as part of an updraft fireball.
	[1] loose powder	4.00E-01	1		
	[2] air-dried solution or adherent contamination	8.00E-02	1		
5.2.2	Explosive Stress				
	(a) shock effect				No data. Assume to be venting of pressurized gases over material.
	(b) blast effect				No data. Assume to be venting of pressurized gases over material.
	(c) venting of pressurized gases over contaminated combustible waste	1.00E-03	1		
5.2.3	Free-Fall and Impaction Stress				See Chapter 2 of this report.
	(a) materials with high surface area to mass ratios	0	0		No significant suspension is expected for freefall spill from working heights (~1 to 1.5 m)
	(b) combustible material is unpackaged/lightly packaged and strongly impacts the floor	1.00E-03	1		Or is impacted by falling debris. The values are based on reasoned judgment.
	(c) combustible material is packaged in a relatively robust container that is opened or fails due to impact with the floor or impaction by falling objects	1.00E-03	0.1		

Chapter /section	Category	ARF	RF	Initial Size Distribution	Comments*
5.2.4	Aerodynamic Entrainment and Resuspensions				Note that no applicable data found. Reasoned judgment is used. (For < 100 hours)
	(a) indoor or outdoor exposed to ambient conditions	ARR = 4E-5/hr	1		Normal process facility ventilation flow, nominal atmospheric wind speed < 2 m/s, gusts up to 20 m/s, following the event.
	(b) buried under debris exposed to ambient condition	ARR = 4E-6/hr	1		
5.3	*Contaminated, noncombustible materials*				
5.3.1	Thermal Stress	6.00E-03	0.01		Reasoned judgment applies
5.3.2	Explosive Stress				
	(a) shock effects				No recommended value is given. It refers to the surface contamination section of the handbook. For shock effects, it refers to the size of the TNT equivalent for respirable release.
	(b) blast effects				bounded by venting of pressurized gases in (c) below
	(c) venting of pressurized gases				These apply only to a loose surface contamination on the solid, not the solid as a whole. It includes corroded solids.
	[1] accelerated gas flows in area without significant pressurization	5.00E-03	0.3		
	[2] venting of pressurized volumes				
	(> 0.17 MPa)	5.00E-03	0.4		
	(< 0.17 MPa)	1.00E-01	0.7		
5.3.3	Free-Fall and Impaction Stress				See Chapter 2 of this report.
	(a) free-fall				Most materials will not experience free-fall spill. It is bounded by impact, shock vibration (b) below
	(b) impact, shock-vibration				
	[1] under brittle fracture	see comment	see comment		A correlation for a combined value of ARF*RF is given as A*P*g*h, where A is an empirical correlation of 2E-11 cm3 per g-cm2/s2, P specimen density, g/cm3, g is gravity at sea level, and h is fall height in cm. (See Chapter 4)
	[2] materials that do not undergo brittle fracture	1.00E-03	1		
5.3.4	Aerodynamic Entrainment and Resuspensions				It is bounded by powders estimates
	(a) indoor or outdoor exposed to ambient conditions	ARR = 4E-5/hr	1		Normal process facility ventilation flow, nominal atmospheric wind speed < 2 m/s, gusts up to 20 m/s, following the event.
	(b) buried under debris exposed to ambient condition	ARR = 4E-6/hr	1		
5.4	*HEPA Filters*				
5.4.1	Thermal Stress	1.00E-04	1		Extrapolation of maximum experimental of release of particles accumulated by the passage heated air through HEPA filters
5.4.2	Explosive Stress				

Chapter /section	Category	ARF	RF	Initial Size Distribution	Comments*
	(a) shock effects	2.00E-05	1		Based on experimentally measured release of accumulated particles from HEPA filers, localized failure from a momentary high-pressure pulse.
	(b) blast effects	1.00E-02	1		High velocity air flow through up to filter break pressure
	(c) venting of pressurized gases	1.00E-02	1		
5.4.3	Free-Fall and Impaction Stress				No applicable experimental data for airborne release during free-fall of HEPA filters were uncovered. (See Chapter 2 of this report.)
	(a) HEPA filter upon impact with hard unyielding surface				Bounded by conservative extrapolation of maximum releases measured for contained and uncontained HEPA filters.
	[1] enclosed (e.g., packages, filter or plena housing)	5.00E-04	1		
	[2] unenclosed	1.00E-02	1		
5.4.4	Aerodynamic Entrainment and Resuspensions				No significant release by nominal air velocities. See Section 2.6 for the update.
6.0	***INADVERTENT NUCLEAR CRITICALITY***				This chapter has been revised and described in Chapter 4 of NSRD-15 report.
	Solution	see comment	none		The criticality is generically considered terminated by the evaporation of 100 liters of water or some lesser amount. The airborne source term is given by $(MAR_{c1}*DR_{c1}*ARF_{c1})+(MAR_{s1}+DR_{s1}+ARF_{s1})$, where MAR_{c1} = inventory of gas and volatile, DR_{c1}=damage ratio for gases and volatiles generated in criticality, 1.0, ARF_{c1}=1 for noble gas, MAR_{s1}=inventory of non-volatile fission products generated, DR_{s1}=damage ratio radionuclides in solution, 1.0, and ARF_{s1}=5E-4 for non-volatiles, 1E-3 for ruthenium in fuel reprocessing solutions.
	Fully Moderated/Reflected Solids	see comment	none		This includes reflected bulk metal and metal pieces or solid fines such as powders that are moderated or reflected. It assumes no severe molten eructation, reactions and vaporization. Airborne source term = $MAR_{c2}*DR_{c2}*ARF_{C2}$, where MAR_{c2}=inventory of fissionable material and radionuclides from criticality, DR_{c2}=damage ratio, metal pieces=0.1, fines or powder=1.0, and ARF_{c2}=non-volatile can be neglected, 5E-1 for noble gases, and 5E-2 for iodine.
	Bare, Dry solids	see comment	none		No moderation, rather reflection. Airborne source term = $MAR_{c3}*DR_{c3}*ARF_{c3}$, where MAR_{c3}=inventory of radionuclides from fission, DR_{c3}=damage ratio, metal pieces=0.1, fines or powder=0.1, and ARF_{c3}=5E-1 for noble gas, 5E-2 for iodine.
	Large Storage Arrays				No data available

*NSRD-6 [Louie 2015], NSRD-11 [Louie 2016]

APPENDIX B. RECENT LITERATURE REVIEW FOR CHAPTER 2

B.1. Recent Literature on Brittle Material Impacts

B.1.1. Koch Experiment

This section describes a recent paper [Koch 2004] describes a laboratory experiment using an acceleration tube to impact a brittle material into an unyielding iron plate surface, which is intended to be used in transporting spent nuclear fuel. For these experiments, the impact energy (E) into brittle material is given by:

$$\mathrm{E} = \frac{1}{2}\mathrm{mv}^2 \tag{B-1}$$

Note v is the measured impact velocity, and m is the mass of the test specimen. Wm is the specific energy for the impact which is given by:

$$\mathrm{W_m} = \frac{\mathrm{E}}{\mathrm{m}} \text{ or } \mathrm{W_m} = \frac{1}{2}\mathrm{v}^2 \tag{B-2}$$

Thus, v is given by:

$$\mathrm{v} = \sqrt{2\mathrm{W_m}} \tag{B-3}$$

The brittle material includes small specimens of ceramic materials (such as depleted uranium (DUO2) pellets, $\mathrm{CeO_2}$, $\mathrm{WZrO_2}$) at a volume size of 2 $\mathrm{cm^3}$, glass at volume between 2 to 20 $\mathrm{cm^3}$ [Koch 2004]. Figure B-1 shows the apparatus of this experiment. Reference [Koch 2004] described how the airborne release fraction of < 100 μm as η_{100} (ARF), and < 10 μm as η_{10} (RF) are calculated or correlated. Figure B-2 shows the results from this test apparatus using various materials and impact energies. As shown in this figure, the η_{100} behaves linearly with increasing impact energy. [Koch 2004] correlates each of the materials into a linear equation:

$$\eta_{100} = \mathrm{C1} + \mathrm{C2}\ \mathrm{W_m} \tag{B-4}$$

Where C1 and C2 are given in Table B-1.

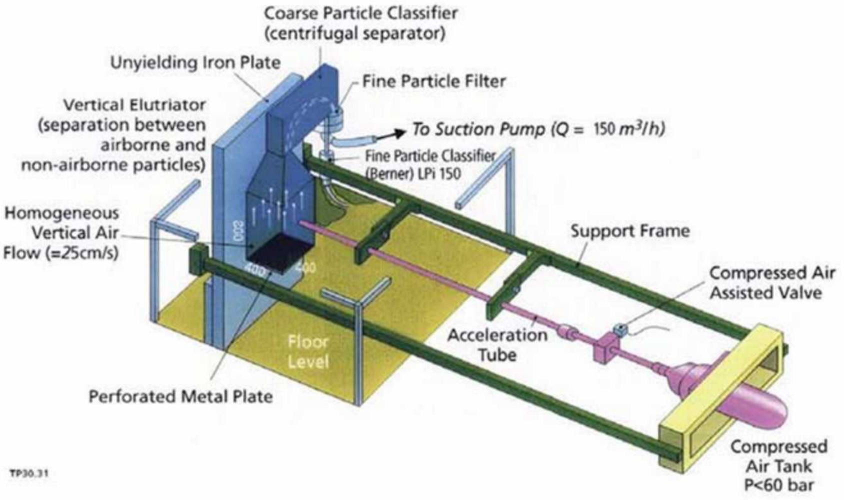

Figure B-1. Apparatus for Airborne Release Measurement for Impact Test [Koch 2004]

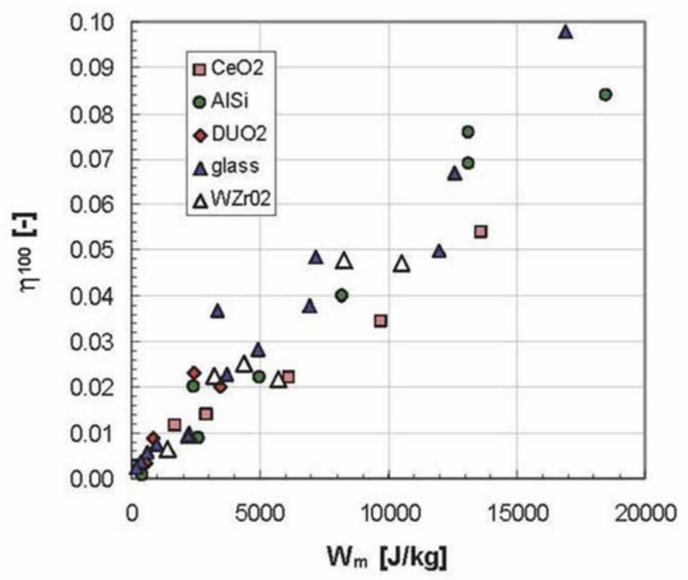

Figure B-2. Airborne Release Fraction, η100 (ARF) versus Impact Energy for the Impact Test [Koch 2004]

Table B-1. Fitted Constants C1 and C2 for Equation (B-1) [Koch 2004]

Impact material	C1 [-]	C2 [kg/J]	ρ_m [g/cm^3]
AlSi	9.27E-04	4.93E-06	1.6
Glass	3.77E-03	5.15E-06	2.2
CeO2	2.77E-03	3.56E-06	6.8
WZrO2	1.92E-03	4.69E-06	10.3
DUO2	2.82E-03	6.08E-06	11.0

To characterize the airborne release fraction as a cumulative mass fraction as a function of aerodynamic diameter, χ_{AED}:

$$Q_3(\chi_{AED}) = \frac{m(\chi_{AED})}{m_s}, \qquad 0 < Q_3(\chi_{AED}) < 1, \tag{B-5}$$

Where $m(\chi_{AED})$ is the total mass of all particles released in the size range < χ_{AED}, and m_s is the test specimen mass. Thus $\eta_{100} = Q_3(100\ \mu m)$ and $\eta_{10} = Q_3(10\ \mu m)$. Using this relation, [Koch 2004] derived a cumulative size distribution to fit the experimental data:

$$Q_3(\chi_{AED}) = a\, \chi_{AED}^{\mu} \tag{B-6}$$

Both a and μ are the fitted coefficients. See Figure B-3 for the plot of the experimental data fitted to the log scale. As shown in this figure, the straight-line fit to the data which indicated that μ is 1.

In further, [Koch 2004] fitted η_{10} for the following relation:

$$\eta_{10} = A\, \rho_m W_m \tag{B-7}$$

Note A in Equation (B-7 is an empirical correlation constant, 2E-11 (cm s^2/g) documented in Equation (4-1) of the Handbook. In this Equation (B-7), the respirable fraction is proportional to the material density, which A in Equation (4-1) in the Handbook does not. For example, for DUO2 sample tests, using A from Equation (4-1) in the Handbook, η_{10} is 1.1% at W_m of 5000E4 cm^2/s^2. Using Equation (B-4), η_{100}=0.03 for this example. Using Figure B-3, at X_{AED} =10 μm, it is at about 0.08 for Q_3/η_{100}, thus Q_3 = 0.027.

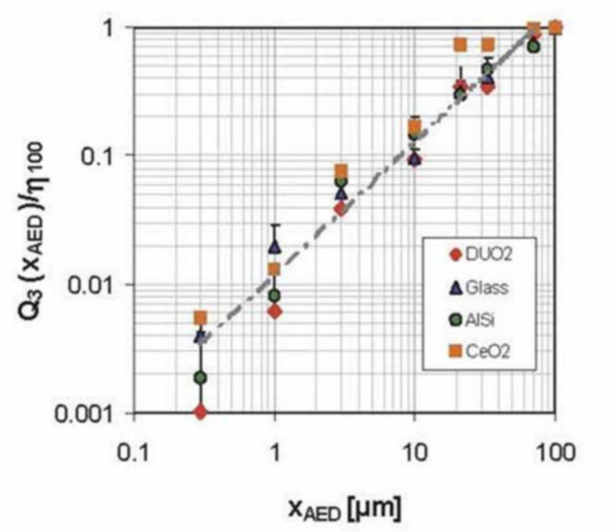

Figure B-3. Cumulative mass size distribution of the airborne release normalized to its value at X_{AED}=100 μm for impact tests with small pellets of various materials (different impact speeds up to 300 m/s). In the submicron size range, the scatter of the data becomes quite large for some ceramic materials (DUO2, AlSi) due to the fact that intra-grain boundary cracks are required for the particle formation [Koch 2004]

For the validation, we only use the DUO2 pellet results. Note that there is no specification of the dimension of the pellets in [Koch 2004]. Therefore, an assumption was made about the dimension of the pellet. Since the total volume is given as 2 cm^3, it is assumed that the pellet is a right cylinder with 1.5 cm in diameter. Then with the volume given, the length of the pellet would be 1.13 cm. In terms of the DUO2 properties, it is assumed that the UO_2 properties are applicable to DUO2.

B.1.2. Fragmentation of Large Particles

This section describes a paper on a comminution measurement where a larger particle is being reduced to a smaller particle by impaction [Lecoq 2003]. Although this paper focuses on comminution, it may be useful for identifying the breakup of larger particles into smaller particles where the kinetic energy is higher than a free-fall situation, such as an explosion, or high-pressure release, which are not covered in the free-fall powders. Free-fall powder may not yield the breakup of the larger particles. The experimental setup [Lecoq 2003] is shown in Figure B-4. The large particles are fed into a pressurized chamber and then released into the grinding chamber as a jet hitting a vertical hard disk (60-mm diameter) made of silicon carbide at an angle of 90°. The distance between the jet nozzle and the disk is about 55 mm and jet dispersion is about 1.5°. A filter bag and cyclone devices are used to collect the fragments after impact. The bottom fraction of the first cyclone, as shown in this figure, is used to determine the solid flow rate by a continuous weighing method. To minimize the particle-to-particle interactions, the jet composed of solids and air is a flow rate ratio, μ:

$$\mu = \frac{W_s}{W_j} < 0.1$$

where W_s is the mass flow rate of solids, and W_j is the mass flow rate of air. The solid kinetic energy is determined using a laser sheet, optical probe, and high shutter speed video camera. The size distribution of the particles is measured before and after the impact using a sieving technique. A scanning electron microscope is also used to observe the morphology of the grains before and after the impact.

One major observation from this experiment is that the size reduction ratio of the solids upon impact is linear dependent on the square of the impact velocity above the attrition threshold. This threshold corresponds to the beginning of the breakage of the solids, thus, broken fragments will appear. Figure B-5 shows the glass bead size distribution results as a function of the particle velocity in weight percent. As shown in this figure, increasing particle velocity will shift the size distribution to the smaller sieve size. Figure B-6 shows the SEM results from the experiments at the particle velocity corresponding to breakup. The size reduction ratios from the experiment are shown in Figure B-7. As shown in this figure, the size reduction behaves linearly with the impact or particle kinetic energy.

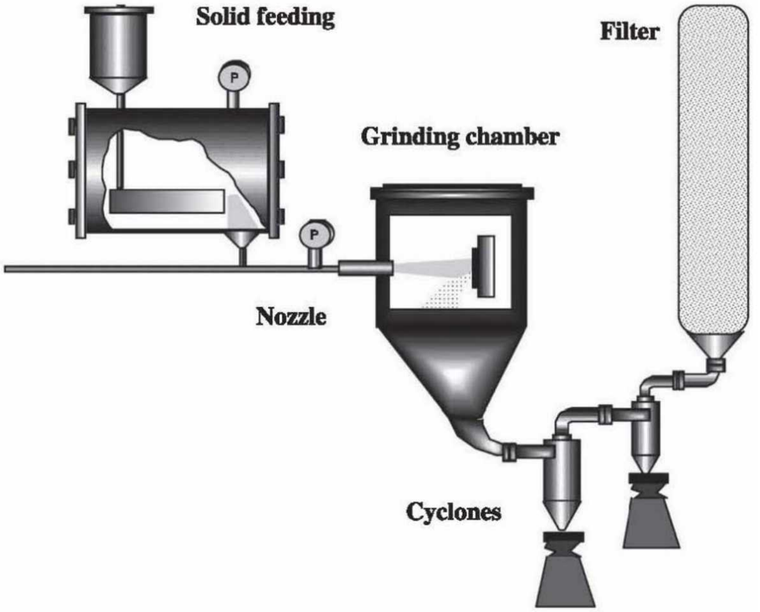

Figure B-4. Apparatus Schematic for Single Jet Mill [Lecoq 2003]

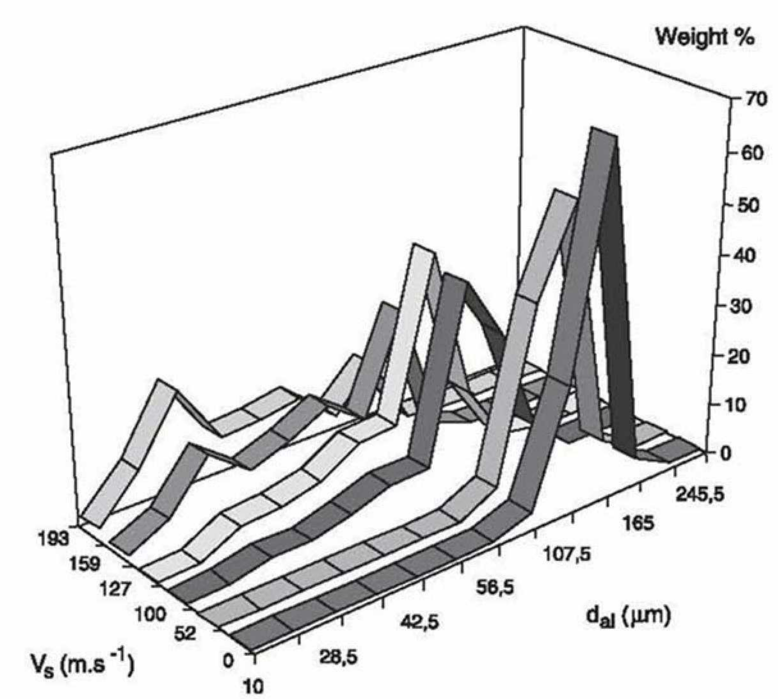

Figure B-5. Impact Result of the Glass Beads as Functions of Particle Velocity (V_s) and Mean Sieve Size (d_{al})

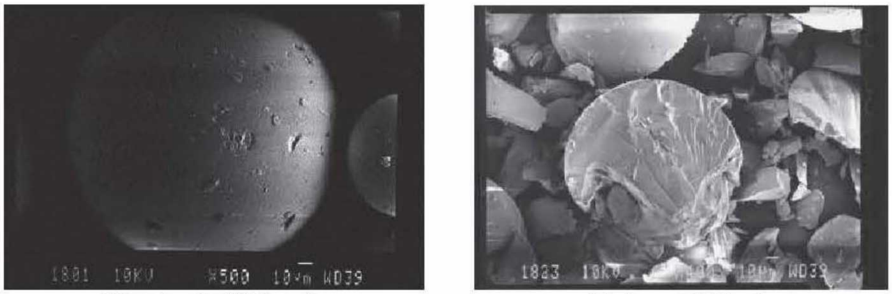

Glass beads (129 μm)

Broken at 125 m/s

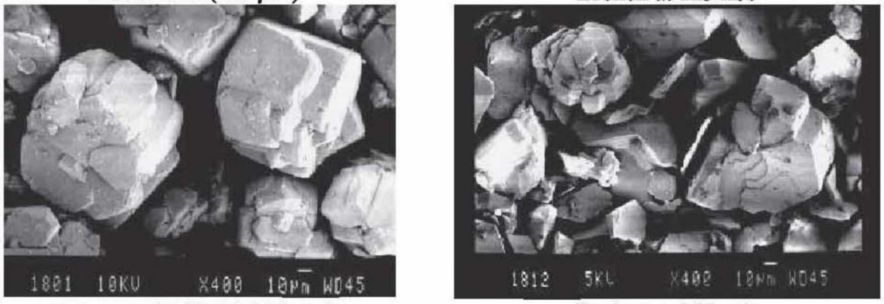

European A1(OH)3 (93 μm)

Broken at 155 m/s

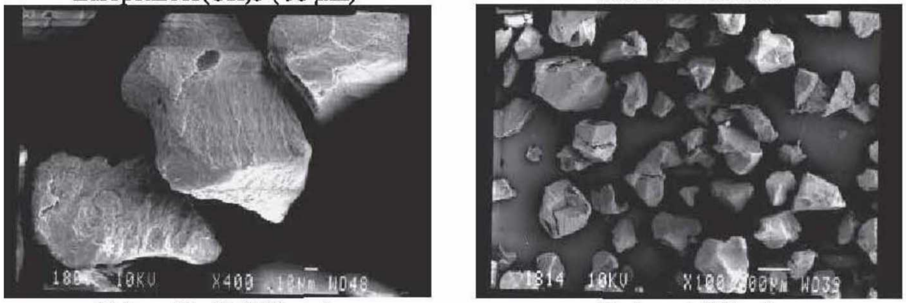

Polyamide 11 (123 μm)

Broken at 270 m/s

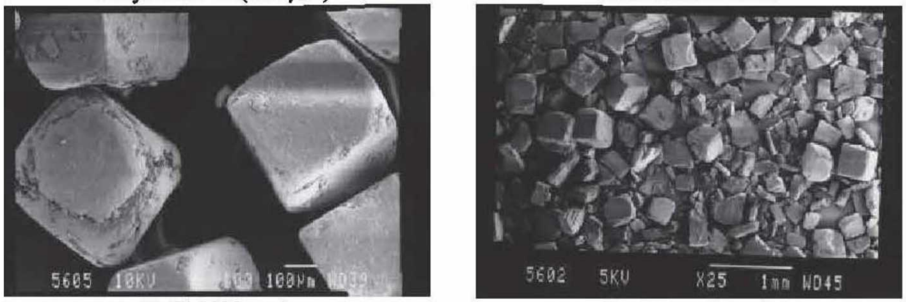

NaCl (400 μm)

Broken at 47 m/s

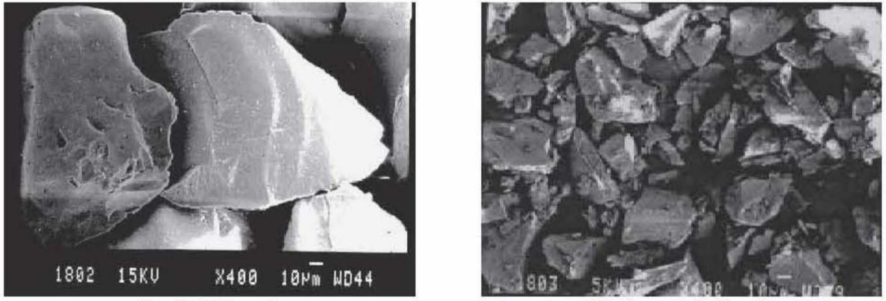

Sand(108 μm)

Broken at 170 m/s

Figure B-6. SEM Results of IMPACT Studies [Lecoq 2003]

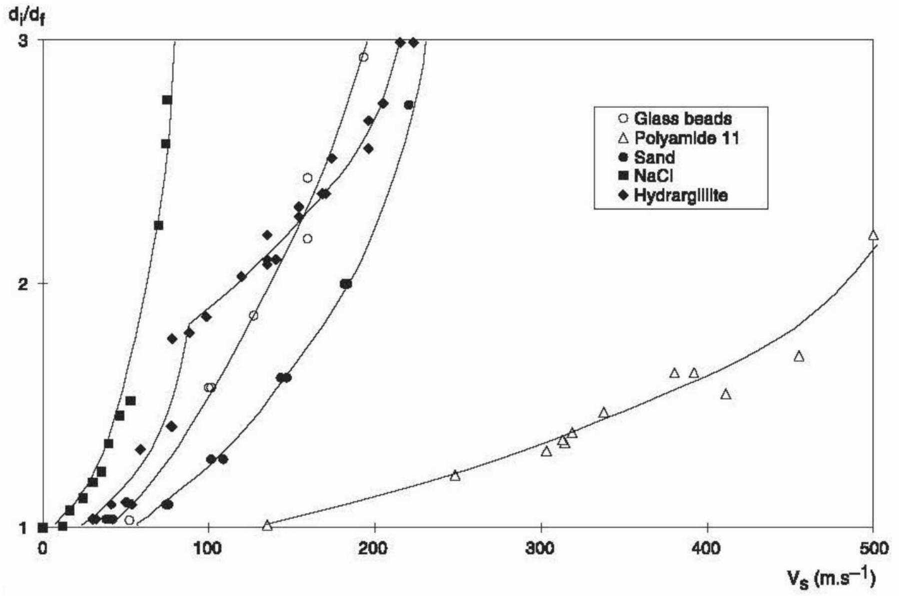

(a) Function of Particle Velocity (V_s)

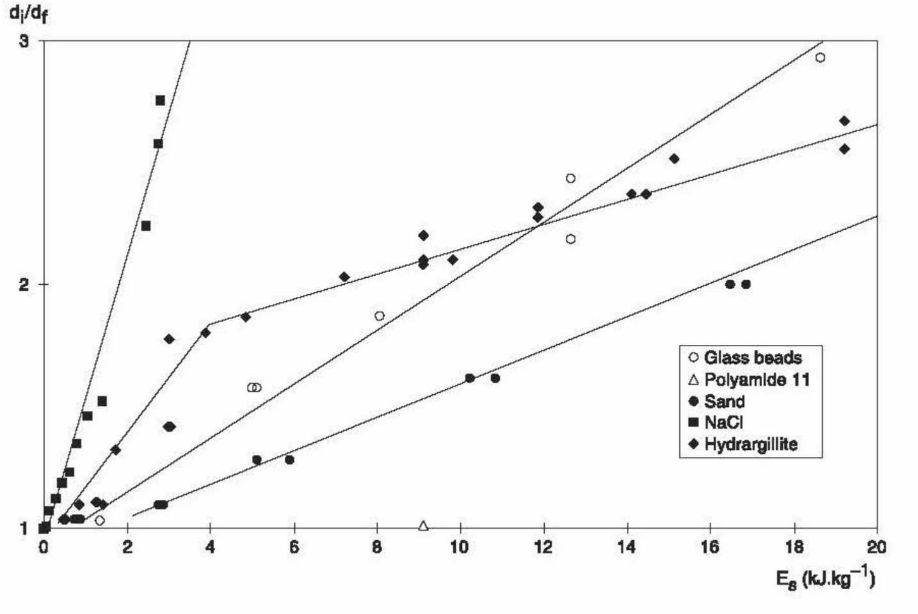

(b) Function of Particle Kinetic Energy ($E_s = 0.5\rho_s V_s^2$), ρ_s= particle density

Figure B-7. Size Reduction Ratio Results from Experiments as Function of (a) Impact Velocity and (b) Impact Kinetic Energy

B.2. Recent Literature on Free-Fall Bulk Flow

No significant experimental data was obtained from nuclear related areas, however, extensive data was found for dust emissions by industrial processes, such as feed bins, vibrating feeders and conveyors of materials [Liu 2003]. Liu [Liu 2003] describes theory and experiments related to the dust generation during free fall. Fugitive dust is often used to describe the particulate in air by wind action or human activities – machinery.

Free fall of bulk materials in air can be influenced by many parameters such as particle size distribution and density, as well as drop height and solids mass flow rate. A steady stream of bulk materials flowing downward behave differently when a bucket of bulk materials inverts and falls onto the floor. In addition to above parameters, the recent work has shown that particle stream behavior to the quantity of induced air is very important [Liu 2003]. Thus Liu [Liu 2003] developed an air entrainment model for steady stream of falling powder/particles (see Figure B-8). This model would allow for better understanding of small particle (i.e., < 10 μm) buoyancy.

Mechanisms that affect a stream of particles under free-fall condition:

- Moving particles are not only affected by gravity, but also affected by the drag force generation through the interaction with the surrounding air
- Collisions between falling particles may occur under free-fall conditions due to the irregular size and size distribution of the particles.
- The value of the specific air entrainment decreases with increasing mass flow of material.

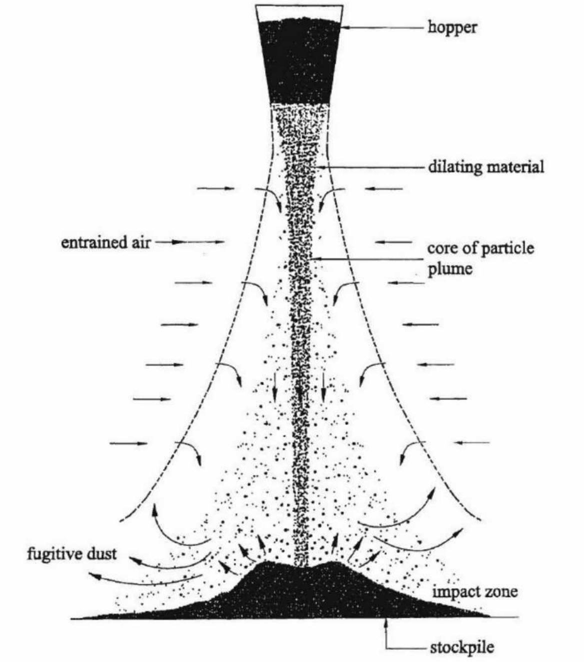

Figure B-8. Free Falling Particle Plume Schematic [Liu 2003]

To explain further, Liu [Liu 2003] adapted the liquid spray model in terms of 3 distinct zones (see Figure B-9). The zoning in Figure B-9 can be explained as:

1. Drop region close to the outlet of the hopper or bucket – it is assumed that the droplet velocity is constant and the air entrained velocity is much less than the droplet velocity.
2. In this zone, the magnitude of the droplet velocity is assumed to be the same as the air entrained velocity. Thus, the momentum flow of the droplets is smaller compared to the momentum flux of the entrained air within the spray droplet plume (including entrained air).
3. In the final zone, it is assumed that the droplet velocity reaches its terminal velocity. Lui [Liu 2003] uses this droplet spray behavior to explain the free fall of the bulk solids from a discharging hopper in quiescent air.

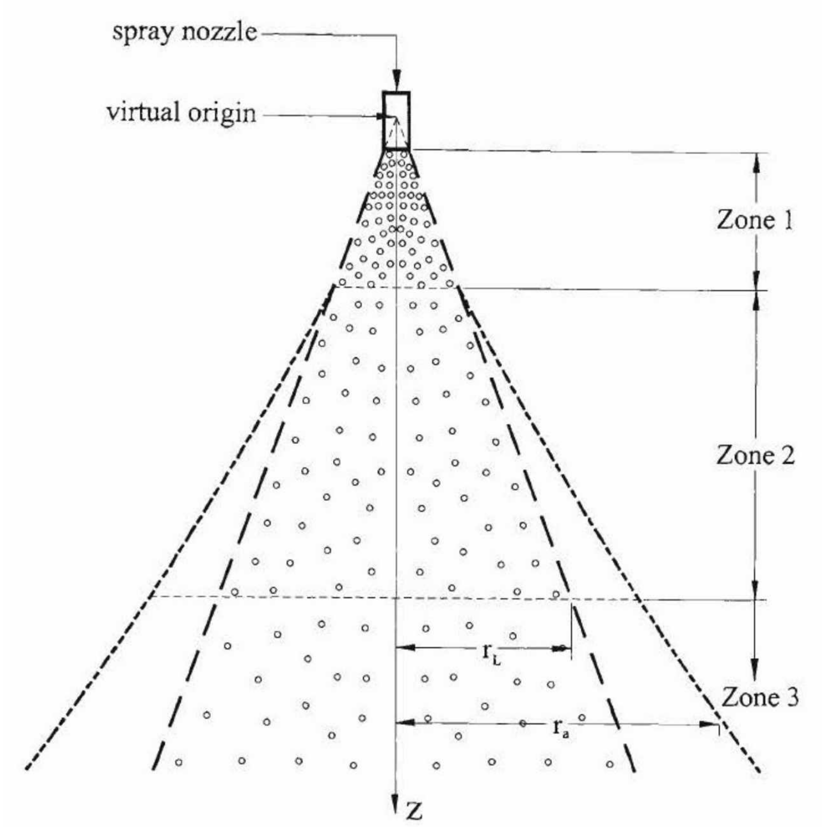

Figure B-9. Three Zones Spray Droplet Flow Models (r_L is the radius of the liquid droplet, r_a is the radius of the air entrainment) [Lui 2003]

Lui [Liu 2003] recommends use of the following equations, which are solved simultaneously to estimate the air entrainment in a particle plume in terms of the air entrainment and particle velocity in the core. The first equation is particle momentum flux rate of change as a function of drop height.

$$\dot{m}_p \frac{dv_p}{dz} = \frac{\left[B^* - K_l (v_p - v_0)^{4/3} C_s\right]}{v_p} \qquad \text{(B-8)}$$

where B^* is given by:

$$B^* = (\rho_p - \rho_a)\pi g \beta_0 v_0 {r_0}^2 \qquad \text{(B-9)}$$

For Equations (B-8) and (B-9), subscript 0 is evaluated at the outlet of the hopper or bucket, where the particles originate. Subscript p is evaluated for the particle. Subscript a is evaluated at air condition. v is the velocity. β_0 is the bulk solids volumetric fraction which is approximately equal to ρ_b/ρ_p, where ρ_b equals bulk density (i.e., loose poured condition), and ρ_p equals particle density. g is represents gravity and v_0 in Equations (B-8) and (B-9) can be expressed as:

$$v_0 = \frac{\dot{m}_p}{\rho_b \pi {r_0}^2} \qquad \text{(B-10)}$$

where r_0 is the radius of the hopper/bucket outlet. Note that K_l in Equation (B-8) is given by:

$$K_l = \frac{15}{2}\pi\beta_0 v_0 {r_0}^2 {\rho_a}^{1/3} {\mu_a}^{2/3} {d_p}^{-5/3} \tag{B-11}$$

where μ represents viscosity, and d is the diameter.

The second equation is air entrainment in a particle plume, which can be expressed in differential form as a function of the height z:

$$\frac{d}{dZ}(\pi {r_a}^2 v_a) = 2\pi {r_a}^2 \alpha v_a \tag{B-12}$$

where α is the entrainment constant, which may strongly influence the volume of air entrained in the free-fall particles. Subscript a is evaluated in the air stream as a function of drop height, Z. Bulk material properties may also affect the air entrained. α is equal to 0.021 for sand and 0.0196 for alumina.

For the third equation, the momentum flux of entrained air as a function of drop height is given by:

$$\frac{d}{dZ}(\rho_a \pi {r_a}^2 {v_a}^2) = \frac{K_l}{v_p}\left(v_p - v_a\right)^{4/3} C_s \tag{B-13}$$

where C_s is a dimensionless stream coefficient, intended to model the sum of the drag forces acting on a stream of particles:

$$C_s = \left(\frac{\rho_p - \rho_{b-core}}{\rho_p - \rho_a}\right)^{-4.7} \tag{B-14}$$

ρ_{b-core} is bulk density of the core in the particle plume and is given by:

$$\rho_{b-core} = \frac{\dot{m}_p \rho_a}{\pi {r_a}^2 v_p} \tag{B-15}$$

According to Liu [Liu 2003], Equations (B-8), (B-12) and (B-13) can be used to predict the air entrainment of a free-fall particle plume and provide information on air entrainment and particle velocity in the particle core (see Figure B-8).

As shown in Figure B-8 and Figure B-9, the plume spreads as the particles fall from the hopper or spray nozzle. The spreading angle θ is given by:

$$\theta_s = \mathrm{arcTan}\left[\frac{b}{Z+Z_0}\right] \tag{B-16}$$

where b is the particle plume radius and Z_0 is the height of virtual origin of the particle plume (see Figure B-10). The particle plume radius, b, in Equation (B-16) can be related to Z as:

$$b = 1.2\alpha\, Z \qquad \text{for a pure miscible plume} \tag{B-17}$$

$$b = 0.151\, Z \tag{B-18}$$

where α in Equation (B-17) is the entrainment constant relating to the induced fluid velocity in the surrounding that enters the plume. Equation (B-18) expresses the relationship between the Gaussian radius and the jet flow distance in the jet theory [Lui 2003].

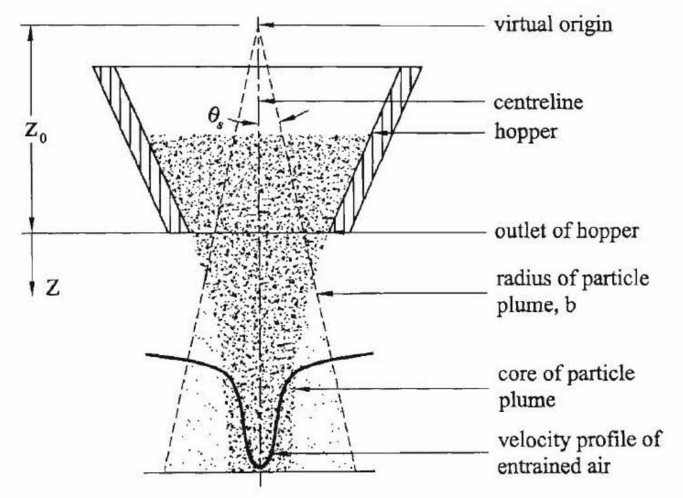

Figure B-10. Schematic of the Spreading Angle and Location of the Virtual Origin of Particle Plume, and Air Entrained Profile [Lui 2003]

Note that for an infinitely large room and still air, the air entrainment velocity calculated from these equations may not significantly affect the small particles in the bulk material, compared to the small room with turbulence created by air entrainment of the falling stream of particles. If the buoyancy force induced by the air entrainment is sufficient large to create turbulence in the surroundings, the small particles will remain suspend, particularly the particles less than 10 μm.

By using the theory above, Liu 2003 conducted experiments of free fall solids in a hopper. Liu 2003 uses 3 bulk materials in the experiments. Only two materials are of interest for this research and the properties of the materials are given in Table B-2.

Table B-2. Bulk Material Properties for Hopper Free-Fall Experiments [Lui 2003]

Material	Alumina	Sand
Particle Size (μm)	96	367
Bulk Density (kg/m^3)	1010	1400
Particle Density (kg/m^3)	2465	2803

To better characterize the particle velocities in Zone 1 (see Figure B-9), Lui 2003 compares the particle velocities in Zone 1 to the particle velocities in vacuum (see Figure B-11). As shown in Figure B-11 the particle velocities in Zone 1 are bounded by the particle velocity in vacuum. Using the velocity in vacuum is a good approximation. However, this approximation would not be valid in the other zones as drop height increases.

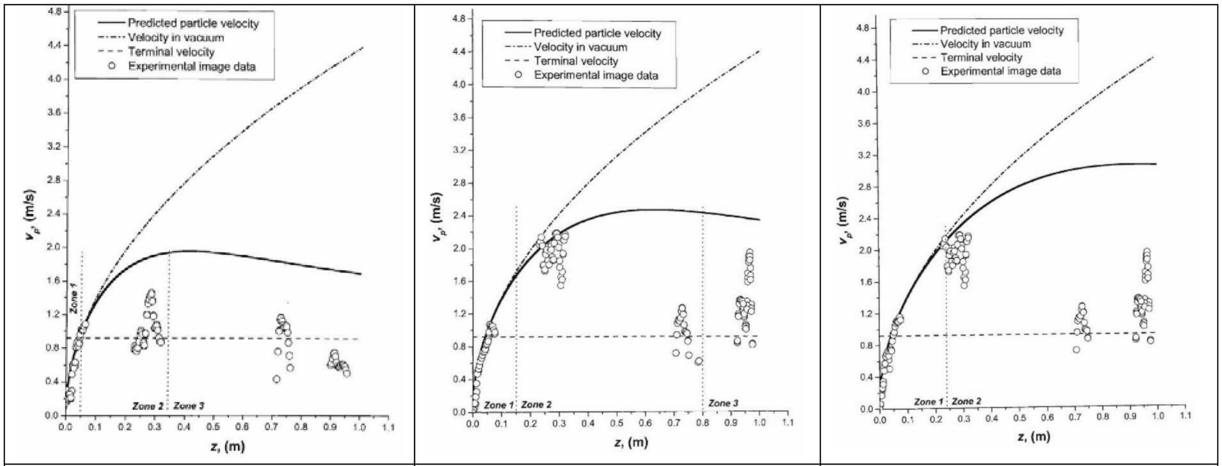

(a) $\dot{m}_p$=0.27g/s, r_0=1mm, α=0.0196 | (b) $\dot{m}_p$=1.1g/s, r_0=1.75mm, α=0.0196 | (a) $\dot{m}_p$=3.82g/s, r_0=2.5mm, α=0.0196

Figure B-11. Particle Velocities in Particle Stream of Alumina as a Function of Drop Height (Z), Mass Flow Rate ($\dot{m}_p$), Entainment Constant (α), and Outlet Radius (r_0)

To estimate air entrainment velocities from the falling stream, Lui [Liu 2003] uses a Gaussian distribution to describe the self-similarity behavior of buoyancy-driven flows, such as the miscible plume (see Figure B-12). Using the distribution formula in Figure B-13, the air entrained velocities measured from the experiments were correlated as shown in Figure B-14. In Figure B-14, increasing the drop height, Z, would increase air velocity and the spreading of the air stream radius. The functionalities of $\dot{m}_p$ to influence the air entrained velocities are plotted in Figure B-15. As shown in Figure B-15, increasing the mass flow rate results in an increase in both the air velocity at a given location and an increase in the radius of the stream. Furthermore, the spreading radius of the plume, as shown in Equation (B-16), can be defined as a function of drop height. Both Table B-3 and Table B-4 show the results of Equation (B-16) parameters estimated from the experiments [Lui 2003] for alumina and sand, respectively. As concluded by Lui 2003, the larger the spreading angle, the stronger the air entrainment in the surroundings of the particle main stream flow. The results further demonstrate that the virtual origin of the plume is a distance away from the outlet of the hopper as compared to the drop height. This suggests that the particle plume may not be fully developed. Based on these experiments, Lui 2003 estimated that the entrainment constant is on the order of 0.02 to 0.03 for the materials examined in the experiments.

Gaussian Velocity and Top-Hat Average Velocity Profile	Gaussian Distribution Formula
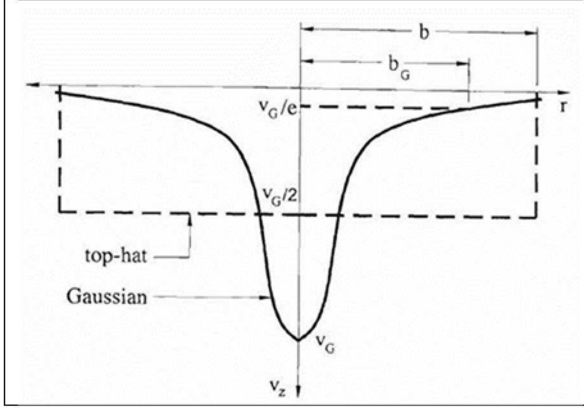	$v = v_G e^{-r^2/{b_G}^2}$ where v is the local velocity within the stream flow, r is the radius within the stream, v_G is the maximum velocity of the plume at the centerline, and b_G is the radius of the Gaussian distribution.

Figure B-12. Characteristic of Air Stream Velocities in Falling Particle Stream [Lui 2003]

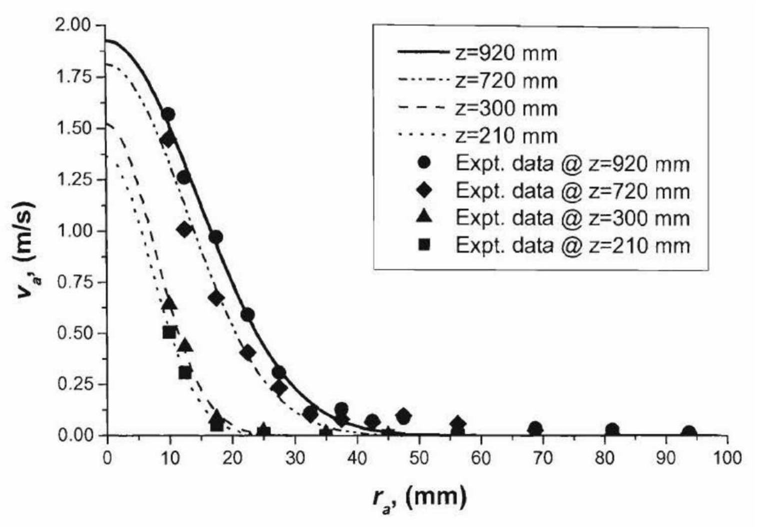

(a) Alumina @ $\dot{m}_p$=0.075 kg/s

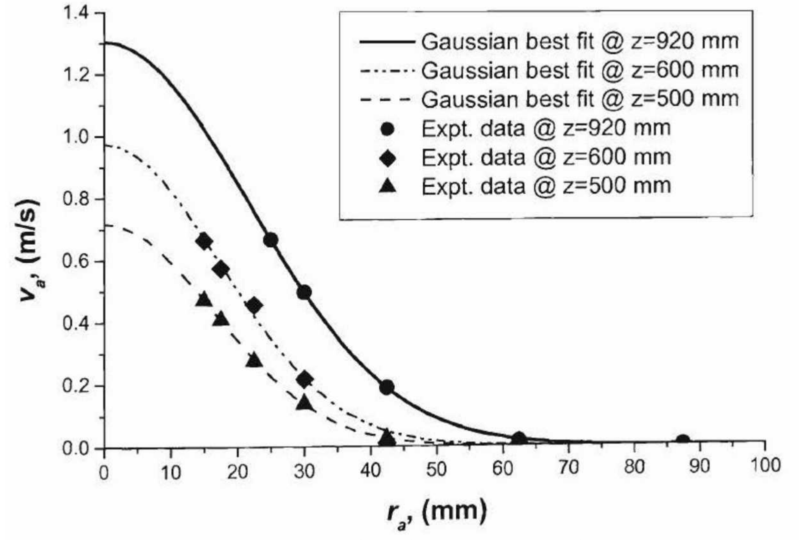

(b) Sand @ $\dot{m}_p$=0.0677 kg/s

Figure B-13. Air Entrained Velocities Profile as Function of Air Stream Radius (r_a)

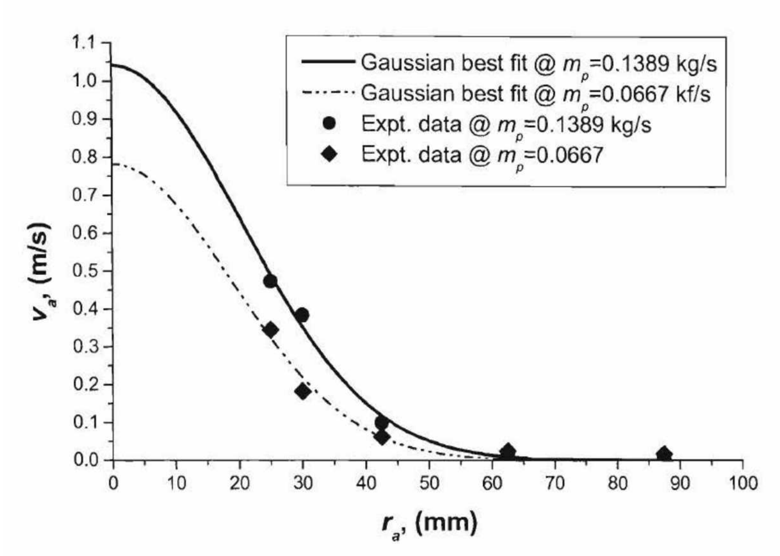

(a) Alumina @ Z=920 mm

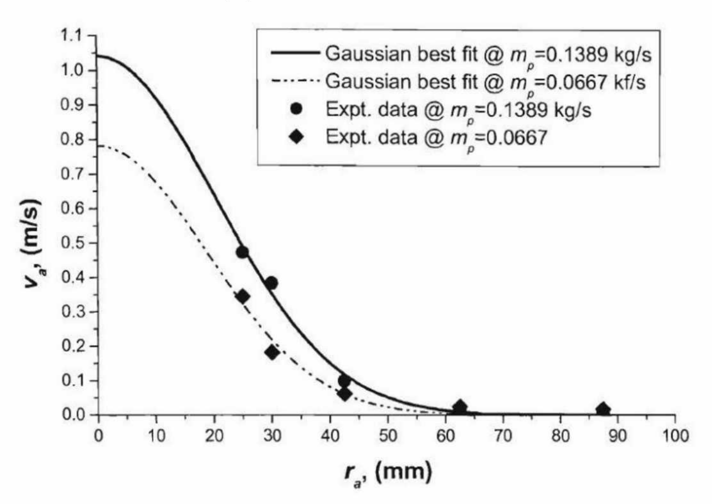

(b) Sand @ Z=720 mm

Figure B-14. Air Entrained Velocity Profiles as Function of Bulk Mass Flow Rate, $\dot{m}_p$

Table B-3. Equation (B-16) Parameters for Computing Spreading Angle as Functions of $\dot{m}_p$ and r_0 for Alumina

$\dot{m}_p$ (kg/s)	r_0 (m)	b (m)	θ_s(°)	Z_0(m)
0.0435	0.0075	0.0243 Z ±0.0120	1.392	-0.494
0.0606	0.0092	0.0231 Z ±0.0109	1.323	-0.472
0.0740	0.0091	0.0212 Z ±0.0098	1.214	-0.463
0.0995	0.0114	0.0250 Z ±0.0112	1.432	-0.448

Table B-4. Equation (B-16) Parameters for Computing Spreading Angle as Functions of $\dot{m}_p$ and r_0 for Sands

$\dot{m}_p$ (kg/s)	r_0 (m)	b (m)	θ_s(°)	Z_0(m)
0.0108	0.0035	0.0246 Z ±0.0108	1.409	-0.439
0.0667	0.0066	0.0267 Z ±0.0186	1.529	-0.697
0.1389	0.0091	0.0278 Z ±0.0194	1.590	-0.698

Other researchers also conducted experiments to examine the characteristics of the free-fall particle plume [Ansart 2009]. In these experiments (see Figure B-15), the powder was a silica gel with a particle density of 1000 kg/m^3; loose bulk density of 535 kg/m^3; particle size of 34 μm (d_{10}), 60 μm (d_{50}), and 97 μm (d_{90}); silo diameter of 10 mm, which generates a mass flow of 1.5 g/s; and silo diameter of 20 mm, which generates a mass flow of 15 g/s. These researchers examined the radial spreading of the plume and air entrainment. Figure B-16 shows a schematic of the plume spreading based on the experimental results. As shown in this figure, between a drop height of 500 mm and 1070 mm, jet expansion occurred, yielding a plume that spread with a slope of approximately 6.3% (reported as a mass fraction). 83% of the mass remains inside the 40-mm cone, and 17% is outside of the cone that could be suspended. In addition, these researchers also measured the horizontal particle velocity from the experiments (see Figure B-17). As shown in Figure B-17, the mean horizontal particle velocity from the center of the particle stream (or jet) moves from the center to the edge. In fact, the figure shows that the particles on the right side of the axis have a positive horizontal velocity and the particles on the left side a negative velocity. The slope of the curve decreases with increasing drop height, which means that the horizontal migration decreases with the drop height corresponding to the flattening of the particle plume. The same researchers also examined the effect of an obstruction in a free fall of steady stream particles [Ansart 2011]. In the experiments using silica gel with particles between 40 to 60 μm, particle density of 1000 kg/m^3, and loose bulk density of 550 kg/m^3, the obstruction object was a stainless tube installed below the silo which was made of PMMA (see Figure B-15). Figure B-18 shows the radial particle profile at a 50 cm drop height and a particle mass flow rate of 0.9/s. As shown in this figure, the particle velocity reduces due to the presence of tubing (obstruction). The authors concluded that the tube slows down the particles and concentrates the plume by friction forces, and reduces airborne particles [Ansart 2011]. For Figure B-18, the experiment could reduce the width of the plume by 14%.

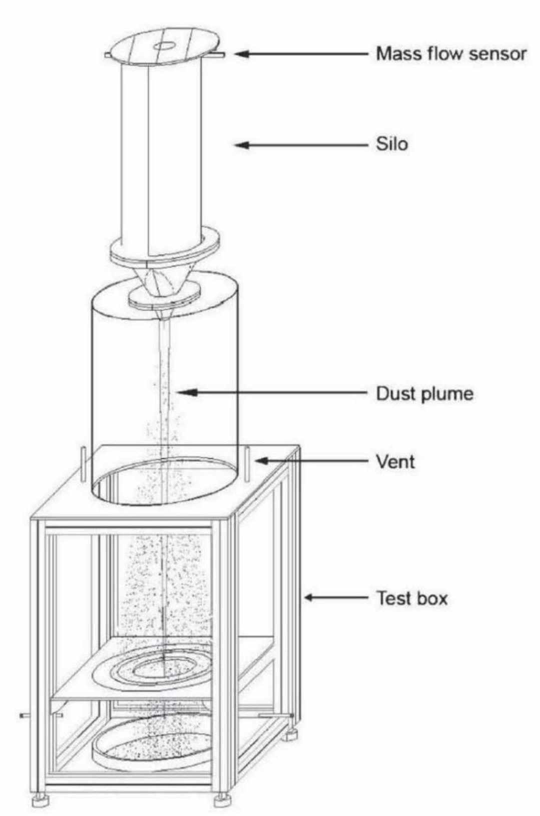

Figure B-15. Schematics of Experiments Set-Up for Free Fall Stream of Powder [Ansart 2009]

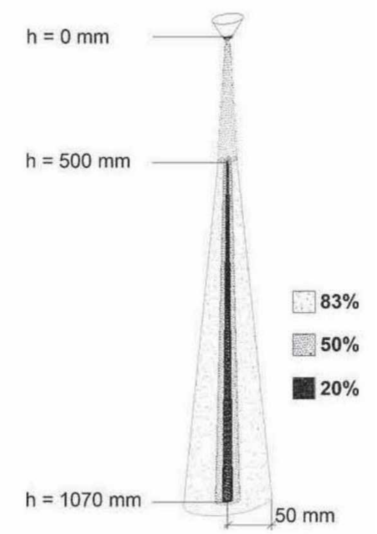

Figure B-16. Schematic of Plume Spread, Percentage Reported as Mass Fraction [Ansart 2009]

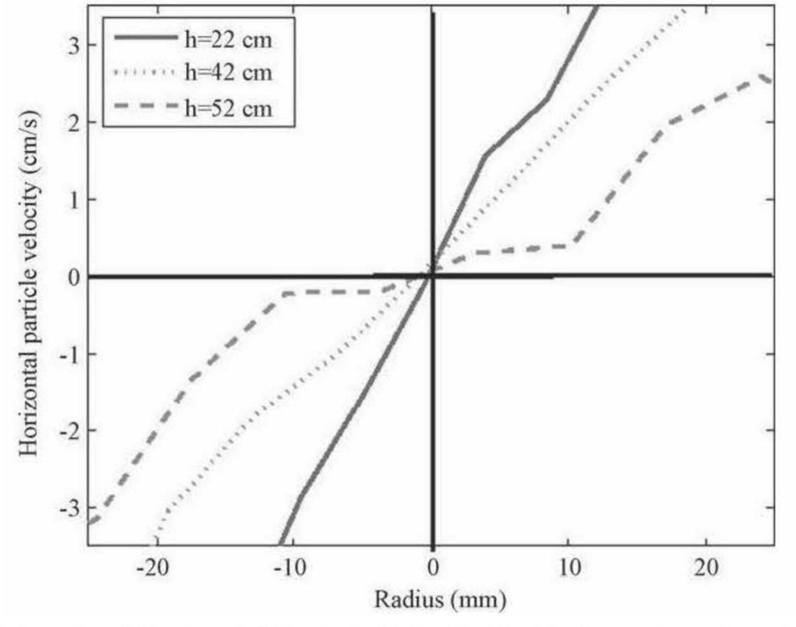

Figure B-17. Determined Horizontal Particle Velocity Profile from Experiments [Ansart 2009]

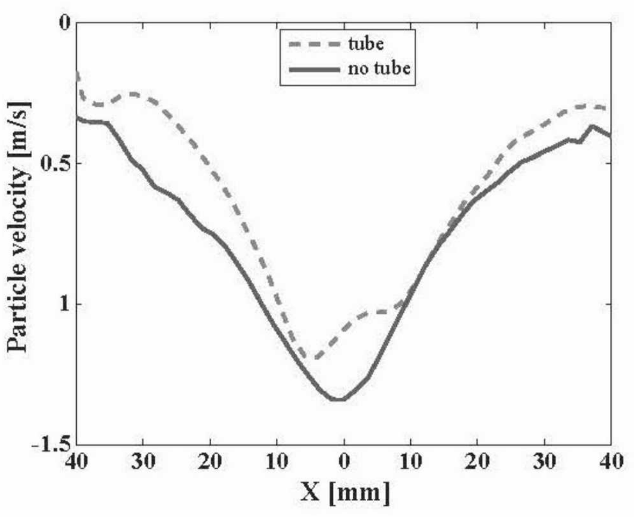

Figure B-18. Particle Velocity Profile as Function of X, Radial Distance from Centerline of Particle Stream at Mass Flow Rate of 0.9/s and Drop Height of 50 cm [Ansart 2011]

In the above studies, researchers investigated a free fall stream of particles to estimate air entrainment and particle velocities. No attempts were made to estimate or calculate the number of airborne particles. Perhaps, the particle size ranges in the experiments are larger, on the order of 10 to 100 μm. The following researchers measured the respirable dust from low mass powder samples [O'Shaughnessy 2012]. In this research, [O'Shaughnessy 2012] used a low mass dustiness tester, as shown in Figure B-19, to measure small quantities of free fall nanometer powder resulting from a single drop of 15 mg. As shown in this figure, the 400-ml glass jar at the end of the tubing was used to collect the falling powder. An aerodynamic particle sizer was used to measure the particle size distribution in the pipe by particle counting in 51 size channels ranging from 0.5 to 20 μm per second and a total volumetric flow rate of 5 l/minute.

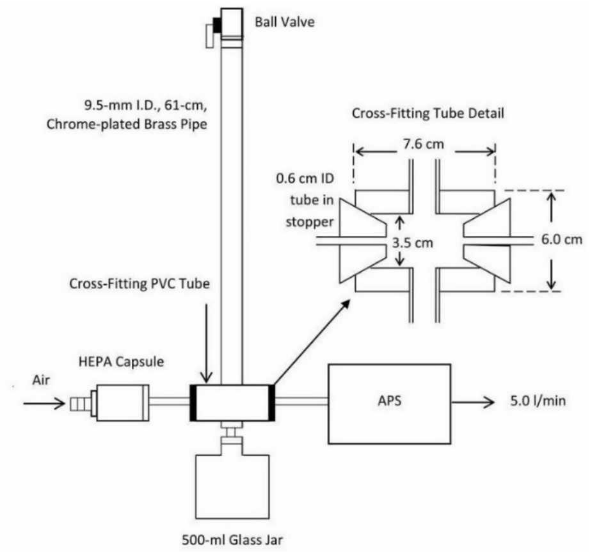

Figure B-19. Dustiness-Test Apparatus [O'Shaughnessy 2012]

The powders used in the experiments include those in Table B-5. In this table, the medium size of the powders, in nanometers, is reported, as well as, mass and bulk densities, and moisture content. Table B-6 shows the resulting diameters of the falling powder, corresponding geometric standard deviations, and respirable dustiness fraction. As shown in this table, the aerosol size distribution indicates that the particle distribution produced by this test yielded many micron-sized particles from nano-powders due to the agglomeration effect. As particle size decreases to micron sizes, attractive forces, such as van der Waals, electrostatic and covalent, increase the chances for agglomeration to occur. Also shown in this table is that the smaller particles are expected to develop smaller agglomerates which will settle more slowly to allow capture by measuring devices. Based on its fluffiness, SiO_2 tends to yield a higher respirable dustiness.

Table B-5. Tested Powder Properties [O'Shaughnessy 2012]

Powder	Medium Size (nm)	Mass Density (g/cc)	Bulk Density (g/cc)	Moisture Content (%)
Al_2O_3	10	3.9	0.24	0.05
Al_2O_3	50	3.9	1.28	0.07
Carbon black	14	2.0	0.56	0.07
Cu	25	8.9	0.25	0.01
Fe_2O_3	35	5.2	1.20	0.70
SiO_2	20	2.2	0.03	0.20
TiO_2	5	4.3	0.26	1.08
TiO_2	21	4.3	0.12	0.19

Table B-6. Respirable Dustiness Mass Fraction in mg/kg and Falling Powder Characteristics [O'Shaughnessy 2012]

Powder	Medium Size (nm)	Count Median Diameter (µm)	Mass Median Diameter (µm)	Geometric Standard Deviation (µm)	Respirable Dustiness (mg/kg)
Al_2O_3	10	3.9	0.24	0.05	40.4±0.7
Al_2O_3	50	3.9	1.28	0.07	16.5±1.5
Carbon black	14	2.0	0.56	0.07	42.9±6.0
Cu	25	8.9	0.25	0.01	3.9±1.3
Fe_2O_3	35	5.2	1.20	0.70	8.1±0.8
SiO_2	20	2.2	0.03	0.20	121.4±14.6
TiO_2	5	4.3	0.26	1.08	60.4±5.7
TiO_2	21	4.3	0.12	0.19	45.3±8.5

APPENDIX C. SELECTED FINAL TIME SNAPSHOT OF THE CONTAINER SIMULATION

This appendix provides the selected final time snapshot image for the containment simulation. Legend explanation for each image are:

- For drop, they are drop height and angle of impact: zero degree means upright position.
- For puncture, they are the impact speed, free movement or being fixed at the wall, and the location of the impact of the container.

C.1. 7A (55-gal) Drum Drop

Content Type: CS

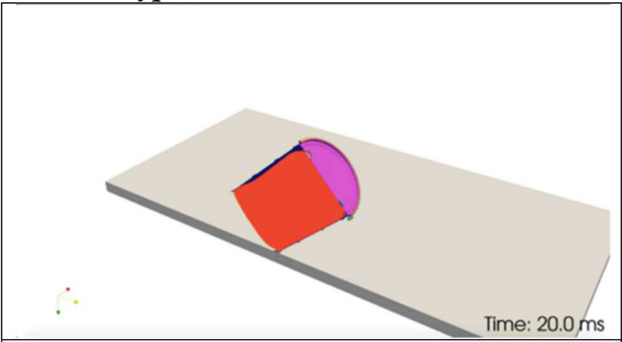	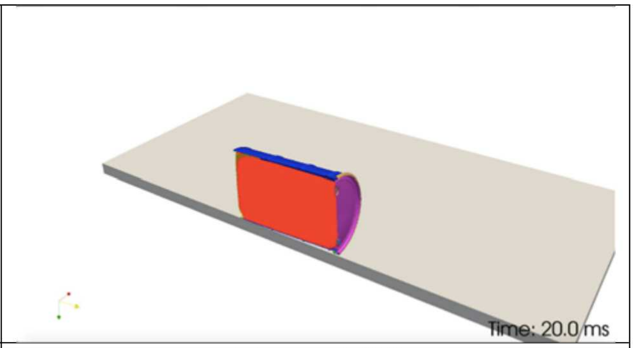
2.5 m and 45°	**2.5 m and 90°**
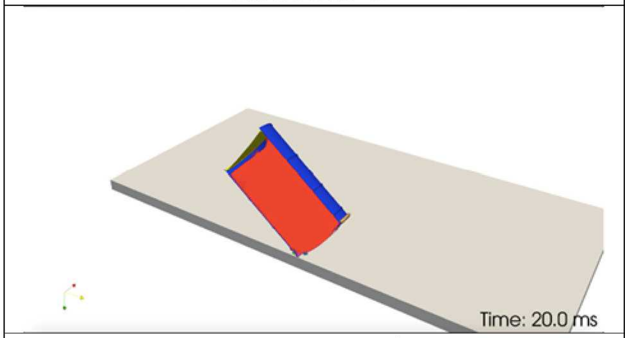	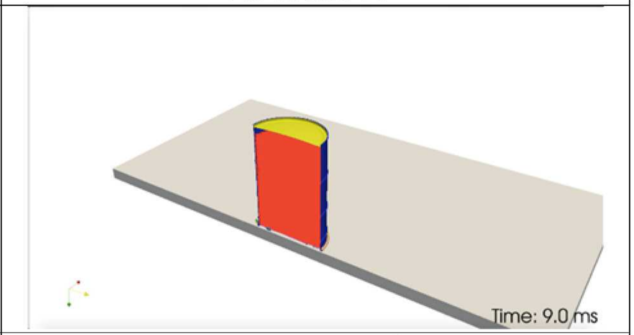
2.5 m and 135°	**2.5 m and 180°**
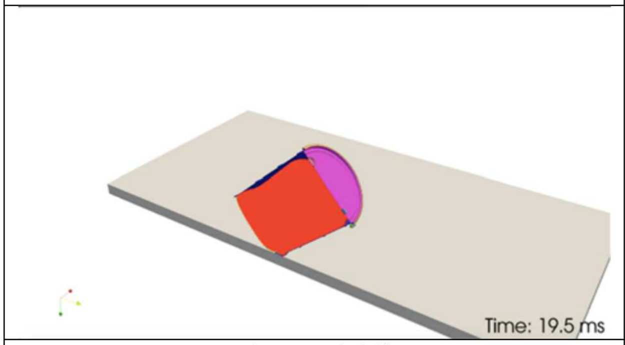	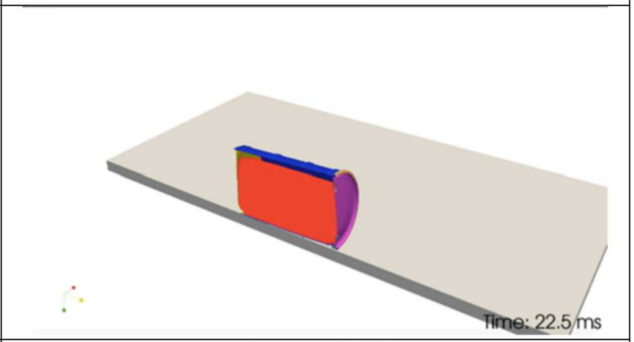
5 m and 45°	**5 m and 90°**

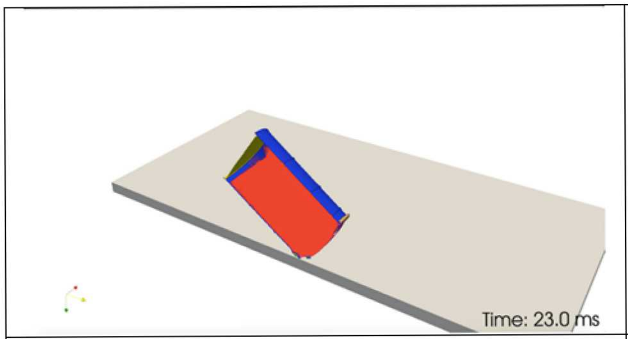

5 m and 135°

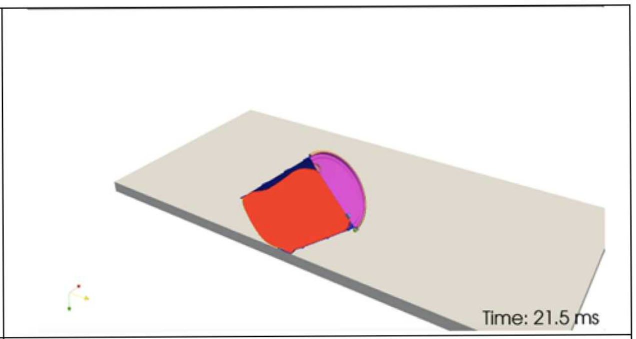

10 m and 45°

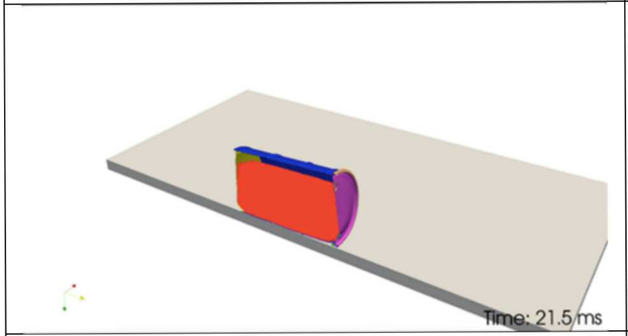

10 m and 90°

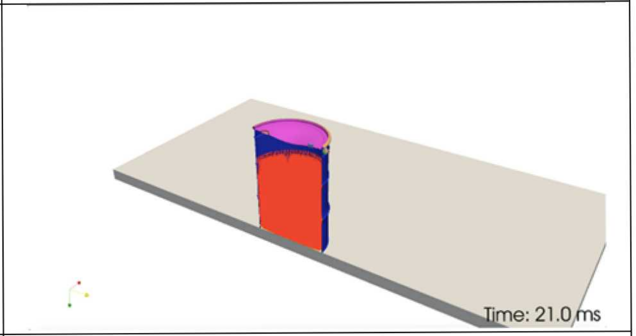

20 m and 0°

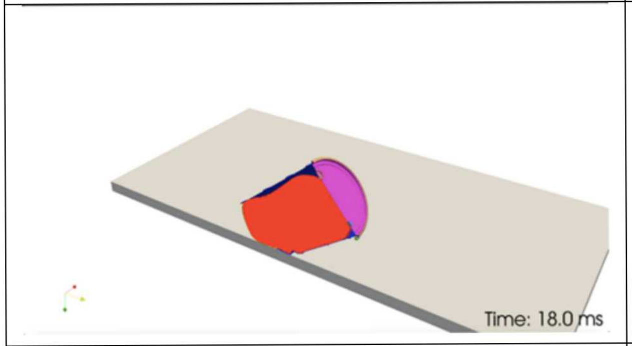

20 m and 45°

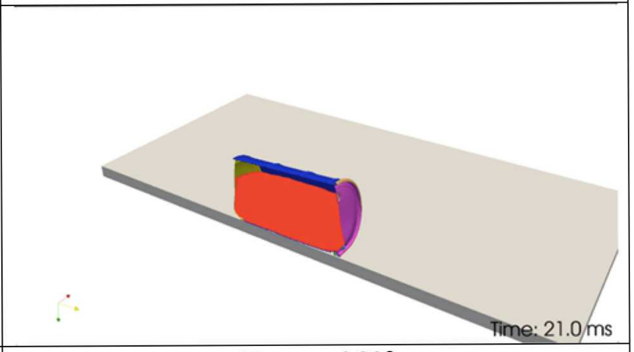

20 m and 90°

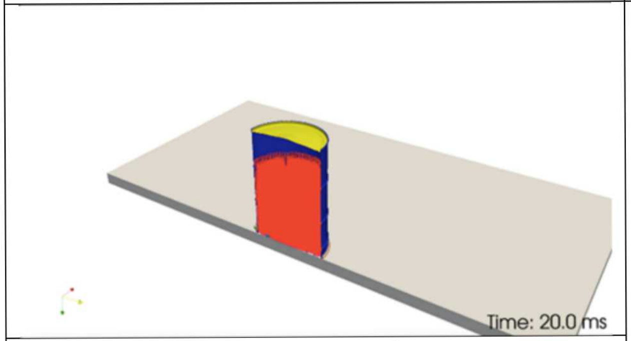

20 m and 180°

Content Type: HD

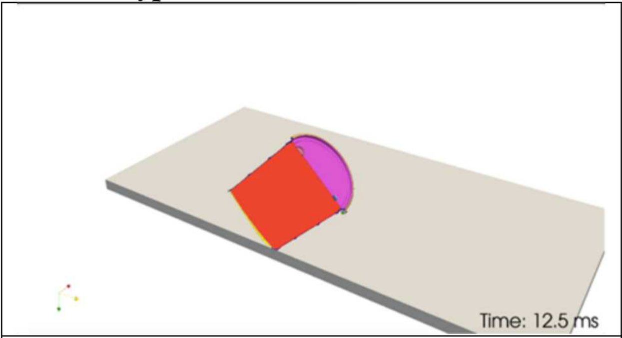

2.5 m and 45°

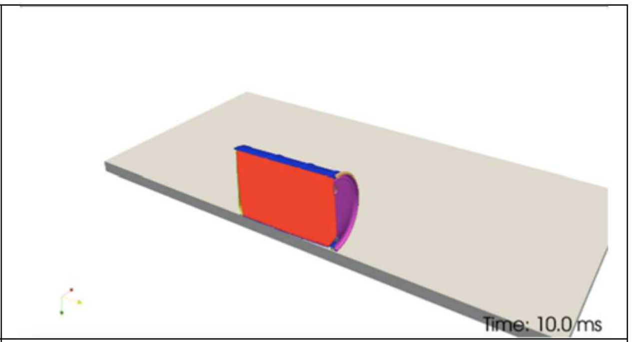

2.5 m and 90°

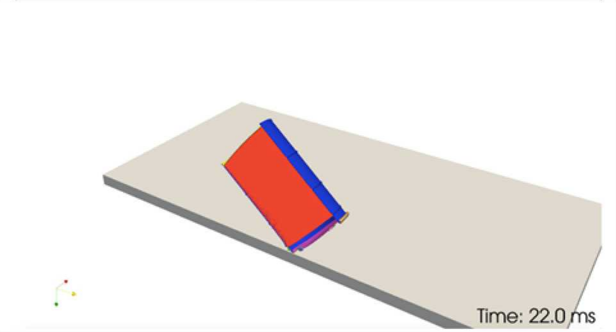

2.5 m and 135°

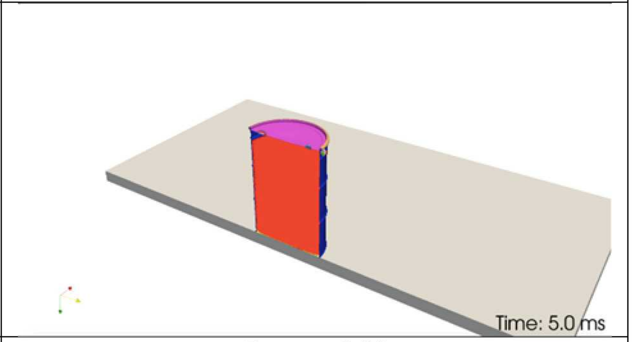

5 m and 0°

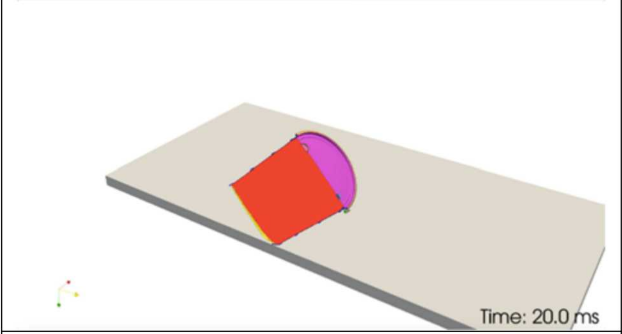

5 m and 45°

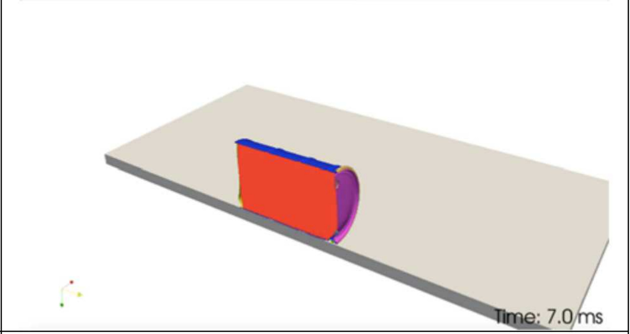

5 m and 90°

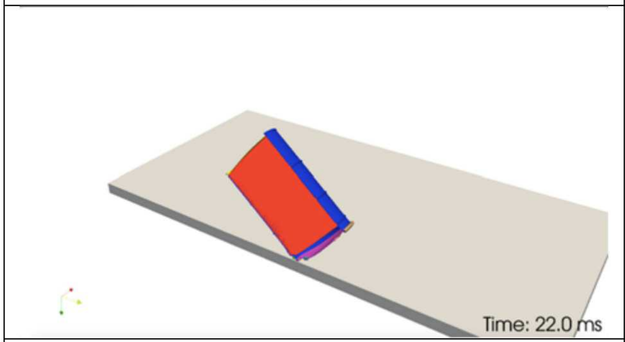

5 m and 135°

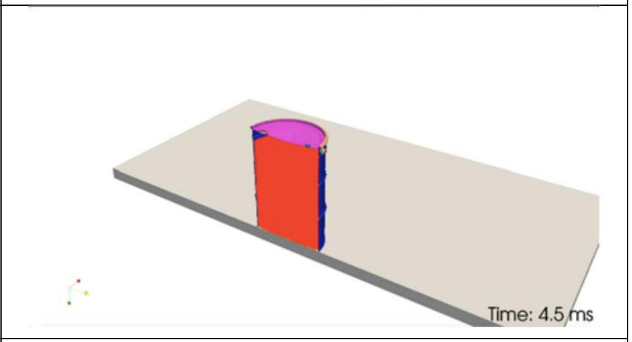

10 m and 0°

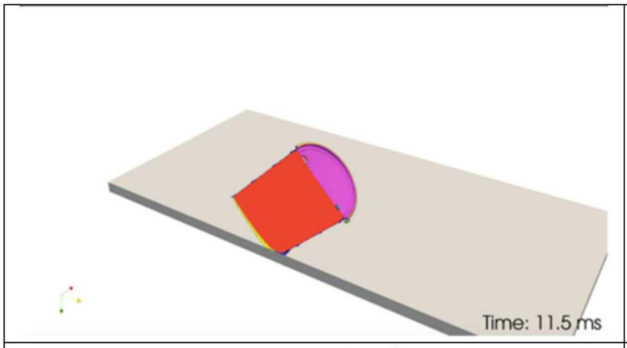	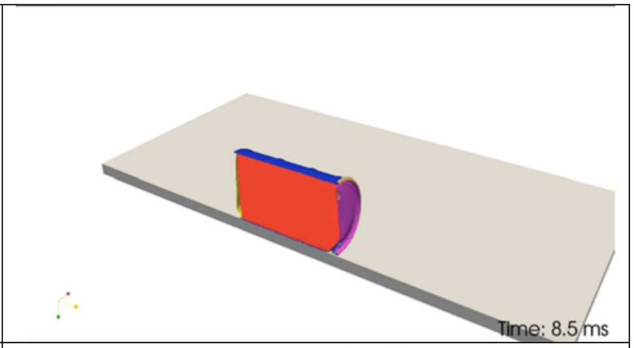
10 m and 45°	**10 m and 90°**
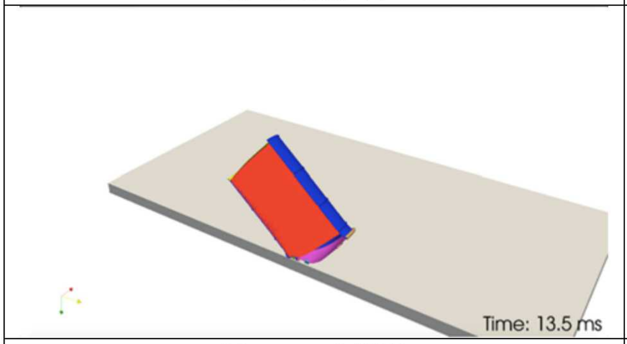	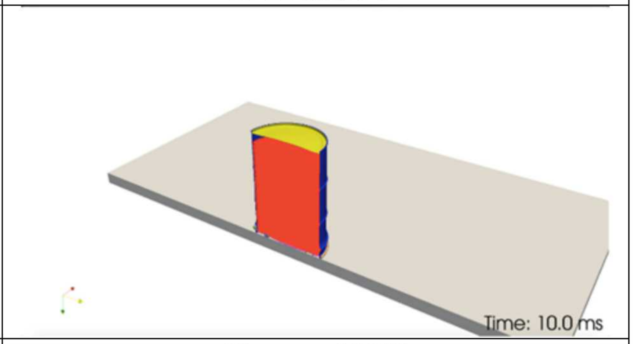
10 m and 135°	**10 m and 180°**
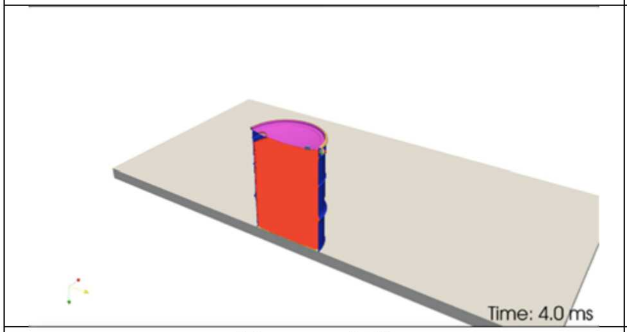	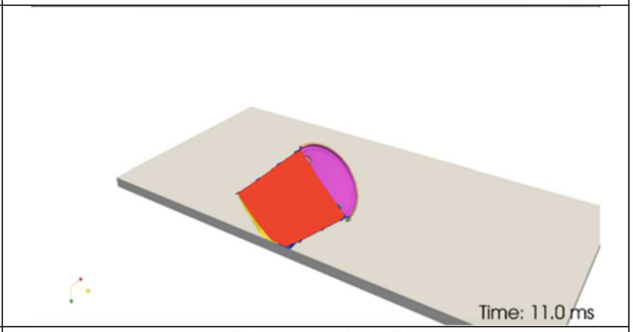
20 m and 0°	**20 m and 45°**
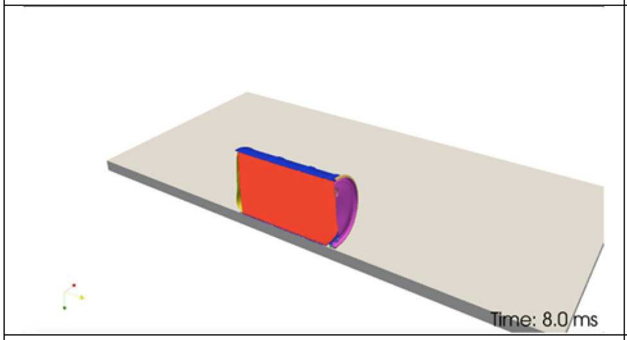	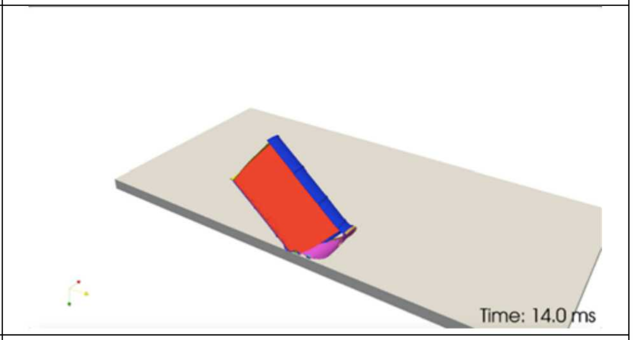
20 m and 90°	**20 m and 135°**

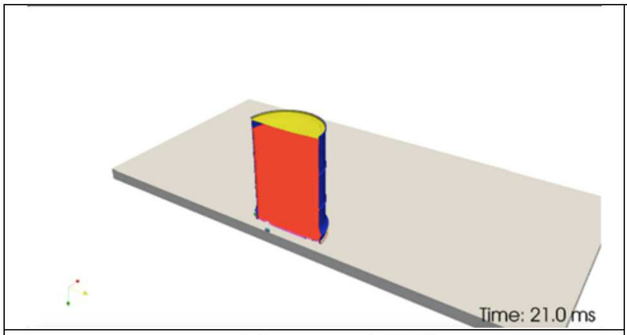	
20 m and 180°	

Content Type: SI

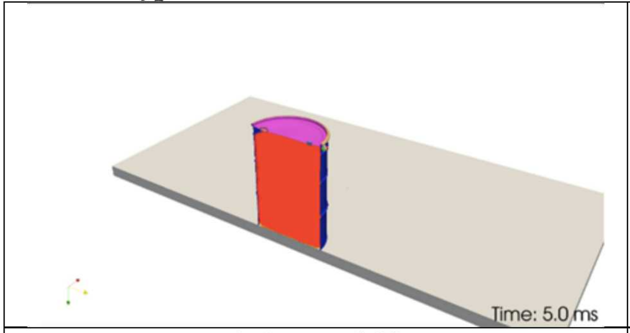	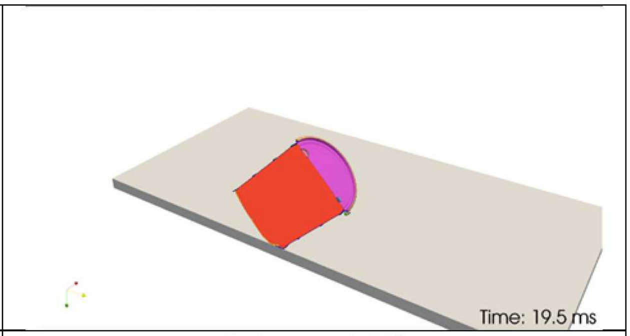
2.5 m and 0°	**2.5 m and 45°**
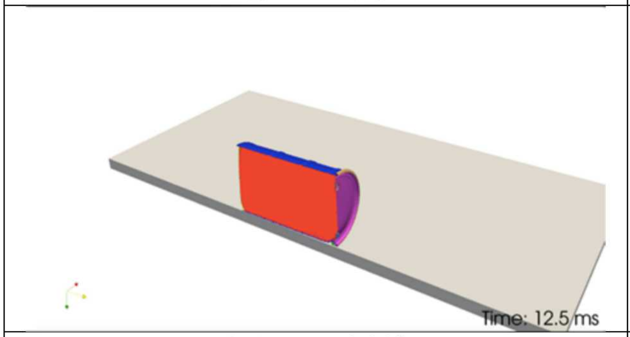	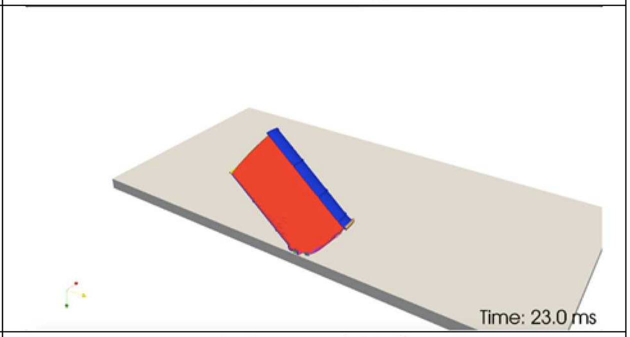
2.5 m and 90°	**2.5 m and 135°**
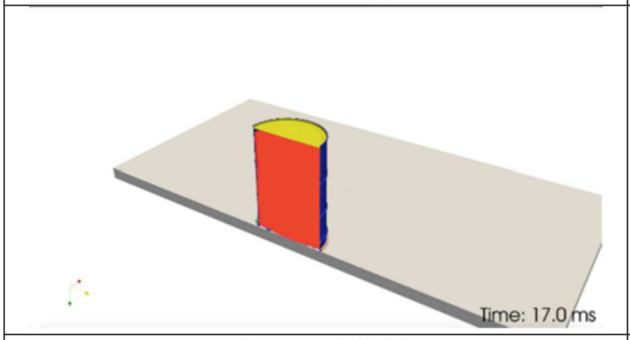	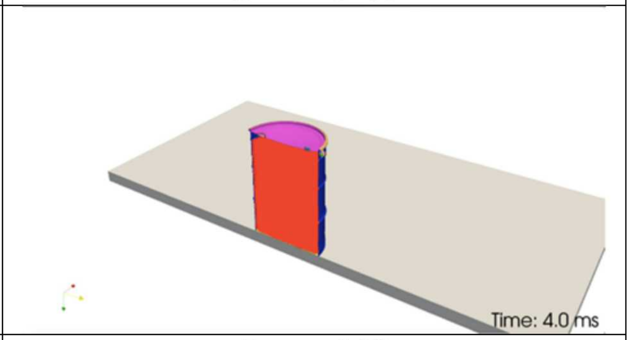
2.5 m and 180°	**5 m and 0°**

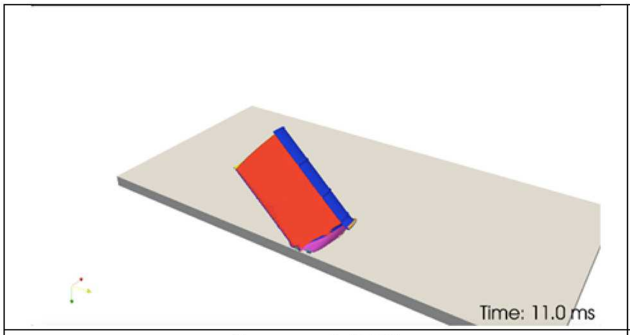	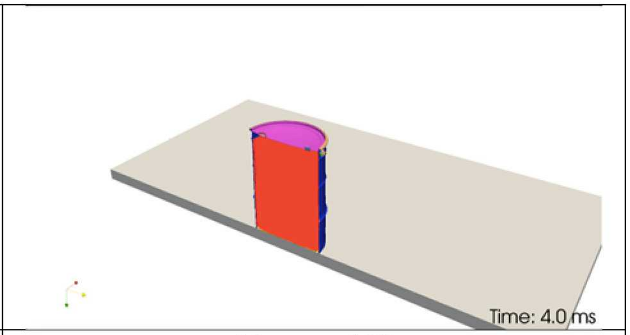
5 m and 135°	**10 m and 0°**
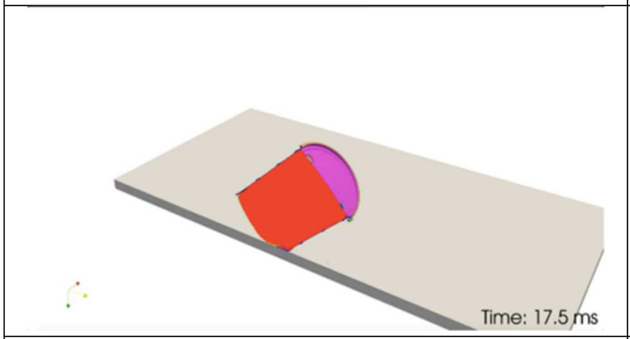	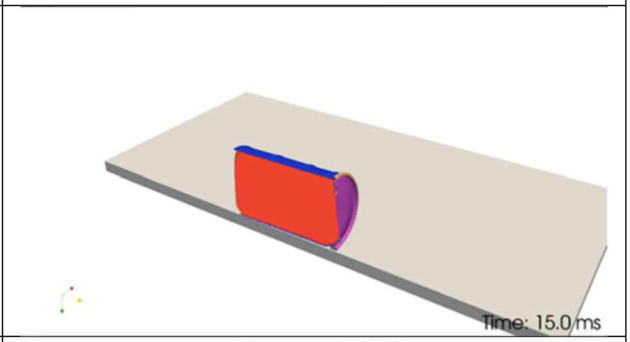
10 m and 45°	**10 m and 90°**
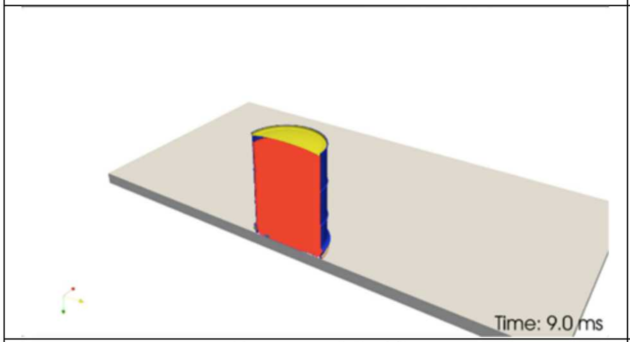	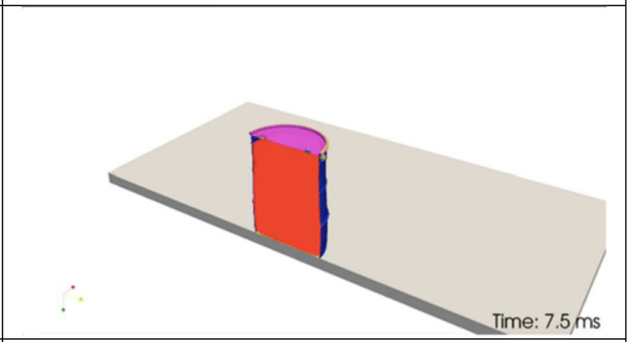
10 m and 180°	**20 m and 0°**
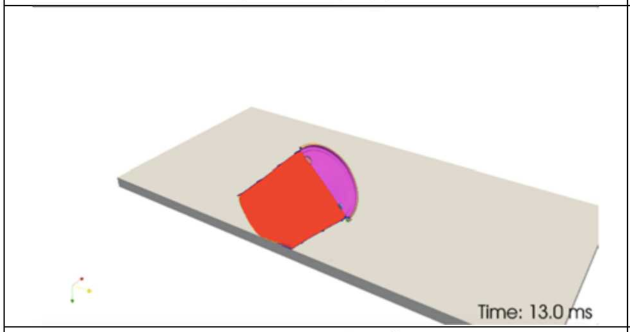	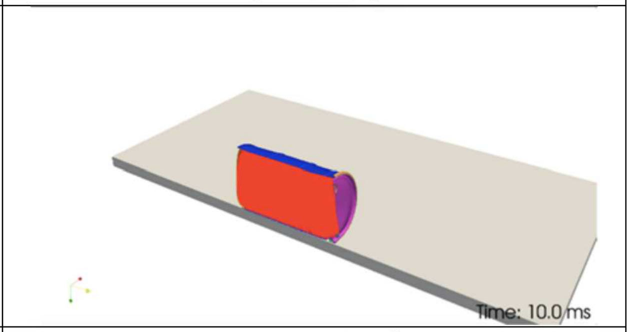
20 m and 45°	**20 m and 90°**

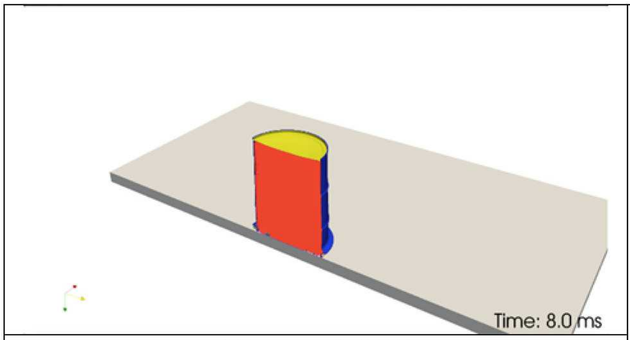	
20 m and 180°	

C.2. 7A (55-gal) Drum Puncture

Content Type: CS

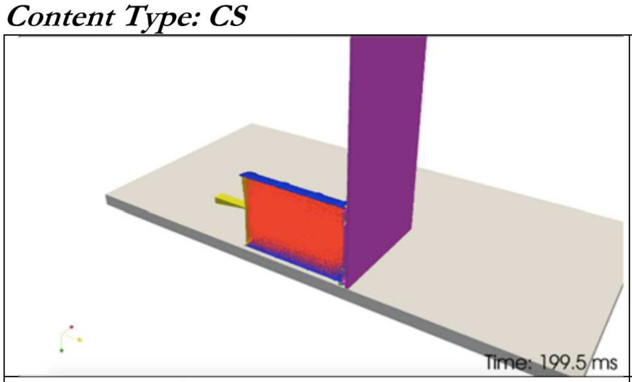	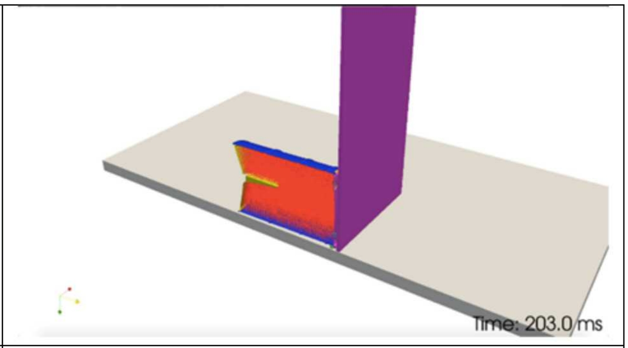
0.5 m/s, fixed and center bottom	**2.5 m/s, fixed and center bottom**
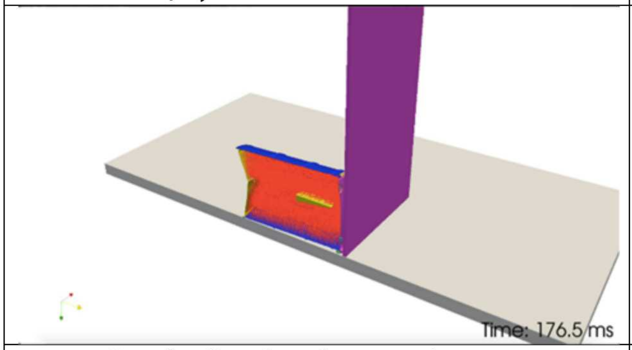	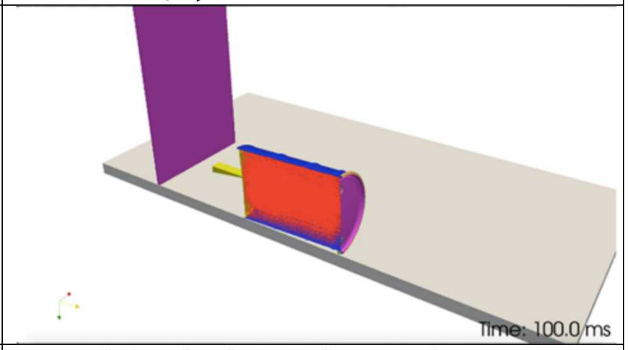
5 m/s, fixed and center bottom	**0.5 m/s, free and center bottom**
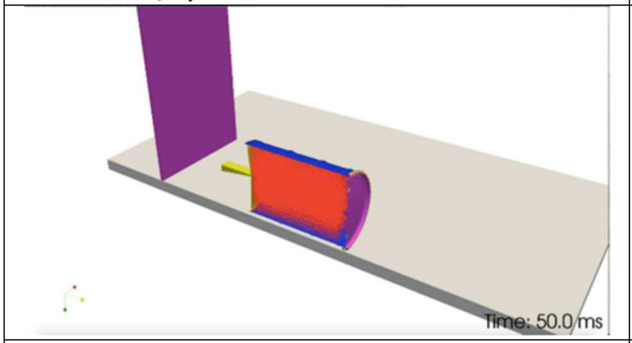	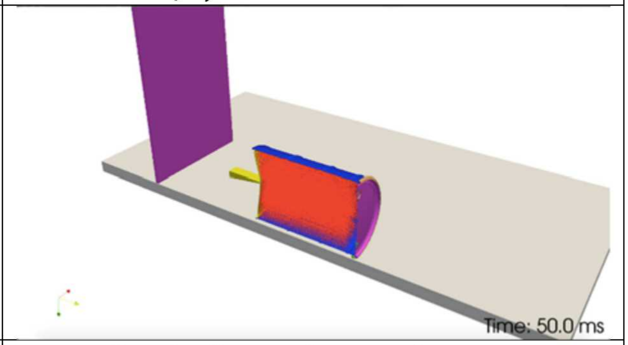
2.5 m/s, free and center bottom	**5 m/s, free and center bottom**

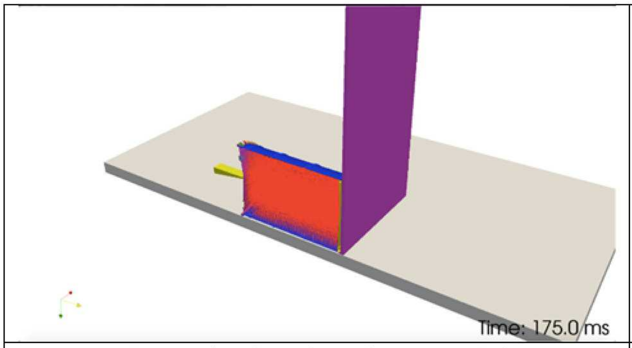	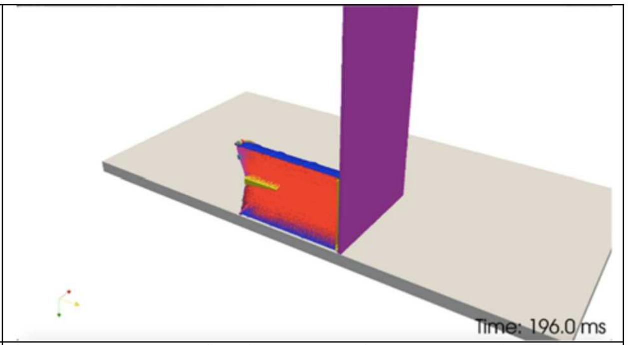
0.5 m/s, fixed and center lid	**2.5 m/s, fixed and center lid**
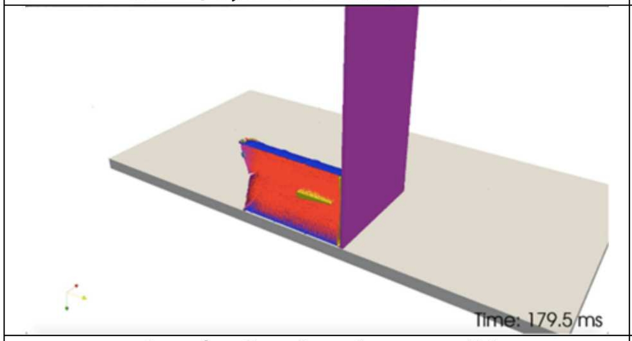	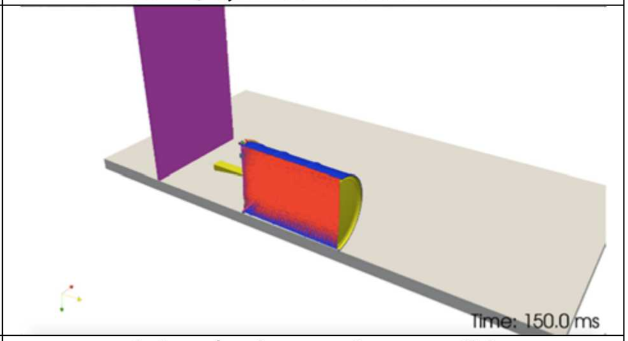
5 m/s, fixed and center lid	**0.5 m/s, free and center lid**
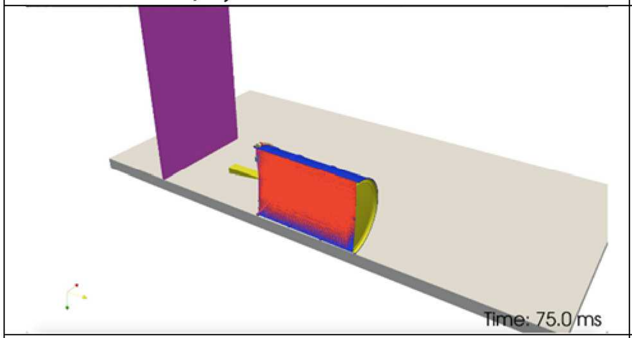	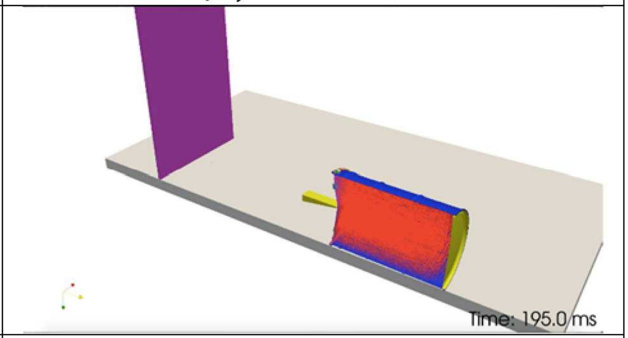
2.5 m/s, free and center lid	**5 m/s, free and center lid**
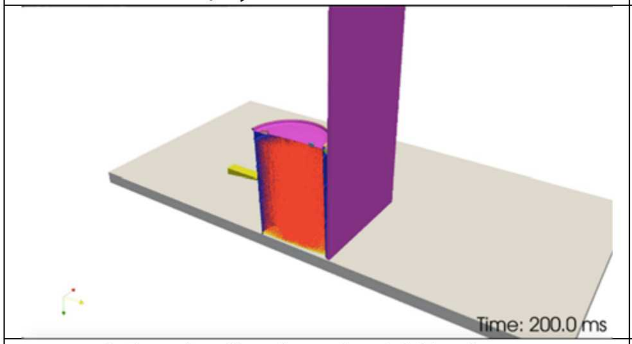	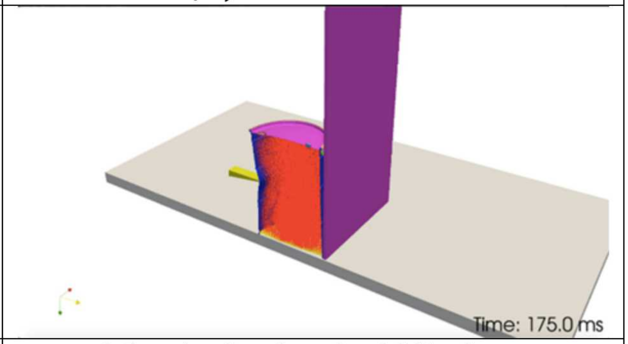
0.5 m/s, fixed and middle drum	**2.5 m/s, fixed and middle drum**

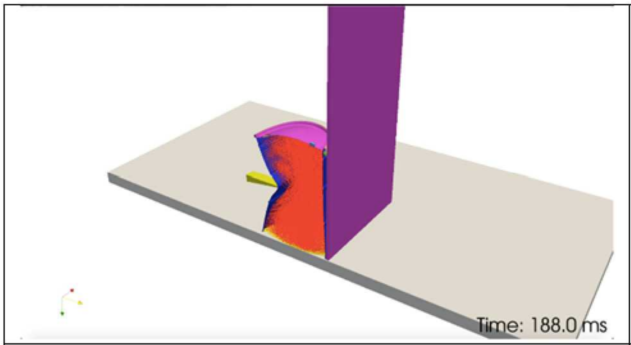

5 m/s, fixed and middle drum

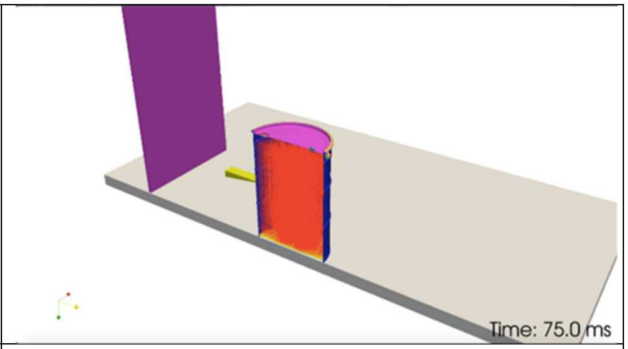

0.5 m/s, free and middle drum

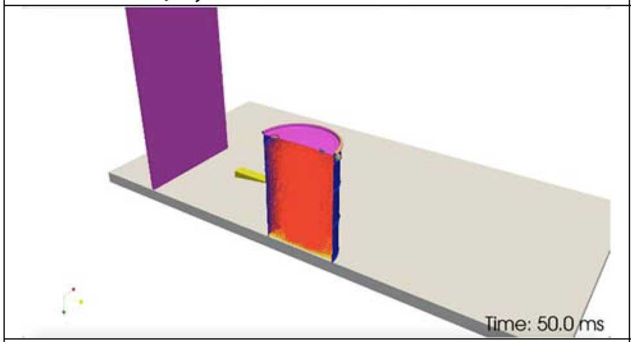

2.5 m/s, free and middle drum

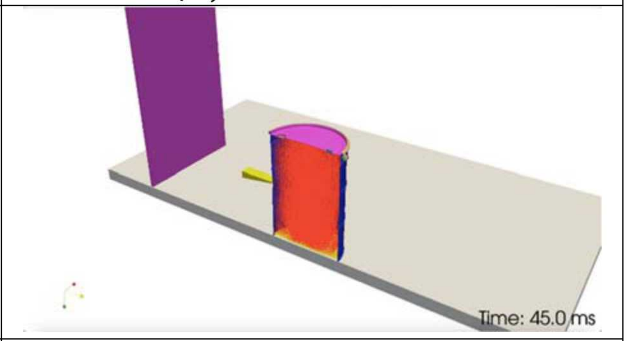

5 m/s, free and middle drum

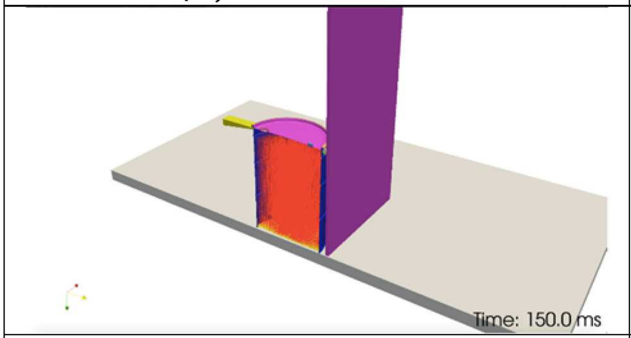

0.5 m/s, fixed and top near lid

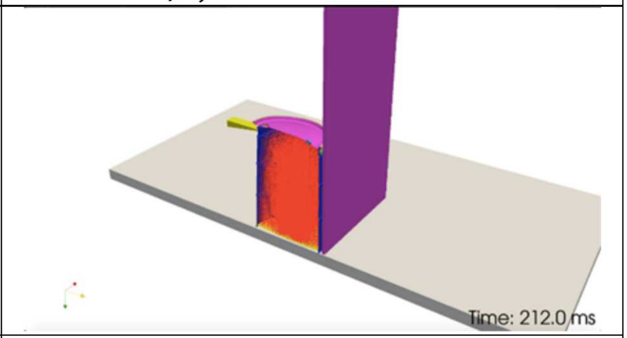

2.5 m/s, fixed and top near lid

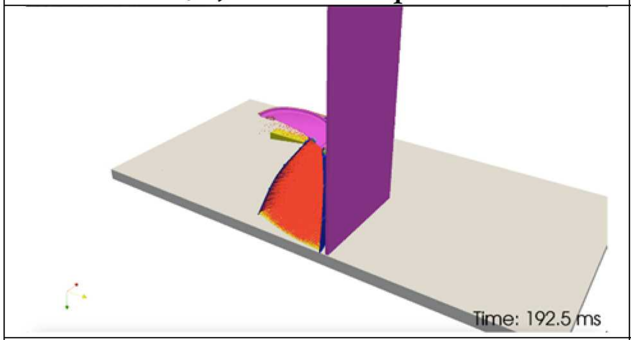

5 m/s, fixed and top near lid

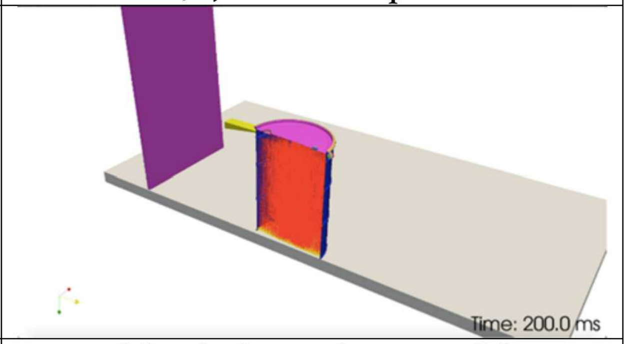

0.5 m/s, free and top near lid

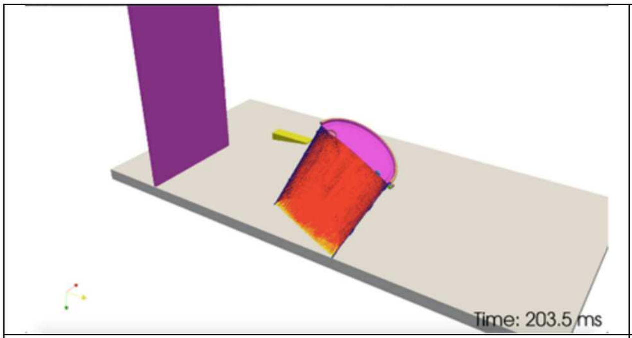	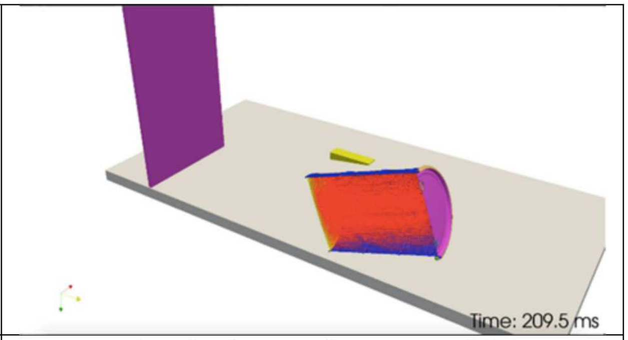
2.5 m/s, free and top near lid	**5 m/s, free and top near lid**

Content Type: HD

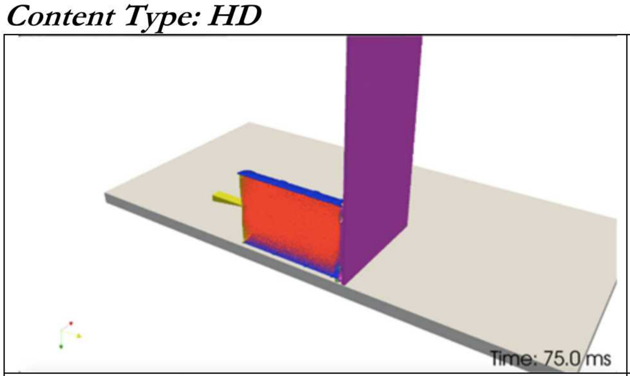	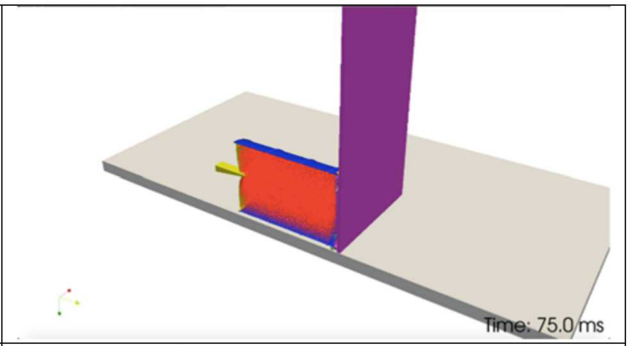
0.5 m/s, fixed and center bottom	**2.5 m/s, fixed and center bottom**
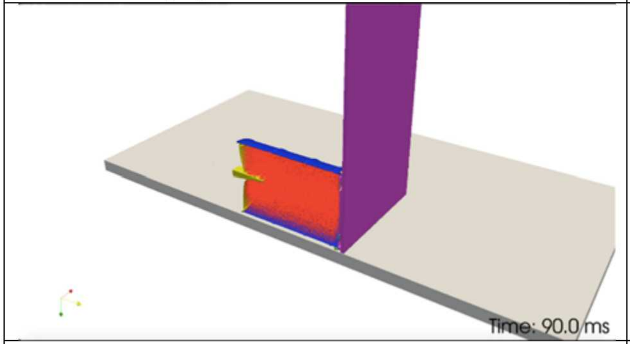	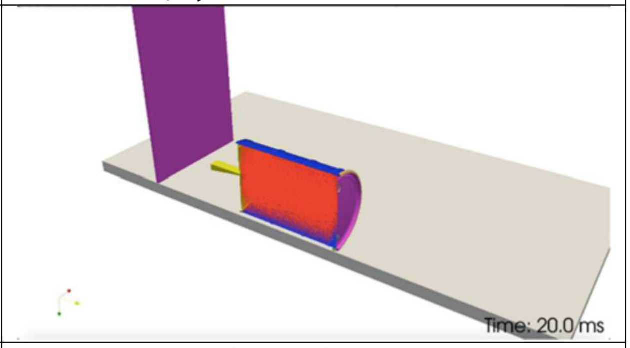
5 m/s, fixed and center bottom	**0.5 m/s, free and center bottom**
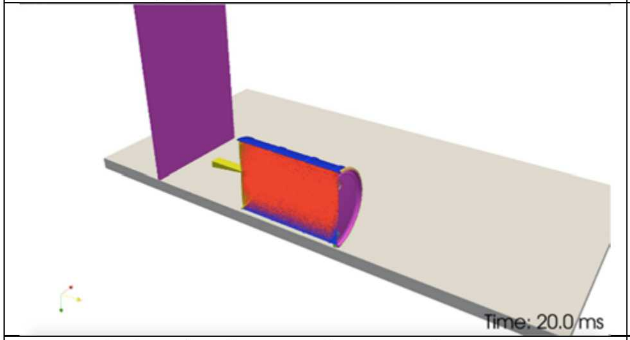	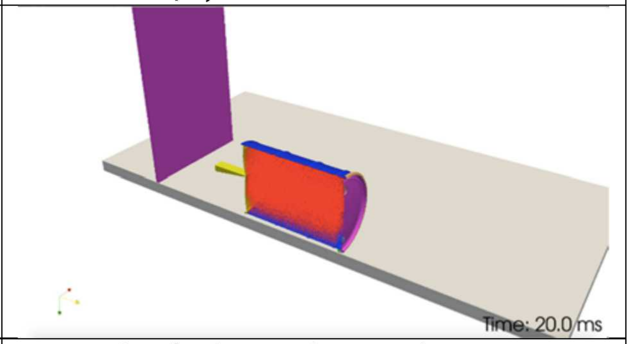
2.5 m/s, free and center bottom	**5 m/s, free and center bottom**

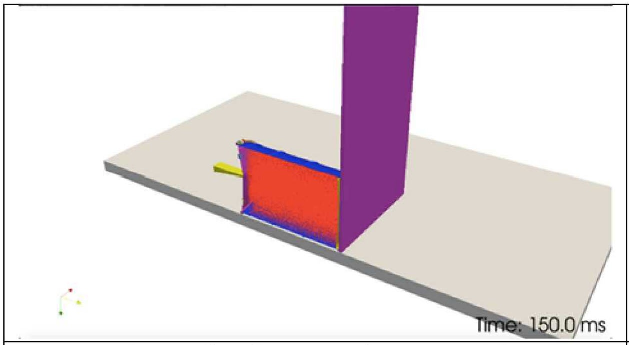	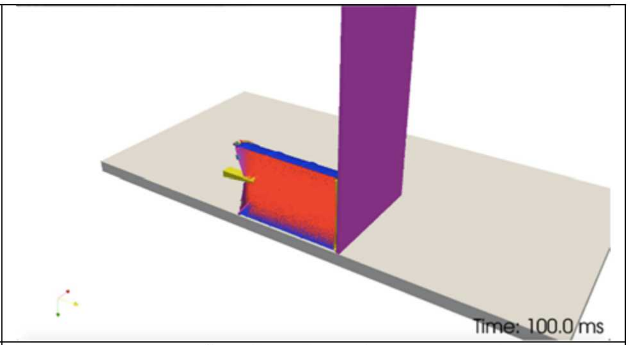
0.5 m/s, fixed and center lid	**2.5 m/s, fixed and center lid**
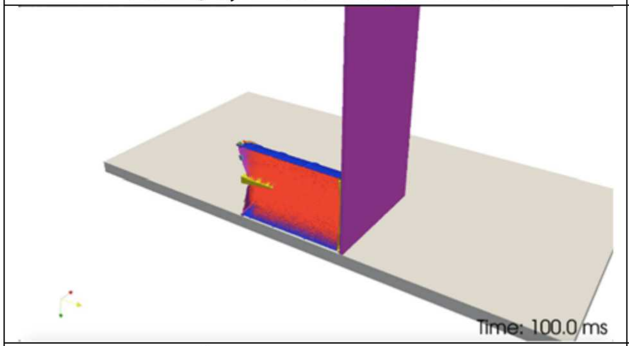	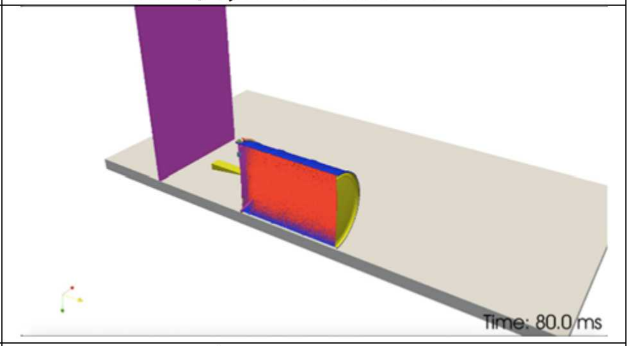
5 m/s, fixed and center lid	**0.5 m/s, free and center lid**
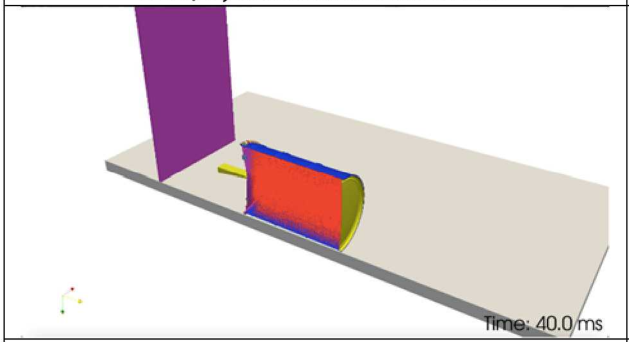	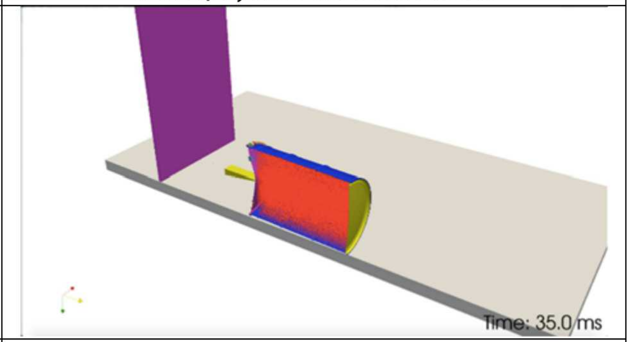
2.5 m/s, free and center lid	**5 m/s, free and center lid**
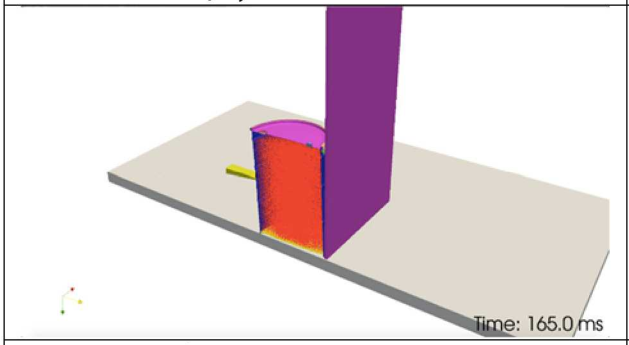	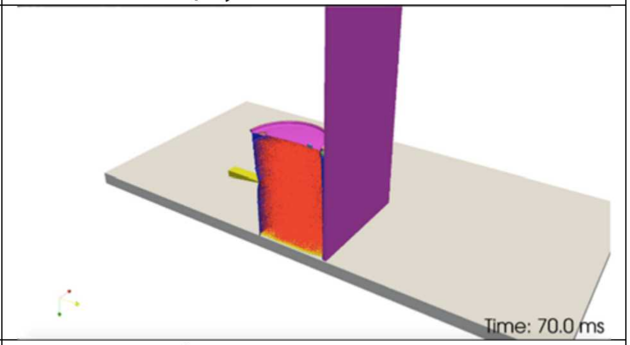
0.5 m/s, fixed and middle drum	**2.5 m/s, fixed and middle drum**

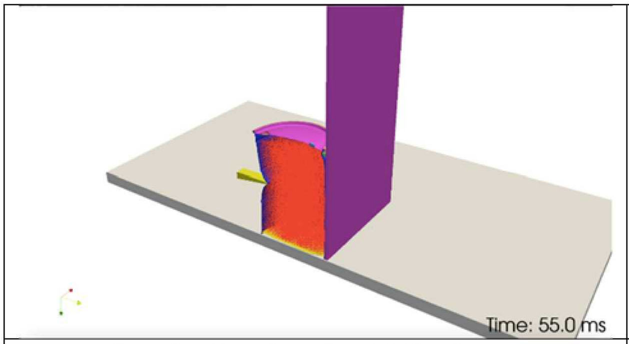

5 m/s, fixed and middle drum

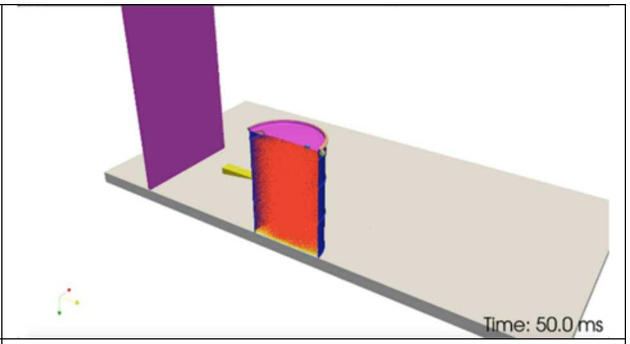

0.5 m/s, free and middle drum

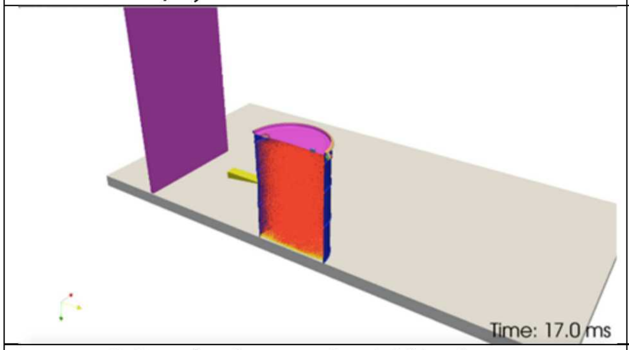

2.5 m/s, free and middle drum

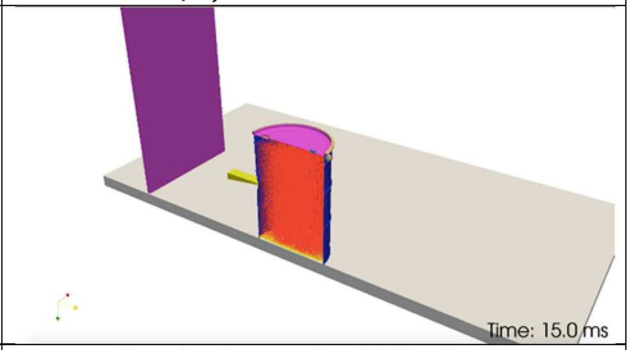

5 m/s, free and middle drum

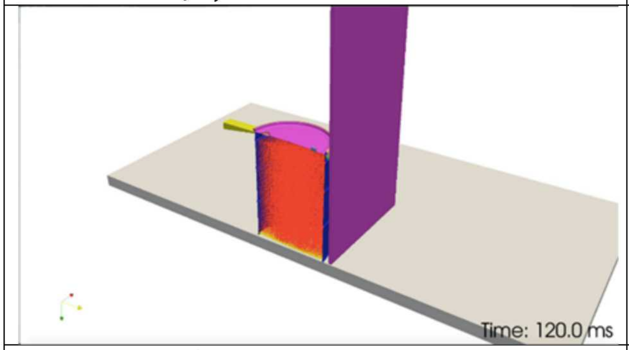

0.5 m/s, fixed and top near lid

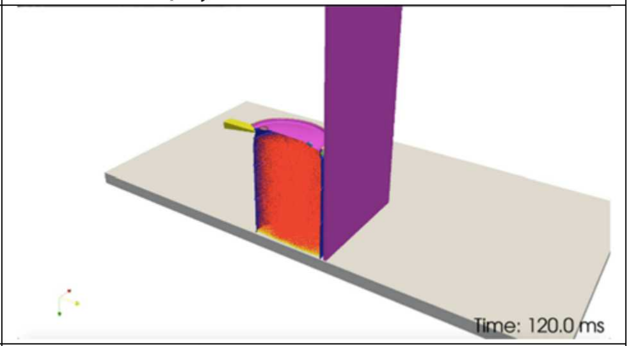

2.5 m/s, fixed and top near lid

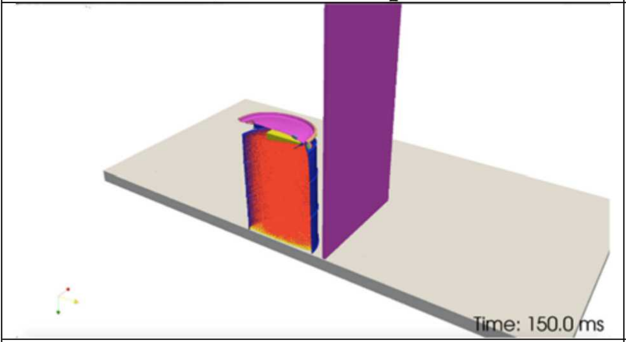

5 m/s, fixed and top near lid

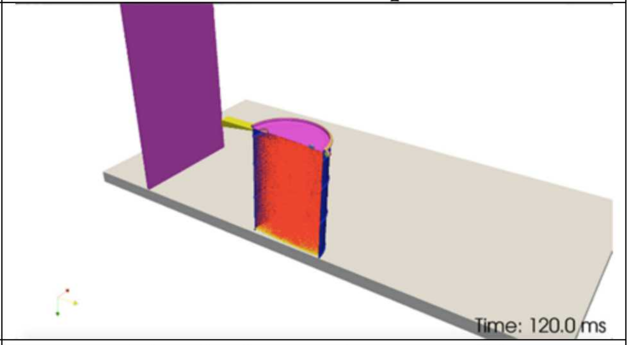

0.5 m/s, free and top near lid

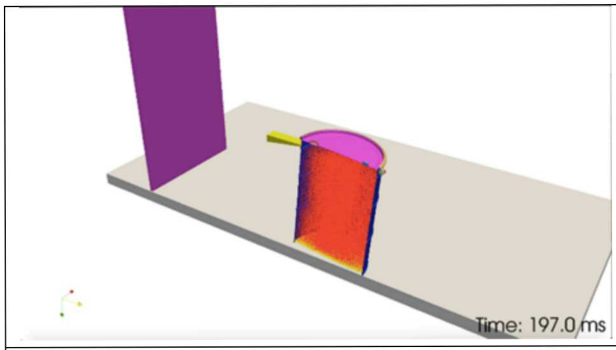

2.5 m/s, free and top near lid

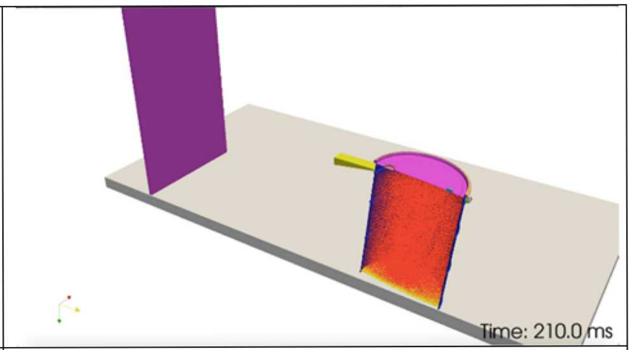

5 m/s, free and top near lid

Content Type: SI

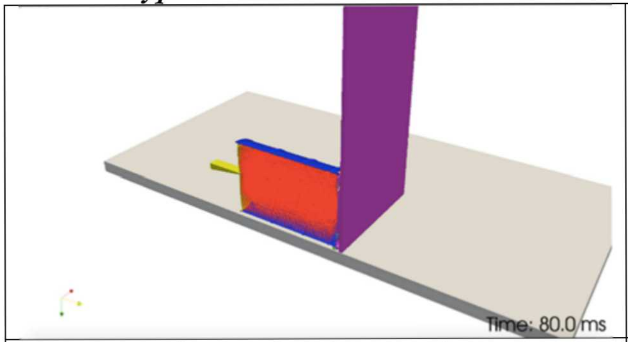

0.5 m/s, fixed and center bottom

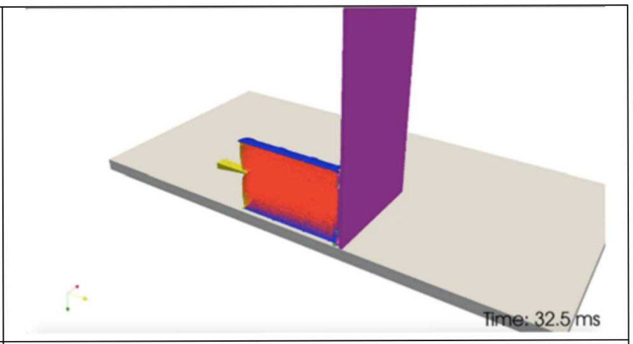

2.5 m/s, fixed and center bottom

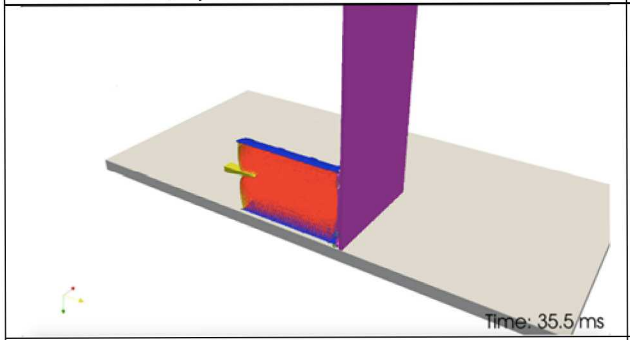

5 m/s, fixed and center bottom

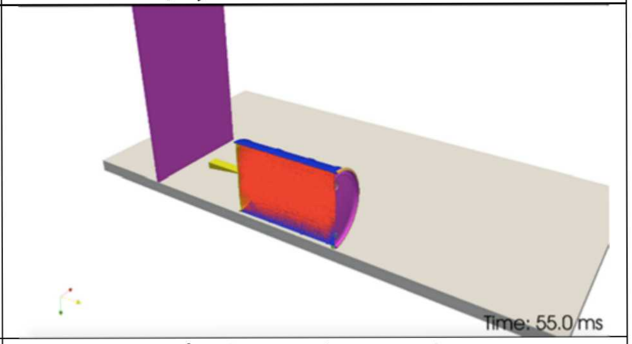

0.5 m/s, free and center bottom

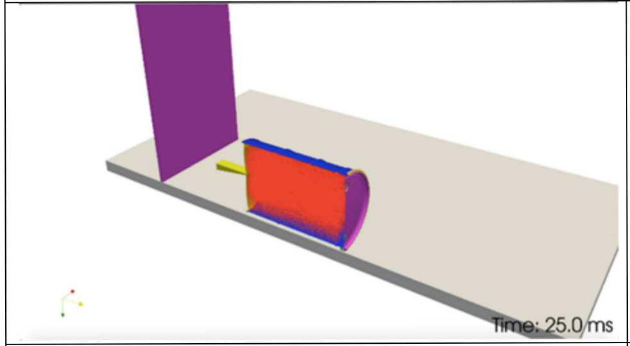

2.5 m/s, free and center bottom

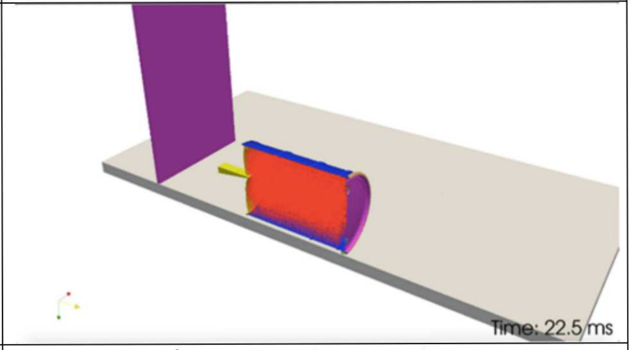

5 m/s, free and center bottom

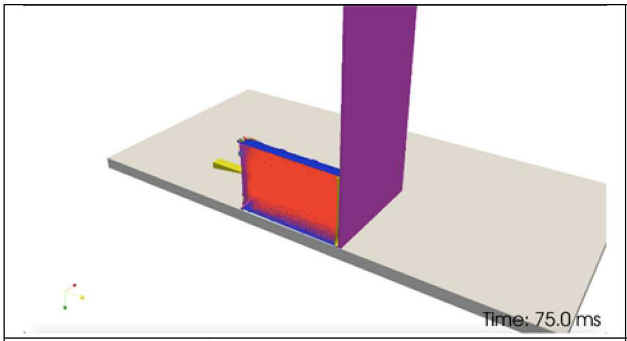	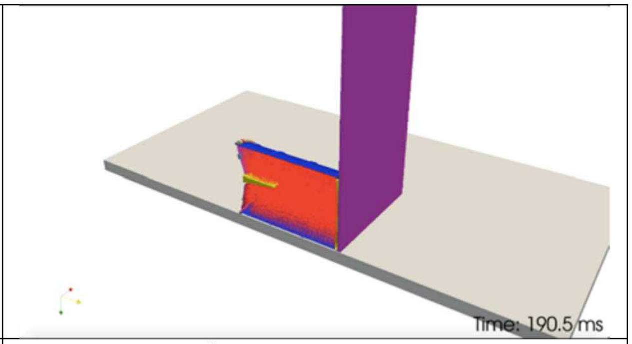
0.5 m/s, fixed and center lid	**2.5 m/s, fixed and center lid**
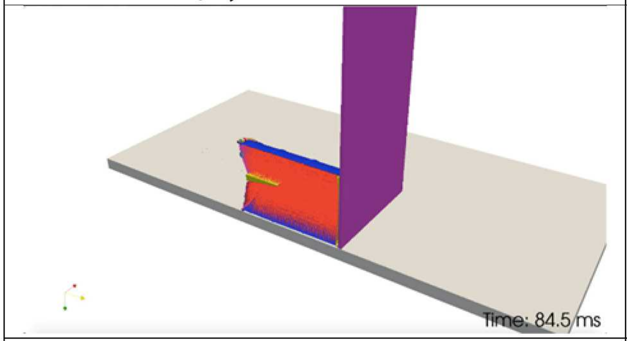	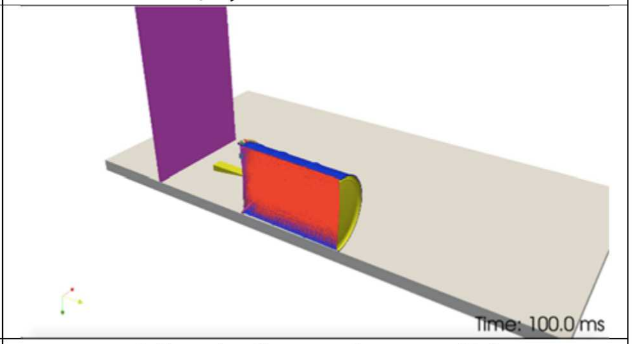
5 m/s, fixed and center lid	**0.5 m/s, free and center lid**
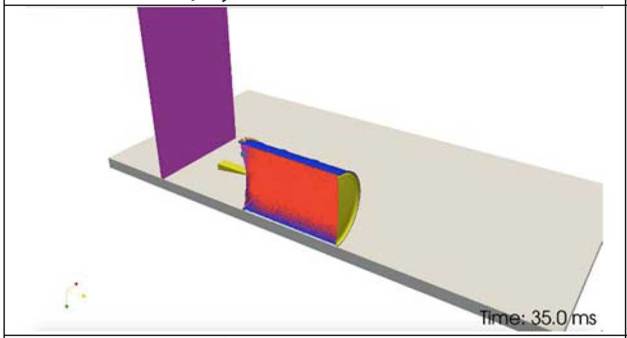	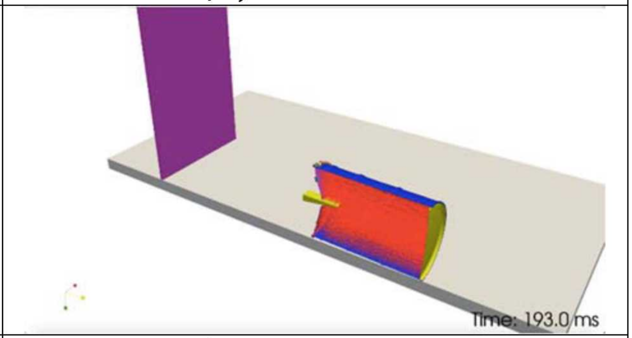
2.5 m/s, free and center lid	**5 m/s, free and center lid**
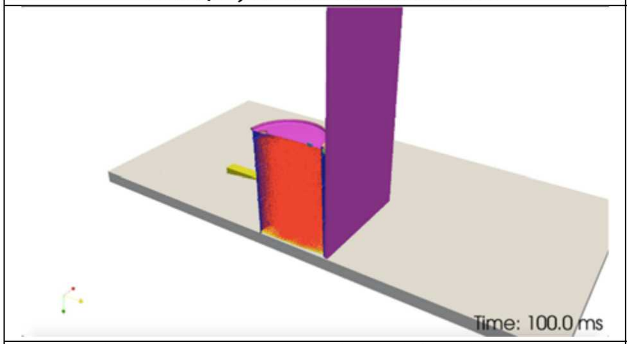	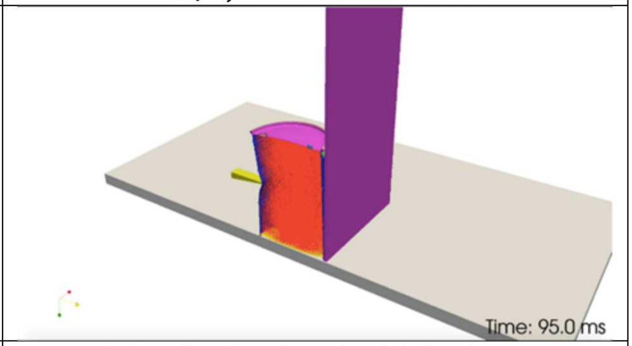
0.5 m/s, fixed and middle drum	**2.5 m/s, fixed and middle drum**

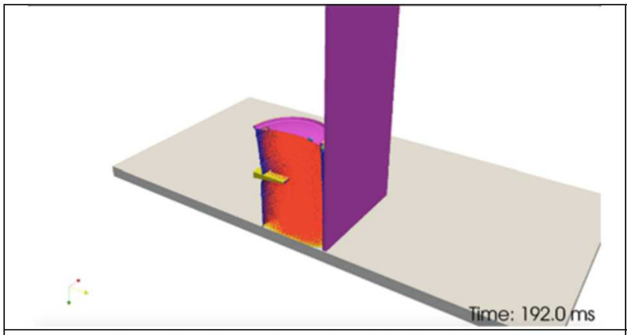	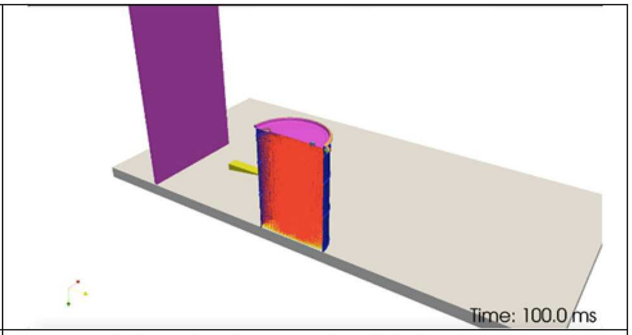
5 m/s, fixed and middle drum	**0.5 m/s, free and middle drum**
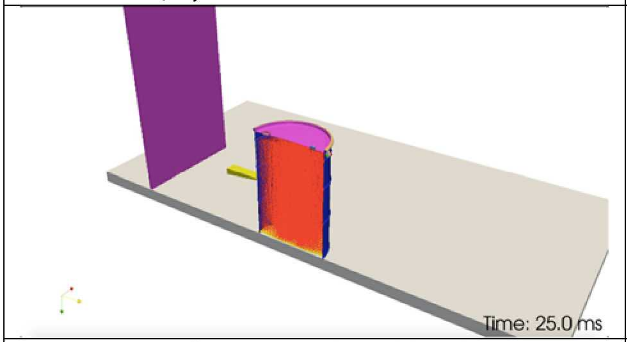	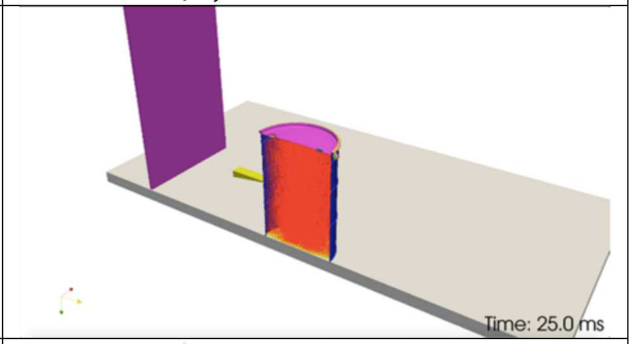
2.5 m/s, free and middle drum	**5 m/s, free and middle drum**
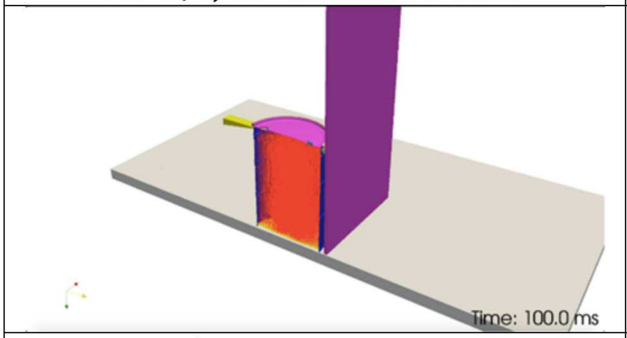	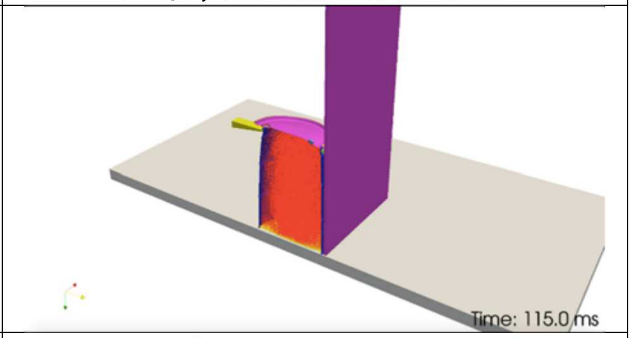
0.5 m/s, fixed and top near lid	**2.5 m/s, fixed and top near lid**
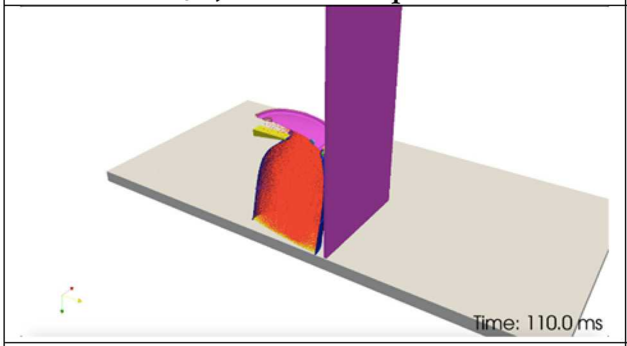	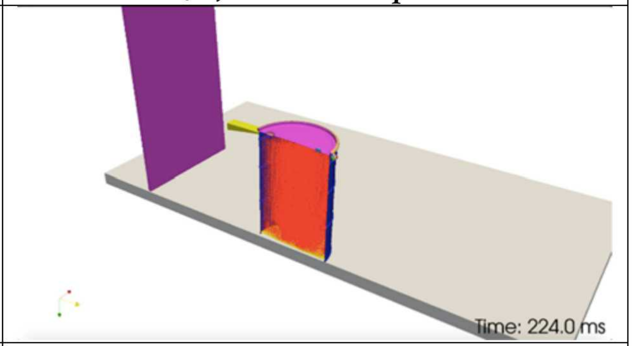
5 m/s, fixed and top near lid	**0.5 m/s, free and top near lid**

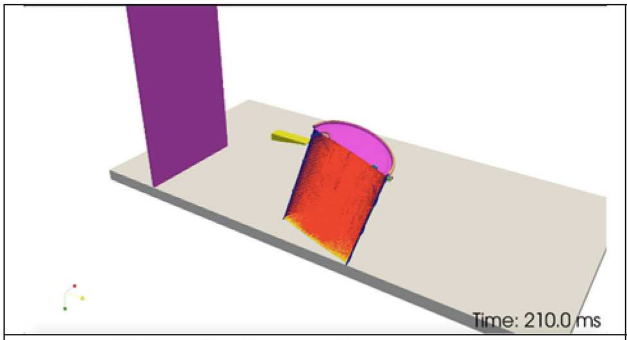	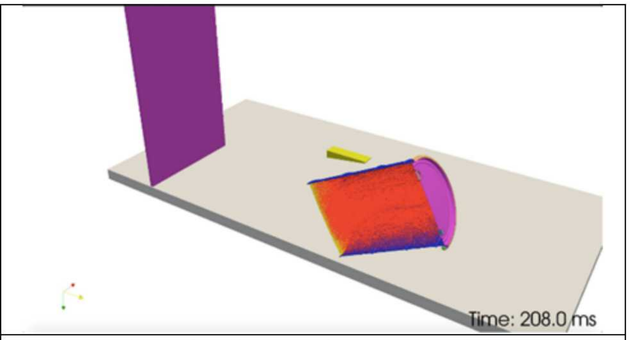
2.5 m/s, free and top near lid	**5 m/s, free and top near lid**

C.3. SWB Drop with Content Type CS

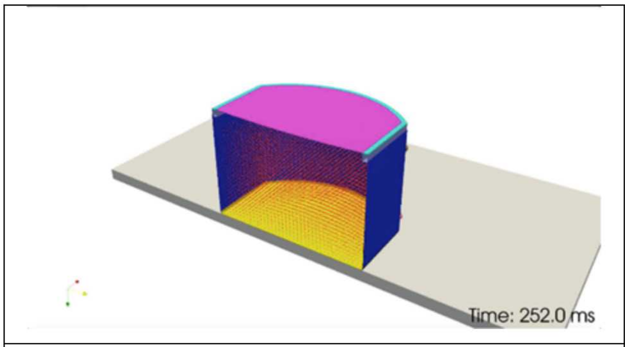	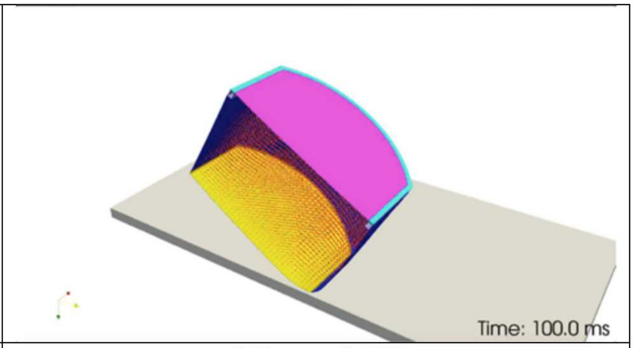
2.5 m and 0°	**2.5 m and 45°**
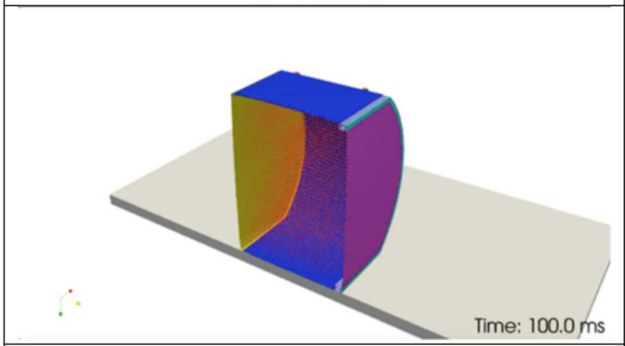	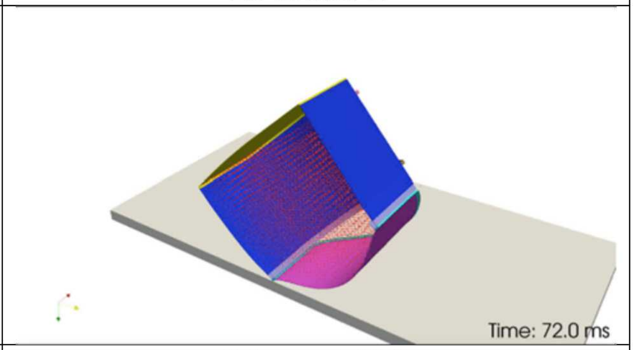
2.5 m and 90°	**2.5 m and 135°**
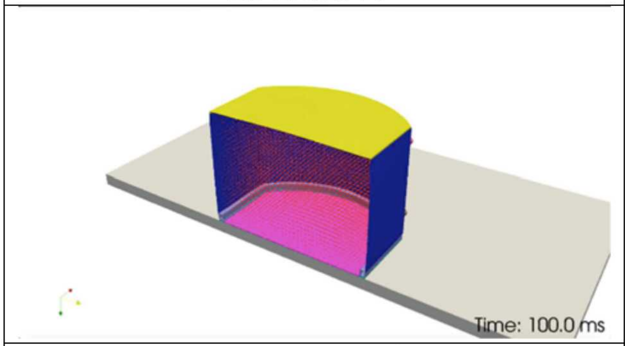	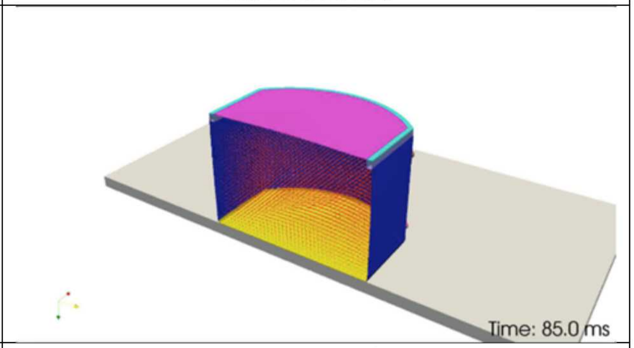
2.5 m and 180°	**5 m and 0°**

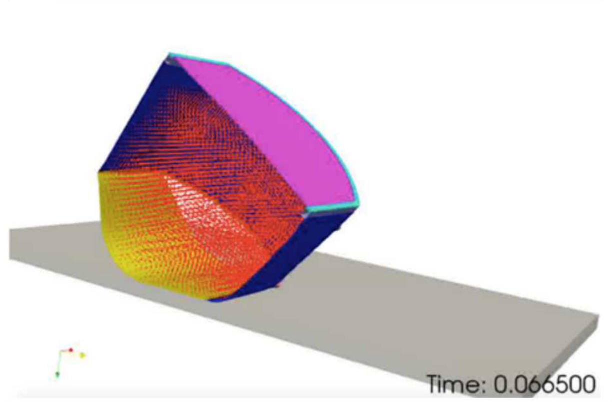

5 m and 45°

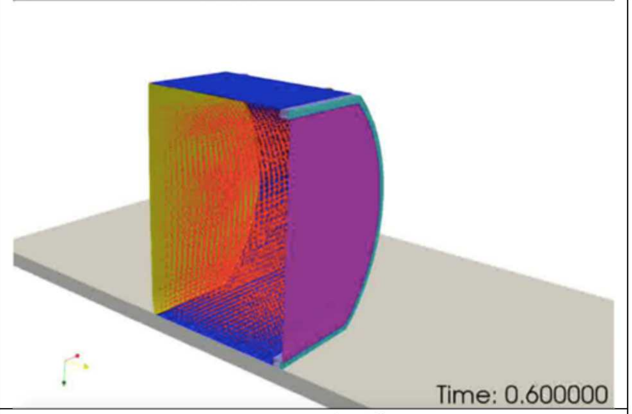

5 m and 90°

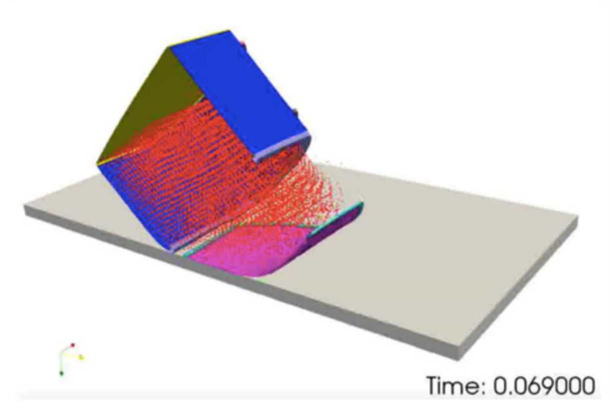

5 m and 135°

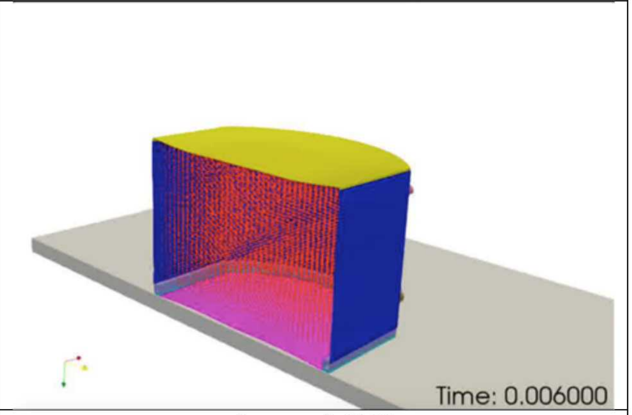

5 m and 180°

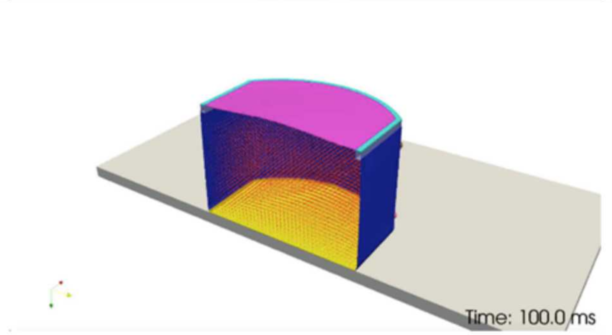

10 m and 0°

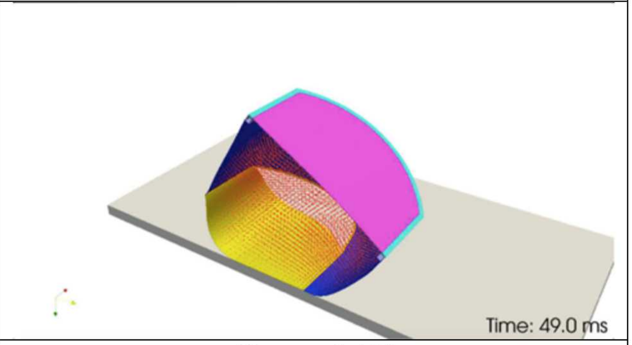

10 m and 45°

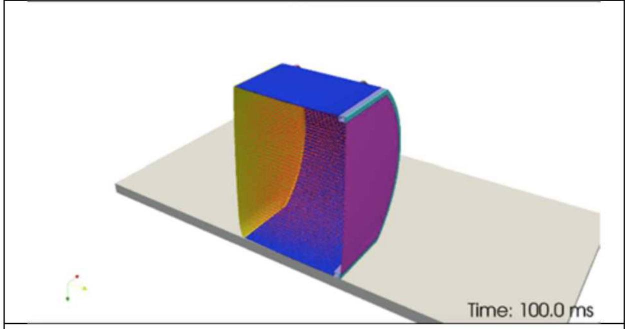

10 m and 90°

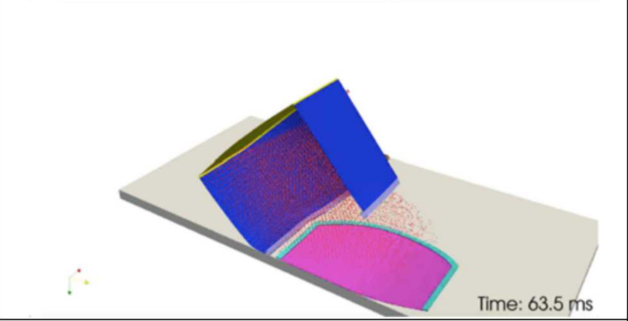

10 m and 135°

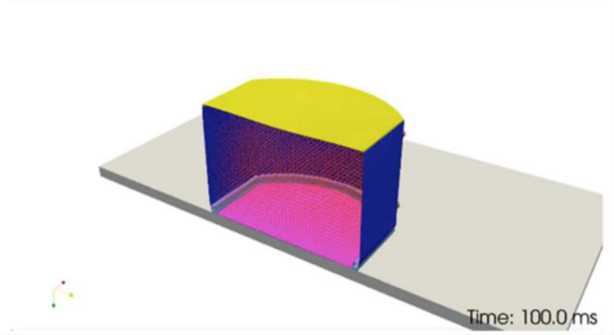	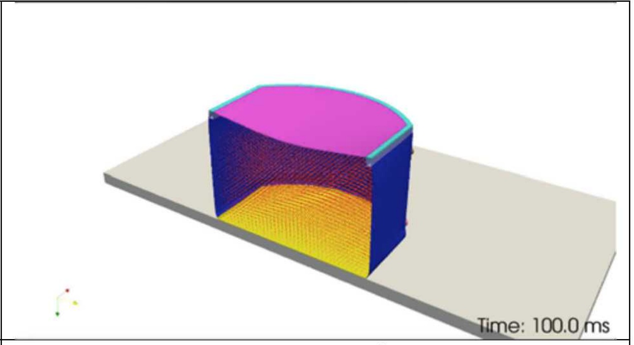
10 m and 180°	**20 m and 0°**
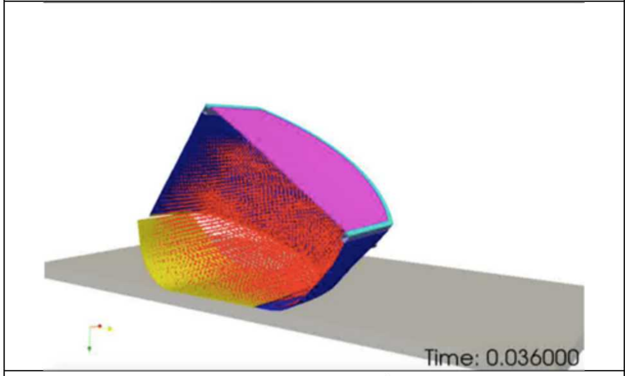	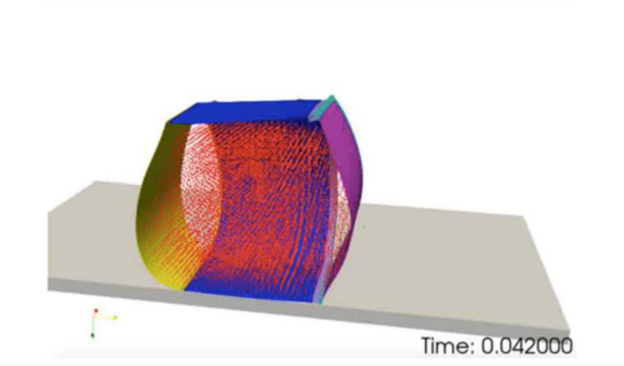
20 m and 45°	**20 m and 90°**
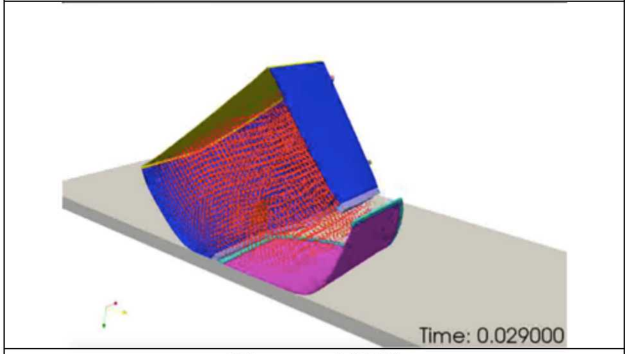	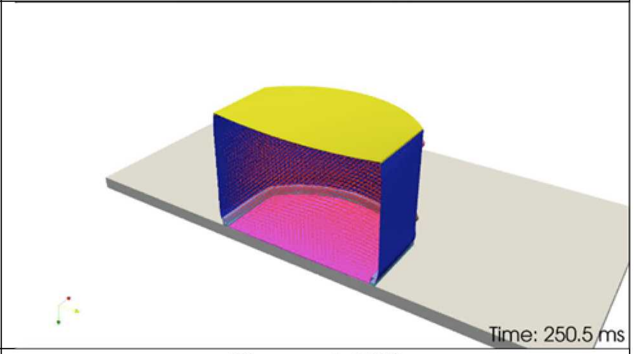
20 m and 135°	**20 m and 180°**

C.4. SWB Puncture with Content Type CS

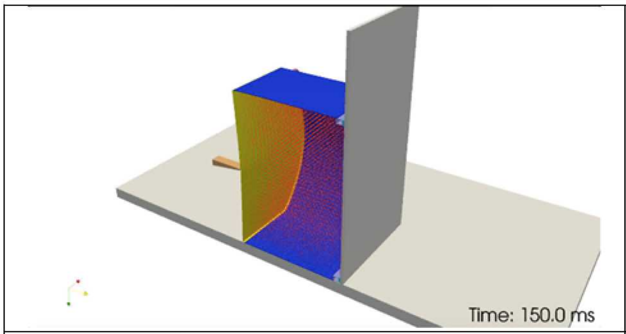	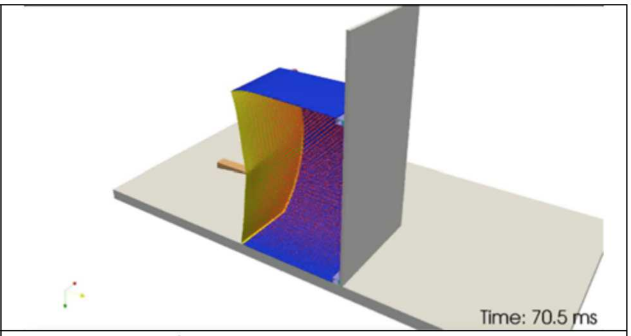
0.5 m/s, fixed and center bottom	**2.5 m/s, fixed and center bottom**
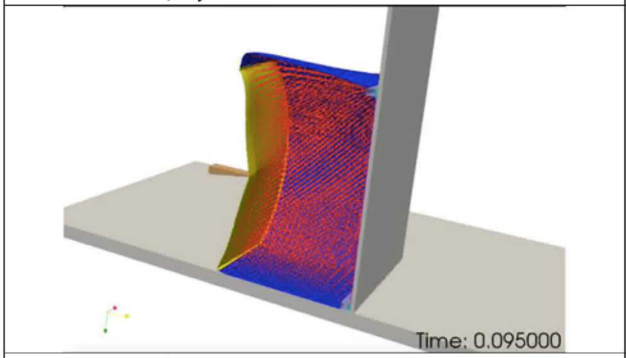	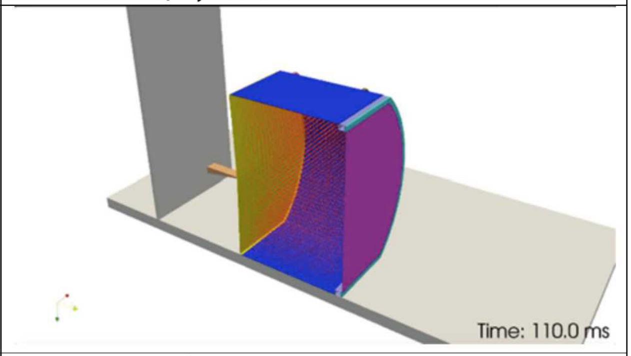
5 m/s, fixed and center bottom	**0.5 m/s, free and center bottom**
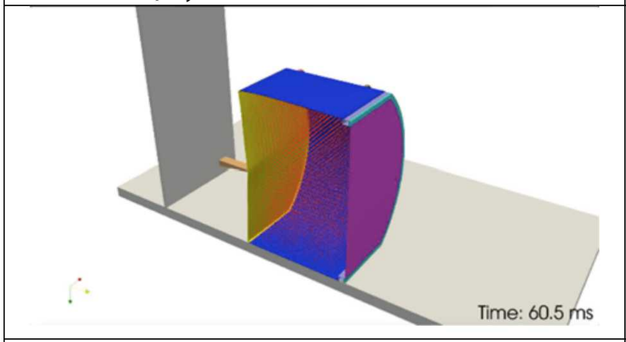	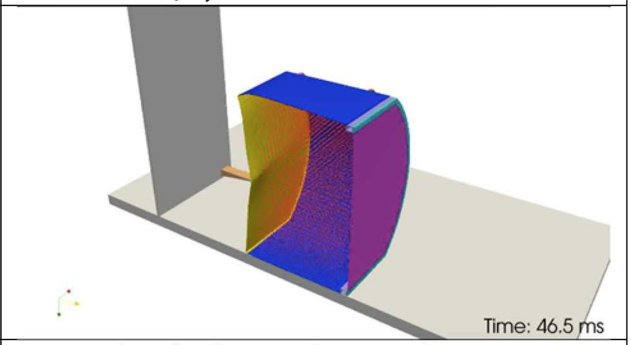
2.5 m/s, free and center bottom	**5 m/s, free and center bottom**
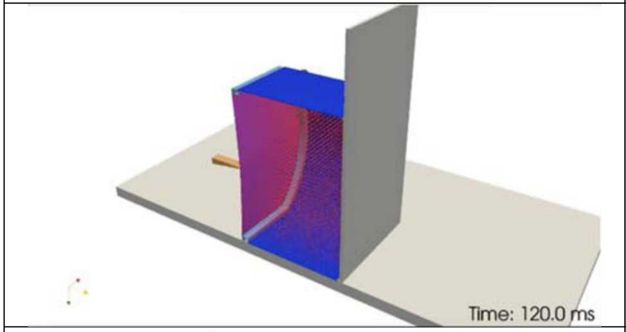	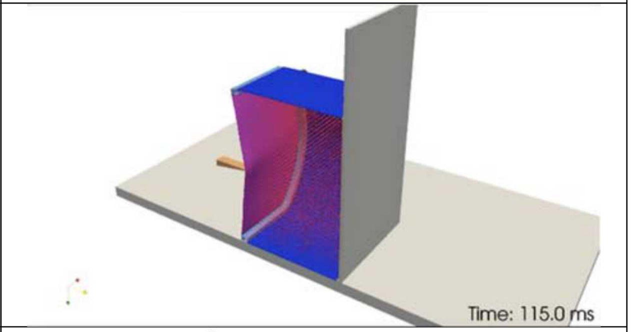
0.5 m/s, fixed and center lid	**2.5 m/s, fixed and center lid**

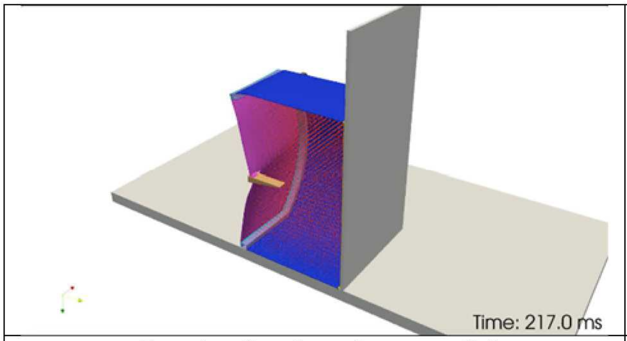

5 m/s, fixed and center lid

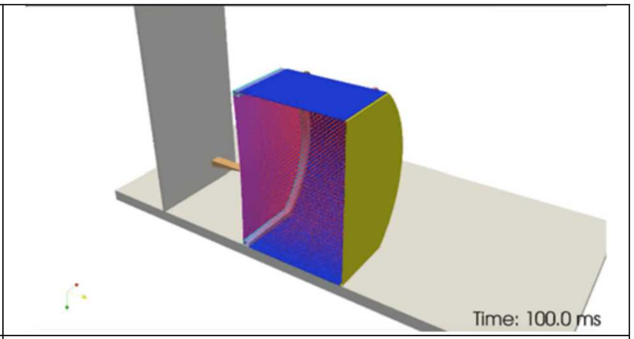

0.5 m/s, free and center lid

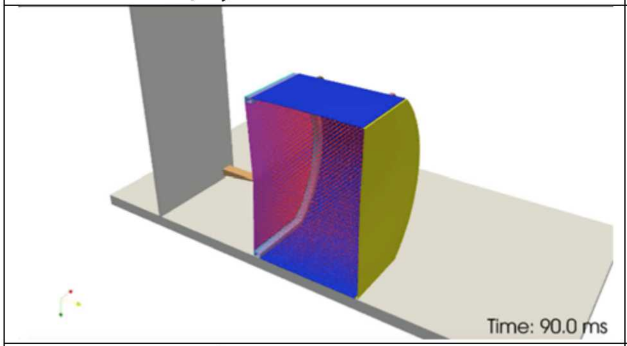

2.5 m/s, free and center lid

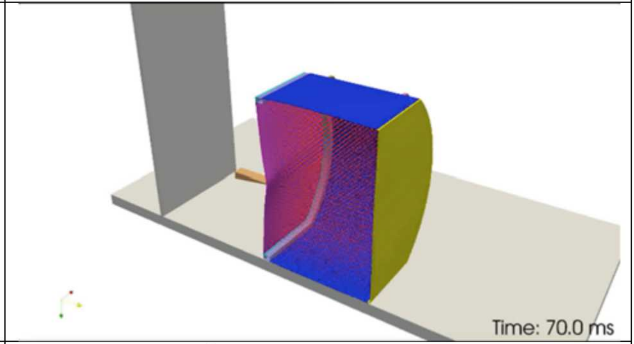

5 m/s, free and center lid

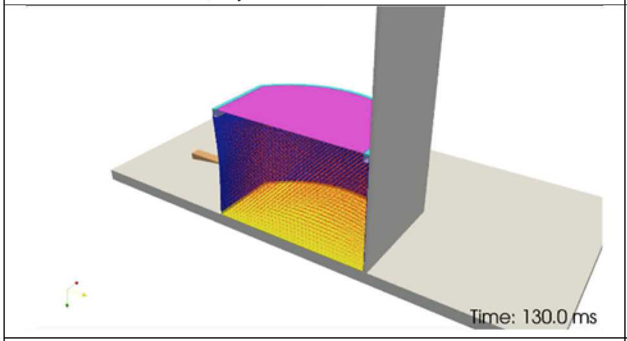

0.5 m/s, fixed and middle SWB

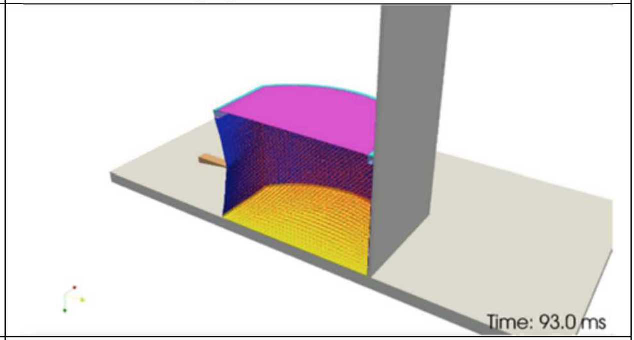

2.5 m/s, fixed and middle SWB

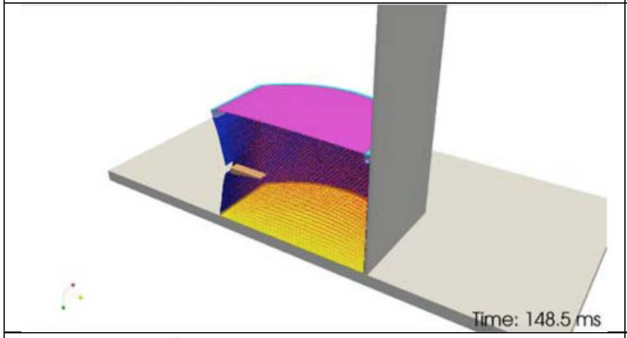

5 m/s, fixed and middle SWB

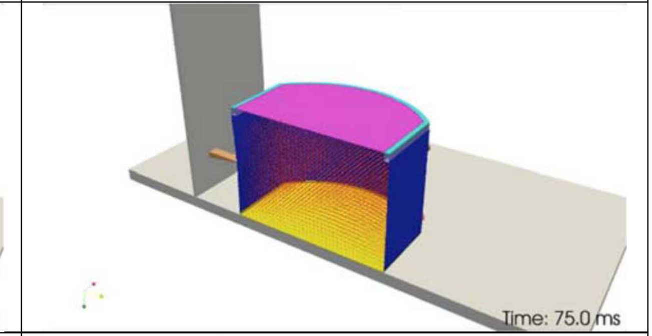

0.5 m/s, free and middle SWB

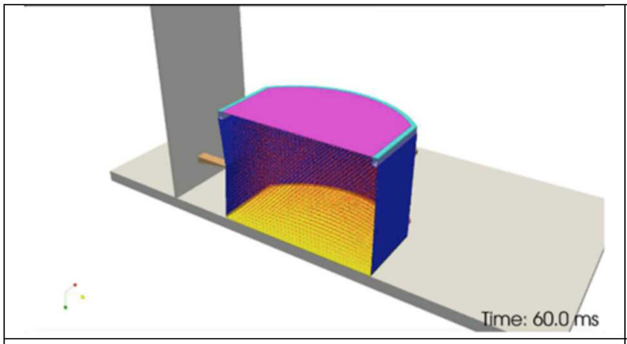	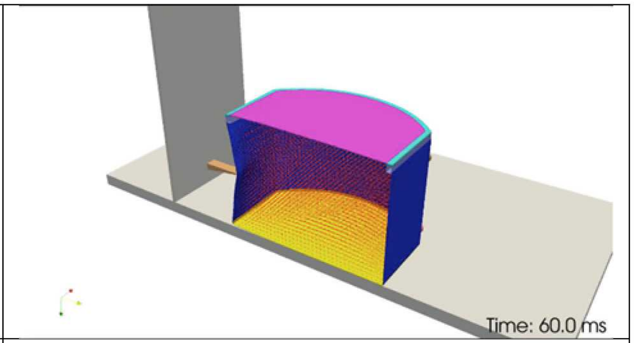
2.5 m/s, free and middle SWB	**5 m/s, free and middle SWB**
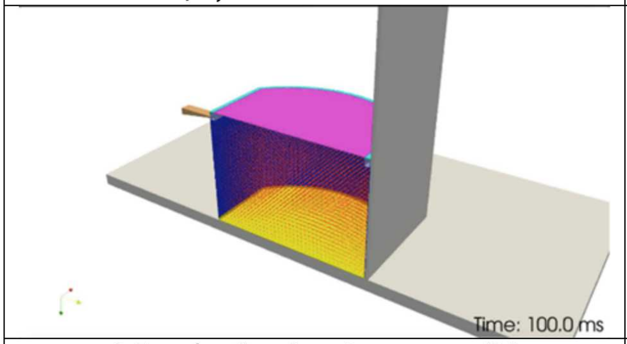	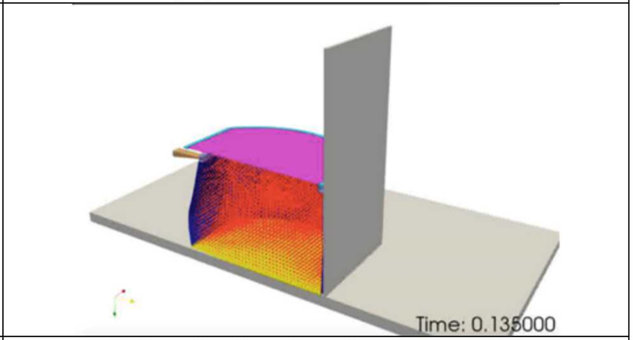
0.5 m/s, fixed and top near lid	**2.5 m/s, fixed and top near lid**
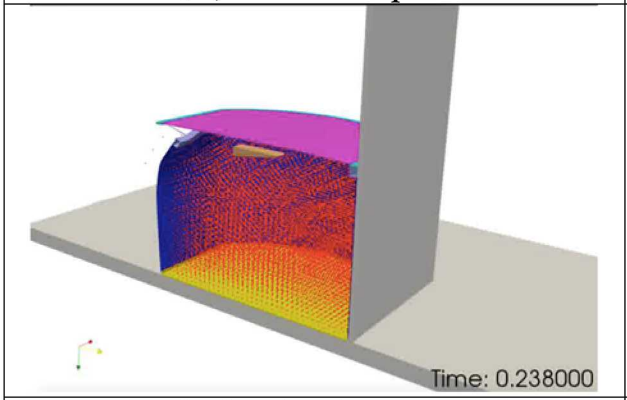	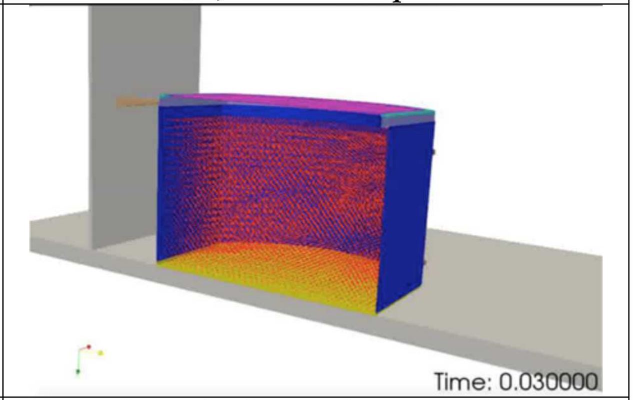
5 m/s, fixed and top near lid	**0.5 m/s, free and top near lid**
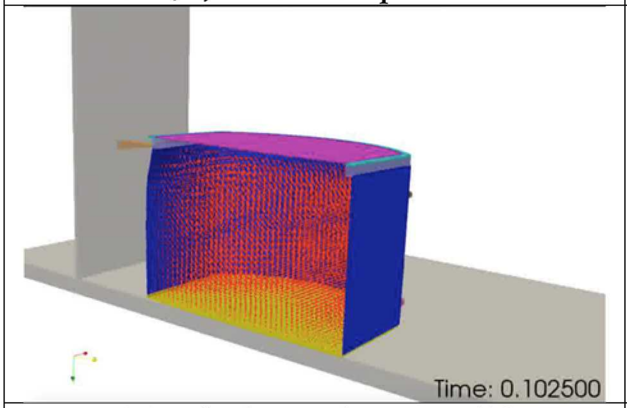	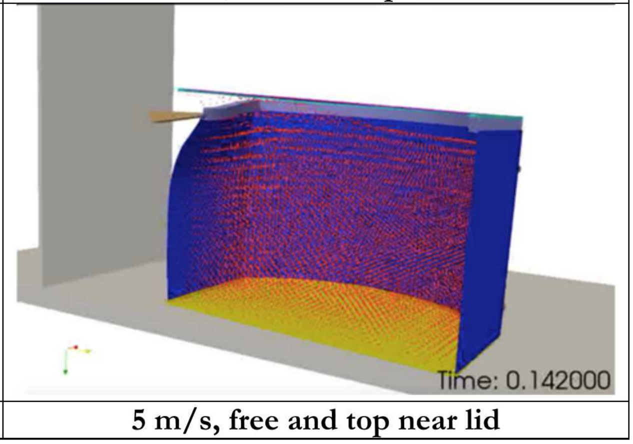
2.5 m/s, free and top near lid	**5 m/s, free and top near lid**

APPENDIX D. VALIDATION DATA FOR CHAPTER 4 ON FRAGMENTATION MODELING

This appendix describes the experimental data to be used to validate the SIERRA models developed in Section 4.1. As shown in Section 4.1, the concurrent fragmentation model involves two stages: macro-fragment and micro-fragment models. Macro-fragment model in SIERRA/SM is based on the GDE model, which are responsible the large fragment development from the impact energy onto the solids (brittle materials). The micro-fragment model is a 1-D model that considers for the fracture energy from the macro-fragment model and its predicted particles to estimate the further reduction of the larger particles into smaller particles in the micron range. The subsequent subsections describe the recent experiments on this topic. Section 4.3.1. describes an experiment to investigate the fracture methodology and graphical results of the large spherical solid, and characterize the level of fractures for the brittle spheres. This subsection is useful to test the GDE model for the macro-fragment model.

D.1. Brittle Sphere Fragment Experiment for Macro-Fragment

This section describes a paper on the crushing and fragmentation of brittle spheres under the impact test [Wu 2004] that was similar to the experiment done by [Jardine 1982]. However, unlike in [Jardine 1982], [Wu 2004] used spherical samples of brittle materials, rather than pellet type of ceramic or other brittle materials. The double impact tests were conducted using a Dynatup 8250 impact tester (see Figure D-1). The impactor apparatus for the experiment can produce the impact velocity ranging from 1 to 3.66 m/s for a gravitational drop mode. It also can produce impact velocities up to 13.41 m/s using the "pneumatically assisted mode." The mass of the impactor ranges from 2.25 to 45.34 kg, which translate into the impact energies of 0.6 to 303 J for the gravitational mode and 16.2 to 840 J for the pneumatical mode [Wu 2004]. The experiments only were conducted at impact velocities from 1.6 to 9 m/s and weight from 3.227 to 13.351 kg, which yields the impact energies from 8 to 310 J. The samples are made of a plaster made by the dental stone that yields the long-term compressive strengths at about 37 and 59 MPa for Material A and B, respectively (see Table D-1). Three sizes of spheres were used in the experiments, and their corresponding impact energy is shown in TableD-2. The results of the images from post-tests are shown in Figure D-2.

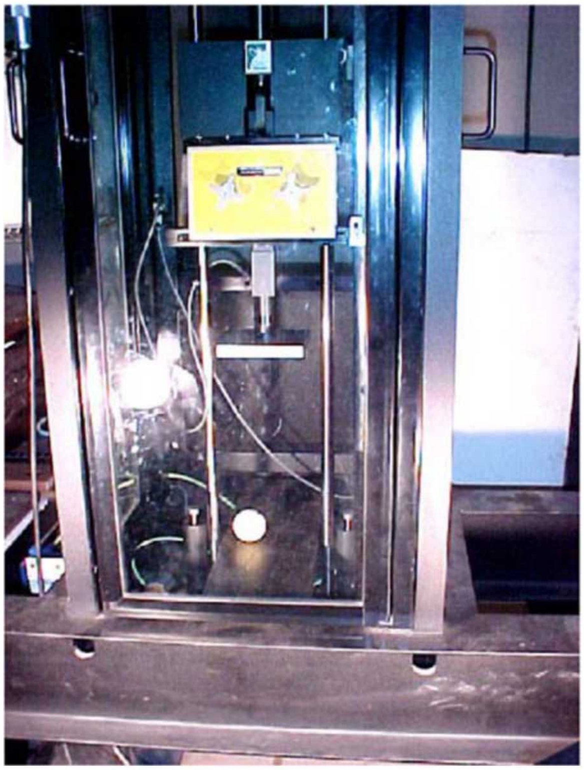

Figure D-1. Impact Apparatus to Fracture Brittle Spheres [Wu 2004]

Table D-1. Brittle Sphere Material Properties [Wu 2004]

Properties	Material A	Material B
Composition* – water content	40%	30%
Unit weight, kN/m^3	15	17.4
Young's modulus, GPa	13	20
Poisson ratio	0.22	0.26
Uniaxial compressive strength, MPa	37	59

*Dental stone powder and water mixture

Table D-2. Initial Tests of the Plaster Spheres (A and B Materials).

Sample/ Material	MPa	Diameter (mm)	Maximum Load at Failure (kN)	Total Deformation (mm)	Energy Input at Failure (J)
A	37	50	7.98	1.08	3.19
		60	12.45	1.16	5.29
		75	15.86	1.49	6.61
B	59	50	10.27	0.68	3.48
		60	13.41	0.91	6.07
		75	23.38	1.14	13.32

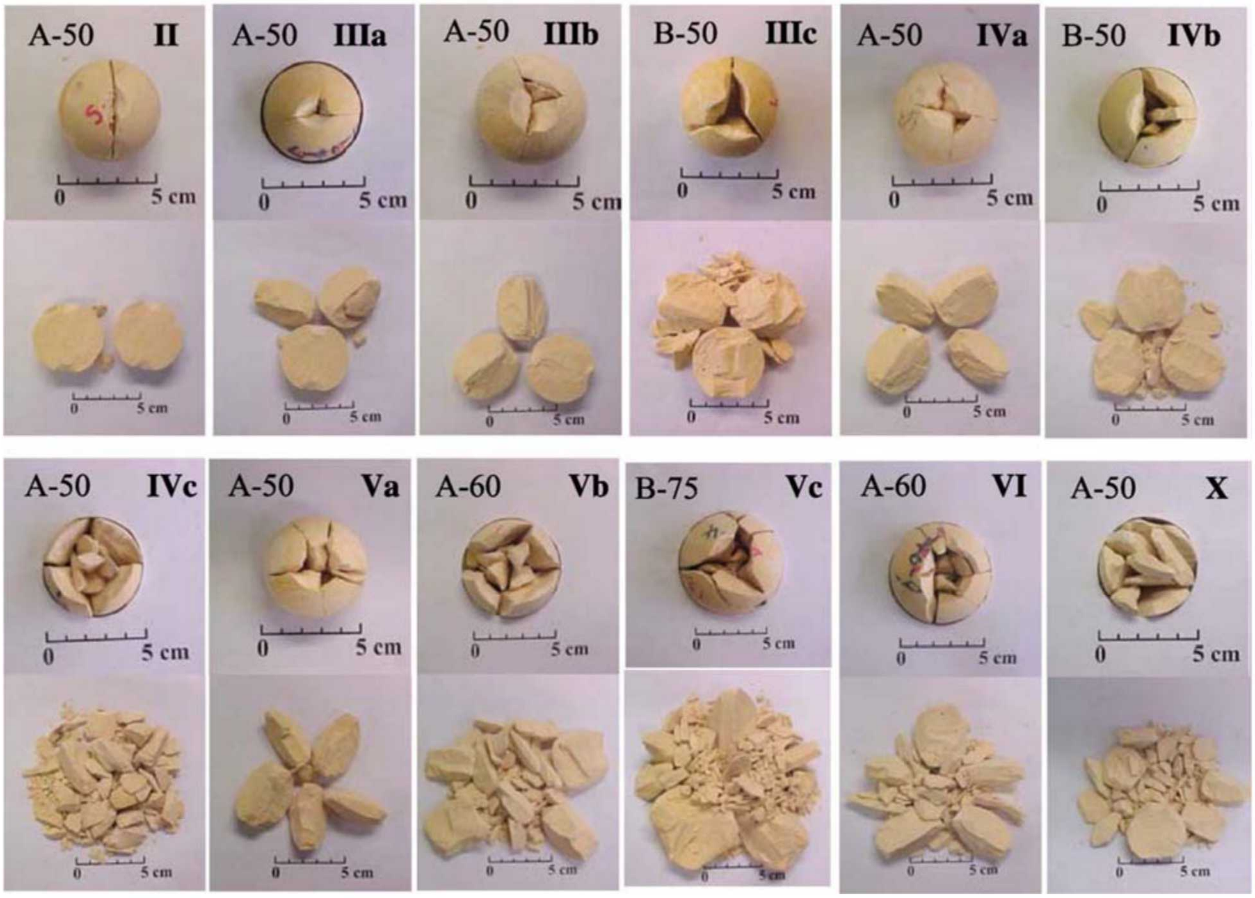

Figure D-2. Images of the Test Results. Description: Material-Diameter. The impact energy is shown in Table D-2.

APPENDIX E. USERS GUIDE FOR TWO-SCALE DAMAGE MECHANICS MODEL

In this appendix, the proposed users guide for the implementation of a micromorphic fragmentation described in Chapter 4 are provided. The sequential fragmentation material model description is provided first. Then the current proposed concurrent fragmentation material model follow.

The two-scale damage mechanics model with fragmentation implemented in LAME is accessed as HGDE (Hierarchal Gradient Damage Explicit). The material model is intended to calculate fragmentation of brittle materials with a two-scale modeling paradigm. At the continuum length-scale, the material is described using SIERRA/SM's Gradient Damage Explicit (GDE) scheme to distribute nonlocal damage evolution in the material and determine the size of the macroscale fragments produced; The resolution is limited by the length-scale inherent in the GDE approach. The unique capability of the material model described is the ability to calculate the distribution of microscale fragments. Microscale fragments are assumed to originate from elements that have exceeded the element critical stress or strain energy value according to the GDE model. Once element has exceeded this critical threshold, a microscale model solves the elasto-dynamic governing equation with a finite difference scheme. The strain rate applied to the element is supplied by the macroscale model. The length of fragments formed must be in a unit length of material defined by regularly spaced preexisting cohesive zones. The cohesive zones open upon reaching a critical stress. These cohesive zones are able to support a load in compression after separation occurs, but the loss in tensile strength is permanent. The microscale model calculates the energy dissipated and supplies this information back to the macroscale model. This model reports the resulting fragment mass distribution in the form of a histogram with the range and bin sizes specified by the user in the input file. Summary statistics (average size and standard deviation) are calculated on a per element basis.

E.1. Implementation

The two-scale fragmentation model is implemented in two separate stages. First, the GDE model is employed to calculate macroscale damage evolution in the system. Second, the 1D microfragmentation model [Louie 2017] is applied to a bar of equivalent mass for each element that exceeds a critical stress or strain energy threshold as calculated by the GDE model. After running the 1D microfragmentation model, the energy dissipated by the 1D model is used to update the fracture energy in the GDE model to ensure that the energy dissipated by both length scales is consistent.

The GDE model is implemented within SIERRA/SM and documented elsewhere. The GDE model governs the damage evolution in the material such that the GDE calculated damage is compared with the FAILURE CRITERIA to determine which elements are removed from the system. In the microscale mode, each element is represented by a 1D bar with length $L = \sqrt[3]{V}$, equivalent to the size of a cube with the same mass as the element. It is also possible for the user to specify a different 1D bar length with the same mass as the element. The 1D bar is divided into N_{seg} segments of length Δx. The value of N_{seg} is dependent on the material grain size and grain boundary thickness. A cohesive zone is assumed to exist between each segment with a cohesive law proposed by [Zhou 2005] specified for cohesive zone opening

$$\frac{\sigma_{\mathrm{coh}}}{\sigma_{\mathrm{c}}} = 1 - \frac{\delta_{\mathrm{coh}}}{\delta_{\mathrm{c}}}, \mathrm{for}\ \dot{\delta}_{\mathrm{coh}} > 0, \delta_{\mathrm{coh}} = \delta_{\mathrm{max}}$$

and for cohesive zone closing

$$\frac{\sigma_{\text{coh}}}{\sigma_{\text{c}}} = 1 - \frac{\delta_{\text{coh}}}{\delta_{\text{c}}}, \text{for } \delta_{\text{coh}} < \delta_{\text{max}}$$

where δ_{coh} and σ_{coh} are crack opening displacement and stress, σ_{c} is the critical stress, δ_{c} is the critical crack opening displacement, δ_{max} is the maximum crack opening displacement, and $\dot{\delta}_{\text{coh}}$ is the rate of crack opening.

The strain energy calculated by the continuum model is used to calculate an equivalent 1D strain, and then the equivalent 1D strain rate. The 1D strain rate is used to update the boundary conditions of the 1D fragmentation model that will be run for as many microscale timesteps (based on the speed of sound and minimum fragment size) as necessary to reach the next continuum timestep.

As soon as the maximum principle stresses in an element reaches or exceeds the critical stress for fracture, the direction of applied stress is recorded so that only the component of tension in that direction can cause opening of the cracks. This choice was made to ensure that once cohesive zones begin to separate (cracks start to form) they will effectively concentrate stress and suppress crack formation in other directions.

SIERRA/SM provides the strain tensor for the present time-step to the material model: ϵ_i. The continuum stress is calculated from the continuum strain at the current time-step *i* without damage as $\sigma_i = E\epsilon_i^{el}$. This is accomplished by directly calculating the stress from the given strain without applying the damage. The microscale model is initiated upon an element stress exceeding the element critical stress value (for the stress-based approach) or the critical strain energy (for the strain energy based approach) as defined as $\hat{\psi}_c = \frac{1}{2}\sigma_c^2 / E$, with E as Young's modulus. At this point, the direction of applied stress ς is stored and the current continuum state of stress is projected onto that direction thereafter.

The strain applied to the microscale model is calculated at the current time-step as

$$\epsilon_i = \frac{\sigma_i \cdot \varsigma}{E}$$

The strain-rate projected from the macroscale model $\dot{\epsilon}_\iota$ is provided by SIERRA/SM at a mid-step value. The strain-rate at the current timestep $\dot{\epsilon}_{\iota-1}$ therefor calculated consistent with the 1D strain by using the prior value of the 1D strain ϵ_{i-1} to calculate the current value of strain rate,

$$\dot{\epsilon}_i = \frac{\epsilon_i - \epsilon_{i-1}}{\Delta t}$$

The microscale fragmentation model then calculates the evolution of cohesive-zone opening and stress in the bar. This microscale damage in each cohesive-zone is used to update the value of the fracture energy at the next timestep as described previously.

E.2. User Guide

This guide is intended to assist the user in controlling the model, what is computed, and how to interpret the information provided by the model.

Results are reported as state variables. Summary statistics of the resulting fragmentation distributions (mean and standard deviation of fragment size along with the total number of fragments) are provided for visualization or postprocessing. Due to limitations in the number of state variables that may be stored, and the fact that the total number are not known ahead of time, it is not possible to output the length and mass of individual microfragments. Instead, the material model creates a histogram using user supplied parameters to more compactly represent the resulting fragment size distribution.

E.2.1. Prerequisites

Element Death must be handled by the material model by including the command material criterion = on| in the material death block. Other death conditions can be added, such as death on inversion, minimum timestep, or nodal Jacobian ratio limits, but are not required.

The material model requires the use of Gradient Damage block within the region specification.

```
begin gradient damage
 initial value = 0.0
 solve explicit = on
end
```

In order for the provided post-processing script to capture the full range of fragments produced, the resulting macroscale fragments must also be reported. This is done through a built-in feature of SIERRA/SM that is invoked using the following block within the results output block:

```
begin identify fragments
 output file = out.frag
 increment = 1.0e-6
end
```

Make sure to output the macroscale fragments at the same interval as the microfragmentation data is reported to ensure consistency.

E.2.2. Material Model Inputs

There are a number of mandatory material properties and reporting parameters that must be provided.

YOUNGS MODULUS: Alternatively, provide LAMBDA and SHEAR MODULUS in lieu of Young's Modulus.

DENSITY: Density of material.

FRACTURE ENERGY: (G_c) Fracture Energy of material.

CRITICAL STRESS: (σ_c) Critical Stress to cause crack formation (cohesive zone opening stress).

FRACTURE LENGTH SCALE: Characteristic length scale for the gradient damage model. Recommended length is approximately at least three times the nominal element size.

COHESIVE SHAPE: Parameter needed for parameterizing gradient damage model. A positive sign indicates that the strain energy approach is being used. A negative sign indicates that the stress-based approach is being used.

PHASE VISCOSITY SCALE FACTOR: Parameter needed for parameterizing gradient damage model.

MAX MICROFRAGMENTATION STEPS: Number of timesteps to run the 1D microfragmentation model. Parameter used to prematurely stop the 1D fragmentation model. It is recommended to be set to a very large number (1e+20) unless the 1D microfragmentation model needs to be limited.

KILL ELEMENT IF 1D BAR BREAKS: Used to enable or disable element death if the 1D bar breaks into two or more fragments. It is recommended to set this parameter as FALSE.

USE CUSTOM 1D BAR LENGTH: Used to enable or disable the option to set the length of the 1D bar in the microfragmentation model to a user specified value.

CUSTOM 1D BAR LENGTH: Length of the 1D bar in the microfragmentation model, if USE CUSTOM 1D BAR LENGTH is set as TRUE. If USE CUSTOM 1D BAR LENGTH is FALSE, this value will be ignored.

MAX ELEMENT 1D SEGMENTS: Maximum number of anticipated segments in the 1D bar, used to initialize the state variables associated with the microfragmentation model. If this value is too small, SIERRA/SM will output the number of segments calculated in the 1D bar and exit with an error.

AVERAGE GRAIN SIZE: Parameter used to determine the number of segments in the 1D bar. See [Louie 2018] for details how this is used.

GRAIN THICKNESS: Parameter used to determine the number of segments in the 1D bar. See [Louie 2018] for details how this is used.

CRITICAL STRESS SHAPE FACTOR: Shape parameter of Weibull function used to determine the distribution of the critical stress values in the microfragmentation model. See [Louie 2018] for details how this is used.

BIN MIN: Minimum fragment size that will be included in the mass histogram of microscale fragments. It is recommended to set this value equal to the spatial resolution of the 1D model MIN FRAGMENT SIZE.

BIN MAX: Maximum length of fragment that will be included in mass histogram of microscale fragments. It is recommended to set this value to L_{bar} or smaller.

NBINS: Number of bins (N_{bins}) to use in histogram to report results over the range BIN MIN to BIN MAX.

HIGH RESOLUTION BINS: Number of bins for the high-resolution portion of the histogram in the low mass (length) region. Must be less than or equal to NBINS.

HIGH RESOLUTION LIMIT: Size of largest bin included high resolution portion of the histogram in the low mass (length) region.

FAILURE CRITERIA: Value of stress degradation, $1 - d$, that will result in element death and initiation of the microfragmentation model.

E.2.3. Available Outputs

The state variables available for output, on a per-integration point basis, are described below.

ELASTIC STRAIN ENERGY: Local value of elastic strain predicted by FEM model without damage. This quantity is equated to 1D model's strain energy, so damage cancels.

FRAG N TOTAL: Number of possible fragments $\leq N_{seg}$.

FRAG N PARTIAL: Number of damaged cohesive zones that are still able to bear load in tension.

FRAG N BROKEN: Number of completely damaged cohesive zones that are unable to sustain tensile load.

FRAG N CRITICAL: Number of cohesive zones where the stress has exceeded the critical stress to initiate separation of the zone.

FRAG AVERAGE SIZE: Average fragment length at integration point.

FRAG STD DEVIATION: First standard deviation of average fragment length.

FRAG ELEMENT MASS: Mass of integration point that is conserved throughout the execution of the model.

FRAG M UNDER: Total mass of fragments of length less than BIN MIN.

FRAG M OVER: Total mass of fragments of length greater than BIN MAX.

CRITICAL STRESS: Initially set equal to the material parameter of the same name but stored in a state variable to be available for modification.

FRACTURE ENERGY: Initially set equal to the material parameter of the same name but stored in a state variable to be available for modification.

DAMAGE DRIVING ENERGY: Energy driving the evolution of the Gradient Damage model.

HISTOGRAM BIN: Total mass of fragments contained in a bin of the histogram generated from data provided in the material properties specification. Note that each bin must be requested separately as HISTOGRAM BIN 0, HISTOGRAM BIN 1, etc., with a maximum index of $N_{bins} - 1$.

E.3. Post-Processing Scripts

After executing the model, the extract_histogram.py script must be executed to extract the fragment size histogram and other relevant data. The data can then be summarized and plotted using the plot_fragmentation_histogram.py script. Both scripts require certain outputs be included in the EXODUS file generated by SIERRA/SM.

The extract_histogram.py script uses SIERRA/SM python tools, so it must be executed where these are available and in PYTHON's path. In the listings below, default values for the parameters (if present) are provided within [ ]. The extract_histogram.py script has the options:

-h, --help: show this help message and exit

Mandatory Mutually exclusive options (c/s):
-c, --concurrent: Assume HGDE Material Model
-s, --sequential: Assume MicroFragmentation Sequential Material Model

Optional Arguments:
-ep EPATH, --epath EPATH: Local path to the directory containing exodus files to be processed. [current working directory]
-e [EFILES [EFILES ...]], --efiles [EFILES [EFILES ...]]: Exodus files to be processed (if not specified, script searches for *.e*.* or *.e files)
-r REXT, --rext REXT: Restart file extension used to filter exodus files for processing. [none]
-b FRAC_BLOCK, --frac_block FRAC_BLOCK: Define block ID to be processed
-n NBINS, --nbins NBINS: Number of histogram bins [50]
-v, --verbose: Increase verbosity
-t, --time: Pick time step [last]
--bins_lo BINS_LO: Minimum Length Bin [0 m]
--bins_hi BINS_HI: Maximum Length Bin [500.0e-6 m]

The plot_fragmentation_histogram.py post-processing script calculates and plots fragment size distribution histogram and the cumulative mass distribution. Many options are available for post-processing and generating the plots. Arguments available to this command-line tool are listed below:

-h, --help: show this help message and exit

Mandatory Mutually exclusive options (c/s):
-c, --concurrent: Assume HGDE Material Model
-s, --sequential: Assume MicroFragmentation Sequential Material Model

Optional Mutually exclusive options (m/M):
-m, --micro: Plot only MicroScale Fragments
-M, --Macro: Plot only MacroScale Fragments

Mandatory Arguments:
-t THICKNESS, --thickness: Thickness of ceramic [20e-6 m]
-d INPUT_DATA, --input_data: Input datafile (*.data from extract_histogram.py)

Optional arguments:
-b FRAG_BLOCK, --frag_block: Block name of pellet [string: block_100]
--bin-min BIN_MIN: Minimum bin size of histogram [default reads from data file] (bin_min in SIERRA input)
--bin-max BIN_MAX: Maximum bin size of histogram [default reads from data file] (bin_max in SIERRA input)
-e, --exp: Plot experimental data? Choose: Jardin 1982: {UO2,pyrex}, Kraftwerk Union: {210,1050,5250,9502}
-f FRAGFILENAME, --fragfilename: Specifies fragment file generated by SIERRA/SM
--high_res_limit HIGH_RES_LIMIT: Maximum Fragment length of high resolution region [20um]
--high_res_bins HIGH_RES_BINS: Number of high resolution bins [20]

-k, --cut: Cut-off last bin (prevent spike)?
-l LBAR, --lbar: Length of 1D bar [1000.0e-6 m] (LBAR or Max Fragment Size in SIERRA input, needed for sequential analysis option only)
--logy: Make number of particle y-axis logarithmic
-n, --norm_length_hist: Normalize the length histogram by the total number of fragments
-p RHO, --rho RHO: Density of ceramic [10500.0 kg/m^3]
--time TIME: Enter time to find [last time in seconds]
--two-scale TWO_SCALE: Use two-scales for fragment lengths
-w DIAM, --diam: Diameter of pellet [13.7e-3 m]
--xlim_rate XLIM_RATE X: Limits of strain rate histogram
--ylim_rate YLIM_RATE Y: Limits of strain rate histogram
-y YLIM YLIM, --ylim Y: Limits of histogram [0-1e6 scale]
--ylim_mass YLIM_MASS Y: Limits of histogram [1e-8 to 1 default, set to [0,0] for autoscale]

E.4. Notes

The element type used with this material model should contain only a single integration point. If more than one integration point is present, the 1D fragmentation analysis will be applied to each integration point separately. This will result in inconsistent behavior as the fragment mass distribution is generated assuming that each material point has the same mass as the element.

This page left blank

DISTRIBUTION

Hardcopy—External

Number of Copies	Name	Company Name and Company Mailing Address
2	U.S. Department of Energy Office of Nuclear Safety - Nuclear Safety R&D Program	Attn: Alan Levin, NSR&D Program Manager 1000 Independence Avenue, SW Germantown, MD 20585
2	U.S. Department of Energy Office of Nuclear Safety Basis and Facility Design (AU-31)	Attn: Patrick Frias, NSR&D Project Manager 19901 Germantown Road (AU-31) Germantown, MD 20874
1	U.S. Department of Energy Office of Nuclear Safety	Attn: Garrett Smith, Director, Office of Nuclear Safety 1000 Independence Avenue, SW Germantown, MD 20585
1	U.S. Department of Energy Office of Nuclear Safety Basis and Facility Design (AU-31)	Attn: Pranab Guha, Director, Office of Nuclear Safety Basis and Faclity Design 19901 Germantown Road (AU-31) Germantown, MD 20874
1	U.S. Department of Energy Office of Nuclear Safety Basis and Facility Design (AU-31)	Attn: Caroline Garzon 19901 Germantown Road (AU-31) Germantown, MD 20874
1	U.S. Nuclear Regulatory Commission Office of Nuclear Material Safety and Safeguards	Attn: Wendy Reed, Division of Spent Fuel Management/LTSF Mail Stop TWFN 4 B34 Washington DC, 20555-0001
1	U.S. Nuclear Regulatory Commission Office of Nuclear Regulatory Research, Environmental Transport Branch	Attn: Mark Fuhrmann Mail Stop TWFN 10 A12 Washington, DC 20555-0001
1	Louis F. Restrepo Vice President, Business Development	Atkins Nuclear 1100 Rhode Island St. NE Albuquerque, NM 87110
1	Jose R.O. Munoz Assistant Manager for Operations	DOE-NNSA, Los Alamos Field Office 3747 West Jemez Road Los Alamos, NM 87544
1	James Leslie Clark, Deputy Group Leader – Safety Basis	Los Alamos National Laboratory Mail Stop E578 Los Alamos, New Mexico 87544

Email—Internal

Number of Copies	Name	Org.	Mailstop
1	MS0346	Natalie Gordon	1553
1	MS0721	Carol L. Adkins	8800
1	MS0736	Richard O Griffith	8850
1	MS0748	John Bignell	6621
1	MS0744	Patrick D. Mattie	8853
1	MS0748	Randall O. Gauntt	8852
1	MS0748	David L.Y. Louie	8852
1	MS0747	Dominic Fascitelli	8853
1	MS0748	Lindsay Gilkey	8853
1	MS0748	San Le	8853
1	MS1315	Remi Dingreville	1881
1	MS0899	Technical Library	(electronic copy)

This page left blank

Sandia
National
Laboratories